Dissertation zur Erlangung des Doktorgrades
der Fakultät für Chemie und Pharmazie
der Ludwig-Maximilians-Universität München

Development and Application of Software for Analyzing Advanced Fluorescence Spectroscopy Data

Waldemar Schrimpf

aus

Karaganda, Kasachstan

2016

Erklärung

Diese Dissertation wurde im Sinne von §7 der Promotionsordnung vom 28. November 2011 von Herrn Prof. Don C. Lamb, PhD betreut.

Eidesstattliche Versicherung

Diese Dissertation mit dem Titel "Development and Application of Software for Analyzing Advanced Fluorescence Spectroscopy Data" wurde eigenständig und ohne unerlaubte Hilfe erarbeitet.

München, den 01.08.2016

Waldemar Schrimpf

Dissertation eingereicht am	23.06.2016
1. Gutachter	Prof. Don C. Lamb, PhD
2. Gutachter	Prof. Dr. Christoph Bräuchle
Mündliche Prüfung am	21.07.2016

Abstract

Fluorescence is a process that can be utilized in many different ways for scientific research. This potential and versatility has also been noticed by the Nobel Committee, which, in the last ten years, awarded two Nobel Prizes in Chemistry to the field, 2008 "for the discovery and development of the green fluorescent protein, GFP" [1] and just recently in 2014 "for the development of super-resolved fluorescence microscopy".[2] The former greatly extended the capabilities for specifically tagging individual proteins, opening the doors for the application of fluorescence microscopy and spectroscopy in studying biological systems. Super-resolution spectroscopy, on the other hand, covers less the preparation and more the analysis of a scientific experimentat. It is the most prominent representative of a wide variety of fluorescence based methods that have emerged in the last 20 years and were made possible by advancements in three different fields. The first includes developments in chemistry and biochemistry that provided fluorescence dyes with better and unique properties, and also new ways of attaching them to the analyte of interest in an efficient and specific manner. Another requirement was the improvement of instrumentation like excitation sources, optical elements, or detectors and other electronic devices. The third field involves advancements in new analysis methods, algorithms and software. Extracting the maximum amount of information from the data reveals more details about the investigated systems and results in a deeper understanding of their nature.
This thesis puts a strong focus on this last aspect. It describes the development of software for analyzing advanced fluorescence methods and subsequently the implementation and application of these techniques.
After a brief introduction in chapter 1, the concepts and methods relevant to this work are presented in chapters 2 and 3. Hereby, chapter 2 briefly describes the basics of fluorescence and microscopy in general and the instrumentation used in the other chapters. Chapter 3 than provides a quick overview of the covered methods, mainly focusing on fluorescence fluctuation and fluorescence lifetime techniques.
The developed software called *PIE Analysis with Matlab* (*PAM*) is introduced in chapter 4. *PAM* was designed as a platform for a multitude of advanced fluorescence analysis techniques, with a focus on combining them with pulsed interleaved excitation. The included methods can be used to analyze single point data (e.g. fluorescence correlation spectroscopy), images (e.g. image correlation spectroscopy), as well as fluorescence lifetime information (e.g. phasor fluorescence lifetime microscopy). Additionally, (*PAM*) contains a simulation program allowing the user to generate data with known parameters, making it possible to test new methods and theories. The core concepts and focus of the central platform and the individual applications are presented, followed by a more detailed description of their main features and most important underlying algorithms.
Chapter 5 focuses on the application of the presented techniques and software for studying metal-organic frameworks (MOFs). They constitute a group of materials

formed by connecting inorganic building blocks via organic linkers to a three dimensional crystalline lattice. Due to their high porosity and relative surface area, MOFs show big potential for a variety of industrial applications, ranging from analyte sensing, over gas storage, to catalysis. Here, two different MOFs were investigated. The first one, MIL-101(Al)-NH_2, is an aluminum based MOFs with free amino groups on the organic linker that can be used for posy-synthetic modifications, e.g. with fluorophores. Using correlative fluorescence lifetime and scanning electron microscopy, two quenching mechanisms of fluorescein bound to the MOF were identified. The first one is a photo electron transfer type quenching via unmodified amino groups, while the second mechanism depends on the particle morphology and is most likely caused by defects in the structure.
In the second part of chapter 5, different methods for functionalizing the zirconium MOF UiO-67 were investigated using fluorescence lifetime microscopy. The analysis showed that *de novo* incorporation of large, complex functionalities during synthesis can introduce small defects to the crystal structure. Solvent assisted linker exchange, the second method investigated, showed less effect on the lattice. During this process, functional groups are bound in two distinct steps. The first involves a fast binding of the modified linker to under-coordinated metal sites at the crystal exterior. The much slower linker exchange only takes place at elevated temperatures. Since the rate limiting step is the substitution of a bound linker, the exchange is spatially homogeneous throughout the whole crystal.
In chapter 6 the influence of chrome nano patterns on the diffusion in supported lipid bilayers is investigated. Since they are believed to completely halt mobility, chrome barriers are often used to divide lipid layers into individual, non-connected segments. We could show that, under the investigated conditions, diffusion across the barriers can still be maintained, albeit at a reduced rate. Detailed pair correlation spectroscopy and scanning electron microscopy analysis revealed no clear correlation between this mobility and barrier width or height. On the other hand, fluorescence recovery after photobleaching indicates the presence of a cutoff barrier thickness that determines whether diffusion is possible or not.

Contents

1. Introduction

A scientific experiment has changed dramatically over the course of history. The earliest researchers relied on observations and reasoning to describe natural phenomena and place them in a philosophical or theological context. Using their own senses, they looked at things happening around them. While this approach of measuring parameters and using the observations to deduce general concepts and laws still stands today, it has gotten more complex and less straightforward over time. As our knowledge and understanding of the natural world grew, so did the complexity of the analyzed topics and the requirements for more intricate experiments. Rarely can a modern measurement be conducted without a meticulous design of the experimental conditions and the help of sophisticated equipment.
This definitely holds true for the field of optics and microscopy. With the invention and improvements of the light microscope, a whole new world on the cellular and sub-cellular level was uncovered that was previously not observable with the human eye alone. Traditional microscopy soon reached its limit in the diffraction of light. Only with the development of new techniques - such as electron, near-field or super-resolution microscopy - was it possible to resolve structures smaller than a few hundred nanometers.
However, not only the resolution power but also the contrast is important to distinguish between different objects. Small structures usually scatter or absorb light only weakly, making it very hard to differentiate between different objects. One way to increase the contrast is to stain the sample, a method widely used for biological samples. The dyes used for staining bind to specific components of a cell, thus enhancing the contrast between the targeted organelles and the surrounding cell. Another approach to achieve high contrast and specificity is to switch from observing transmitted light to measuring photon emission by using florescence. Although fluorescence is ubiquitous, most molecules show only very low emission efficiencies in the visible spectrum (e.g. quantum yield of $\approx 10^{-4}$ for DNA). This means that the fluorescence background is also very low and the signal from fluorophores - chemical groups with high fluorescence quantum yields - can be detected with very high sensitivity, even down to the single molecule level. Using modern chemical and biochemical tools, these fluorescent dyes can be attached specifically to molecules or structures of interest and imaged with high contrast and specificity, even in such crowded environments like cells.
Fluorescent light not only contains spatial data, used in microscopy, but also a variety of other parameters like wavelength, polarization or temporal information. Fluorescence spectroscopy utilizes these data without necessarily imaging the sample. Depending on the method and experimental conditions, a multitude of different sample properties can be measured, including molecular interactions, dynamics or the nanoscopic environment of the probe. In chapters 2 and 3, I introduce some of these fluorescence spectroscopy methods, especially those that are used in the following chapters.

One aspect common to many of these advanced fluorescence techniques is the need for sophisticated analysis algorithms. Since most of these methods are performed at very low concentrations and only observe a small volume, the signal is governed by Brownian motion and random distribution statistics. This makes direct interpretation of the raw data very difficult and thus requires complex mathematical treatment. However, in many cases, a single type of analysis only reveals a certain aspect of the data (e.g. temporal fluctuations), and other methods are needed to investigate additional parameters (e.g. spatial fluctuation). This means that the maximum amount of information can only be extracted by using multiple analysis approaches, each one with its own algorithms and software code. This optimal data utilization is facilitated by programs that combine such a multitude of analysis methods, especially when they still allow the user flexibility in their application. The development and implementation of such a versatile and flexible program for fluorescence spectroscopy is described in detail in chapter 4.
Different fluorescence techniques are nowadays widely used in the life sciences, both in *in vitro* applications, as well as in measurements in cell or even whole organisms. Outside of biological topics, fluorescence is rarely utilized even though it has many potential applications. One field that can greatly benefit from fluorescence methods is material science, especially the study of porous materials. This porosity leaves space for dyes to be incorporated into the material, either during synthesis or afterwards through diffusion. Using fluorescence imaging, the spatial distribution, connectivity and accessibility of such porous networks can be mapped. Extending the measured parameters to the fluorescence lifetime further increases the amount of information available about the material. Most fluorophores are very sensitive to their immediate surroundings, resulting in a change in lifetime. This can then be used to deduce the nanoscopic environment of the dye, even below the diffraction limit. Chapter 5 presents two studies where fluorescence lifetime imaging was used to investigate different functionalization methods of metal-organic frameworks, a type of porous material that is currently receiving a lot of attention as potential candidates for industrial applications.
One important group of advanced fluorescence techniques is fluorescence fluctuation spectroscopy (FFS). Unlike most other methods, FFS techniques do not try to minimize random fluctuations, but rather use them to extract information about the sample. These variations in the fluorescence signal are not only caused by noise, but also by differences in concentration or molecular brightness. Thus, temporal fluctuations contain information about dynamic processes such as diffusion, while heterogeneities in space reveal the spatial distribution of fluorophores. Fluorescence pair correlation analysis is a fluctuation technique thats utilizes both the spatial and the temporal information, and can be used to investigate the local diffusion behavior. In chapter 6, pair correlation is applied to study the effect of obstacles on two dimensional diffusion. Here, supported lipid bilayers on chrome nano patterns are used as a simple model system. Since the size of both barriers and gaps between them can be controlled precisely, the influence of these parameters on the local lipid mobility was investigated.

2. Confocal Fluorescence Microscopy

In this chapter I will introduce the basic concepts of time-resolved confocal laser scanning fluorescence microscopy, the key technique of the experiments presented in this thesis. Starting with the fundamentals of fluorescence, I will then briefly describe the principles of confocal laser scanning microscopy followed by the concepts of time-correlated single photon counting and pulsed interleaved excitation. The last part of the chapter describes the microscope used for the measurements and its key components. The actual methods and the principles of data analysis are featured in chapters 3 and 4, respectively.

2.1 Fundamentals of Fluorescence Microscopy

Molecules that were excited by light have a chance to emit a photon when relaxing to the electronic ground state. When this transition happens between two singlet states, the process is called fluorescence and molecules that have a high probability of photon emission are known as fluorophores.
A normal fluorescence cycle consists of four steps, illustrated in Figure 2.1. First, an electron undergoes a transition to an excited electronic state, usually S_1 or S_2. According to the Franck-Condon principle, this change is too fast for the nuclei to follow so that the transition also includes a change in the vibrational level. The next step is a non-radiative relaxation to the lowest vibrational state of S_1, called internal conversion. This is followed by the actual fluorescent transition to the electronic ground state S_0, again to a vibrationally excited level due to the Franck-Condon principle. The cycle is completed by a second vibronic relaxation. Besides photon emission, there are several other pathways to the ground state, such as internal conversion, inter-system crossing, energy transfer or other quenching mechanisms.
During the two vibrational relaxations, a fraction of the energy is lost to heat so that the wavelength of the emitted photon is longer than that of the excitation light. This spectral shift, called the Stokes' shift, makes it possible to efficiently separate the excitation light from the fluorescence by using special filters and polychroic mirrors, that transmit certain wavelength, but reflect or absorb others. This allows the detection of even weak signals, turning fluorescence into a powerful tool in microscopy and spectroscopy. Since most molecules show next to no fluorescence intensity in the visible range, good fluorophores can be imaged with very high contrast, even down to single molecules. Combined with the specificity achieved by labeling biomolecules chemically with organic dyes or biochemically with fluorescent proteins, this makes fluorescence the primary readout parameter of many medical and biological microscopy applications. Furthermore, unlike x-ray crystallography

or electron microscopy, fluorescence measurements generally do not require special experimental conditions, such as fixed or crystallized samples. Therefore, biological samples can be studies in their natural environment, e.g. a living cell.

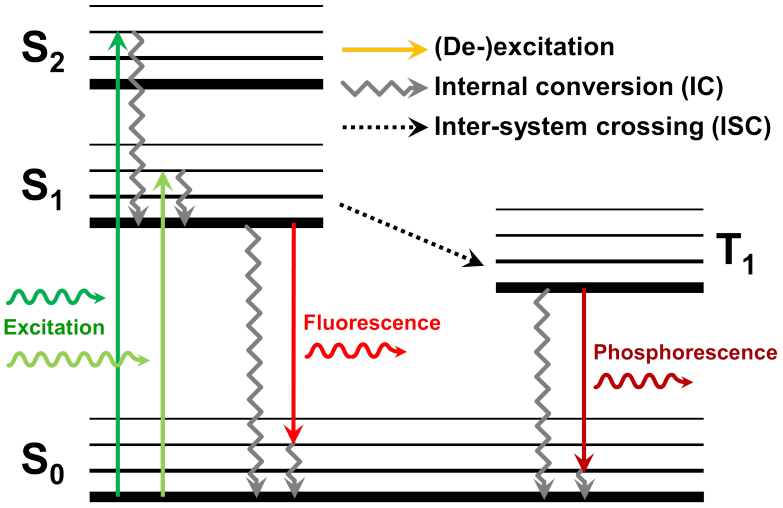

Figure 2.1: Jablonski diagram illustrating the most common pathways in an excitation/de-excitation cycle of a fluorophore.

2.2 Principles of Confocal Microscopy

The first confocal microscope was already described in 1957 by Marvin Minsky [3] and, although almost six decades have passed since then and a lot of new inventions and improvements have been added to it, the basic concepts are still the same. Unlike wide-field microscopy where the whole sample is illuminated, a confocal microscope focuses the light to a small spot. However, a signal can also originate from the light cones before and after the focal plane, since the total excitation intensity is the same for each axial plane (if the changes due to absoption or reflection are neglected). By introducing a pinhole in the conjugated focal plane, most of the out-of-focus light can be blocked, resulting in a small detection volume. The concept is illustrated in Figure 2.2.
The minimal size of this focus spot, called point the spread function (PSF), is defined by Abbe's diffraction limit:

$$d = \frac{\lambda}{2NA} \tag{2.1}$$

In modern microscopes, this is usually 200–300 nm laterally and around a factor of 5 to 10 larger in the axial dimension. This small observation volume (<1 fL), especially when combined with fluorescence detection, enables many techniques not possible with conventional wide-field microscopes.

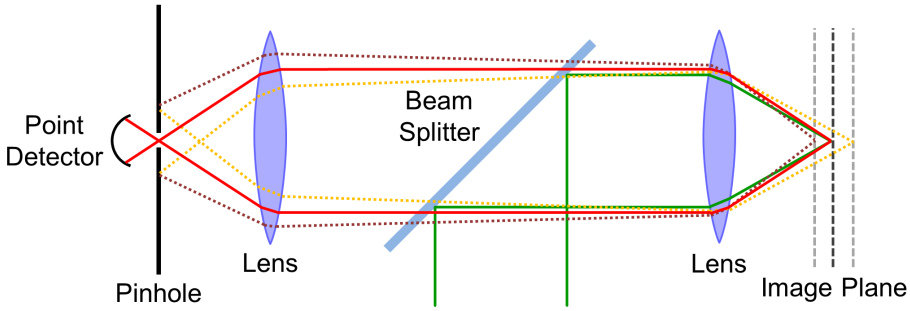

Figure 2.2: Principle of a confocal microscope. The green solid lines indicate excitation light. While light from the focal plane (red solid line) can pass through the pinhole in the conjugated plane, out of focus emission (dark red and orange dotted lines) is blocked.

The confocal principle alone, however, cannot resolve an image, because only a single spot is observed. In order to gather spatial information, different position in the sample have to be measured sequentially and the full image reconstructed from the individual data points. Hereby, either the sample or the focus can be moved. The former is easy to implement, but it is quite slow and the movement might introduce vibrations, decreasing image quality. The concept of moving the excitation volume instead of the sample is called laser scanning confocal microscopy (LSCM) and is discussed in the next section.

2.3 Laser Scanning Confocal Microscopy

In order to move the focus laterally, the incident angle of the excitation beam at the back focal plane has to be changed. The easiest way to achieve that is to place a movable mirror in the excitation path. Tilting this mirror along the horizontal or the vertical axis then translates the focus in the x and y direction. This tilting, however, does not only result in a change of angle, but also shifts the beam position, so that the mirror has to be placed very close to the objective or only a small region can be scanned. This problem can be solved by placing relay optics (such as telescope lenses or parabolic mirrors) in between the scanning mirror and the objective. If the focal planes or the tilt axes of neighboring elements coincide, the lateral translation at the objective back focal plane is eliminated and large regions of interest can be scanned without any artifacts (see Figure 2.3). In such a setup, a polychroic mirror is placed before the scanner so that excitation and fluorescence take the same path. This way, the image is "descanned", meaning the fluorescence light hits the polychroic always under the same angle, independent of the scanner position, so that a static pinhole and detector can be used.
In camera-based microscopy methods, magnification is fixed and defined by the optics. Laser scanning, on the other hand, allows free and continuous zooming, only limited by the minimal angle step as the lower border and by the maximal deflection that does not overstep the dimensions of the optics as upper limit.

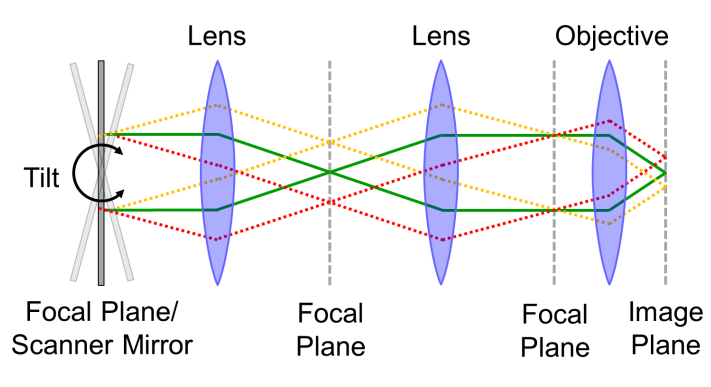

Figure 2.3: Schematic of confocal laser scanning. If the scan mirror position and the focal planes of neighboring lenses overlap, a tilting of the mirror is relayed to a translation of the focus in the image plane.

Mirrors that are capable of being tilted in two axes (mainly piezoelectric mirrors) are usually quite slow and do not improve scanning speed much compared to sample scanning. Therefore, most LSCMs use galvanometric mirrors that can be moved with a response that is approximately two orders of magnitude faster, with line scan frequencies of around 1 kHz. Unfortunately, they only rotate around a single axis, so that two individual mirrors with perpendicular rotation have to be used to perform two dimensional scans. In this case, the mirrors are placed very close together with the focus point of the first telescope lens in between them to minimize beam shift at the objective back focal plane. For measurements that require very high precision (like super resolution microscopy), additional relay optics are placed between the mirrors to eliminate even these small remaining deviations.
The maximal line scan frequency of standard galvanometric mirrors lies at about 1 kHz, corresponding to an imaging rate of about 1-10 frames per second, depending on the resolution. At higher rates, the mirrors cannot follow the sawtooth signal due to inertia, resulting in non-linear scanning and distorted images. It is possible to push this limit by adjusting the input signal to account for the physical properties of the mirrors. A way to achieve even faster imaging up to video rate is to use resonant scanners. Hereby, the mirror for the fast axis oscillates at its resonance frequency. This movement is very regular, but sinusoidal, so that the pixel times vary and a more complicated image reconstruction is needed. In addition, it is generally not possible to statically move the beam to a certain position, so that selection of regions of interest is more limited.

2.4 Time Correlated Single Photon Counting

Many of the methods described later in this thesis (especially pulsed interleaved excitation and fluorescence lifetime) require a very accurate measurement of the photon arrival time over many orders of magnitude, ranging from a few picoseconds

up to seconds or even minutes. To achieve this, time correlated single photon counting (TCSPC) is employed.[4,5] The individual photons are registered with counting detectors like photomultiplier tubes (PMTs) or, in this case, avalanche photodiodes (APDs). Each detected photon results in an electronic pulse that is sent to the TCSPC device, where two different times are recorded for each photon: the macro- and the micro-time (Figure 2.4).
The macro- or measurement time contains low resolution (about 10–100 ns) information about the photon arrival relative to the start of the experiment. The TCSPC card counts the ticks of a synchronization clock since the measurement began and assigns this value to the detected signal. Because all clocks have a slight, but noticeable divergence, all time sensitive devices, like TCSPC cards, lasers or scanners, are ideally synchronized to a single clock.
The high temporal resolution of TCSPC is encoded in the micro- or pulse-time. This parameter only contains the relative delay between the detected photon and the previous or following sync pulse, but with a timing accuracy down to a few picoseconds. Hereby, a synchronization pulse starts a high precision timer (usually a time-to-amplitude converter, TAC, or a time-to-digital converter, TDC), that is stopped by the photon signal. Due to the dead time of TACs and TDCs, most modern devices actually use an inverted start-stop configuration, where the photon acts as trigger and the sync as terminator. Since photons are much more sparse compared to clock ticks, this setup reduces the effects of dead time and allows higher measurement frequencies. The sum of both macro- and micro-time gives the absolute photon arrival time.

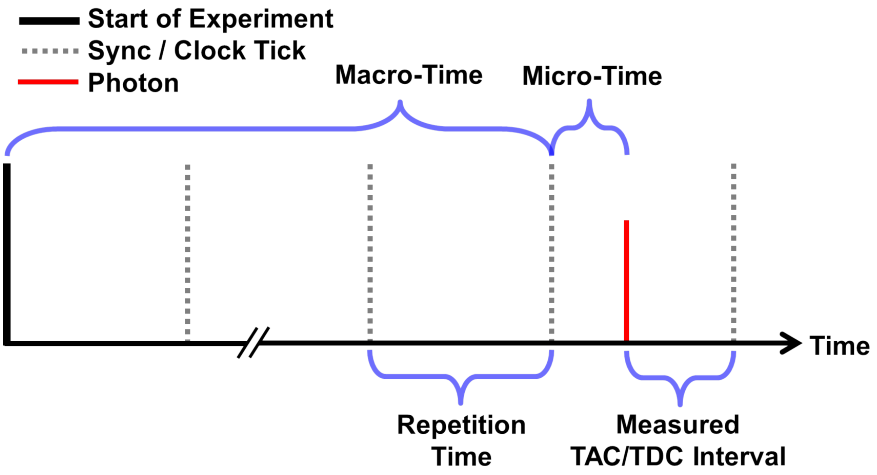

Figure 2.4: Schematic of TCSPC detection. The macro-time counts the synchronization pulses since the start of the experiment, while the micro-time measures the delay of the photon arrival with respect to the previous clock tick.

2.5 Pulsed Interleaved Excitation

An important measurement mode that strongly benefits from using TCSPC detection is called pulsed interleaved excitation (PIE).[6,7] In PIE, multiple pulsed lasers - usually different colors, but other parameters like polarization can also be used - are triggered within one pulse cycle, but shifted in time, creating an alternating excitation sequence. When the delay between them is significantly longer than the lifetime of the fluorophores, the responses to the lasers will be clearly separated in time and each photon can be unambiguously assigned to an excitation source. This way the signal is not only divided into channels by emission (via dichroic mirrors and filters), but also by excitation wavelength (via the micro-time), adding important information otherwise not available (see Figure 2.5).

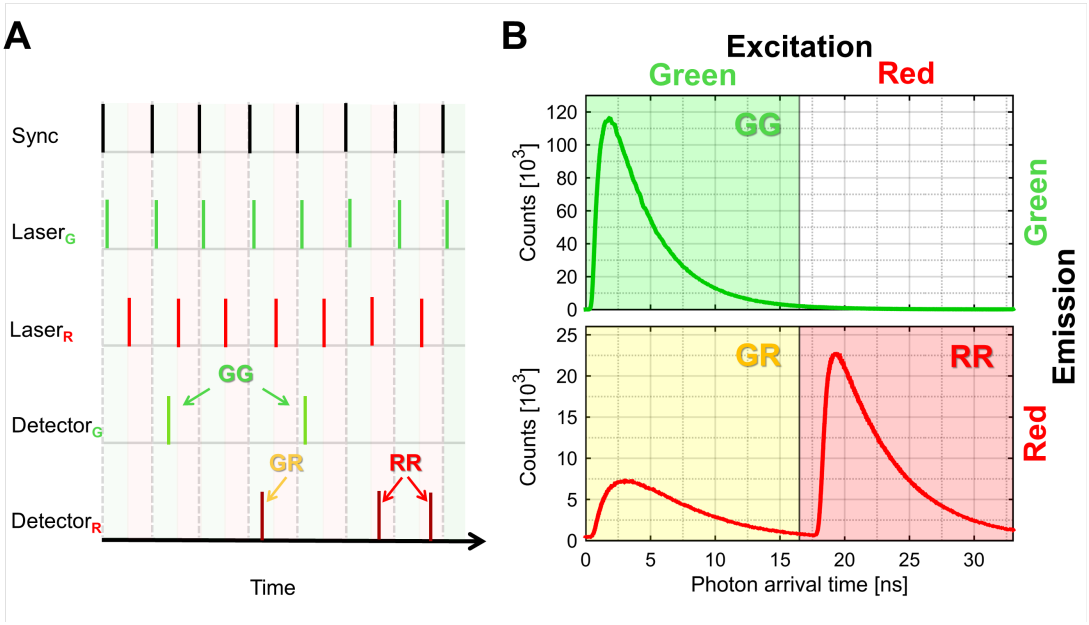

Figure 2.5: Schematic of the concept of two-color pulsed interleaved excitation (PIE). A) During each excitation cycle (determined by a sync pulse), two lasers (green and red) are triggered with a short time delay, defining two timed channels, GX and RX. Photons are additionally divided by their color, resulting in a total of four channels. Green photons after green excitation (GG) and red photons after red excitation (RR) originate from the green and red dye, respectively, after the corresponding laser excitation. Red photons after green excitation (GR) can be caused by spectral crosstalk of the green dye, direct excitation of the red dye by the green laser or energy transfer from the green to the red dye. Due to the fluorescence properties of common dyes, green photons after red excitation (RG) are highly unlikely and usually negligible. B) Micro time histograms of a DNA labeled with Atto488 and Atto647N showing fluorescence decays for the channels GG, GR and RR.

Being able to distinguish excitation sources is a feature that greatly increases sensitivity of fluorescence cross-correlation methods (described in chapter 3.1 and 3.2).

In the case of a two-color experiment, green emission after green excitation and red photons after a red laser pulse can only originate from the corresponding dyes, ensuring that no artificial cross-correlation amplitude is observed between those channels. Without alternating excitation, spectral crosstalk from the lower wavelength fluorophore will be detected in the red channel, causing a non-vanishing cross-correlation signal even in a non interacting sample (green curves in Figure 2.6). Furthermore, photons from the green dye are added to the red signal and thus affect the red auto-correlation (red curves in Figure 2.6).

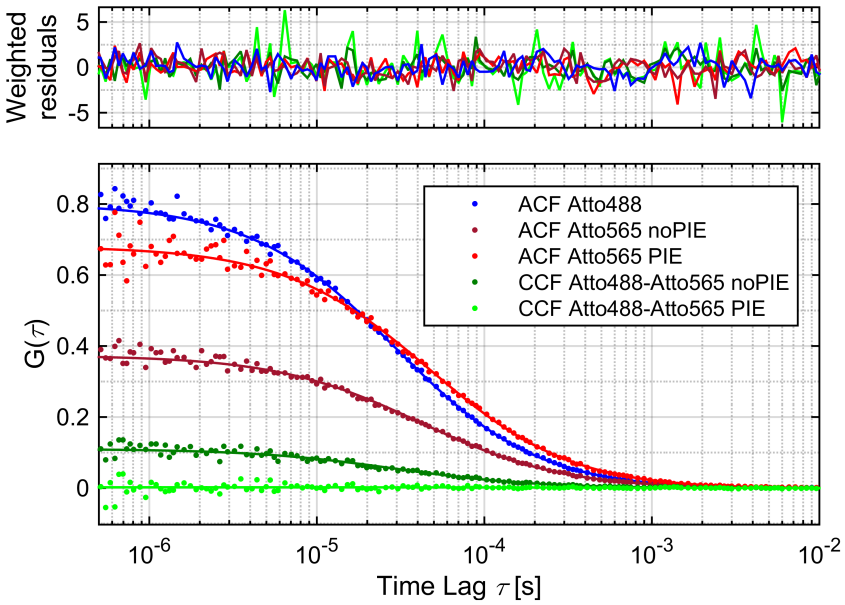

Figure 2.6: Fluorescence cross-correlation curves of Atto488-carboxylic acid and Atto565-carboxylic acid diffusing independently. Without PIE, the spectral crosstalk affects the red auto-correlation function (dark red curve) and introduces an artificial cross-correlation amplitude (dark green curve).

Another method that greatly profits from PIE is single molecule Förster resonance energy transfer (smFRET).[8] In normal smFRET experiments, only the donor fluorophore is excited by a single laser. From the intensity observed in the donor (I_{GG}) and acceptor (I_{GR}) channels, the apparent FRET efficiency can be calculated:

$$E = \frac{I_{GR}}{I_{GR} + I_{GG}} \tag{2.2}$$

This way, molecules showing very low FRET and the ones lacking an acceptor fluorophore altogether cannot be distinguished. However, by additionally probing the presence of the acceptor via red excitation (I_{RR}), a new parameter, the stoichiometry, defined as the ratio of the intensity after green excitation and the total photon

signal, can be determined:

$$S = \frac{I_{GG} + I_{GR}}{I_{GG} + I_{GR} + I_{RR}} \tag{2.3}$$

If only one fluorophore is present, either the signal after green excitation ($I_{GG}+I_{GR}$) or after red excitation (I_{RR}) vanishes, and the stoichiometry becomes 1 (for donor only) or 0 (for acceptor only). For a molecule labeled with both dyes, on the other hand, the value will be somewhere in between. Intuitively, a value of 0.5 seems ideal, since here the contrast between dual- and single-labeled molecules is highest. However, in this case half of all photons are detected, red excitation and thus cannot be used for determining the FRET efficiency. Therefore, it might be better to increase the stoichiometry and record more photons from green excitation by adjusting the relative laser intensities.
Alternating excitation is also very useful when performing quantitative FRET measurements. In order to be able to calculate absolute and setup independent FRET efficiencies, direct acceptor excitation (α), spectral crosstalk of the donor (β), and differences between green and red detection efficiencies (γ) need to be accounted for:

$$E = \frac{I_{GR} - \alpha I_{RR} - \beta I_{GG}}{I_{GR} - \alpha I_{RR} - \beta I_{GG} + \gamma I_{GG}} \tag{2.4}$$

$$S = \frac{I_{GR} - \alpha I_{RR} - \beta I_{GG} + \gamma I_{GG}}{I_{GR} - \alpha I_{RR} - \beta I_{GG} + \gamma I_{GG} + I_{RR}} \tag{2.5}$$

Without PIE, I_{RR} is not accessible and a static value for the direct excitation has to be used, increasing potential errors in the measurement. Furthermore, the stoichiometry can be used for directly determining the γ-factor, if the sample shows multiple species with different FRET values. Since the corrected stoichiometry (Equation 2.5) is independent of the FRET efficiency, the correct γ can be extracted, but adjusting it until all species show the same stoichiometry value.
The advantages described so far can also be achieved by quickly alternating continuous wave lasers. By using PIE, however, also the exact photon arrival time and therefore the fluorescence lifetime is measured, maximizing the information extracted from each photon. In fluorescence fluctuation methods, this additional knowledge can be used to recognize and separate different species while in smFRET, the lifetime might reveal other quenching processes or molecular dynamics.

2.6 Confocal Microscope

For almost all fluorescence experiments described in this work, a home-built confocal laser scanning microscope with TCSPC detection was used. A schematic representation of the setup is shown in Figure 2.7. The individual components are described in the following sections. The transmission spectra of the filters and polychroic mirrors are shown in the appendix.

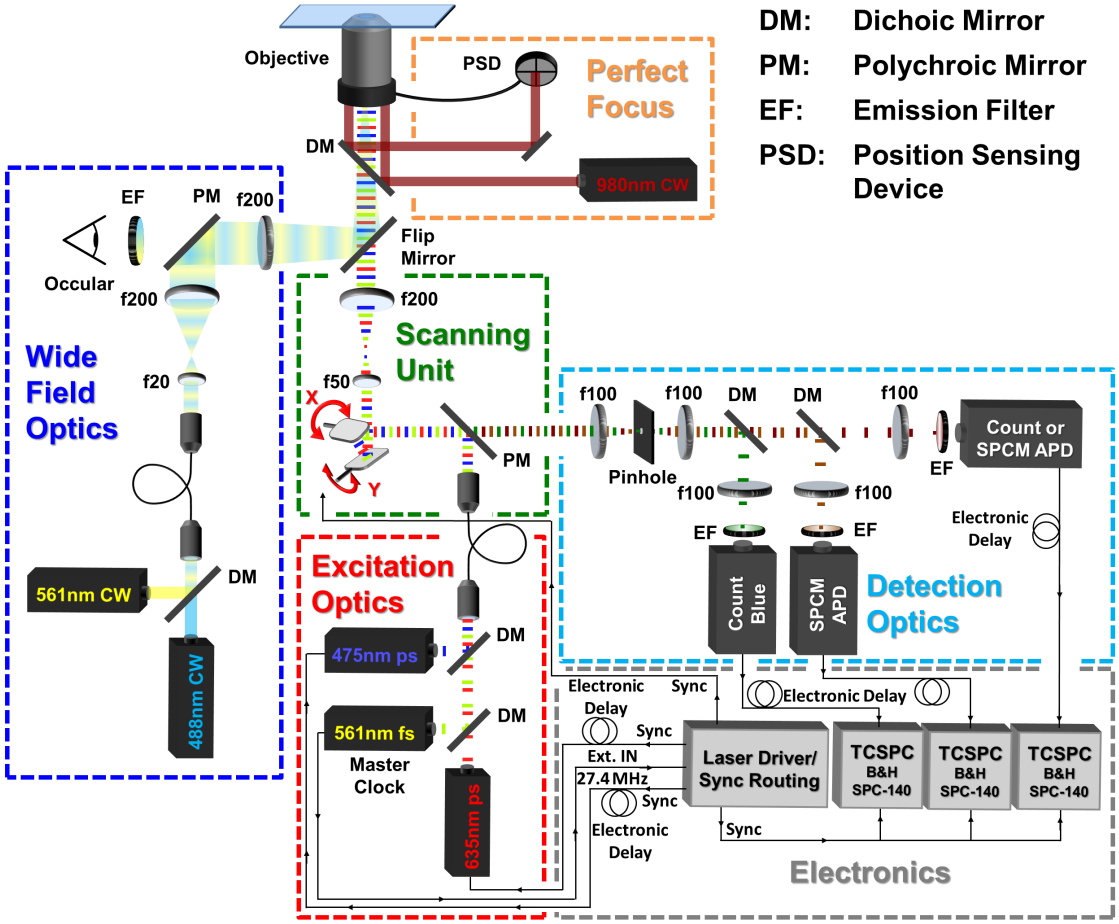

Figure 2.7: Schematic of the confocal laser scanning microscope used for fluorescence experiments presented in this work. The individual components are described in the following section of this chapter.

2.6.1 Lasers and Excitation Optics

The excitation unit is shown in the red box in Figure 2.7. It consists of three lasers, a pulsed erbium doped fiber laser with a fixed repetition rate of 27.4 MHz (FFS.SYS-CONT-COMP-TSHG, Toptica Photonics) tuned to 561 nm, and two pulsed diode lasers, one at 475 nm (LDH-P-C-470, Picoquant) and the second one at 635 nm (LDH-P-C-635b, Picoquant). The pulse frequency of the 561 nm laser serves as a master clock for the other lasers, as well as for all other synchronized devices (scanner and TSCPC cards). To optimize interleaved excitation, triggering the other two lasers can be variably delayed electronically with delay intervals of 2 ns.

The red and yellow lasers are superimposed with a Chroma AT600DC dichroic mirror and afterwards both are combined with the blue laser using a Chroma 500DCXR dichroic mirror (AHF Analysentechnik). To ensure optimal beam shape and overlay of the different lasers, the light is coupled into the same single mode fiber

(coupler: HRJC-23AF-400/700-P-20AC; fiber: QPMJ-A3A,3AF-488-3.5/125-3-5-1, OZ Optics). At the fiber exit the beam is again collimated with a 60FC-4-RGB11-47 achromatic broadband collimator (Schäfter+Kirchhoff).
To adjust the laser power, continuous neutral density filter wheels (OD 0–2) are used before the beam is coupled into the fiber. For experiments requiring very low light intensities (<100 nW), an additional neutral density filter (OD 3) is added.

2.6.2 Laser Scanning Fluorescence Microscopy Path

After the fiber, the light is guided through the scanning unit (green box in Figure 2.7). The light beam is reflected toward the microscope with a polychroic mirror (Semrock Di01-R405/488/561/635, AHF Analysentechnik) used for separating excitation and fluorescence light. Fast beam scanning is achieved via two closely-spaced galvanometer scanners (scanner: 6210H; controller: MicroMax 673 Series, Cambridge Technology). Scanning shape, size and speed are controlled with an arbitrary waveform generator (M2i.6034, Spectrum Systementwicklung Microelectronic GmbH) that is synchronized with the lasers and detection to ensure precise position reconstruction without the need of pixel- or line-synchronization. The midpoint between the scanning mirrors is expanded and projected onto the back focal plane of the objective through an achromatic Keplerian telescope (achromatic lens doublets AC254-050-A and AC254-200-A, Thorlabs), slightly overfilling the back aperture.
The laser light is focused with one of three different objectives, depending on the experimental conditions. For measurements close to the glass surface, which require a high axial stability and lateral resolution, a 1.49 NA 100× oil immersion objective (CFI Apo TIRF 100×, Nikon) is used. Experiments at larger distances from the cover glass (>3 µm) or in homogeneous solutions are performed with a 60× 1.27 NA water immersion objective (Plan Apo IR 60× WI, Nikon). In the case that a dried sample is imaged from the top (i.e. not going through the glass) or when a bigger field of view is needed, the Nikon 0.6 NA air objective Plan Apo Lambda 20× is employed.

2.6.3 Detection Optics and Electronics

The fluorescence is collected with the same objective used for focusing and travels the excitation path backward, until it is separated from the lasers at the polychroic mirror and enters the detection unit of the microscope (cyan box in Figure 2.7). The transmitted light is then focused on a 80 µm pinhole and recollimated with an identical achromatic lens (AC254-100-A, Thorlabs). Afterwards, the emission is split spectrally, first by reflecting the blue/green range (565DCXR, AHF Analysentechnik) and then the orange/red wavelengths (Chroma Q660LP, AHF Analysentechnik). The three different light beams for the blue/green, the orange/red and the red/IR spectrum are then focused on single photon avalanche photodiodes (SPAD or APD), a CountBlue® (Laser Components), a SPCM-AQR-

14 (Perkin-Elmer) and a Count® module (Laser Components), respectively. To effectively block the reflected or scattered laser light, a Chroma ET520/40 band-pass filter is used for the blue/green, a Chroma ET595/50 for the orange/red, and a Semrock 635 nm EdgeBasic long-pass filter for the red/IR detection modules (all AHF Analysentechnik). The photon detection signals of each APD are timed and recorded with a separate TCSPC card (SPC-150/SPC-140, Becker&Hickl).

2.6.4 Wide-Field Microscopy Path

In order to get a better overview of the sample and to quickly locate and identify appropriate regions of interest or cells, the setup can be switched to a wide-field illumination mode (blue box in Figure 2.7). For this purpose, a flip-mirror is inserted into the beam path, blocking the lasers used for confocal excitation and coupling in a 488 nm and a 561 nm continuous wave laser, which are focused onto the back focal plane of the objective. The collected fluorescence of the wide-field illumination is separated from the excitation light via a polychroic mirror (LC-470-568-690TBDR, Laser Components) and guided to the eye-piece of the TE200 Eclipse microscope base for optical inspection or imaging with an electron multiplying charge-coupled device (EMCCD) based camera (QICAM 12-bit Fast Mono, QImaging).

2.6.5 Perfect Focus Unit

Thermal expansion, air flows or unstable focusing mechanics can lead to drift of the sample, especially in the axial direction. When experiments need to be performed at a certain position, this drift can have strong unwanted effects on the recorded signal. Therefore, a perfect focus device has been incorporated into the microscope (orange box in Figure 2.7). The concept used for achivieng the perfect focus is illustrated in Figure 2.8.

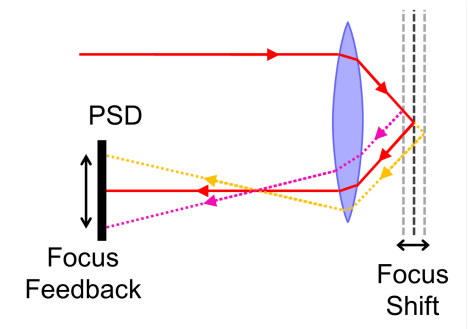

Figure 2.8: Simplified schematic of the perfect focus principle. The laser hits the surface under an oblique angle and is reflected. Depending on the distance between the objective and the reflective surface, the path length of the laser beam changes, resulting in a changed angle and therefore a displacement on the position sensing device.

To achieve this, a 980 nm Laser (MDL-III-980-100 mW, CNI Optoelectronics) passes through a beam splitter that reflects $\approx 90\%$ of the IR light. The weaker laser path is focused onto the objective, creating a strongly inclined collimated beam after the objective. Hereby, the IR light passes through a long pass filter (Semrock FF875, AHF Analysetechnik), with the purpose of guiding both the confocal excitation light (reflected) and the perfect focus laser (transmitted) to the objective. The light reflected on the interface between cover glass and sample medium is collected and again reflected on the 90/10 beam splitter. Hereby, the stronger signal falls onto a position sensing detector (PSD, CONEX-PSD9, Newport). The position information of the PSD is used to adjust the focus via an objective piezo (P-517.3CL; E-501-00, Physik Instrumente). The minimal light intensity required for the PSD is only achieved with total internal reflection on the glass-sample interface. Therefore, the perfect focus system is only used with the oil immersion objective.

3. Advanced Fluorescence Microscopy and Spectroscopy Methods

In recent years, the development of more sensitive and accurate equipment, sophisticated new fluorescent dyes, as well as advanced data analysis transformed fluorescence microscopy from simple imaging to a versatile tool to investigate a wide variety of properties and samples. By expanding the observed parameters beyond position and color, the new fluorescence microscopy methods try to extract the maximum possible information from each photon. This chapter will introduce and shortly describe some of these methods, focusing on techniques used later in this work, namely fluorescence fluctuation spectroscopy [9–13] and lifetime imaging. [14–17]

3.1 Fluorescence Fluctuation Spectroscopy

Most scientific methods either measure a static property or rely on a perturbation-response scheme to probe the dynamics of a system. Fluorescence fluctuation spectroscopy (FFS), on the other hand, uses intrinsic thermal fluctuations to investigate dynamic properties. As the fluctuation-dissipation-theorem states, small perturbations from the equilibrium are governed by the same laws as statistic fluctuations, allowing both approaches to study the same aspects from different perspectives.

Although the first fluctuation experiments on diffusion were performed more than a hundred years ago, [18] it took until the late 20th century for FFS to turn into the powerful tool it is today. One reason for this is that thermal variations are comparatively small and most pronounced for low particle numbers. Therefore, the development and advancement of confocal and two-photon microscopy and their small observation volumes ($V < 1\,\mu m^3$) was needed to establish FFS as more than a niche method. [19] Things are further complicated by the fact that fluctuation data is not immediately interpretable. Although the fluctuations follow strict rules and distributions on average, the occurrence of individual events is random, making pattern recognition more difficult. Thus, the information hidden in fluctuations is only accessible after a statistical analysis, while perturbations shows a clear (in most cases exponential) response.

Over the years, many different FFS methods were developed, but they are all based on two ways of analyzing the data: Techniques like the photon counting histogram (PCH) [20], fluorescence intensity distribution analysis (FIDA) [21] or fluorescence cumulant analysis (FCA) [22] utilize the probability distribution to measure the amplitude of fluctuations. The temporal aspects of fluctuations, on the other

hand, can be best visualized using the correlation function, used by fluorescence correlation spectroscopy (FCS) and its extensions.

3.1.1 Fluorescence Correlation Spectroscopy

Fluorescence correlation spectroscopy (FCS) looks at the self-similarity of a fluorescence photon stream by calculating a temporal auto-correlation function (ACF) to determine the timescales of fluctuations. The theory and first implementation were introduced in the early 1970s by measuring the diffusion and kinetics of ethidium bromide reversibly binding to DNA.[19,23,24]
The auto correlation amplitude G of time lag τ can be expressed via intensity ($I(t)$) or fluctuations ($\delta I(t) = I(t) - \langle I(t)\rangle$):

$$G(\tau) = \frac{\langle I(t) \cdot I(t+\tau)\rangle}{\langle I(t)\rangle^2} - 1 = \frac{\langle \delta I(t) \cdot \delta I(t+\tau)\rangle}{\langle I(t)\rangle^2} \tag{3.1}$$

with I describing the photon count rate for times t and $t+\tau$. The angled brackets indicate the average over all possible time points t.
The most common type of fluctuations investigated by FCS is a variation of the number of particles in the observation volume due to diffusion. Fluorescent particles randomly entering or leaving the focus result in a deviation of the intensity signal from the average value. While they stay inside or outside of the observed volume, the deviation has the same sign for short time lags, leading to a positive net correlation. For long time lags, however, the particles have more time to diffuse and thus their position is randomized. Therefore, long-time fluctuations are also random and, averaged over all time points, cancel out, so that the correlation function decays to zero. The time scale on which the correlation decreases to zero is determined by the average time a particle spends in the focus, which in turn depends on the focus size and the particle's diffusion coefficient.
The second important parameter measured in FCS is the average particle number N within the focus, which is inversely proportional to the correlation amplitude at zero lag $G(0)$. The inverse relationship can be easily understood: Assuming that the movement of different objects is not correlated, the distribution of particles in the focus follows Poissonian statistics. Thus, the particle fluctuations and consequently the intensity deviations $\delta I(t)$ scale with $\sqrt{N}$. The multiplication in the nominator of equation (3.1) results then in a direct proportionality of the unnormalized correlation amplitude and the particle number. Since the average count rate $\langle I(t)\rangle$ is also proportional to the particle number, but contributes as a square to the denominator, the final relationship results in $G(0) \propto \frac{1}{N}$.
For free diffusion through a 3D Gaussian volume (as a good approximation of a confocal focus), the temporal auto-correlation function can be expressed as:

$$G(\tau) = \frac{\gamma}{N} \cdot \left(\frac{1}{1+\frac{4D\tau}{\omega_r^2}}\right) \cdot \sqrt{\frac{1}{1+\frac{4D\tau}{\omega_z^2}}} \tag{3.2}$$

Here, N represents the particle number, D the diffusion coefficient, while ω_r and ω_z denote the radius of the Gaussian for the lateral and axial dimensions, respectively. The radius is defined as the distance from the center at which the intensity decreases to $\frac{1}{e^2}$ of the maximum. The lag time is symbolized by τ. The shape factor, γ, accounts for the fact that the intensity does not constitute a step function with clear borders, but only gradually decreases from the center outwards. For a 3D Gaussian, γ is equal to $2^{-\frac{3}{2}}$ or approximately 0.3536. Figure 3.1 shows an example of a diffusion correlation function of a fluorescent dye.

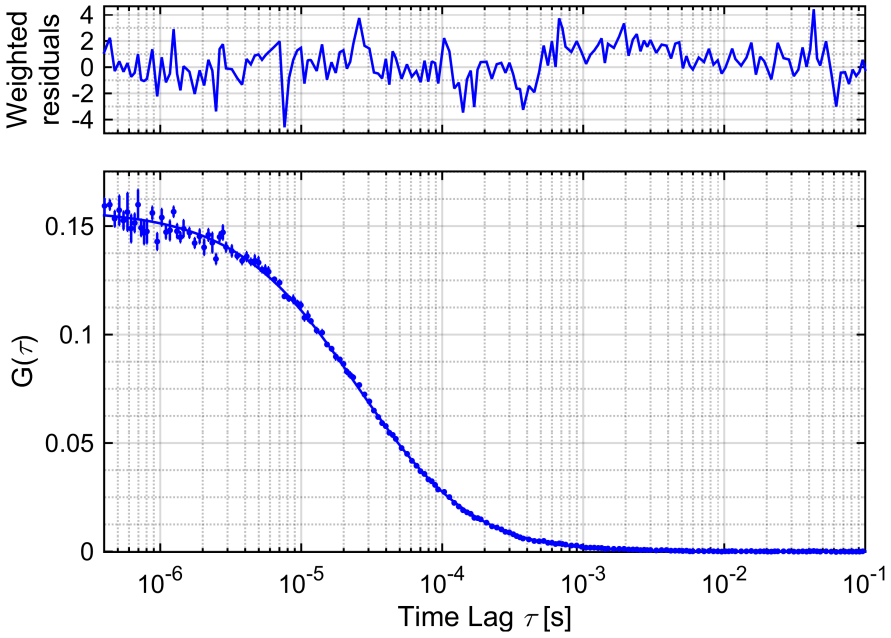

Figure 3.1: FCS curve of Atto655 carboxylic acid acquired on a confocal microscope. Dots represent measured data and the solid line is a fit to equation (3.2). The weighted residuals of the fit are displayed in the upper panel.

Any process affecting the molecular brightness will also show up in the auto-correlation function. Some of them result in unwanted artifacts impeding analysis while others are actually utilized to study the dynamics involved. Some of the most common sources of fluctuations in FCS are illustrated in Figure 3.2. The fastest process observable in FCS is the so called antibunching term (I in Figure 3.2).[25,26] For single emitters, the emission of a second photon is delayed due to the fluorescence lifetime (1–4 ns for most fluorescent dyes). This leads to sub-Poissonian statistics and consequently to a decrease of the correlation amplitude. At zero lag time, the correlation amplitude only drops to zero for truly individual emitters. For particles carrying multiple fluorophores, however, the depression in the curve is inversely proportional to the number of emitters. Using this information, the fluorophore stoichiometry can be measured, e.g. for oligomerization studies.[27,28]
A second fast process in FCS is molecular rotation (II in Figure 3.2),[29–32] ranging from tens of picoseconds for small synthetic dyes to about 50 ns for fluorescent proteins. For excitation to occur, the electric field component of the light has to

align with the fluorohore's dipole moment. Because the lasers used in most FCS experiments are linearly polarized (or are missing the longitudinal component if circular or non-polarized), this leads to a correlation that decays with the rotation of the molecule. Unlike translation, rotational diffusion depends on the cube of the radius, making it more sensitive to small changes of the molecular size.
Correlations due to photophysics (III in Figure 3.2), most prominently blinking from intersystem-crossing to a triplet state, usually appear on the low microsecond scale.[33–36] Although they are, in most cases, an unwanted byproduct of the fluorophores used, one can use the blinking to determine stoichiometry, similar to antibunching.

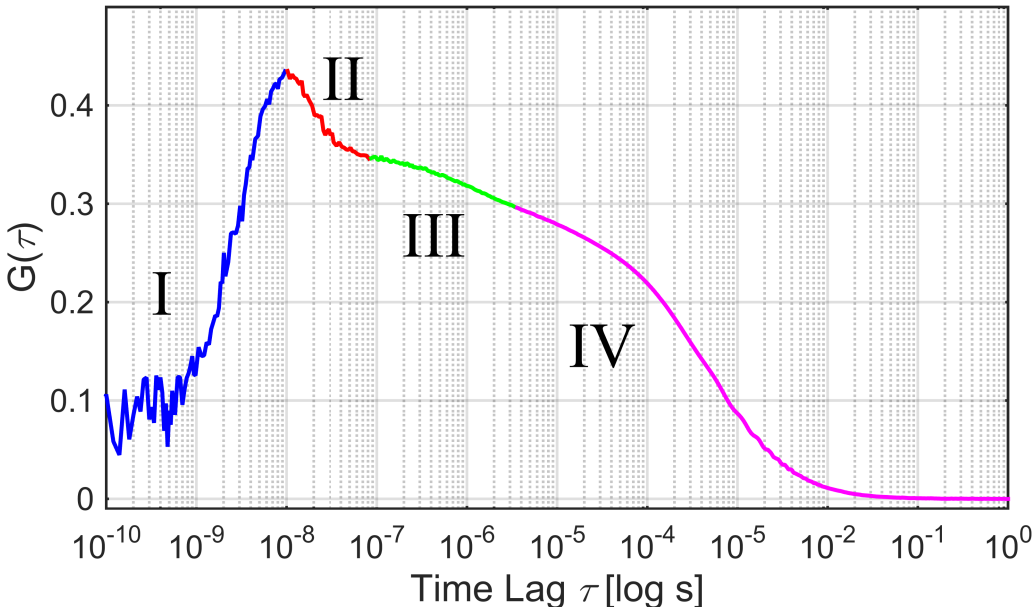

Figure 3.2: Full correlation curve of GFP depicting the different fluctuation sources. I: Antibunching. II: Molecular rotation. III: Photophysical fluctuation. IV: Translational fluctuations.

Diffusion is generally the slowest component of a correlation curve (IV in Figure 3.2). Depending on the particular situation, it takes a particle on average 10 µs up to seconds to diffuse through the observation volume. Because the transit time depends on the particle size, interactions with other molecules and the viscosity of the medium, any process affecting these properties can be measured. In most cases, diffusional FCS is used to investigate binding or dissociation. When a molecule labeled with a fluorophore binds to a larger component, its hydrodynamic radius increases. The resulting change in diffusion coefficient can, in turn, be observed by FCS, thus identifying and quantifying interactions.
Although most intramolecular dynamics do not directly influence the ACF, they can be measured by adding a quenching moiety via Förster resonance energy transfer (FRET)[37,38] or photoinduced electron transfer (PET)[39,40]. In these cases,

changes in proximity between the quencher and the fluorophore result in intensity fluctuations, measurable with FCS. Since these fluctuations can originate from a multitude of different sources, they can appear on any time scale.
Not only dynamic processes of the sample lead to changes in the correlation function. Properties of the instruments used for measuring, like laser fluctuations or detector afterpulsing and dead time, might affect the ACF and need to be dealt with in order to interpret FCS data correctly.[41,42]

3.1.2 Fluorescence Cross-Correlation Spectroscopy

Although FCS is widely used to measure molecular interactions, its sensitivity for detecting changes in molecular weight is fairly low. For spherical particles, the diffusion coefficient is directly proportional to the hydrodynamic radius, which, in turn, scales with the cube root of the molecular mass. This means that upon dimerization the diffusion time is only changed by about 26%. While FCS is sensitive enough to detect such a change, substoichiometric interactions resulting in a mixture of monomeric and dimeric species can be much harder to identify.
In such cases fluorescence cross-correlation spectroscopy (FCCS) can be very helpful. FCCS expands FCS from looking at the self-similarity of a single signal to comparing two different signals. When analyzing the signals i and j, the cross-correlation function (CCF) is calculated according to:

$$G_{ij}(\tau) = \frac{\langle \delta I_i(t) \cdot \delta I_j(t+\tau) \rangle}{\langle I_i(t) \rangle \cdot \langle I_j(t) \rangle} \tag{3.3}$$

FCCS follows the same principles as FCS. Indeed, when both signals i and j are identical, equation (3.3) converges to equation (3.2). Although technically the term fluorescence cross-correlation spectroscopy refers to any method of discriminating fluorescent signals (e.g. lifetime,[43] polarization[44–46] or the special case of spatial separation, which will be discussed later in this chapter), it is generally applied to a spectral separation, more specifically called dual-color FCCS.[6,47,48]
The big advantage of FCCS is to be able to unambiguously determine interactions: While the cross-correlation amplitude is inversely proportional to the average particle number in each individual channel, it is directly proportional to the amount of double-color particles. Therefore, the ratio of cross-correlation to auto-correlation amplitude contains information about the fraction of dual color particles.[49] Since the different species are uniquely associated with a particular signal via their dye, the cross-correlation will only show a non-vanishing amplitude in the case of conjoined movement, i.e. interaction between the species. However, this argument is only true if no artificial cross-talk between the signals is present. For dual-color FCCS, this can be achieved by using pulsed interleaved excitation, described in chapter 2.5.

3.1.3 Scanning Fluorescence Correlation Spectroscopy

One problem often encountered when performing FCS is that the diffusion coefficient and the focus size cannot be determined independently. One can overcome this issue by substituting them with the diffusion time $\tau_D = \frac{\omega^2}{4D}$ as a single parameter, when only relative changes are of interest. Another way is to perform a calibration measurement with a sample of known diffusion coefficient. This, however, requires that all parameters influencing the focus size - like cover glass thickness, temperature or viscosity - stay constant between calibration and experiment.[50] If this is not the case, the accuracy of a FCS measurement might suffer. A way to circumvent this problem is to modify the experiment in such a way that the diffusion coefficient and the focus size become independently fittable. This can be achieved by rapidly moving the focus spot during acquisition, as is done in scanning FCS,[51,52] thus introducing an additional spatiotemporal component G_{ST} to the pure diffusion correlation G_D:

$$G(\tau) = G_D(\tau) \cdot G_{ST}(t, \tau) \tag{3.4}$$

Although many different scanning patterns are imaginable, in most cases a sawtooth type line scan or a circular scan are used. Scanning a circle simplifies analysis, since the relative distance between the focus positions is only dependent on the lag and no longer on the absolute measurement time. For the simplest case of free diffusion with circular scanning, equation (3.4) can be described as:

$$G(\tau) = \frac{\gamma}{N} \cdot \left(\frac{1}{1 + \frac{4D\tau}{\omega_r^2}} \right) \cdot \sqrt{\frac{1}{1 + \frac{4D\tau}{\omega_z^2}}} \cdot exp\left(- \frac{d^2 \cdot sin^2(\frac{\omega\tau}{2})}{w_r^2 + 4D\tau} \right) \tag{3.5}$$

Here, d and ω denote the diameter and angular frequency of the scanned circle, respectively. The other parameters are defined the same as in equation (3.2). As is evident in the formula, ω_r and D appear both as a sum and a quotient, making them separately determinable. The scanning parameters are independent of effects changing the focus size and can be easily calibrated.
The effect of scanning on the correlation is shown Figures 3.3 and 3.4. Due to the rapid movement of the observation volume, each particle spends less time in the focus, equivalent to an external flow. This results in a faster initial decay of the correlation function for short lag times. Whenever the focus returns to a previous position, however, the spatial correlation increases again, and with it also the correlation amplitude. This periodic behavior manifest itself as an oscillation in the FCS curve. With increasing scanning frequency, the initial decay becomes faster. At the same time, the repetition time is decreased, shifting the oscillations to shorter lag times (Figure 3.3). A larger diameter, on the other hand, also results in an increased focus velocity, but with a constant repetition rate (Figure 3.4).

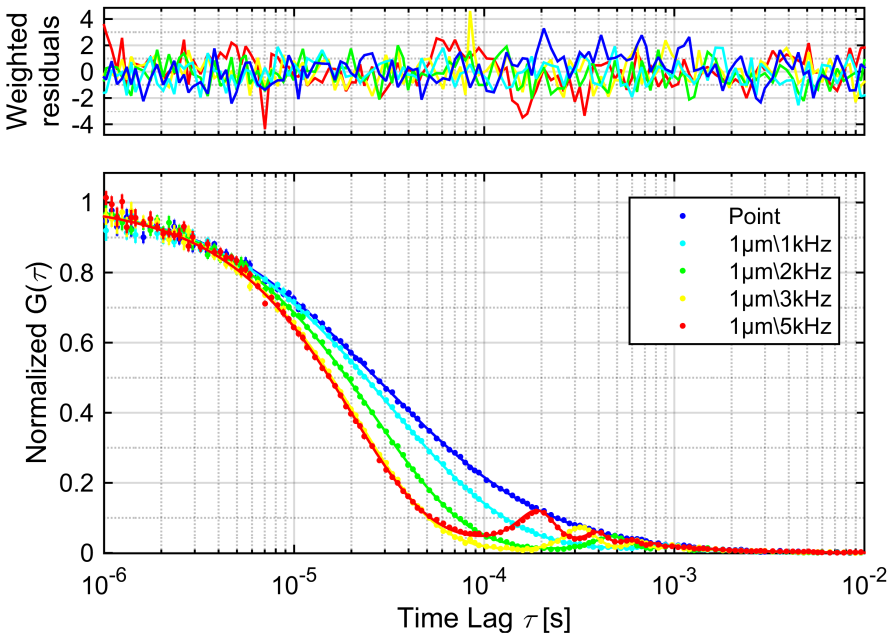

Figure 3.3: FCS curves of Atto488 carboxylic acid acquired on a confocal microscope while scanning a circle of 1 µm diameter at varying frequencies. Dots represent measured data and the solid lines are fits to equation (3.5).

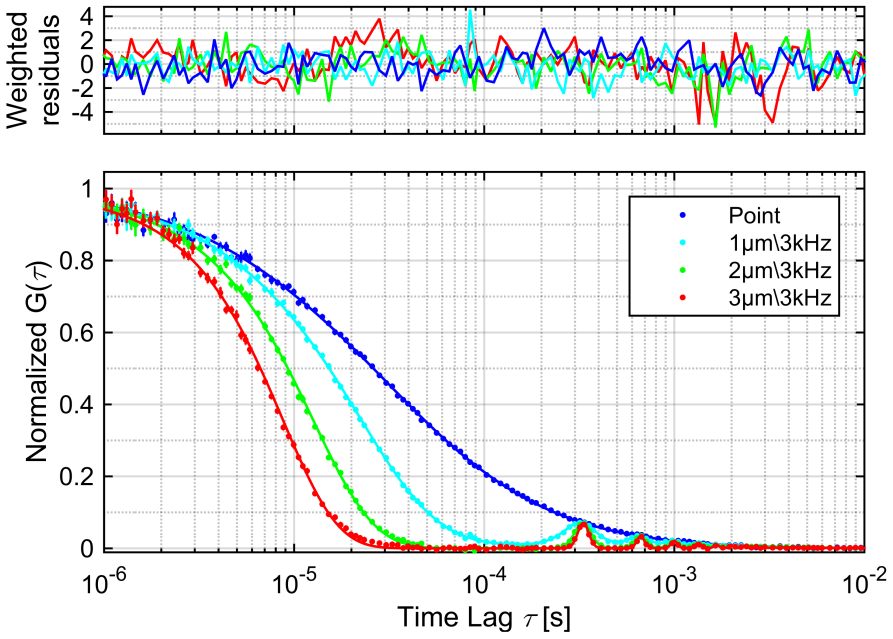

Figure 3.4: FCS curves of Atto488 carboxylic acid acquired on a confocal microscope while scanning a circle of varying diameter at a frequency of 3 kHz. Dots represent measured data and solid lines are fits to equation (3.5).

There are two aspects of scanning FCS that need to be accounted for to ensure a correct interpretation. First, the scanned diameter is highly dependent on the frequency. The focus movement is usually generated by tilting mirrors (sample scanning would be too slow) that have both mass and inertia. The faster the mirrors have to move, the more they are affected by their inertia, resulting in a decreased diameter for higher frequencies. Therefore, the circle width has to be calibrated individually for all settings used in an experiment. An example of this is summarized in Table 3.1, using the data shown in Figure 3.3.

Table 3.1: Determined scan diameter at varying frequencies for data shown in Figure 3.3. The input diameter was kept constant at 1 µm.

Scanning frequency	1 kHz	2 kHz	3 kHz	5 kHz
Effective diameter	0.91 µm	0.89 µm	0.84 µm	0.53 µm

The second drawback of scanning FCS arises from its incompatibility with the multiple-*tau* algorithm most commonly used for temporally correlating fluorescence data. Hereby, the temporal resolution for longer lag times is reduced, thus allowing correlations over many orders of magnitude at significantly shorter calculation times. This binning, however, interferes strongly with scanning FCS data. As the binning increases, more focus positions are averaged, leading to a smearing of the effective PSF. Once a bin exceeds the revolution time, the apparent focus deforms into the shape of a static donut. A standard fit model would not account for this, resulting in analysis artifacts.
A positive side effect of the scanning is a reduced bleaching rate. Due to rapid movement of the focus, the light intensity is spread out over a larger area and a greater number of particles. This way, each fluorophore is illuminated for a much shorter time, thus decreasing its probability of bleaching. At the same time, the average number of molecules simultaneously in the focus and therefore the maximal correlation amplitude stay constant and the signal to noise ratio is maintained.

3.1.4 Two-Focus Fluorescence Cross-Correlation Spectroscopy

A different approach to introduce an external ruler to FCS is two-focus fluorescence cross-correlation spectroscopy (2fFCCS).[53,54] Unlike scanning FCS, where a single signal is used and the spatial displacement is generated over time by moving the focus, 2fFCCS generates two signals with a constant focal shift. A schematic of how these two foci can be generated and separated is depicted in Figure 3.5. Two pulsed laser beams with orthogonal polarization are combined in such a way that a single beam with alternating polarization is created. This can be done by either using two independent lasers or by splitting a single light source via a polarizing beam splitter and optically delaying one path in respect to the other (Figure 3.5 A). The

actual separation of the foci is achieved by adding Nomarski prism in front of the objective. Due to their orthogonal polarization, the alternating pulses are displaced differently by the prism, creating two foci spaced a few hundred nanometers apart (Figure 3.5 B). By using time gated or TCSPC detection, photons can be sorted by their excitation (Figure 3.5 C), resulting in separate signals for the two foci (Figure 3.5 D).

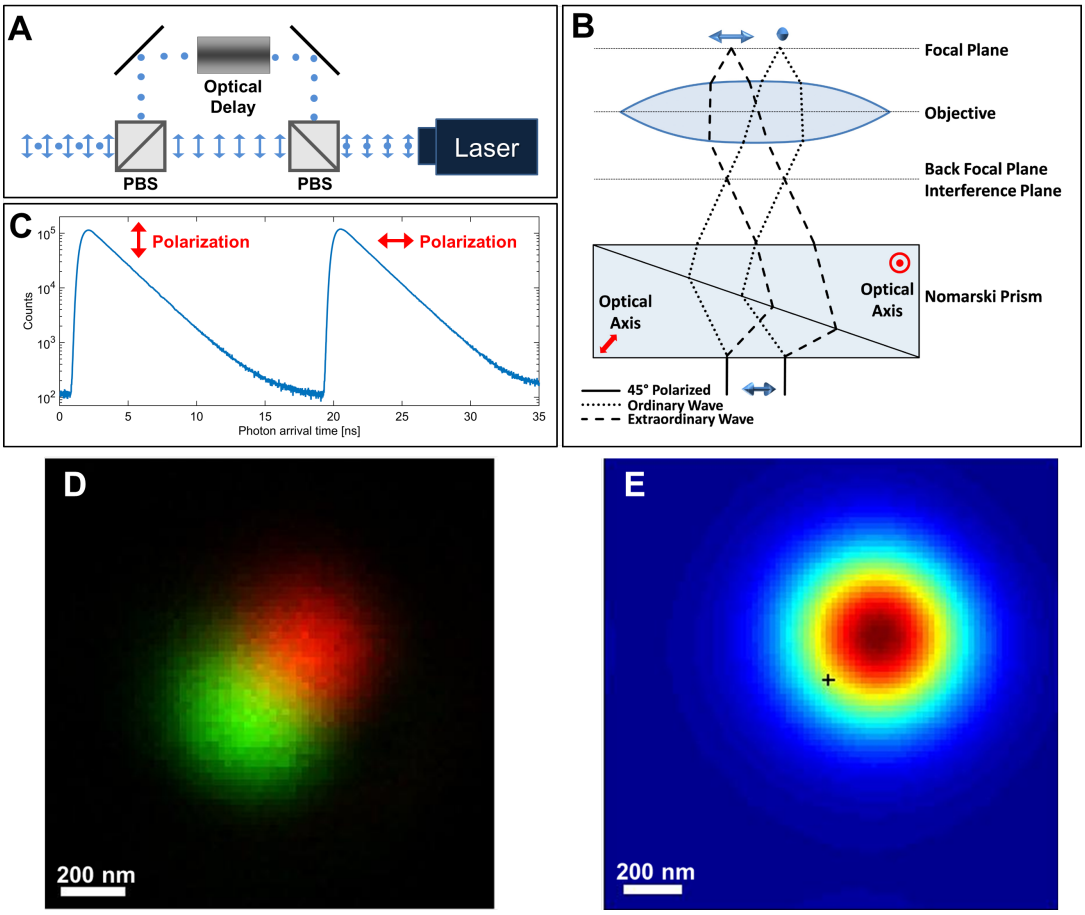

Figure 3.5: 2fFCCS principles. A) Schematic showing the generation of laser pulses with alternating orthogonal polarizations. PBS stands for polarizing beam splitter. B) Illustration of the mechanism to separate foci using a Nomarski prism. C) Photon arrival time histogram of two focus excitation. D) Scan of a fluorescent bead. The photon intensities of the two excitation polarizations are represented with green and red. E) Cross-correlation function of the two foci. The maximum is shifted from the center (indicated by the black cross) by the distance between foci.

Unlike in scanning FCS, the distance between foci stays constant over time, so that the CCF can be expressed as:

$$G(\tau) = \frac{\gamma}{N} \cdot \left(\frac{1}{1 + \frac{4D\tau}{\omega_r^2}} \right) \cdot \sqrt{\frac{1}{1 + \frac{4D\tau}{\omega_z^2}}} \cdot exp\left(- \frac{\xi^2}{w_r^2 + 4D\tau} \right) \tag{3.6}$$

In this case ξ represent the distance between the center positions of the foci. In general, the two auto-correlation functions (representing standard FCS data) and the cross-correlation are fit globally to maximize efficient photon use. An example of a 2fFCCS measurement is shown in Figure 3.6.

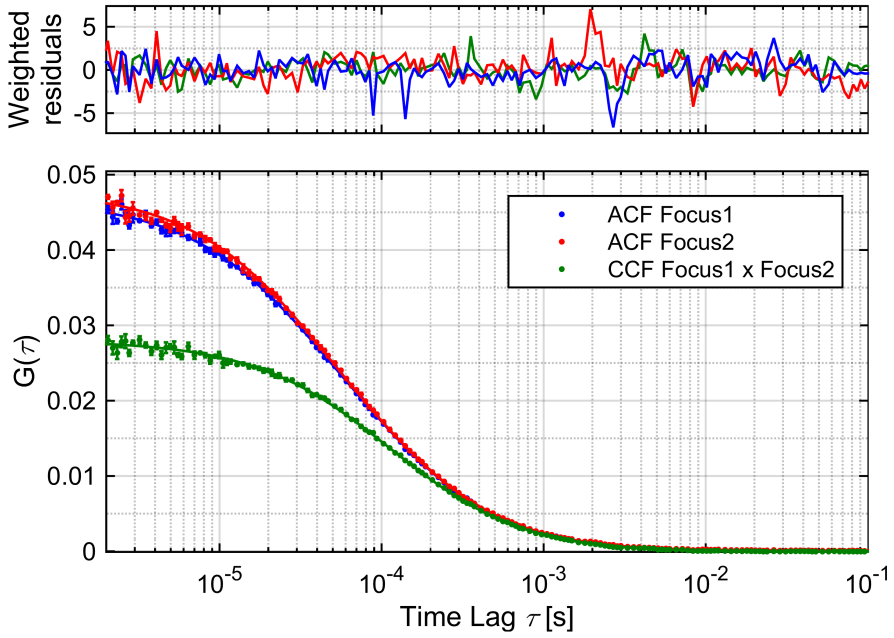

Figure 3.6: 2fFCCS curves for Atto655 carboxylic acid with a lateral focus size of 300 nm and a focal shift of about 200 nm.

Besides using a sample with known diffusion coefficient to calibrate the distance between foci, it is also possible to use scanning to determine the focal distance. When recording an image of a fluorescent bead, its position will be slightly shifted in the two channels (Figure 3.5 D). The inter-focus distance can then be extracted directly from the images or determined via image cross correlation (Figure 3.5 E). The later has the advantage that not only single beads, but also images with higher particle concentrations can be used (an introduction on image correlation is given in chapter 3.2).
The spatial asymmetry of 2fFCS also allows one to measure directions of flow or active particle movement. In normal FCS, the focus is symmetrical so that no spatial information about the particles' path can be gathered. The second focus, however, provides additional data that connects the spatial and the temporal aspects of the movement. A particle moving along the shift axis will pass through the foci sequentially, while a trajectory orthogonal to the focal displacement will be simultaneously detected in both channels or only in one focus. For free and random diffusion, all these effects will be averaged out, but any directed motion creates a bias that can be measured with 2fFCS.

3.1.5 Fluorescence Pair Correlation Spectroscopy

When a laser scanning confocal microscope is well calibrated, the exact position of the focus at any time of the measurement is known. Scanning FCS, however, averages over all times and therefore also positions and only the time lag and relative distance in space contribute to the correlation function. But also the absolute position can contain important information, e.g. when diffusion dynamics differ depending on the local environment inside a cell. Fluorescence pair correlation spectroscopy[55,56] extracts the full information about position by separating the data into spatial bins. Each bin represents an intensity time trace of that location and can be treated like a single point FCS measurement, although with a reduced temporal resolution (corresponding to the scanning repetition rate). The individual traces can be auto-correlated providing an FCS curve for each position. But it is also possible to cross-correlate pairs of bins, adding a spatial component to the analysis.

A full pair correlation analysis results in a large three-dimensional dataset with the correlation amplitude G as a function of time lag τ, spatial lag ξ, and absolute position x or bin n, making the data display a challenge in itself. In most cases only certain spatial lags are of actual interest, so that the pair correlation function (PCF) can be represented as a 2D false color carpet $G_\xi(n, \tau)$ for a given ξ, as is shown in Figure 3.7 A.

For increasing spatial lag and therefore also decreasing focal overlap, the correlation amplitude at low time lags decreases due to the fact that the particle cannot be at different positions at the same time. For a sufficiently large separation and low concentration, this can even lead to a negative amplitude. With longer time lags, however, particles can move further and diffuse to a new focus position, resulting in an increasing correlation function for low overlap. This is illustrated in Figure 3.8 B.

Although the PCF can be expressed with equation (3.6) for free and homogeneous diffusion, in most cases, a full quantitative analysis of pair correlation data is not feasible. A spatially resolved analysis is only needed when the diffusion behavior changes with the position, which in turn complicates the underlying mechanisms. For such complex processes, it is almost impossible to find an analytical solution. But even in these cases, a qualitative or semi-quantitative approach might reveal a lot of details about the sample that are not as easily detectable with other methods. One example of this is the case of asymmetric diffusion across barriers, e.g. in the nucleus.[57,58] If the movement in one direction is inhibited, the correlations forwards and backwards in space show a clear difference.

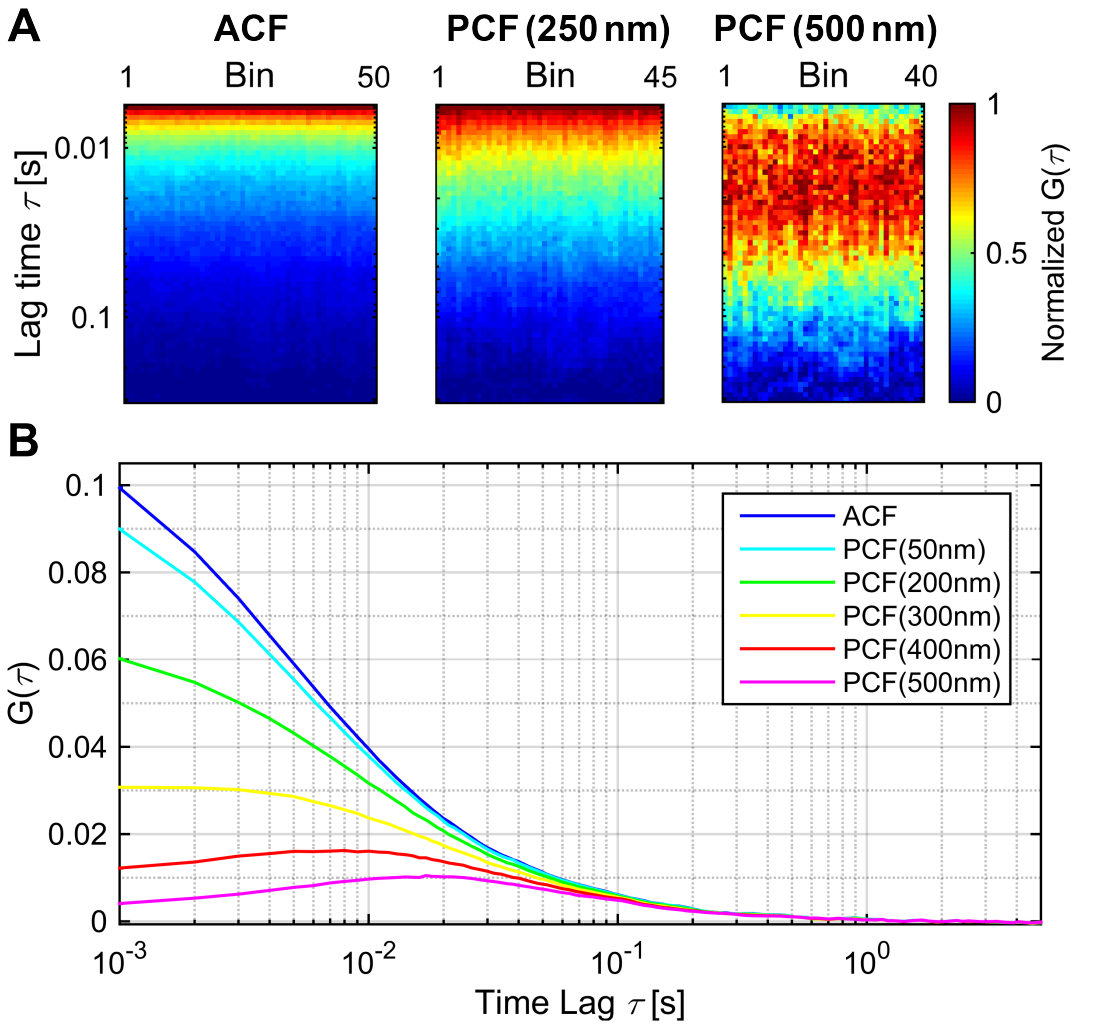

Figure 3.7: A) Pair correlation carpets for Atto647N-DPPE diffusion in a supported DOPC lipid bilayer for 0 nm (ACF, left), 250 nm (center) and 500 nm (right) spatial lag. B) Pair correlation curves for Atto647N-DPPE diffusion in a supported DOPC lipid bilayer for different spatial lags. The curves represent averages over all bins.

3.2 Image Fluctuation Spectroscopy

All techniques previously discussed in this chapter use a temporal correlation to investigate diffusion or other dynamics. However, most data acquired with a microscope consist of spatial information, namely images, with the time component usually being a secondary parameter. So the logical step is to apply the same ideas to the spatial fluctuations using image correlation spectroscopy (ICS) and related methods.[12,59–61] While the time domain reveals the kinetics of the processes, the spatial component contains information about the shape and size of the investigated sample, as well as its distribution in space.

3.2.1 Image Correlation Spectroscopy

The spatial equivalent to FCS is image correlation spectroscopy (ICS).[62,63] Unlike its temporal counterpart, image correlation is performed in two dimensions:

$$G(\xi,\psi) = \frac{\langle I_i(x,y)\cdot I_j(x+\xi,y+\psi)\rangle}{\langle I_i(x,y)\rangle\cdot\langle I_j(x,y)\rangle} - 1 = \frac{\langle \delta I_i((x,y)\cdot \delta I_j(x+\xi,y+\psi)\rangle}{\langle I_i(x,y)\rangle\cdot\langle I_j(x,y)\rangle} \tag{3.7}$$

Here, x and y denote the position in the two dimensions in space, while ξ and ψ represent the corresponding spatial lags in pixels. The intensity of the signals i and j is expressed as I. The angled brackets indicate the average over all spatial positions.
For randomly distributed particles that are significantly smaller than the focus size, the resulting auto correlation can be fit by a 2D Gaussian function:

$$G(\xi,\psi) = \frac{\gamma}{N}\cdot\exp\left(-\frac{\delta r^2\cdot(\xi^2+\psi^2)}{\omega_r^2}\right) \tag{3.8}$$

As in FCS, ω_r^2 describes the radius at which the fluorescence signal decreases to e^{-2} with respect to the intensity at the center of the focus. N corresponds to the average number of particles in the focus, while γ represents the shape factor ($2^{-\frac{3}{2}}$ for a 3D and 2^{-1} for a 2D Gaussian focus profile). The pixel size is denoted by δr. An example of a spatial correlation function is shown in Figure 3.8.
A spatial correlation function represents the average size and position of particles, and thus requires sufficient sampling of the underlying distributions in order to yield reliable results. While in FCS the measurement time can be increased to sample more temporal fluctuations, the imaged area for ICS is in most case limited by the maximal field-of-view of the instrument. This means that the correlation function of a single frame often shows artifacts from under-sampling and multiple frames are needed for accurate measurements.

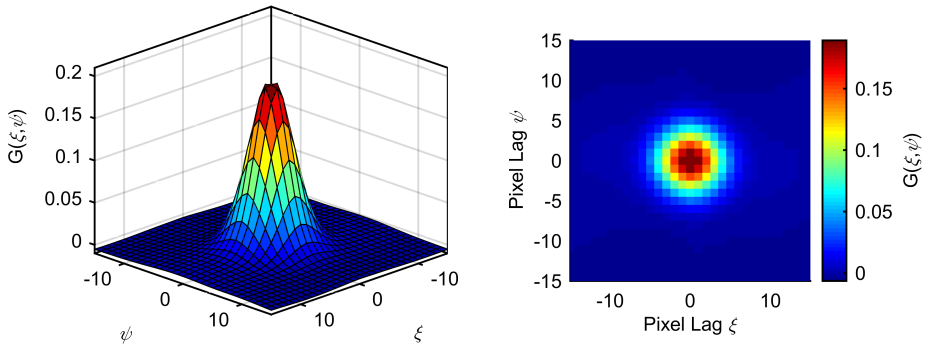

Figure 3.8: ICS surface (left) and image (right) plot of simulated immobile particles with a focus size of 200 nm.

Since the correlation amplitude is inversely proportional to the number, ICS is well suited for measuring the density and distribution of particles. By taking the average intensity $\langle I \rangle$ into account, the molecular brightness ($\epsilon = \frac{\langle I \rangle}{N}$) can be additionally determined. When the shape factor γ is accounted for, ϵ represent the countrate from a single molecule in the center of the focus. When the value of ϵ for a single emitter is known, the measured molecular brightness can be then be used to determine the fluorophore stoichiometry and therefore also the oligomerization state of the sample. In cases when the particle size exceeds the focal spot, it is necessary to replace w_r from (3.8) with the convolution of focus and particle dimensions, making it in turn possible to measure the average particle size.
Just as with FCS and FCCS, image correlation can be extended to cross-correlation, called image cross-correlation spectroscopy (ICCS).[64] When cross-correlating two different images, the resulting function only shows a non-vanishing amplitude in case of spatial similarity between the data sets. In most cases, the two images correspond to spectrally separated signals originating from different dyes so that cross-correlation only occurs when the differently labeled particles colocalize.

3.2.2 Raster Image Correlation Spectroscopy

All the arguments about ICS so far assumed that all pixels of an image are acquired at the same time. While this is true for widefield microscopy data recorded with a camera, an image is generated very differently with a confocal scanning microscope. Here, pixel acquisition happens one after another with a slight delay in time. This introduces a temporal component to the resulting spatial correlation. Raster image correlation spectroscopy (RICS)[7,65] uses exactly this temporal component to investigate dynamic processes happening on the timescale of image acquisition. In a raster scan, the focus is moved along the x-axis (continuously or stepwise for each pixel). When the end of the line is reached, the beam is quickly retracted to the start and at the same time moved one pixel in the y-direction. This results in a different temporal behavior along the fast x-axis (determined by the pixel dwell time τ_p) and the slow y-axis (defined by the line time τ_l) that can be several orders of magnitude apart. Rapidly diffusing molecules move significantly faster than the focus, so that the correlation function is mainly determined by the temporal component and decays quickly. Slow particles, on the other hand, barely move during a line scan, resulting in a curve along the fast axis that resembles the focus profile. In the slow spatial dimension, however, the focus velocity is strongly reduced, thus increasing the temporal contribution to the correlation. This asymmetry in the spatial dimensions allows RICS to measure diffusion coefficients on a large range of timescales. An example is shown Figure 3.9.
While the correlation algorithm is the same as for ICS, the fit function has to be adjusted. Assuming free diffusion measured with a 3D Gaussian focus, the image correlation function can be expressed as:

$$G(\xi,\psi) = \frac{\gamma}{N} \cdot \left(1 + \frac{4D \cdot (\tau_p \xi + \tau_l \psi)}{\omega_r^2}\right)^{-1} \cdot \left(1 + \frac{4D \cdot (\tau_p \xi + \tau_l \psi)}{\omega_z^2}\right)^{-\frac{1}{2}} \cdot \exp\left(-\frac{\delta r^2 \cdot (\xi^2 + \psi^2)}{\omega_r^2 + \left(4D \cdot (\tau_p \xi + \tau_l \psi)\right)}\right) \quad (3.9)$$

Here, N denotes the average particle number in the focus, D the diffusion coefficient and γ the shape factor. The radius of the focus is described by ω_r and ω_z for the lateral and axial dimensions, respectively. The pixel size is represented by δr, while τ_p and τ_l describe the pixel and line times, respectively.

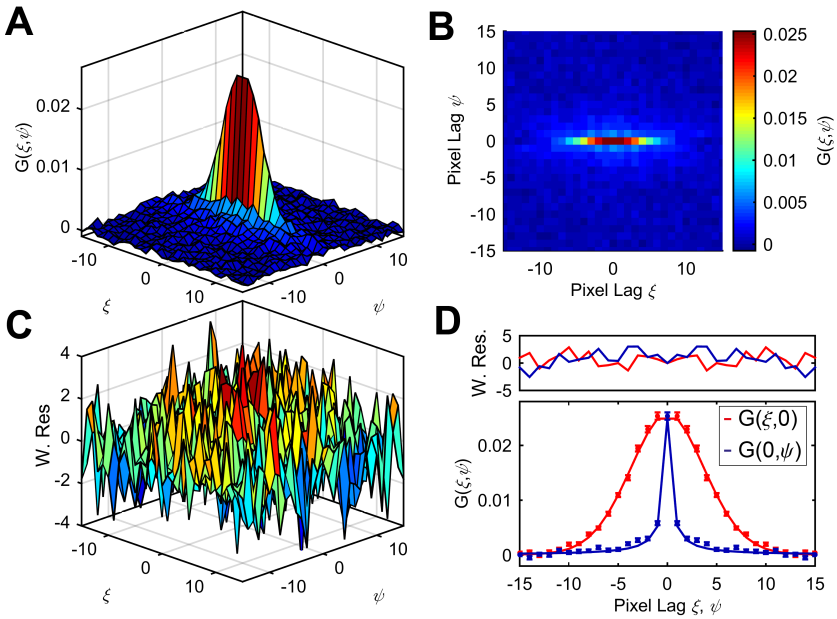

Figure 3.9: RICS of eGFP diffusion in a HeLa cell. Surface (A) and image (B) representation of the RICS correlation function. C) Surface plot of the weighted residuals of the data shown in (A) fit to equation (3.9). D) On-axis correlation curves for the slow (red) and fast (blue) scanning axis. Dots represent data with standard error of mean, while the solid line shows a fit.

Just like scanning FCS, RICS shows many advantages compared to point measurements. The pixel radius serves as an external ruler making it possible to simultaneously measure the focus size and diffusion coefficients. Due to the scanning, each particle is illuminated for a much shorter time. This strongly decreases bleaching, which is especially important for cell measurements, where diffusion is slowed down and mostly fluorescent proteins are used that do not exhibit a very high photostability.
The same principles for going from an auto- to a cross-correlation that were mentioned for FCCS and ICCS, are also applicable to raster image cross correlation

(ccRICS):[66] Only concerted movement of different dyes results in a cross-correlation amplitude, making accurate investigations of molecular interactions possible (Figure 3.10).

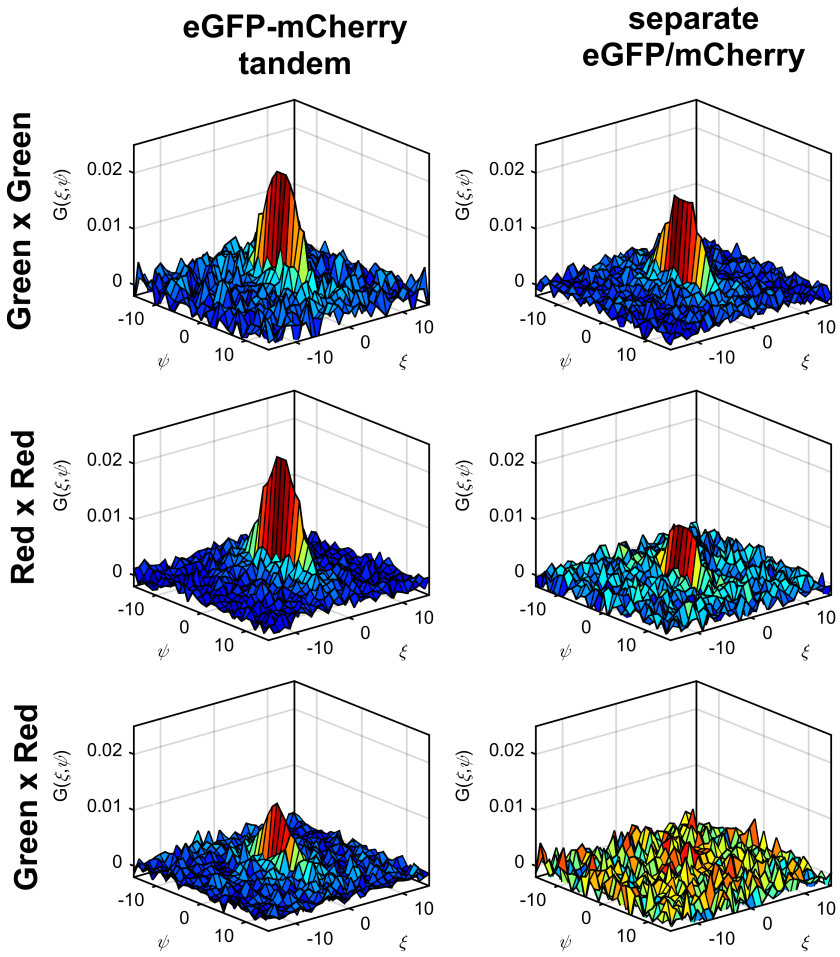

Figure 3.10: Raster image auto- (green top; red middle) and cross-correlation (bottom) of eGFP and mCherry diffusing separately (right) as well as of an eGFP-mCherry tandem construct (left) in a HeLa cell. The data is an average over 100 frames.

The spatial component of RICS also allows one to account for a wavelength dependent lateral focus shift. In this case, the spatial component is also shifted, while the temporal correlation is not affected. Adding the shift (δx and δy) to equation (3.9) results in:

$$G(\xi,\psi) = \frac{\gamma}{N} \cdot \left(1 + \frac{4D \cdot (\tau_p \xi + \tau_l \psi)}{\omega_r^2}\right)^{-1} \cdot \left(1 + \frac{4D \cdot (\tau_p \xi + \tau_l \psi)}{\omega_z^2}\right)^{-\frac{1}{2}} \cdot \exp\left(-\frac{\delta r^2 \cdot \left((\xi - \delta x)^2 + (\psi - \delta y)^2\right)}{\omega_r^2 + \left(4D \cdot (\tau_p \xi + \tau_l \psi)\right)}\right) \quad (3.10)$$

3.2.3 Temporal Image Correlation Spectroscopy

The application of RICS is limited to processes happening on the timescale of image acquisition, mainly relatively fast diffusion down to approximately $0.1\,\mu m^2\,s^{-1}$. But there is still information of slower dynamics hidden in the fluctuations between consecutive frames. This information can be extracted using temporal image correlation (TICS).[63,67] Hereby, the individual pixels are correlated with themselves within consecutive frames, resulting in a temporal correlation function, very similar to FCS. The time resolution is determined by the frame acquisition speed and is therefore several orders of magnitude slower than for FCS measurements. However, many different locations are measured at the same time, presenting a big advantage compared to point measurements. They can either be averaged to get a higher sampling of slow and rare events, or analyzed individually. The later method generates a diffusion map, allowing for the investigation of spatially heterogeneous dynamics.

3.2.4 Spatio-Temporal Image Correlation Spectroscopy and Image Mean-Square Displacement

The next step from the purely spatial correlation like in ICS or the solely temporal one in TICS is to combine both, as is done in spatio-temporal image correlation spectroscopy (STICS).[59,68,69] In STICS, space and time correlations are analysed together, thus generating a 3D correlation matrix that links the different dimensions together and contains more information than the purely spatial or temporal analyses. The spatio-temporal correlation function can be calculated according to equation (3.11):

$$\begin{aligned} G(\xi,\psi,\tau) &= \frac{\langle I_i(x,y,t)\cdot I_j(x+\xi,y+\psi,t+\tau)\rangle}{\langle I_i(x,,ty)\rangle\cdot\langle I_j(x,y,t)\rangle} - 1 \\ &= \frac{\langle \delta I_i((x,y,t)\cdot \delta I_j(x+\xi,y+\psi,t+\tau)\rangle}{\langle I_i(x,y,t)\rangle\cdot\langle I_j(x,y,t)\rangle} \end{aligned} \tag{3.11}$$

In this case, the angled brackets correspond to an averaging over both space and time. The three dimensional STICS data contains all aspects of both ICS (corresponds to zero time lag) and TICS (zero spatial lags), but also additional information, not accessible through the other two methods alone. It is especially interesting to look at how free diffusion and flow affect STICS when looking at the spatial correlation as a function of time lag: Freely diffusing molecules move with equal probability in all directions. This results in a spreading of the spatial correlation with time (Figure 3.11 left). However, if the movement is biased towards one direction, e.g. drift or flow, the maximum amplitude of the correlation will shift off center, depending on velocity and direction of the movement (Figure 3.11 right).

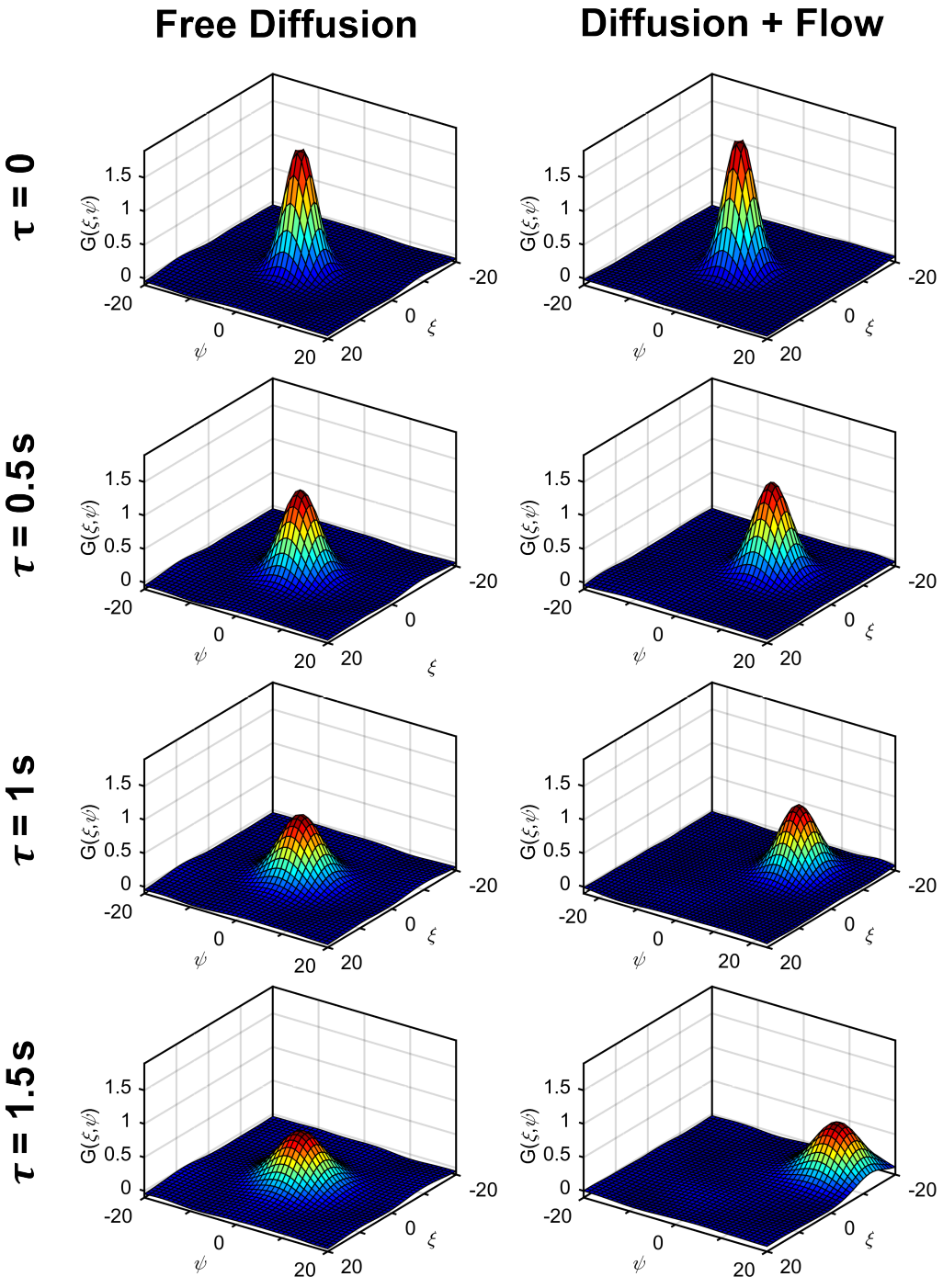

Figure 3.11: Simulated data showing the effect of free diffusion (left) and diffusion with constant displacement (right) on the spatio-temporal correlation function. In both cases, the diffusion coefficient was set to $0.01\,\mu m^2\,s^{-1}$. The flow rate for the data on the right corresponds to $0.6\,\mu m\,s^{-1}$.

In the case that only one of several species is affected by directed motion, the resulting STICS function will show two peaks that separate over time (Figure 3.12).

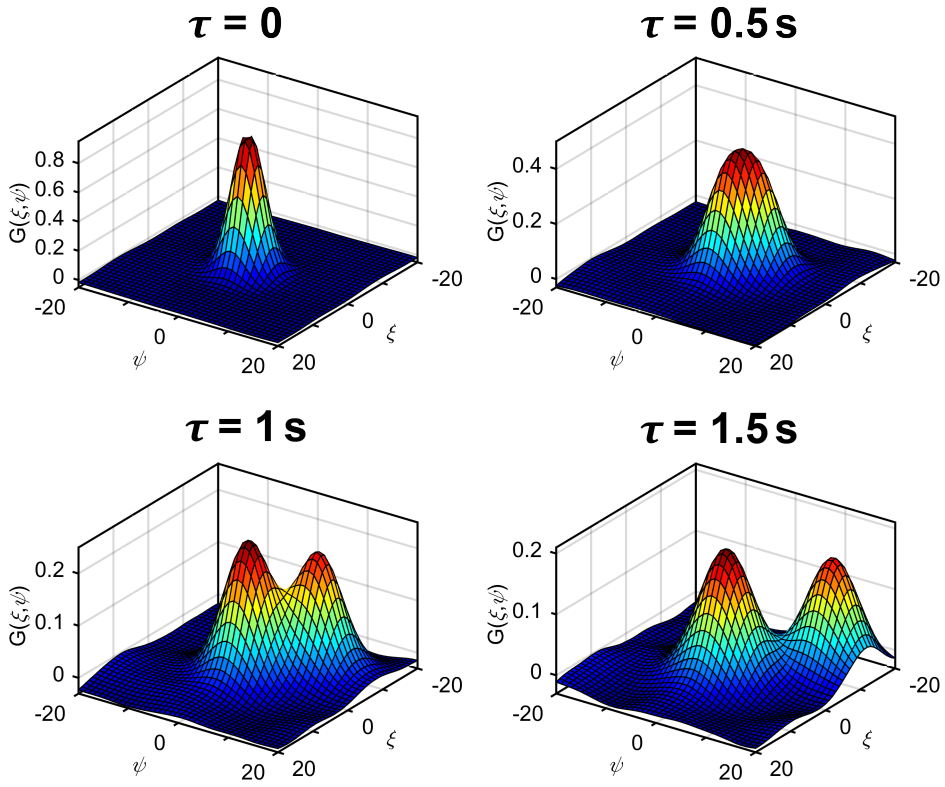

Figure 3.12: Simulated STICS data for two freely diffusing species, where only one is affected by directed movement.

One application of spatio-temporal correlation data to investigate diffusive behavior is called image mean square displacement (iMSD).[70] Hereby, the square of the width of the spatial correlation σ_r is plotted as a function of temporal lag. The intercept at zero time lag, corresponding to the focus size, is usually subtracted, so that the curve starts from the origin (Figure 3.13). The resulting graph shows the same behavior as a standard mean square displacement plot calculated with tracking data: While free diffusion results in a straight line, sub- or super-diffusion have a positive or negative curvature, respectively, indicated by the anomaly factor α:

$$\sigma_r(\tau)^2 = \sigma_r(0)^2 + 4D\tau^\alpha \tag{3.12}$$

More complicated behaviors like corralled motion or hop diffusion will also show their unique effects and can be identified by their particular curves in the iMSD plots.

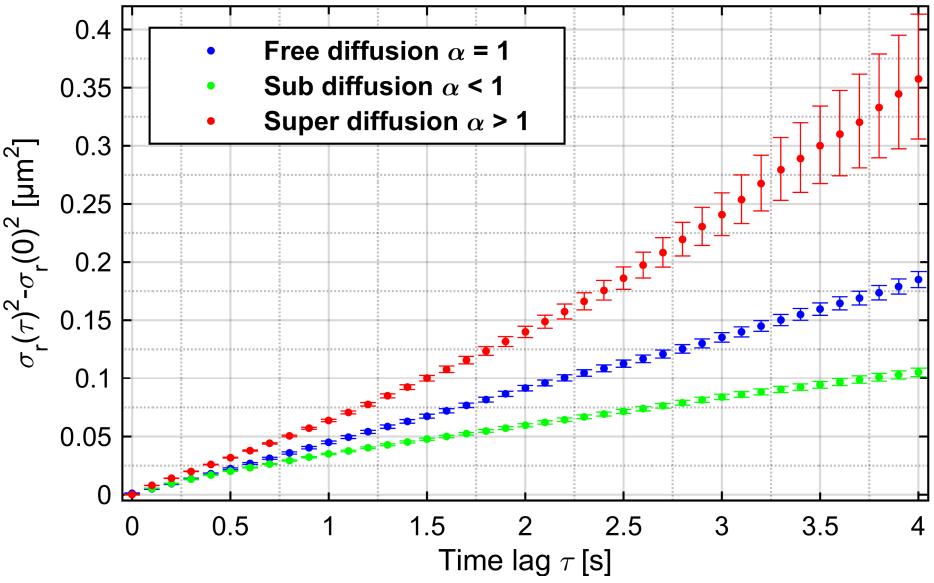

Figure 3.13: iMSD plot of simulated STICS data for free, sub- and super-diffusion.

3.2.5 Number and Brightness Analysis

Unlike the previously mentioned techniques for analyzing image fluctuations, the number and brightness analysis (N&B) [60,71–73] method does not use a full correlation, but utilizes the moments of the photon count distribution. From the first two moments (mean intensity $\langle I \rangle$ and variance σ^2) one can calculate the apparent number N and apparent brightness B:

$$B = \frac{\sigma^2}{\langle I \rangle} \quad \text{and} \quad N = \frac{\langle I \rangle^2}{\sigma^2} \tag{3.13}$$

It has to be noted that these values still contain contributions from the shot noise and the focus shape. To make the results comparable with the corresponding values from a correlation analysis, equation (3.13) has to be modified to:

$$\epsilon = \frac{1}{\gamma} \cdot \frac{\sigma^2 - \langle I \rangle}{\langle I \rangle} = \frac{1}{\gamma} \cdot (B - 1) \quad \text{and} \quad n = \gamma \cdot \frac{\langle I \rangle^2}{\sigma^2 - \langle I \rangle} = \gamma \cdot N \cdot \left(1 + \frac{1}{\epsilon}\right) \tag{3.14}$$

By performing these calculations for each individual pixel it is possible to create a brightness map of the imaged region. This, in turn, contains information about the oligomerization state of the sample in different parts of the sample. The N&B method is usually used to interpret the data in a qualitative fashion by analyzing, if certain regions show a higher or lower brightness as compared to the rest. In order to properly quantify the data, especially in the presence of several fluorescent species, a higher order moment analysis is required.

3.3 Fluorescence Lifetime Analysis

Although the actual transition between electronic states happens almost instantaneously (10^{-15} s), a fluorophore still spends a significantly longer time in the excited state before de-excitation can occur. This fluorescence lifetime is not only determined by the particular fluorophore, but it is also highly dependent on the local, nano-scale environment of the molecule. Accurately determining the fluorescence decay reveals a lot of information about the fluorophore and its surroundings. The true strength of fluorescence lifetime analysis lies in spatially resolved measurements. In FLIM, short for fluorescence lifetime imaging microscopy, the lifetime is determined for each individual pixel of an image.[14–17] Thus, changes in fluorescence decay can be correlated with features of the imaged region, revealing the spatial distribution of parameters affecting the fluorescent probe.

3.3.1 Fundamentals of Fluorescence Lifetime

A standard fluorescence relaxation cycle constitutes a multi step process (see chapter 2.2). The internal conversions are on a much faster (10^{-12} s) timescale than the $S_1 - S_0$ transition (10^{-9} s), effectively turning fluorescent de-excitation into a first order process. Therefore, the fluorescence lifetime τ and quantum yield Q can be calculated by:

$$\tau = \frac{1}{\Gamma + k_{nr}} \tag{3.15}$$

$$Q = \frac{\Gamma}{\Gamma + k_{nr}} \tag{3.16}$$

where Γ is the fluorescent rate constant while k_{nr} represents the sum of all non-radiative rate constants, like internal conversion, energy transfer or other quenching mechanisms.
The fact that fluorescence is a first order process leads to an exponential decay. This means that whenever two or more exponentials are observed, the sample must contain multiple species. In most cases this is caused by different fractions of the sample being quenched to a varying degree, a parameter of high interest in many measurements. Some fluorophores like eGFP, however, exhibit multiple states with different fluorescent properties. Since these states interchange quite quickly, but slower than the fluorescence de-excitation timescale, these dyes will always show a multi-exponential decay.
For a given fluorophore and solvent, Γ is fairly stable and depends mainly on the excitation and emission spectra. The non-radiative rate constants, on the other hand, can be strongly influenced by the local environment or the presence and absence of certain moieties. By choosing a fluorescent dye that is both sensitive and specific to a certain parameter or analyte, one can use the change in lifetime

as a readout for the property of interest.[74–78]
A common application for fluorescence lifetime spectroscopy is quenching in a donor-acceptor system.[79–81] Hereby the energy is transfered from the donor to the acceptor either via an electron (photo-induced electron transfer, PET) or a dipole-dipole interaction (Förster resonance energy transfer, FRET), creating a new relaxation pathway and reducing the observed fluorescence lifetime. This quenching only happens if the acceptor is in close proximity (about 10 Å for PET and up to 100 Å for FRET) to the donor. When the dye and the quencher are placed on different molecules or domains of a macromolecule, these methods can resolve interactions or conformational rearrangements, if they result in a change of the donor-acceptor distance. The distance dependence of the dipole-dipole interactions in FRET can even be used to accurately measure the spatial separation of dyes.

$$E = 1 - \frac{\tau_{FRET}}{\tau_0} \tag{3.17}$$

Here, E is the FRET efficiency, defined as the ratio between the FRET rate and the total de-excitation rate (including FRET). The measured lifetime is denoted by τ_{FRET}, while τ_0 represents the native fluorescence lifetime of the donor dye in the absence of the acceptor.
The efficiency E shows a power of six dependence on the distance according to:

$$E = \frac{{R_0}^6}{{R_0}^6 + r^6} \tag{3.18}$$

The donor-acceptor distance is represented with r and R_0 is the so called Förster radius, the dye pair specific distance at which the probability for energy transfer is 50%. For a known R_0, the lifetime and therefore the FRET efficiency can be measured and used as a molecular ruler.

3.3.2 Time Domain Fluorescence Lifetime Imaging Microscopy

The conceptually easiest way of measuring the fluorescence lifetime is by exciting the sample with a short laser pulse and looking at the fluorescence intensity as a function of time. For a first order process, this results in a fast rise of intensity after the excitation, followed by an exponential decay. The time dependent intensity, $I(t)$, for a system with k independent species can be described by:

$$I(t) = \sum_{i=1}^{k} \alpha_i e^{-t/\tau_i} \tag{3.19}$$

where τ represents the lifetime of species i and α its relative amplitude at time point 0. The fractional intensity, f, for each species is given by:

$$f_i = \frac{\alpha_i \tau_i}{\sum_j \alpha_j \tau_j} \tag{3.20}$$

In a confocal microscope, however, a single pulse is not enough. The small focal volume combined with the relatively low sample concentration result in only a few fluorophores being excited at a time. Since each molecule can only emit one photon per excitation, the number of photons detected per pulse is also low and an accurate measurement of the fluorescence lifetime is not possible. Therefore, in modern confocal lifetime microscopes, TCSPC detection is employed.[4,5] Hereby, the precise time, down to a few picoseconds, of each photon is recorded. Because the detectors are synchronized with the laser pulses, this allows determination of the delay of a photon relative to the laser pulse. The fluorescence decay is then reconstructed by histogramming the arrival time of many pulse cycles.
Ideally, the sample is excited instantaneously, resulting in a nice decay. Practically, however, the situation is more complicated. First, laser pulses have a non-vanishing duration. Furthermore, all electronics used in photon detection and timing exhibit a small amount of temporal jitter. Together, these cause even infinitely short signals to be detected with a significant temporal width, called the instrument response function (IRF). For longer lifetimes, the measured signal is therefore a convolution of the actual decay and the IRF. This concept is illustrated in Figure 3.14.

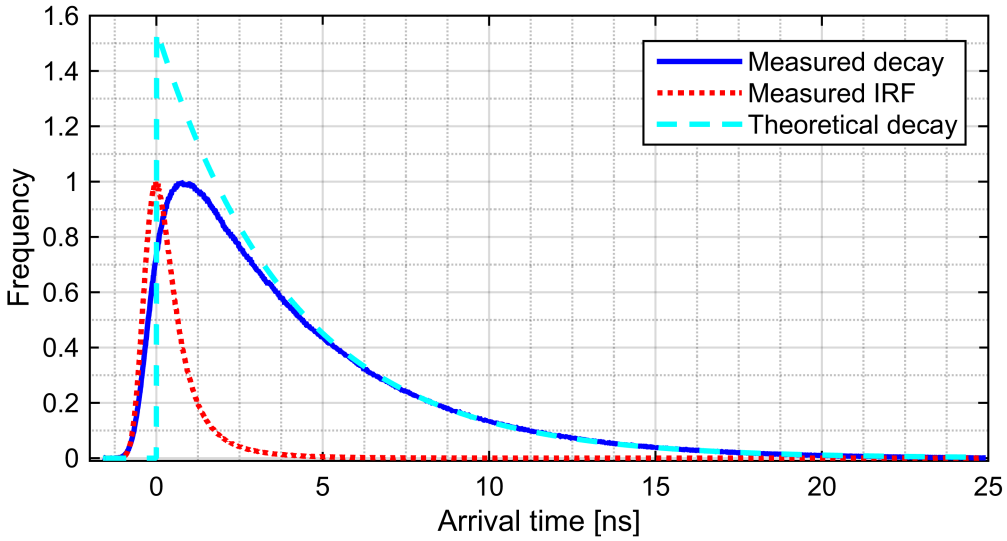

Figure 3.14: TCSPC data for the fluorescence decay of Atto488 carboxylic acid. The measured data (blue solid line) and instrument response function (IRF, red dotted line) are normalized at the maximum. The theoretical decay for an instantaneous excitation (cyan dashed line) is scaled such that the tail matches the measured curve

There are several ways to analyze time-domain fluorescence lifetime data. The most accurate approach is to perform a convolution fit that takes the instrument response function into account.[82,83] This way, the photon information is used most efficiently and complex signals with multiple components can be analyzed correctly. The limits of the applicability of this approach are dictated by the data quality and calculation time. For a single point experiment, it is common to measure millions and sometimes even billions of photons. Here, the signal-to-noise ratio is

very high and the single fit is completed in almost no time. In FLIM, on the other hand, the situation is very different. The signal is spread out over many individual pixels, so that each point only contains a few hundred to maybe a few thousand photons. In such a case, the fit quickly becomes unreliable, especially when multiple components are involved. Furthermore, the fitting routine has to be performed for many thousands or even millions of pixels, turning calculation time into a critical issue.
A way to deal with this problem exploits the fact that, in most images, the individual lifetimes stay constant, while their relative contribution varies. Therefore, all the photons are pooled and one multi-exponential fit is performed on the full data set. In a second step, the individual pixels are fit, but the lifetimes, determined by the initial analysis, are kept constant and only their fraction optimized. This not only makes the procedure less prone to misfitting, but also increases speed, because only one parameter is fit and a convolution at every step is no longer required.
A second approach to simplify the fitting procedure it to perform a tail fit. Hereby, only the later part of the fluorescence decay is used, where the influence of the IRF is negligible. It has the advantage that knowledge about the IRF is no longer needed and a very simple fit procedure without convolution can be used. Although this makes the analysis easier, in many cases, it might not give the right results. It is often hard to estimate how far the influence of the IRF extends (see Figure 3.14). Choosing an early cutoff can affect the fit and give wrong results. A late cutoff, however, discards too much data, decreasing the signal-to-noise. Besides that, tail-fitting is not applicable for multi-exponential signals. Since the decay rates are different, the relative contributions of the individual species to the photon signal changes with the lag time. Therefore, the initial decay is needed in order to determine the relative fractions of multiple species correctly. By omitting these first time points from analysis, tail-fitting creates a bias towards the longer lifetime components.
An even simpler and faster way of interpreting lifetime data is to simply calculate the mean arrival time. For mono-exponential decays, this calculation yields the correct lifetime. But this approach has several shortcomings that must be considered before applying it. Just calculating the mean does not account for the actual shape of the distribution. This means that, for multi-exponential decays, it is impossible to distinguish a shift of the actual lifetimes from a change in their relative contribution. Besides that, this method attributes a lot of weight to photons at late time points, where the signal is usually low. This leads to an over proportional contribution of background noise. Still, the mean arrival time analysis is widely used due to its simplicity.
In recent years, a new method that utilizes analysis in the Fourier space has been gaining in popularity. This method, called the phasor approach to FLIM, will be discussed in greater detail later in chapter 3.3.4.

3.3.3 Frequency Domain Fluorescence Lifetime Imaging Microscopy

A second type of experiment for determining fluorescence lifetimes uses a high frequency modulation (usually 1–100 MHz) of the excitation intensity, resulting in an oscillation of the fluorescence with the same frequency. However, due to the finite lifetime, the oscillation of the recorded signal will be delayed and show a decrease in modulation compared to the excitation, as is illustrated in Figure 3.15.

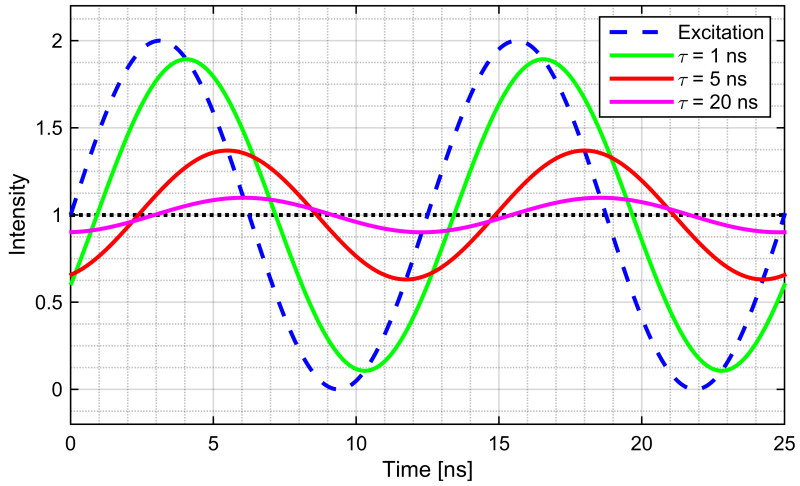

Figure 3.15: Effect of the fluorescence lifetime on the phase shift and the demodulation of the signal for excitation modulated at 80 MHz.

This phase shift, Φ_ω, and demodulation, M_ω, depend on both the circular modulation frequency ω and the sample decay time τ:

$$\tan \Phi_\omega = \omega \tau_\Phi \tag{3.21}$$

$$M_\omega = (1 + \omega^2 {\tau_m}^2)^{-\frac{1}{2}} \tag{3.22}$$

From equations (3.21) and (3.22), one can calculate two apparent lifetimes τ_Φ and τ_m. In the case of a single lifetime component with a mono-exponential decay, these two will be identical. When the signal contains more than one exponential decay, the lifetimes from the phase and the modulation will differ, depending on the measurement frequency, the lifetimes of the individual species and their fractional intensities (Figure 3.16).
For a sample containing multiple species i, the phase shift and demodulation can be calculated according to:

$$\tan \Phi_\omega = \sum_i \frac{f_i \omega \tau_i}{(1 + \omega^2 {\tau_i}^2)} \Big/ \sum_i \frac{f_i}{(1 + \omega^2 {\tau_i}^2)} \tag{3.23}$$

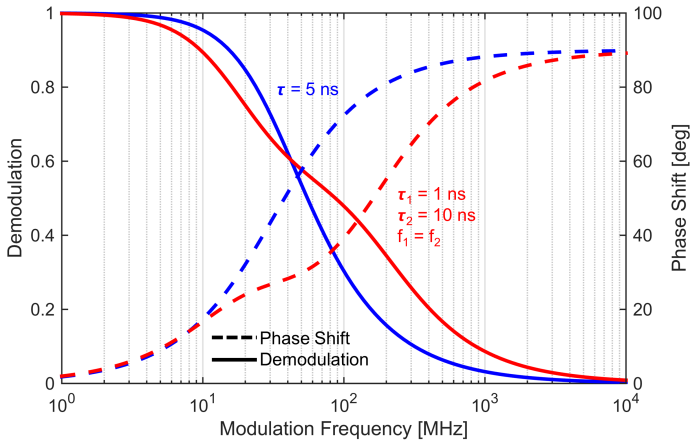

Figure 3.16: Phase shift and demodulation as a function of modulation frequency for a signal with a single exponential lifetime (blue) and for a sample with two lifetimes (red).

$$M_\omega = \left(\left(\sum_i \frac{f_i \omega \tau_i}{(1+\omega^2 {\tau_i}^2)} \right)^2 + \left(\sum_i \frac{f_i}{(1+\omega^2 {\tau_i}^2)} \right)^2 \right)^{\frac{1}{2}} \tag{3.24}$$

The advantage of frequency FLIM[84,85] over time domain measurements is the acquisition speed. Data can be recorded on a camera instead of point detectors, meaning that all pixels are acquired simultaneously. Although cameras are generally not fast enough to resolve the fast signal fluctuation, a small trick helps to recover the phase and modulation. Hereby, the camera sensitivity or gain is modulated with the same frequency as the excitation light. By changing the phase between excitation and detection, the modulation is reconstructed on a slower timescale.
Unlike in the time domain where a single decay, in theory, contains all the information necessary to resolve a system containing any number of lifetimes, a frequency domain measurement only provides two data points (phase and demodulation). However, each additional species introduces two new variables (lifetime and fractional intensity), requiring also two additional parameters to be measured in order to describe the system unambiguously. Therefore, a measurement at a different frequency has to be performed for each lifetime species. Ideally, the sample is measured over a wide range of frequencies and the resulting curves fit with an appropriate model.
A different way of analyzing the data in a graphical manner is called polar- or phasor-plot and is described in the next section of this chapter.

3.3.4 Phasor Approach to Fluorescence Lifetime Imaging Microscopy

In the phasor plot,[86,87] each lifetime measurement or pixel is represented by a vector with the length corresponding to the demodulation M_ω and the angle to

the abscissa being equal to the phase shift Φ_ω. The Cartesian coordinates s and g of this phasor (a contraction of *phas*e vect*or*) represent the first sine and cosine Fourier coefficients of the signal, respectively. They can be calculated according to:

$$s_\omega = M_\omega \cdot \sin(\Phi_\omega) = \int_0^\infty I(t) \cdot \sin(\omega t) dt \,/ \int_0^\infty I(t) dt \tag{3.25}$$

$$g_\omega = M_\omega \cdot \cos(\Phi_\omega) = \int_0^\infty I(t) \cdot \cos(\omega t) dt \,/ \int_0^\infty I(t) dt \tag{3.26}$$

I represents the fluorescence intensity at time t and ω is the angular modulation frequency. It has to be noted that a phasor is specific to a particular frequency. Although the phasor representation is based on frequency domain principles, it can also be applied to the pulsed excitation of time domain data, using the same formulae. After all, repeated pulses are also a kind of modulation, just not sinusoidal. The difference lies only in the IRF and can be corrected, as will be described later. The shift to Fourier space simplifies analysis and representation of lifetime data, based on a few mathematical relationships that are significantly more complicated in regular time space. The three most important rules are:

1. A convolution in time space leads to a change of base in Fourier space, resulting in a rotation and rescaling of the coordinate system.

2. All mono-exponential decays lie on the so called universal circle with radius 0.5 around point (0.5,0).

3. The phasor of a mixture corresponds to the fraction weighted vector addition of the phasors of the pure species.

A consequence of the first rule is that accounting for the IRF becomes very simple. All one has to know is the phase shift Φ_{IRF} and demodulation M_{IRF} caused by the instrument itself and apply them to equations (3.25) and (3.26):

$$s_{\omega,ref} = \frac{M_\omega}{M_{IRF}} \cdot \sin(\Phi_\omega - \Phi_{IRF}) = \frac{1}{M_{IRF}} \cdot \int_0^\infty I(t) \cdot \sin(\omega t - \Phi_{IRF}) dt \,/ \int_0^\infty I(t) dt \tag{3.27}$$

$$g_{\omega,ref} = \frac{M_\omega}{M_{IRF}} \cdot \cos(\Phi_\omega - \Phi_{IRF}) = \frac{1}{M_{IRF}} \cdot \int_0^\infty I(t) \cdot \cos(\omega t - \Phi_{IRF}) dt \,/ \int_0^\infty I(t) dt \tag{3.28}$$

The easiest way to determine the IRF parameters is to measure a sample with known lifetime and choose a new base such that the measured phasor is mapped onto the theoretically expected one in the new coordinate system (Figure 3.17 A). The second rule is a direct result of equations (3.21) and (3.22). For a simple exponential decay, both equations yield the same lifetime, so that an direct relationship between the phase and demodulation can be established:

$$M_\omega = (1 + \tan(\Phi_\omega)^2)^{-\frac{1}{2}} \tag{3.29}$$

In phasor coordinates this translates to:

$$s_\omega{}^2 + (g_\omega - \frac{1}{2})^2 = \frac{1}{4} \tag{3.30}$$

with

$$s_\omega = \frac{\omega\tau}{1 + (\omega\tau)^2} \tag{3.31}$$

and

$$g_\omega = \frac{1}{1 + (\omega\tau)^2} \tag{3.32}$$

As a consequence, all mono-exponential signals will be spread out on the universal circle defined by equation (3.30), with phasors for shorter lifetimes lying close to the point (1,0), while a decay time close to infinity will be close to the origin.

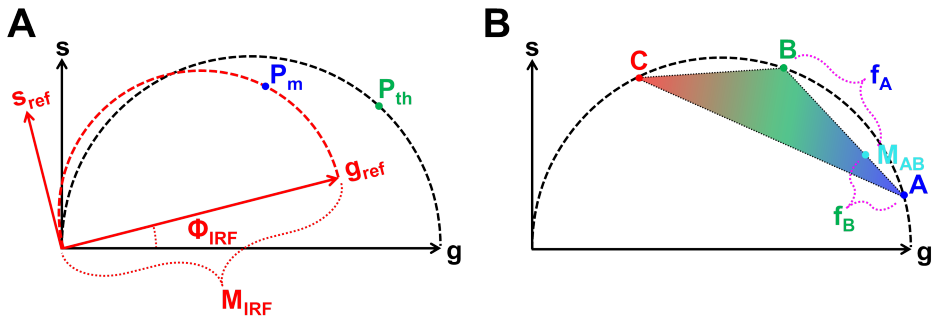

Figure 3.17: A) Accounting for the IRF: A new reference base is chosen such, that the measured phasor P_m falls on the same position in the new coordinate system as the theoretically expected phasor P_{th} does in the standard base. B) Any mixture of the species A, B and C must lie in the colored triangle with A, B and C as vertices. The mixture M_{AB} of components A and B is on the line connecting them. The exact position of M_{AB} is determined by their fractional intensities f_A and f_B.

The last rule is very convenient for analyzing samples containing multiple species. The vector addition results in the fact that any mixture on n components will fall inside a n-sided polygon with the base components as vertices. For just two species,

this means a straight line connecting the pure phasors. The exact position for given fractional intensities is simply the result of the law of the lever (see Figure 3.17 B). The phasor of the mixture M_{AB} of components A and B with their fractions f_A and f_B is given by:

$$\frac{\overline{AM_{AB}}}{\overline{BM_{AB}}} = \frac{f_B}{f_A} \tag{3.33}$$

with $\overline{AM_{AB}}$ and $\overline{BM_{AB}}$ representing the distance between the phasors of the mixture, M_{AB}, and A or B, respectively.
For systems composed of three species, it is still possible to calculate the individual fractions, as long as the phasors of all pure components are known. When four or more different lifetimes are involved, additional information (e.g. higher harmonics) is required to uniquely define the system.
Another consequence of rules two and three is that any combination of one step processes with exponential decay leads to a phasor inside of or on the universal circle. If a population is observed that falls outside of that region, it must be a result of wrong referencing or a multi-step process. A prominent case for the later is FRET. Here, the fluorescence signal in the donor channel will show a normal mono- or multi-exponential decay with a phasor inside the universal circle. The acceptor signal, however, involves two steps: first, the energy is transfered to the acceptor with the donor decay time. Only then can the photon be emitted by the acceptor with its own lifetime. This can be considered as a convolution of the donor and the acceptor decay. Since this corresponds to a change of base in the phasor space, the measured signal might be shifted out of the circle.

4. PIE Analysis in Matlab (PAM)

Advancement of scientific methods is often made possible by the development of more sensitive and sophisticated equipment, so that weaker signals can be detected or subtler changes observed. At the same time, the increase of readily available computational power allows more advanced analysis techniques and algorithms to be applied to the measured data, extracting an ever increasing amount of information from each individual experiment. Especially in the field of fluorescence microscopy and spectroscopy, the last decades have seen a rapid growth in new methodology accompanied by an equal development of algorithms and analysis software (as shown in chapter 3). Although a wide variety of programs for the individual techniques are available, they are usually optimized for a specific application and are not very flexible with respect to changes in algorithms or data type. Modern microscopy data, however, contains a huge amount of information that often cannot be utilized to its maximum potential by a single technique. Therefore, several different and often incompatible programs need to be used, increasing time, effort and expertise required to perform a full analysis of the experiments. Additionally, these single purpose applications are generally very static and not designed to be modified for new ways of data analysis.
In this chapter. I will present *PIE Analysis with Matlab* (*PAM*), a software package that is designed for two very different types of users: As a robust, easy-to-use collection of fluorescence applications for the casual user and as an easily accessible and adjustable platform for the development and implementation of new analysis methods for people with programming experience. To facilitate both types of uses, *PAM* is based on the Matlab programming language and its implemented graphical user interface (GUI) and is available as a modifiable open-source code. The main application methods include the analysis of static (chapter 4.3) and scanning (chapter 4.4) correlation data, fluctuation imaging (chapter 4.5), as well as lifetime analysis using the phasor approach (chapter 4.6). Furthermore, a tool for simulating confocal microscopy and spectroscopy data (chapter 4.7) is included in PAM. Another important group of functionalities focuses on burst-wise two- and three-color FRET measurements. These features were developed by Anders Barth and are therefore not further described in this thesis.
The first and still primary data type of *PAM* is confocal TCSPC data using pulsed interleaved excitation, as is evident from the name. However, the code has since outgrown this single application and is by now compatible with a wide variety of different microscopy data, including confocal data without TCSPC or with scanning, or even camera based microscopy, rendering the name a historical remnant.
The software development was done in collaboration with Anders Barth and Dr. Jelle Hendrix. Several of the presented functionalities are based on previous algorithms and code, mainly written by Dr. Matthias Höller, Dr. Volodymyr Kudryavtsev and Dr. Jelle Hendrix, and were reimplemented, optimized and extended to their current form.

4.1 General Program Structure and Philosophy

The idea behind developing *PAM* was to have a singe versatile and flexible program encompassing many advanced microscopy methods ranging from fluctuation spectroscopy over lifetime analysis to single molecule FRET, so that the information contained in each recorded photon can be maximally utilized. Matlab was chosen as the primary programing language for *PAM* since it is the most suited to fulfill the following basic concepts required for an efficient analysis tool:

- Fast and robust standard algorithms and procedures for efficient analysis of routine experiments.
- Structural and functional expandability enabling incorporation of new input formats or analysis methods.
- Ease of access to data at any stage of processing and on the fly analysis.
- High acceptance and familiarization of the language even among non-programming users.

To facilitate an efficient work flow and user friendliness, *PAM* is based on a graphical user interface (GUI). Using the native capabilities for graphical data visualization of Matlab, the most important and frequently used parameters (like count-rate or photon arrival time histograms) are automatically calculated and displayed when a new file is loaded. In this way, the user can quickly judge the quality of the data without the need of performing a full analysis. At the same time, most computationally intensive steps are parallelized and run in C^{++} code to decrease calculation time. Since many such routine processes (e.g. correlation, burst identification, etc.) usually require no user input beyond the initial setup, these calculations can be executed automatically for several data sets in sequence, minimizing the time investment by the user.
PAM contains a large spectrum of different techniques, each one requiring its own set of parameters, algorithms and variables. To ensure a correct data flow while, at the same time, keeping the complexity of the code low, *PAM* is set up in a modular fashion with mostly indirect interactions between the different parts. The work flow usually consists of three to four individual steps, as can be illustrated by the example of pair correlation analysis. Initially, the raw data is loaded into the core analysis routine and transformed into a standardized format so that a variety of file formats can be read and processed. Here, the data is filtered (PIE channels, chapter 4.2.4), sorted (into position and line bins) and eventually processed (pairwise correlation). Since data loading and calculation are usually the most time intensive steps, the (now reduced) data set is saved as an intermediary file format (.pcor). This way, analysis can be resumed at a later time point without the need to reprocess the data. An independent application (PCFAnalysis) is then used to further analyze the data in a more advanced and specialized way. In some cases, data is further filtered and processed (averaging of different bins and files)

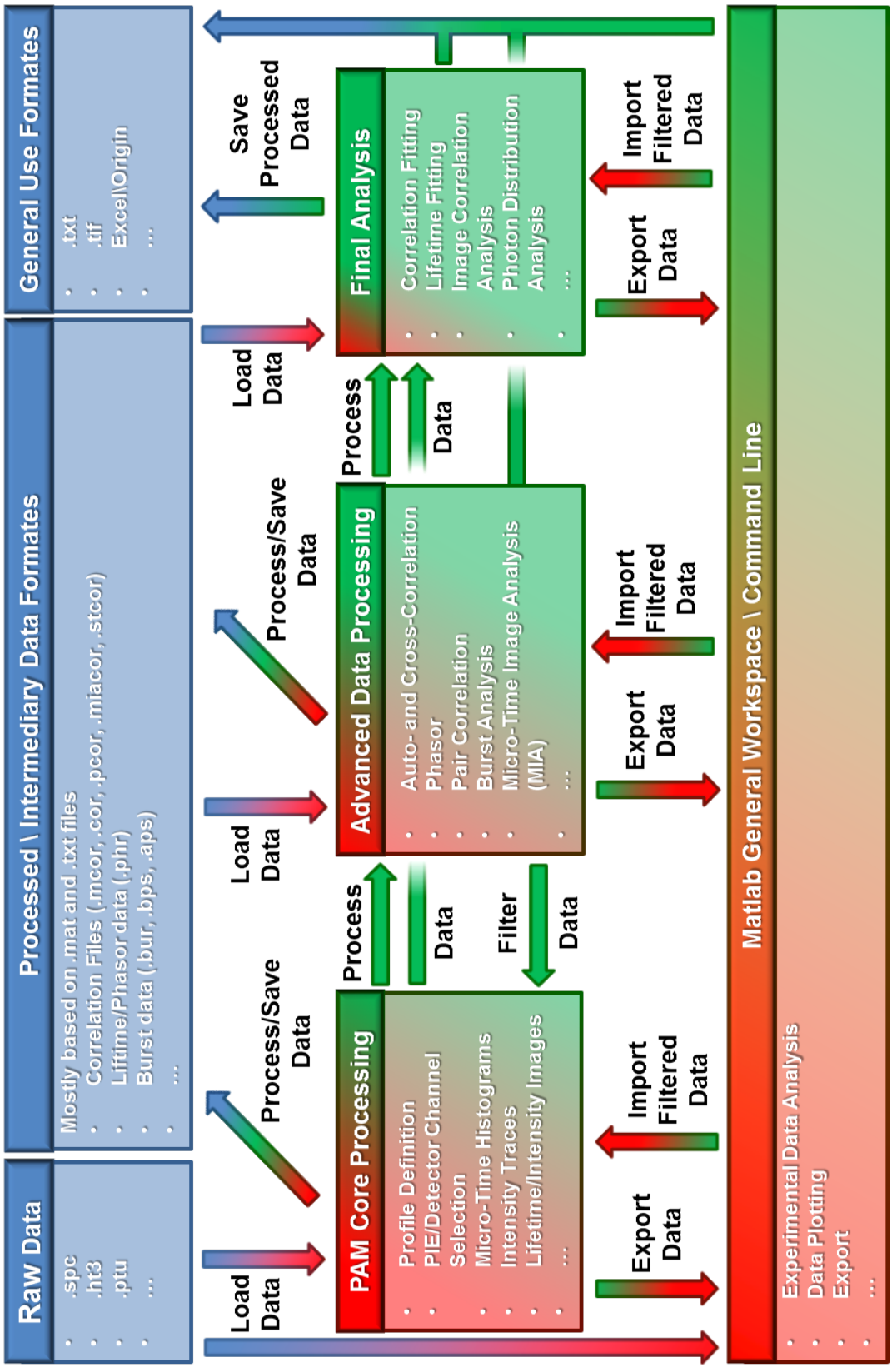

Figure 4.1: Concept of the work and data flow diagram of *PAM*. Blue indicates hard drive memory, red RAM, and green represents computations and calculations.

and exported again (.mcor), before they are finally evaluated (e.g. fitted) in the last step. An illustration of the *PAM* data and work flow is shown in Figure 4.1. This modular structure makes the program easy to expand, both in terms new functionalities as well as input formats.
The third important aspect *PAM* offers is flexibility. When working with advance microscopy or spectroscopy techniques, each new project requires slightly changed approaches and methods, something that no static software can offer. A suitable program needs to be able to accommodate small changes and tweaks without having to overhaul the whole program. In this respect, Matlab constitutes the perfect platform. Since it is an interpreted language (i.e. the code does not need to be compiled), lines can be added or rewritten very quickly, even during execution of the software. Besides that, the powerful command line capabilities of Matlab increase the flexibility even further. By using a break point or a few lines of code, data can be easily transferred to the general workspace, where it can be processed, analyzed or plotted in ways not implemented in *PAM*. To facilitate this freedom in analysis, most data in *PAM* is stored in easily accessible global variables.
Although *PAM* is structured modularly, the individual features are best described according to functionalities to better illustrate the work flow.

4.2 PAM: Core Functionalities

PAM is designed to mainly deal with TCSPC data, especially in combination with pulsed interleaved excitation. Hence, the first steps after loading the raw data are sorting by the micro- and macro-times as well as definition of the PIE channels. Only after the initialization of the PIE channels can the other functions be executed.
Since camera measurements do not contain data of individual photons, but binned intensities, the data requires a very different treatment. Therefore, the corresponding .tif files are loaded directly into the appropriate sub-applications (see chapter 4.5).

4.2.1 Profiles, Settings and User Values

Different kinds of experiments often require different configurations, which involves changing the settings used in analysis. To deal with this *PAM*, contains a profiles selection. In this way, the user can quickly switch between configurations automatically applying the correct parameters. These settings are constantly updated when changed and are stored in a global variable called *UserValues* that includes:

- *Detector settings*: Defines the number of different detectors used and associates them with a file number and routing bit. This way, only data that is needed for the particular profile is loaded, increasing speed and saving memory space.

- *PIE channels*: Sorts photons according to micro time and detector into channels that are then used in further processing (see chapter 4.2.4).

- *Reference data*: Contains processed data needed as reference for some applications (like the IRF in lifetime fitting or dye decays for phasor analysis).
- *Standard settings*: Parameters like file paths for the different sub-functions, previously used fit models, color or plotting schemes, as well as a many other settings are saved and retrieved automatically to decrease the amount of user input required and to increase ease-of-use.

4.2.2 Loading and Data Handling

Since *PAM* needs to be able to deal with a wide variety of input file types, data is transformed into a uniform format upon loading. Hereby, the information is separated into the pure photon data (stored in *TcspcData*) and a structure array containing all additional parameters like clock frequency, scanning settings or file type and name (stored in *FileInfo*). *TcspcData* in itself is divided into the macro-time (photon arrival relative to the start of the measurement) and micro-time (photon arrival relative to the sync pulse). Both variables are $n \times m$ large arrays, with n representing individual TCSPC cards, while m corresponds to the different routing channels when multiple detector signals are recorded with a single TCSPC module. Array positions associated with a detector defined in the profile settings contain an entry for each recorded photon on that detector. The macro-time is stored as a double precision floating number, counting the number of synchronization pulses or macro-time clock ticks. Using a floating data type facilitates subsequent operations that require non-integer values, e.g. fluorescence lifetime correlations (see chapter 4.3). The micro-time is a 16 bit unsigned integer corresponding to the TAC/ADC or TDC resolution. Because a unique macro- and micro-time combination is assigned to each photon, any reorganization and sorting of photons must be applied to both variables in the same manner.

4.2.3 Detector Fluctuation Correction

Many APDs show a strong dependence of the instrument response function on the photon count rate, either due to thermal effects or residual electric charges. In simple cases, this leads to a shift of the mean micro time as a function of inter-photon time (especially for the Count® and CountBlue® detectors). This shift is automatically corrected when loading data with *PAM*, if the dependence has been referenced.[88]
To calibrate the shift, a measurements with a temporally constant (and preferably short) fluorescence lifetime is used. The photons are then sorted by the time (in clock ticks) to the previous photon and a micro-time histogram for each such bin is generated. For each histogram, the mean micro-time is calculated. To decrease the influence of background and noise, this is only done for the 100 TAC bins with the highest number of counts. This results in a relative shift as a function of inter-photon time. The effect of such a correction is illustrated in Figure 4.2.

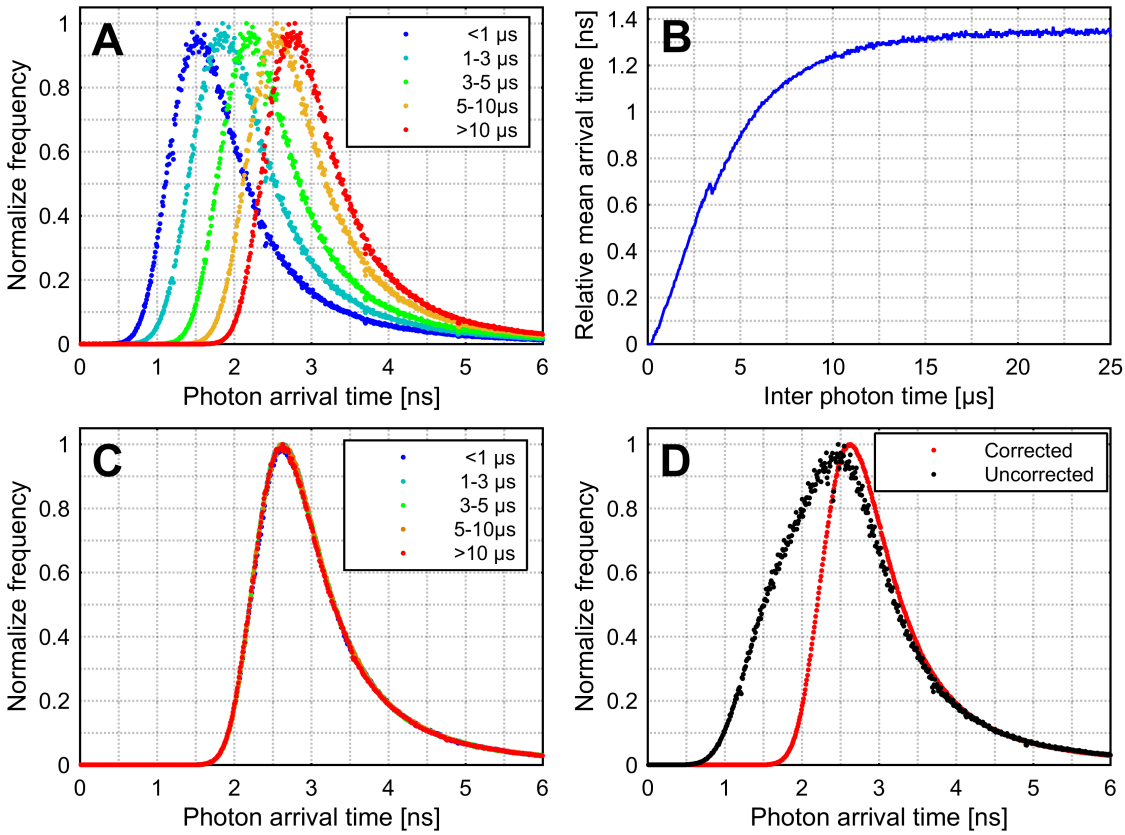

Figure 4.2: Correction of the micro-time dependence of the inter-photon time. A) Mirco-time histograms for different inter-photon times without correction. B) Plot of the mean arrival time as a function of inter-photon time. C) Corrected micro-time histograms for different inter-photon times. D) Total micro-time histograms before and after correction.

4.2.4 PIE Channels

Once the data has been loaded and corrected, most functions in *PAM* do not directly use the micro-time information in further analysis. Still, the photon signal needs to be separated not only by the detection color, but also by the excitation wavelength. To achieve this, PIE channels are used. Each channel is assigned to a TCSPC card, a routing bit and a micro-time range. In this way, only photons falling into the selected channels are used for further processing, such as intensity traces, images, correlation etc.
In some cases, the signal of several detectors is needed for a full analysis. For this, combined PIE channels can be created, which then contain the photons of two or more individual channels.

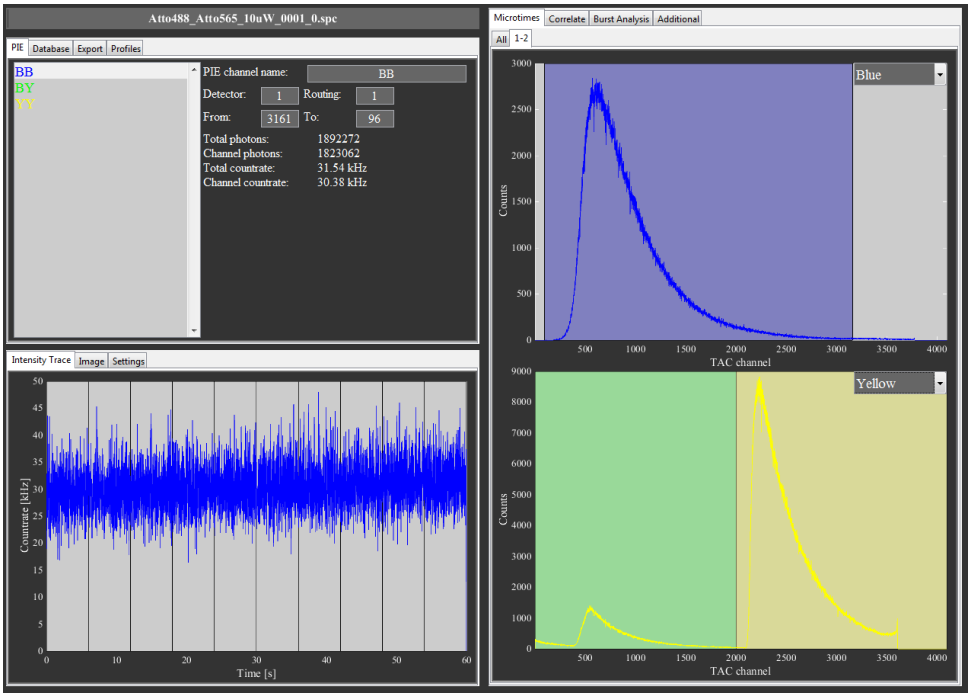

Figure 4.3: Screenshot of the *PAM* core user interface. The PIE channels are defined and selected in the top left region. The micro-time histograms and corresponding color-coded PIE regions are displayed on the right. In the bottom left, information associated with the selected PIE channel, such as an intensity trace or an image, are shown.

4.3 Temporal Correlation

One of the most widely used analysis methods for confocal data is fluorescence auto- and cross-correlation spectroscopy. It is also the field that strongly benefits from pulsed interleaved excitation, since PIE allows spectral cross-talk free analysis, decreasing artificial cross-correlations and increasing sensitivity.
In *PAM*, any combination of two PIE channels (or combined channels) can be cross-correlated (or auto-correlated, if the channels are the same). Although it has been shown that triple signal correlations can be done,[89,90] *PAM* is still limited to two signals at a time. To analyze more channels, each pair of signals has to be correlated individually, yielding enough information for most applications.

4.3.1 Multiple-*tau* Correlation Algorithm

Information in fluorescence correlation data is spread out over multiple orders of magnitude in time, from rotations on the nanosecond scale, to diffusion ranging in the milliseconds or even seconds (see Figure 3.2). Therefore, any algorithm used needs to achieve a high temporal resolution, but also be able to calculate correlations with reasonable speed, even for long lag times. In FCS, the most common approach to deal with these problems is called the photon mode multiple-*tau* algorithm.

There are two different approaches to calculating correlation functions, time mode and photon mode. Time mode uses binned intensities to build up a correlation function, usually by multiplying the intensities of the different bins shifted by the lag time. In photon mode, on the other hand, the individual photons are used by calculating the inter-photon time histogram. This has the big advantage that the calculation time scales with the square of the number of photons and not the square of the number of bins, as in time mode. In most FCS measurements, each individual time bin has far less than one count, while only very few (if any at all) have multiple entries. This means that, in time mode, most calculations are wasted on multiplications with zeros. Assuming a countrate of 100 kHz with 1 µs resolution, photon mode results in a 100 fold decrease of calculation time. Moreover, the computational demand in photon mode is not directly dependent on the bin size, so that the resolution can be increased dramatically without a proportional increase in calculation complexity.
The second method used to reduce computation time is the multiple-*tau* algorithm. Hereby, the temporal resolution is reduced stepwise for increasing time lags, dramatically reducing the data volume (e.g. from 10 000 000 to ∼100 for a correlation up to 1 s with 100 ns resolution). Although this binning introduces a triangular averaging, this effect is $< 0.1\%$ if $\tau_{lag}/\tau_{bin} > 7$. As the binning increases, more and more photons are summed up (gaining a weight of 2 or more), which in turn reduces the total number of calculations.
Several different multiple-*tau* methods were proposed for correlating fluorescence fluctuations data.[91–93] The flow diagram for the algorithm used in *PAM*[94] is illustrated in Figure 4.4. In brief, when correlating signal S_1 with signal S_2, the algorithm goes through every photon n of S_1 and initially searches for the first photon l that arrives at least τ_{min} later in S_2 (green box in Figure 4.4).
Then, starting from $m = l$, the product of the photon weight $I_n I_m$ is added to the correlation function at the corresponding lag time for all photons m in S_2, until the upper window τ_{max} is reached (red box in Figure 4.4). Instead of just summing up, the product $I_n I_m$ is added to allow for combining photons in the re-binning step. At the same time, this can also be used to give different weight to the photons, e.g. for lifetime filtered FCS.
Once the upper window is exceeded, the algorithm steps to the next photon n in S_1 and repeats the previous two steps (green and red box in Figure 4.4). Since n counts upwards, the window of relevant entries also moves upwards. Therefore, the l of the previous n can be used as the starting point for the lowest delay, drastically reducing the number of pairs to be checked.
Once the last photon in S_1 is reached, the binning is increased (blue box in Figure 4.4). To do that, the arrival times of all photons are shifted down by one bit, effectively dividing all times by two and rounding down. In the case that two photons now have the identical arrival time, the weight of the second one is set to the sum of both, while the first one is set to zero. Since the algorithm omits weights of zero, this decreases the number of calculation steps with increasing bin size, further speeding up the calculation.

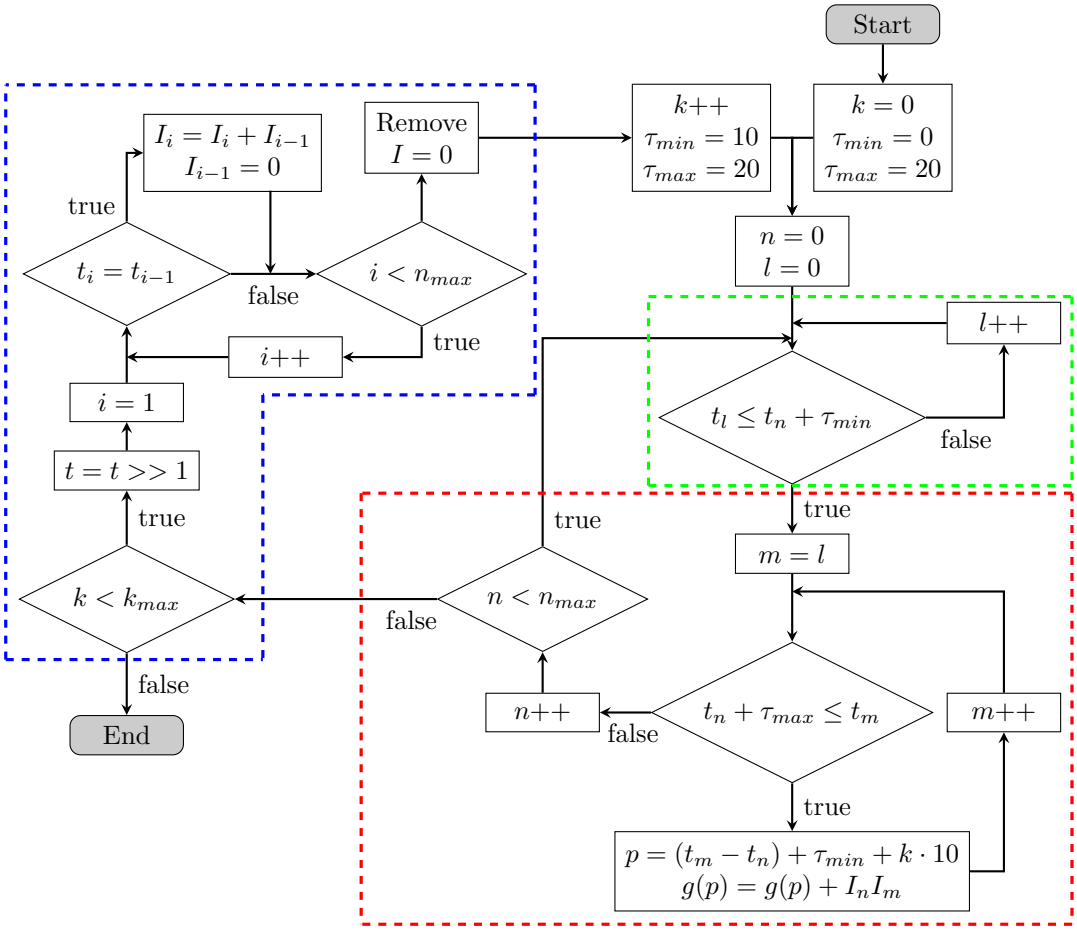

Figure 4.4: Flow diagram of the *PAM* correlation algorithm. The photon arrival time is represented by t, while the weights are indicated by I. The correlation is build up by multiplying and histogramming the photon weights for each binning step (red box). To save calculation time, the process is only done for photons within the lower (l for τ_{min}) and upper (m for τ_{max}) bounds. Since the lower threshold increases with n, l starts at the value of the previous photon (green box). Once the loop runs through all photons, the data are re-binned (blue box) and the process is repeated for the next lag time sequence until the maximal delay time is reached.

As a last step, the resulting correlation function g is normalized according to:

$$G(\tau) = \frac{g(\tau)}{\Delta\tau_\tau \cdot N(t_{max} - \tau) \cdot \big(N(t_{max}) - N(\tau)\big)} - 1 \tag{4.1}$$

with $\Delta\tau_\tau$ representing the bin size at the corresponding lag time in clock cycles, while $N(t)$ describes the total number of photons recorded until time point t. One is subtracted to get the fluctuation and not the intensity correlation function.

4.3.2 Data Sectioning and Selection

For a correct analysis of the correlation data, one needs to know the uncertainty of each data point in order to perform a weighted fit. While it is possible to estimate the error directly from the data,[95], the simplest way to determine the uncertainty is to repeat the experiment several times and calculate the standard error of the mean. As a shortcut, *PAM* automatically divides the data into a set number of segments of equal length, treating each one as an individual measurement. In this way, the uncertainty can be estimated without the need to manually analyze and average repeated experiments.
As an added feature, each of these segments can be unselected and disregarded in the final average, both before and after performing the actual correlation. This is especially useful when the sample contains bright aggregates or air bubbles. Their diffusion through the focus results in short intensity bursts, strongly affecting the correlation analysis. By simply unselecting these regions, the FCS curves of the homogeneous solution can be recovered.
Due to the special form of the correlation function, normal averaging usually results in an overestimation of the errorbars for FCS data. The average number of particle in the focus N changes the correlation amplitude, while not affecting its shape. Since many experiments are performed at very low concentrations, a significant variation in N is to be expected. This does not only increase the apparent error in the amplitude, but also creates an artificial uncertainty in other parameters like the diffusion time. To minimize this effect, *PAM* allows the user to first normalize the total areas of the individual curves to the average and only then calculates the standard error of the mean for the individual lag times.

4.3.3 FCSFit: Analyzing and Fitting FFS Data

Once the correlation function is computed, it is automatically saved, either as a Matlab file (.mcor), a text file (.cor), or both. While the first format is easier to load, analyze and plot with Matlab, the later is compatible with most general programs like Origin or Excel, and can be used for sharing the raw correlation data. The processed correlation files can then be loaded with a separate sub-program called *FCSFit* (Figure 4.5), designed for analyzing various types of 1D temporal correlation data. To make *FCSFit* as versatile as possible, the fit functions are not hard-coded, but are based on text files. In this way, new fits can be added and old ones edited by the user, allowing for maximum flexibility in the data analysis. Furthermore, any fit parameter can be fixed to a set value or globally linked between multiple data sets.

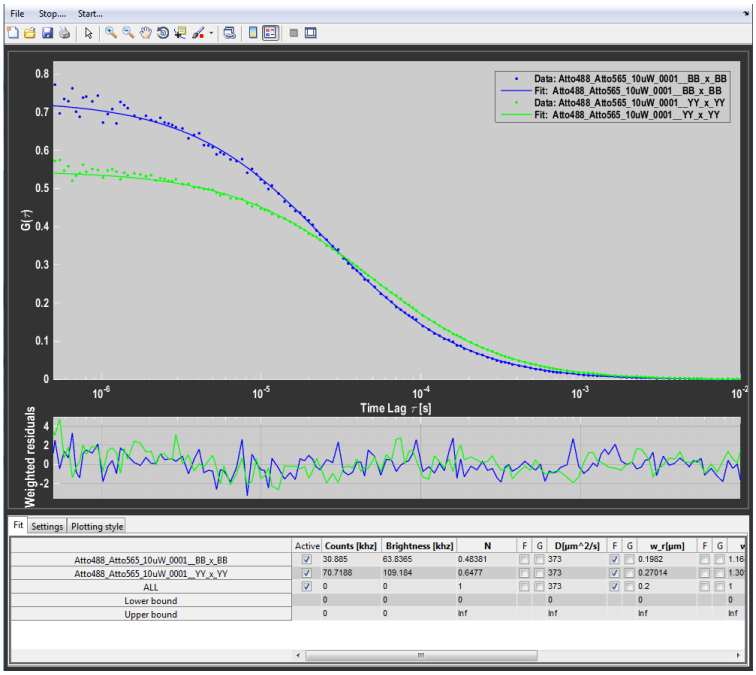

Figure 4.5: Screenshot of the *FCSFit* sub-program of *PAM*. The upper plot shows the correlation data with the corresponding fit, while lower one displays the weighted residuals of the individual datasets. The tabs at the bottom of the screen contain a table for setting and extracting the fit parameters (*Fit*), additional fitting, plotting and exporting settings (*Settings*), and a table to adjust some display parameters (*Plotting style*).

4.4 Fluorescence Pair Correlation

While in one color FCS measurements, all information can be represented with one curve, a single fluorescence pair correlation experiment results in a large number of different correlation functions, up to the square of the number of spatial bins. The added complexity makes it impossible to visualize the full data at once, so that any analysis software needs to be very dynamic and flexible in selecting and displaying parts of the data.

4.4.1 Pair Correlation Algorithm

The basic pair correlation algorithm is the same as for the normal point FCS, with the difference that the photons are first separated into spatial bins. Since the smallest meaningful time lag is now determined by the scanning and not the pulse frequency, the time is therefore transformed to scan tick units, resulting in a lower time resolution.
Calculating any combination of two bins with each other would result in a total of n^2 correlation curves. However, many of them are not useful and just increase computation time. Very small bin lags show a very high overlap of the point spread

functions, meaning that they often do not contain relevant spatial information. Correlation functions for large spatial lags, on the other hand, have a very low amplitude and therefore also a low signal-to-noise ratio. To circumvent this and decrease calculation time, *PAM* allows the user to precisely define which lags to calculate and which not.
In the end, the correlation data is a four dimensional array with size $t \times n \times (l+1) \times 2$, where t is the number of temporal lags, n the spatial bins and l the largest spatial lag (+1 since it also contains the auto correlation). The fourth dimension represents the forward and backward correlations. Due to the size and high complexity, it is only feasible to save this data as a Matlab file (.pcor).

4.4.2 PCFAnalysis: Analyzing Pair Correlation Data

PCF data requires a more sophisticated analysis than point FCS curves. First of all, not all spatial bins are relevant for analysis and have to be filtered. Certain regions might contain artifacts like laser retraction during scanning or are located in a part of the sample that is of no particular interest for the current measurement. Due to the added spatial information, it may be possible to sort the bins into different categories and additionally average the curves to increase signal-to-noise.

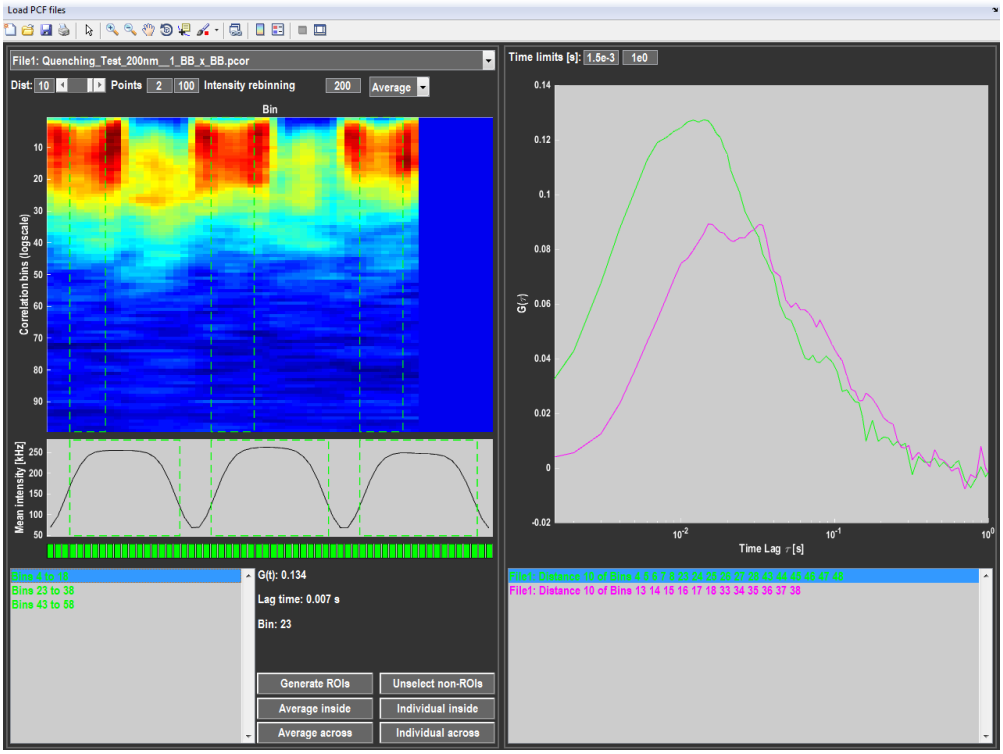

Figure 4.6: Screenshot of the *PCFAnalysis* sub-program of *PAM*. The pair correlation carpet with the corresponding intensity cross-section is plotted in the top left. Selected ROIs (here as green dotted lines) are listed in the bottom left and can be used to display individual or averaged correlation curves in the right plot.

In order to deal with this, *PCFAnalysis* displays a correlation carpet for a selected bin lag with the corresponding intensity profile (Figure 4.6 top left). Here, the user can select regions of interest (Figure 4.6 bottom left). These, in turn, can be used to select bin pair combinations that either lie both in the same or in different ROIs and plot them individually or as an averaged curve (Figure 4.6 right). These can be either averaged further, e.g. for different files, or exported as .mcor files for fitting with *FCSFit*. Only for such simple cases as free diffusion can the PCFs be described with an exact mathematical model. For more complex conditions, the correlation function can only be approximated or analyzed semi-quantitatively. Here, an useful approach is to fit the data with a Gauss curve on the logarithmic scale and extract information about the mode, the amplitude and the width of the correlation function.

4.5 Microtime Image Analysis (MIA)

The functionalities presented so far are all based on time resolved measurements, with the spatial component playing no or only a secondary role. However, most data recorded with a microscope - just as the name suggests - are based on images, both for confocal and wide-field acquisition. The section of *PAM* designed to deal with image data is called *Microtime Image Analysis* or *MIA*.

4.5.1 MIA: General Outline and Functionality

Unlike most other functions of *PAM*, image analysis is not dependent on confocal data, but is just as much (or even more) applicable to camera based acquisition methods. Therefore, *MIA* is more independent and input does not necessarily need to go through the *PAM* core program. Although *MIA* is capable of directly accessing *PAM* data for analysis, the primary input are TIFF files, the standard format for the majority of image acquisition software. Once the data is loaded as temporal image stacks for up to two channels, the program displays the individual frames and some basic parameters (like average count-rate and a photon counting histogram) for a first evaluation of the data quality.
The next step involves the selection of a relevant region of interest. Many parts in a microscopy image might not be relevant for analysis or even affect it negatively, e.g. regions outside an investigated cell. Therefore, the actual analysis is only performed on a user selected rectangular subregion, minimizing the effect of unwanted sections and, due to the smaller size, increasing processing speed. But this ROI can still contain parts that need to be excluded from analysis. There are three ways of dealing with this in *MIA*. In the first one, the user can manually select relevant or de-select unwanted regions. This method is very flexible and can be applied for basically any problem, but it requires a significant amount of user input and might therefore also be biased. The second way is to discard pixels based on their average signal intensity using an upper and lower threshold. Thus, regions with too high or

too low count-rate can be easily, quickly and reliably discarded. Both methods are applied to individual pixels in the full stack. However, sometimes only a few pixels within a single frame need to be discarded. In this case, not using the pixels in all frames would unnecessarily throw away a lot of useful data. On the other hand, going through each individual frame and de-selecting the affected regions requires too much time and is not really feasible when dealing with a lot of data. To deal with this case, *MIA* has a subregion based automatic de-selection method. Hereby, around each pixel in each frame, two differently sized regions are used to calculate the average intensity and variance. If the intensity or variance ratio between these two regions lie outside of the set thresholds, the pixel is rejected, but only for this particular frame. This method is designed to exclude small individual particles or organelles slowly moving through the field of view. Since these objects can have a very high brightness (or a high negative brightness for dark spots), they would have a very strong effect on any fluctuation based method.

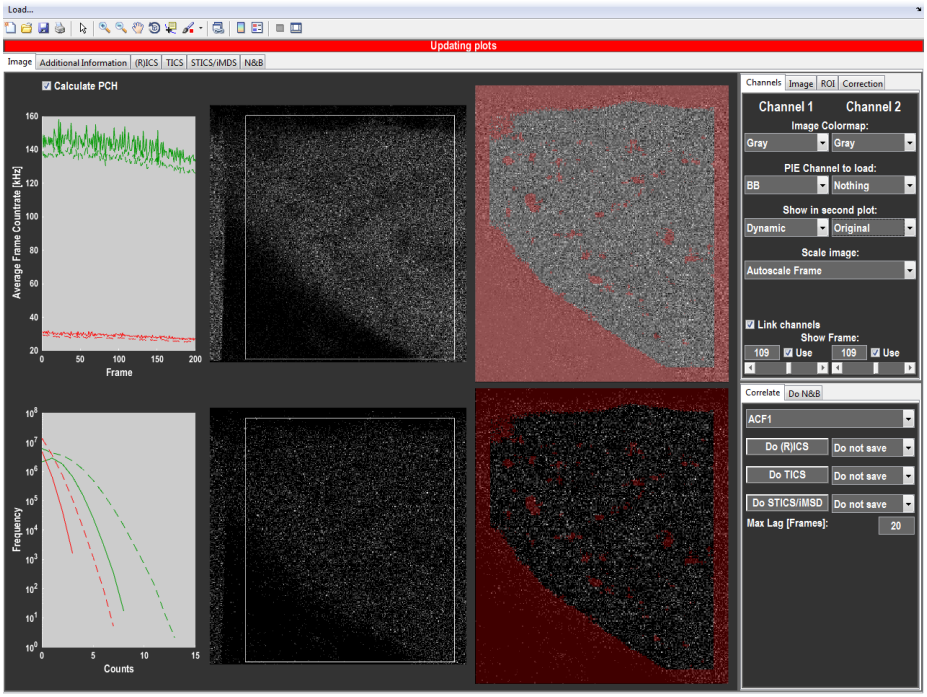

Figure 4.7: Screenshot of the *MIA* sub-program of *PAM*. The two plots on the left display the count-rate and the photon counting histogram for a quick evaluation. The two center images show the full frame for the two channels, while the selected region of interest (white rectangle) is displayed in the two rightmost plots. Pixels with a red hue were de-selected either manually or automatically.

After the relevant ROI is selected, the images are pre-processed in order to remove unwanted contributions, like spatial heterogeneities in RICS or bleaching effects in TICS. Since *MIA* allows a variety of different analysis methods requiring different corrections, the pre-processing includes the addition or subtraction of the pixels mean, the frame mean, or a spatial and temporal running mean.

4.5.2 Spatial Image Correlation (ICS and RICS)

One of the most important analysis methods in *MIA* is image correlation spectroscopy. For each frame, the two dimensional image correlation function is calculated using a Fourier transformation algorithm:

$$G(\xi,\psi) = \mathscr{F}^{-1}\Big(\mathscr{F}\big(\delta I_i(x,y)\big) \odot \mathscr{F}^{*}\big(\delta I_j(x,y)\big)\Big) \oslash \mathscr{F}^{-1}\Big(\mathscr{F}\big(N(x,y)\big) \odot \mathscr{F}^{*}\big(N(x,y)\big)\Big) \;/\; \Big(\langle I_1(x,y)\rangle \cdot \langle I_2(x,y)\rangle\Big) \quad (4.2)$$

Where $\odot$ and $\oslash$ denote an element-wise multiplication and division, respectively. $\mathscr{F}$ indicates a Fourier transformation. δI_n represents the fluctuation image for the nth channel, which can be calculated from the intensity image I_n:

$$\delta I_n(x,y) = I_n(x,y) - \langle I_n(x,y)\rangle \quad (4.3)$$

The selection map N is used to account for any de-selected pixels in the frame, containing a 1 for all used pixels and a 0 for excluded pixels. For any 0 entry in N, the corresponding pixels are also set to 0 in δI, and disregarded when calculating the mean. Although the correlation functions can also be calculated according to the standard definition for the correlation function, using the highly efficient algorithms for a fast Fourier transformation (FFT) greatly increases performance. The calculations are performed for each frame individually. In theory, a single image is enough to get the full spatial correlation. However, due to low signal or molecular brightness the individual frames contain too much noise. Furthermore, the limited size of the image relative to the point spread function can lead to under-sampling, especially for low concentrations. Therefore, the data for the complete stack is averaged automatically to increase signal-to-noise and the amount of sampled particles, but the individual frames can also be analyzed separately, e.g. for time resolved analysis.
The calculated functions are displayed in an extra tab, dedicated to image correlation data (Figure 4.8). Here, the user can make a preliminary estimation of data quality and even perform a simple diffusion model RICS fit. This direct feedback allows for quick evaluation of the image correction and region selection parameters. For detailed analysis, the data is additionally saved as a Matlab based format file (.miacor) that can be loaded and processed with another sub-program called *MIAFit*, presented later in this chapter.
Although both the acquisition mode and the available information between ICS and RICS are very different, the correlation algorithms and data structure are the same and can be used for both methods. The differences only lie in the shape of the resulting correlation function and therefore in the model used to describe it.

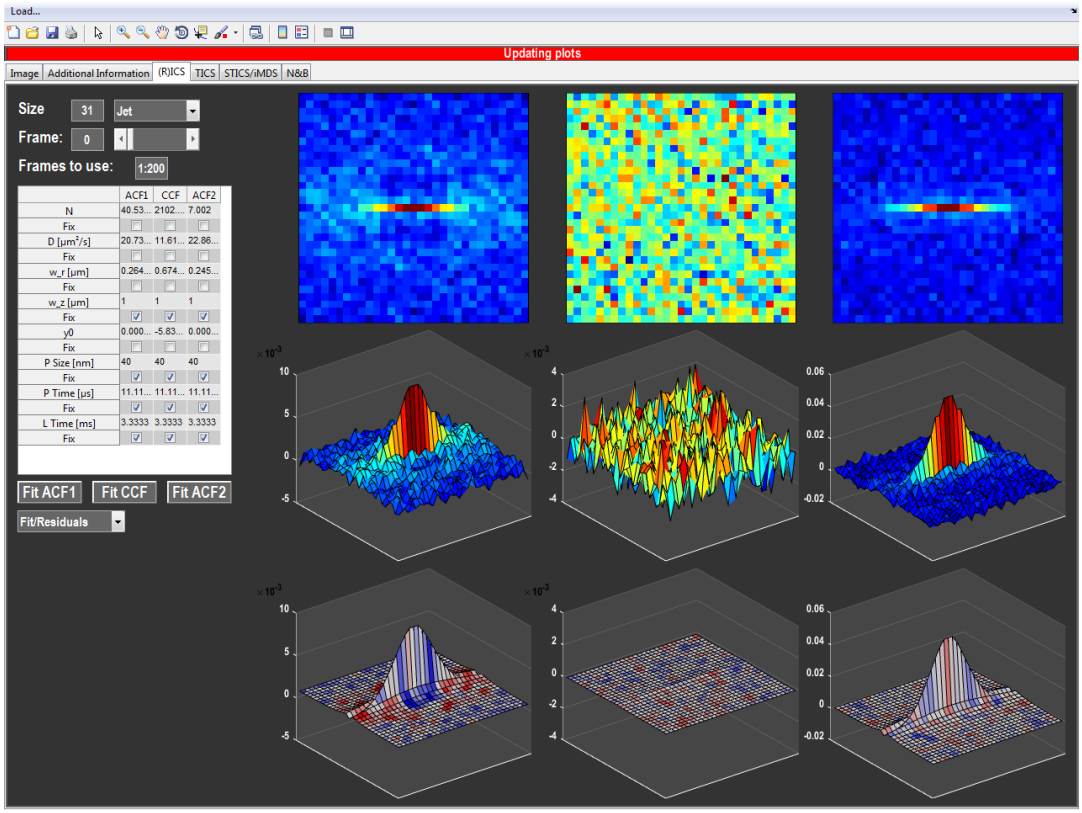

Figure 4.8: Screenshot of the (R)ICS tab of *MIA*. The plots show the image (top row) and a surface representation (middle row), as well as the fit function and/or residuals (bottom row) plots for the two auto- (left and right) and the cross-correlation (center) functions. The table on the left is used for a preliminary fitting to a RICS model.

4.5.3 Temporal Image Correlation (TICS)

ICS and RICS reveal the spatial correlation hidden in an image and use the temporal component only for averaging. In TICS, the approach is inverted, with the temporal correlation being analyzed while the spatial dimensions are used for averaging or for separating into different groups. Since the dimensions in an image stack are conceptually equivalent, the same algorithm presented in equation (4.2) can be also applied for TICS calculations, with the difference that the single time dimension is used instead of the two spatial directions.
As with ICS, the calculated temporal correlations are displayed in a special TICS tab for quick analysis and, since they are essentially equivalent to FCS data, also be exported as .mcor files for further analysis with *FCSFit*.

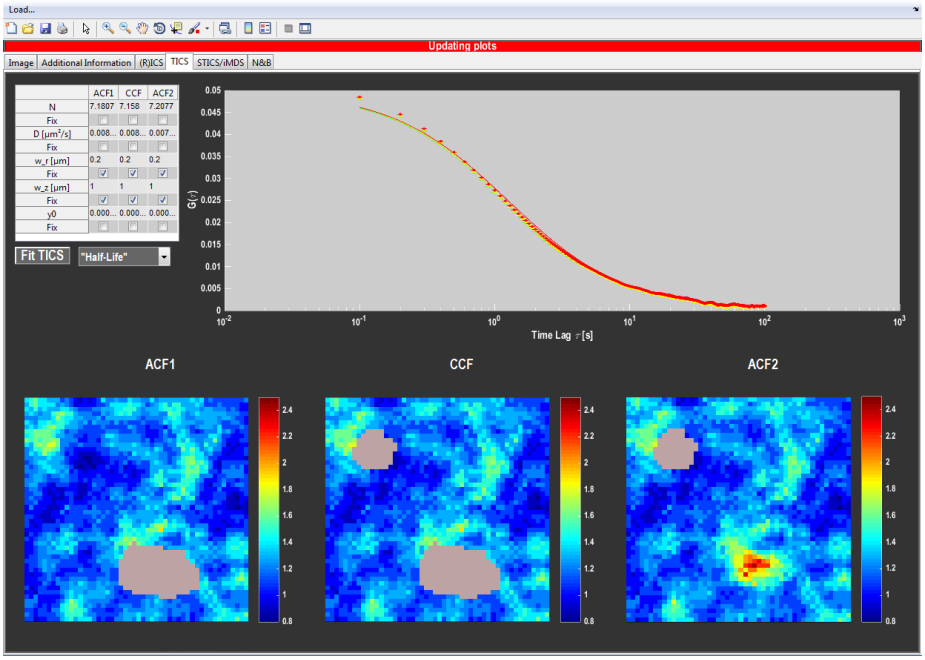

Figure 4.9: Screenshot of the TICS tab. The plot shows the auto and cross correlation functions that can be fit with a simple diffusion model. The green and red curves represent the auto-correlation functions and the yellow curve the cross-correlation function. For the bottom images the user can choose to display the spatially resolved molecular brightness, the correlation amplitude or the half-maximum decay time. The gray regions correspond to areas not used for this particular channel. The table in the top left corner can be used to perform a preliminary fit of the data.

4.5.4 Spatio-Temporal Image Correlation (STICS and iMSD)

The next logical step from ICS and TICS is to correlate the data both through space and time in STICS. The algorithm is identical to the ICS calculation, but the second channel is additionally shifted in time relative to the first one. This generates a 3D correlation matrix $G(\xi, \psi, \tau)$, where zero time lag $G(\xi, \psi, 0)$ is equivalent to ICS data, while a zero spatial lag $G(0, 0, \tau)$ represents the averaged TICS curve.
The sheer size of the data and number of calculations requires a high amount of processing. Fortunately, the temporal correlation function decays quite quickly, so that only relative short lag times are required. The user can set a maximal temporal shift, increasing calculation speed enormously.
Due to its complexity, STICS data is difficult to properly visualize and analyze. A relatively simple method of utilizing STICS data is image mean-square displacement (iMSD), where the width of the spatial correlation is plotted as a function of time lag. To obtain the width, the spatial correlation for each individual lag time is fit to a 2D Gaussian. The iMSD plot contains the same informations as mean-square displacement data obtained from single particle tracking experiments and the slope of the curve can be used to determine both the diffusion coefficient, as well as the type of motion of the sample. For free diffusion the curve shows a linear dependence

on time, meaning that the exponent, α, in the proportionality $iMSD \propto t^{\alpha}$ is equal to one. Higher or lower values of α indicate the presence of directed motion or anomalous sub-diffusion, respectively. For an more detailed analysis with *MIAFit*, the data is saved as a .stcor file.

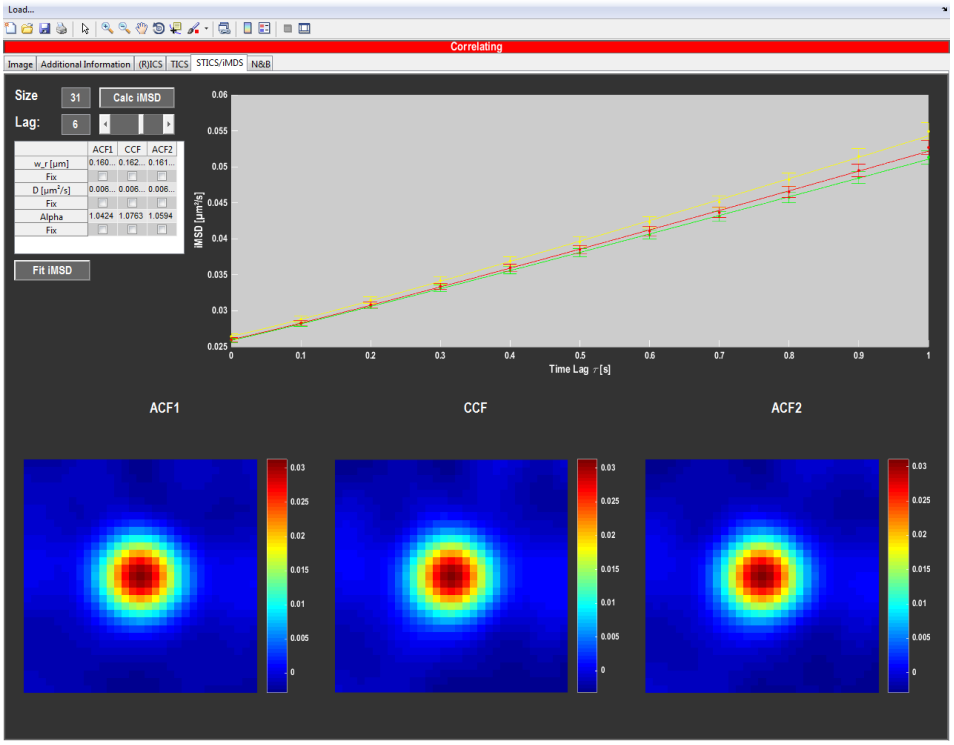

Figure 4.10: Screenshot of the STICS tab of *MIA*. In the top panel, the iMSD plot and a corresponding fit model are displayed. The green and red curves represent the auto-correlation functions and the yellow curve the cross-correlation function. The image plots at the bottom of the screen display the spatial correlation function for a selected time lag. The table in the top left corner can be used to perform a preliminary fit of the iMSD data.

4.5.5 MIAFit: Spatial Image Correlation Analysis and Fitting

MIAFit is the 2D equivalent of *FCSFit* with the same concept of user defined fits and the freedom of fixing or globally linking parameters. In contrast to one dimensional data, it is not possible to plot multiple image correlation functions in a single plot. Because of this, data in displayed in *MIAFit* in two different ways. The first possibility shows the on axis correlation curves $G(\xi, 0)$ and $G(0, \psi)$ for all loaded files (Figure 4.11). This way of plotting the data is usually enough to visually evaluate the data and fits. At the same time, it allows the user to compare different measurements. In some cases, however, the complete shape of the functions

is important. In this cases, *MIAFit* plots a single measurement as a surface plot and additionally the corresponding fit, residuals or both (Figure 4.12).
MIAFit has a special mode when dealing with .stcor files, since the data here are three dimensional. The spatial correlation at each time lag is loaded and treated as a separate file, but gets assigned a value corresponding to its position in the time stack. This value is passed on to the fit function and can be used by the model. Globally linking the appropriate parameters (given the right model) effectively turns the different files into a single 3D matrix.

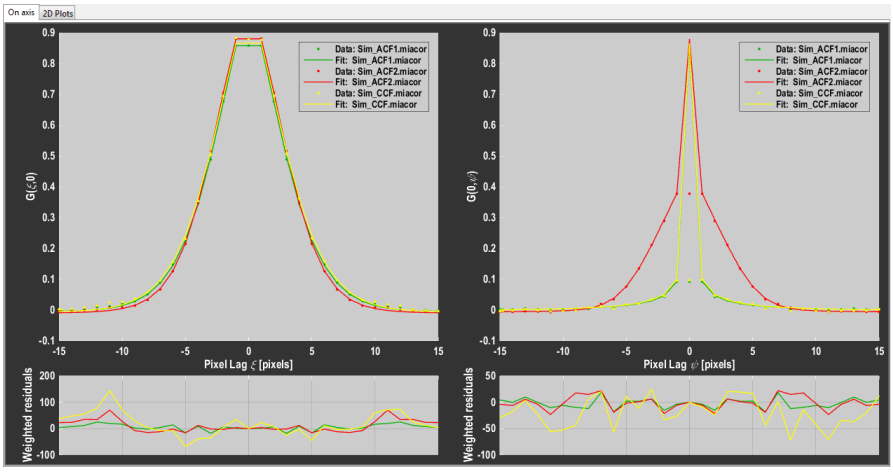

Figure 4.11: 1D data representation of *MIAFit*. The top plots show the on axis correlation functions $G(\xi, 0)$ (left) and $G(0, \psi)$ (right) for all selected files, while the corresponding residuals are displayed in the bottom plots. The dots represent the data and the solid lines show the fit. The different colors indicate different correlation files loaded, in this case two auto-correlation functions (green and red) and one cross-correlation function (yellow).

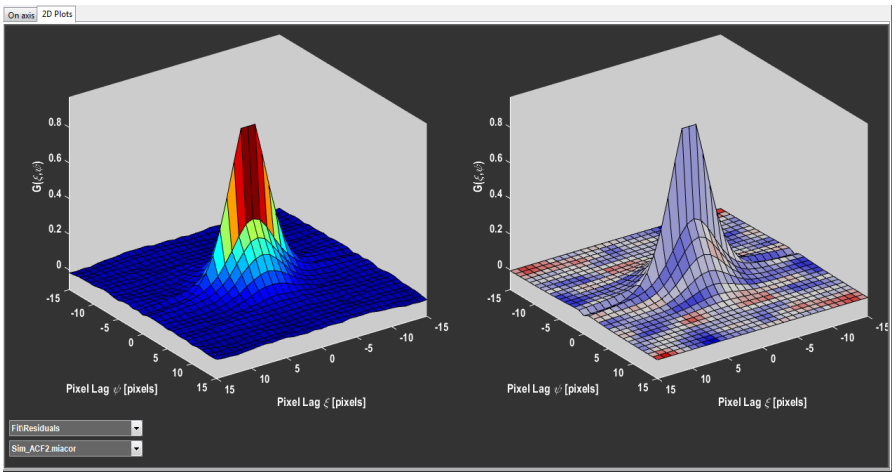

Figure 4.12: 2D data representation of *MIAFit*. On the left, a singe spatial correlation function is displayed as a surface plot. The right plot contains the corresponding fit, residuals or, in this case, the fit with a color code for the residuals.

4.6 Phasor Approach to FLIM

PAM is mainly devised to work with TCSPC data, giving the user access to the lifetime information of the sample. One way of analyzing it in *PAM* is by using the phasor approach to FLIM. Hereby, the data is not fit, but transformed into the Fourier space, thus simplifying many rules and concepts, and allowing a direct interpretation. The Phasor approach is not only limited to TCSPC data in the time domain, but can also be used to analyze frequency domain measurements recorded with a camera.

4.6.1 Phasor Referencing

Digital TCSPC data is not continuous, but binned, so that equations (3.27) and (3.28) need to be adjusted for the actual calculations for each pixel:

$$s = \frac{1}{M_{Ref}} \cdot \sum_{n=1}^{N} \sin\left(\frac{2\pi n}{N} - \Phi_{Ref}\right) \tag{4.4}$$

$$g = \frac{1}{M_{Ref}} \cdot \sum_{n=1}^{N} \cos\left(\frac{2\pi n}{N} - \Phi_{Ref}\right) \tag{4.5}$$

with N corresponding to the total number of ADC or TDC bins. Using these calculations results in a phasor frequency that corresponds to the maximum of the micro-time range and not necessarily to the laser repetition rate.
In the phasor space, the two functions involved in a convolution are equivalent, meaning that the measured demodulation and phase can be expressed as:

$$M_{Measured} = M_{IRF} \cdot M_{Sample} \tag{4.6}$$

$$\Phi_{Measured} = \Phi_{IRF} + \Phi_{Sample} \tag{4.7}$$

From this, it follows that if the theoretical phasor of a sample is known, the IRF parameters can be calculated from the measurement, and vice versa. Therefore, for analyzing an unknown sample, the IRF phasor is needed, which in turn can be determined via a reference measurement with known lifetime. In *PAM* this reference is loaded before the analysis and is stored in the *UserValues*.
The micro-time histogram might contain artifacts like reflections or crosstalk from another channel (see Figure 4.13), which can be removed by restricting the calculation to only a subsection of the full time range, effectively setting the values outside of that range to zero. As long as the remaining time is long enough to sample most of the lifetime decay, cutting the micro-time only has minor effects on the phasor, usually smaller than the statistical noise. Additionally, the reference decay can be shifted relative to the measurement data to account for small arrival time variations due to thermal effects of the single photon counting detectors.

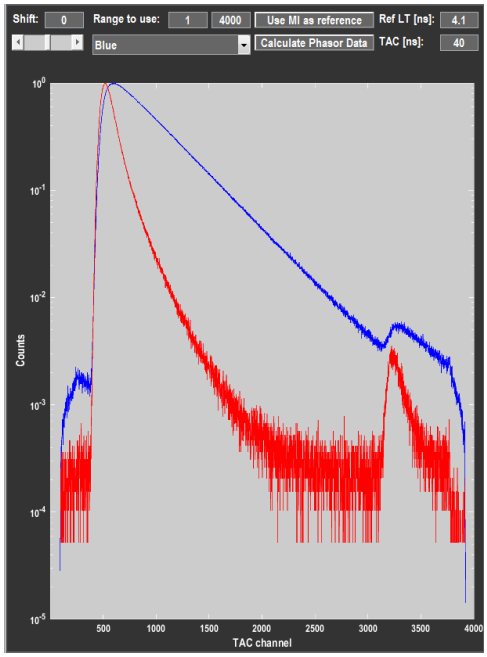

Figure 4.13: Sreenshot of the phasor referencing tab in *PAM*. The red curve shows the total micro-time histogram of the measured data, while the blue represents the reference decay. Since the interval between consecutive laser pulses was lower than the maximal micro-time range, the curves do not extend over the full rang. The reflection peaks at the end as well as the edge artifacts can be removed by restricting the relevant range for the phasor calculations.

The processed data (including parameters like the pixelwise phase, demodulation and the corresponding lifetimes) is saved as a Matlab based file (.phr) to be analyzed with the *Phasor* sub-program.
Since the phasor analysis can be used for both time- and frequency domain data, *PAM* also includes a referencing algorithm for TIFF based FLIM data, that works the same for both acquisition methods, increasing the range of possible applications. All algorithms are essentially the same as for the TCSPC based data, using equations (4.6) and (4.7) for the core calculations. Since the data in TIFFs is stored very differently compared to TCSPC file formats, camera based phasor referencing is performed in a separate sub-function. This circumvention of the core PAM functionality simplifies the algorithms and optimizes performance for the different formats.

4.6.2 Phasor Analysis

When analyzing phasor FLIM, it is important to display the intensity image, to show the actual phasor histogram, and also to visualize the relationship between the two. The first two aspects are easy to achieve. In the *Phasor* sub-program, up to nine individual images and a single phasor plot for all of them (and any number of

other active files) can be displayed at the same time, allowing the user to compare multiple measurements. Alternatively, the user can select to only show a single file with the corresponding histogram in more detail to better visualize the differences and patterns within a single image. Showing the correlation between the intensity and lifetime for each individual pixel is far less straightforward. The amount of data contained in the phasor image is very high and important information might be hidden behind irrelevant details when displaying everything at once. Analysis for each experiment focuses on different relevant aspects, requiring the software to highlight these particular parameters. Therefore, *PAM* has four different approaches to visualize the relationship between the phasor plot and the individual pixels, allowing for maximal flexibility.

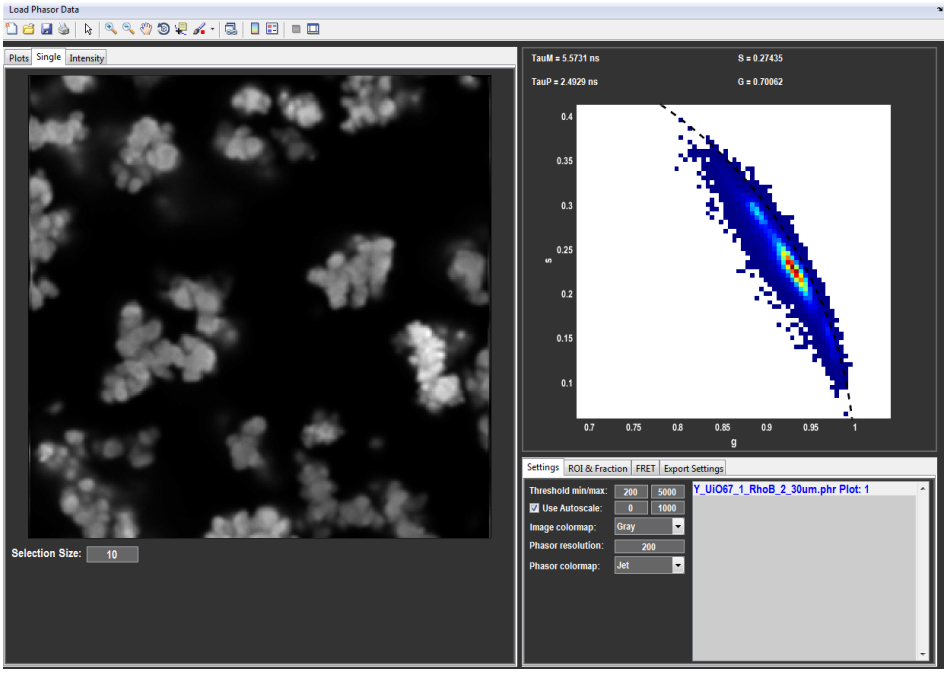

Figure 4.14: Screenshot of the *Phasor* sub-program of *PAM*, with the intensity image for a single file shown on the left and the corresponding phasor histogram on the right.

The fist (and most straightforward) way is to assign a color to a region of interest in the phasor plot and mark all corresponding pixels with the same color (illustrated in Figure 4.15). Simply plotting a constant color over a (false color) intensity or a purely black image can be very useful when only the position or distribution within the frame are important. With this approach, the intensity information is mostly lost. To keep both aspects in the image, *PAM* has a second way of applying the color. Hereby, the photon counts correspond to the pixel brightness, whereas the ROI is color-coded into the hue. Pixels that were not selected or lie outside of the intensity threshold are then displayed in gray-scale. For both methods, up to six different ROIs with user defined colors can be selected. In case that multiple ROIs overlap, the programs simply uses the mean of the individual RGB values.

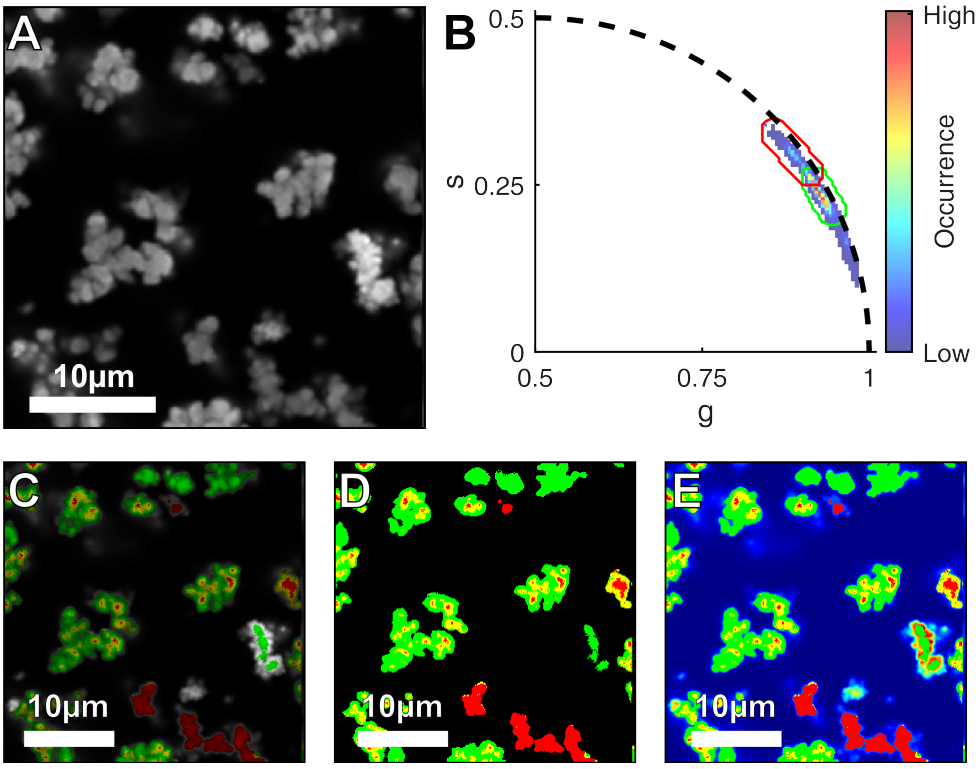

Figure 4.15: Illustration of the color-coding for phasor ROIs. A) Gray-scale intensity image of the metal-organic framework UiO67 with 1% of all linkers modified with Rhodamine B. B) Phasor histogram of Rhodamine B of image A) for a phasor frequency of 25 MHz. C-E) The ROIs selected in the phasor plot (green and red ellipsoids in B)) applied in different ways to the image. Pixels in the overlap between both ROIs are display via their mean color (yellow). C) The hue represents the ROIs, while the brightness indicates the intensity. Unselected pixels are shown in gray-scale. D) Only the selected ROIs are displayed over a black background. E) The intensity of the image is display with the Jet color-map, while the selected ROIs are represented with their constant color.

The second way of relating the lifetime data to the actual image is to reduce the 2D representation of the phasor plot to a single axis. One possibility is to use only the g or the s axis to visualize differences. This, however, reduces the resolution power since, in most cases, changes in the fluorescence lifetime result in shifts along both phasor axes. Therefore, *PAM* allows the user to define a line, that is then used as the base axis (Figure 4.16 A). In this way, changes are mapped to the largest distance in the phasor plot, while still using only one dimension. In practice, the program determines for each pixel, which position on the line is closest to it but excludes all pixels that are further away than a user defined distance (Figure 4.16 B). Each point of the line is assigned a different color, which is used to color-code the individual pixels of the image in much the same way as for the region of interest method (Figure 4.16 C).

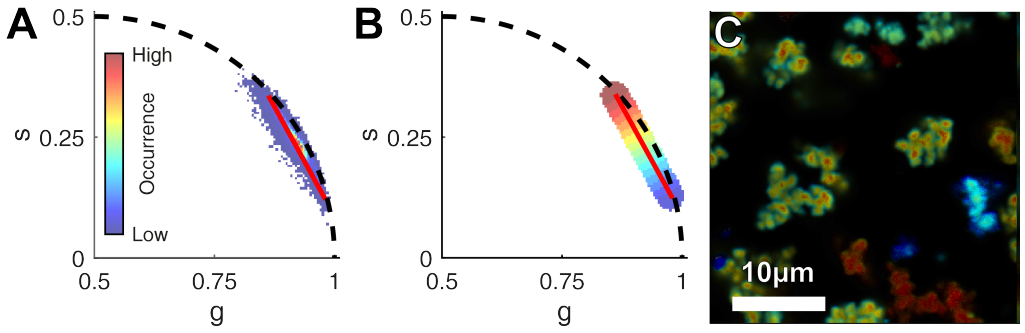

Figure 4.16: Line selection in the *Phasor* program. A) Phasor plot of the same measurement shown in Figure 4.15. B) Illustration of the colors assigned to the different positions in the phasor plot according to the selected red line in A). C) Intensity image with the color-coding corresponding to the selection in B).

While the line selection is best suited for variations in a mixture with multiple components (resulting in straight lines), quenching changes in the actual lifetimes and causes the phasor distribution to follow a curved trajectory. A common source of quenching in FLIM experiments is FRET. *PAM* contains a method to show such a FRET trajectory (or any other quenching mode) and to display the particular FRET value in the image, illustrated in Figure 4.17. First, the user selects the phasor position of the unquenched fluorophore (green circle in Figure 4.17) and the program calculates the corresponding ideal trajectory (green dashed line in Figure 4.17). In cases where the fluorophore lifetime in not mono-exponential, the quenching curve cannot be unambiguously determined. Any phasor not on the universal circle can be the result of different combinations of lifetimes. Therefore, without knowing the individual components, it is also not possible to calculate the correct quenching trajectory. However, for almost all dyes used in fluorescence microscopy the phasor lies very close to the universal circle, meaning that all possible trajectories for that particular phasor position are very similar. Therefore, the curve can be approximated by assuming a mixture of two mono-exponentials and calculate their (unique) trajectories individually, but keeping their fractional contribution constant. This calculation is further simplified by setting one of the lifetimes to zero.
Once the ideal trajectory is calculated (green circle in Figure 4.17), the program also accounts for possible background (blue circle in Figure 4.17), e.g. from cell autofluorescence, and unquenched fluorophores (green circle in Figure 4.17), e.g. donor-only molecules in FRET measurements. The resulting modified trajectory is shown as a orange dotted line in Figure 4.17. Hereby, it is assumed that, with increasing FRET, the fluorophore's quantum yield is decreased. This, in turn, increases the relative contribution of the other sources, so that the trajectory curves back towards the phasor corresponding to a mixture of background and donor only (blue dotted line in Figure 4.17). The final curve is then used to color-code the image in much the same way as for the line selection.

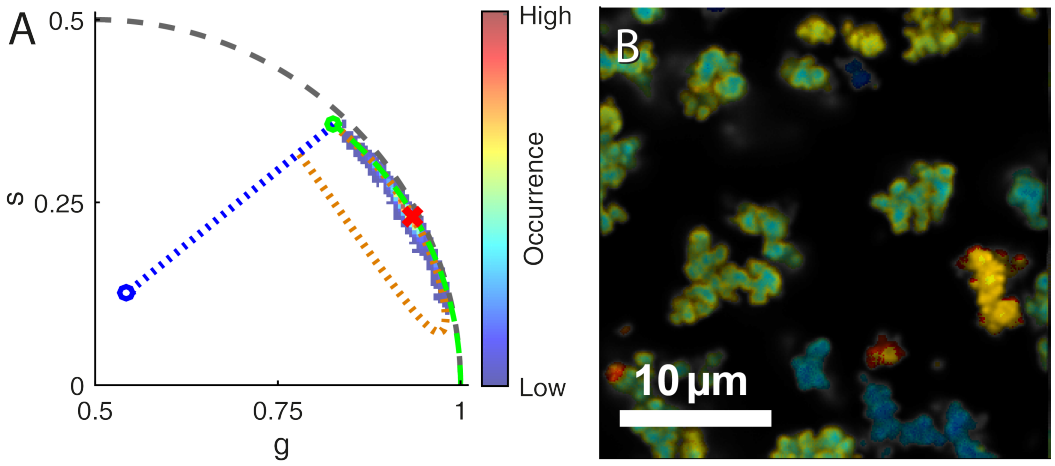

Figure 4.17: FRET trajectory in the *Phasor* program. A) Phasor plot of the same measurement shown in Figures 4.15 and 4.16. The green circle indicates the unquenched fluorophore phasor, with the green dashed line depicting the ideal FRET trajectory. The orange dotted line results from taking donor-only and background (blue circle) photons into account. Due to the decreasing quantum yield, the orange path curves back to a point on the blue dotted line representing all possible combinations of donor-only and background. The red x shows the currently selected FRET value. B) Intensity image color-coded according to the orange FRET trajectory in A). Low FRET values and therefore long lifetimes are represented with blue and cyan, while high FRET and low lifetime is shown in red and orange. Green and yellow colors are used for intermediate values.

So far, the methods presented for relating lifetime and intensity map the phasor position onto the image. In some cases, however, it is more useful to go the opposite direction and select regions in the image that are then highlighted in the phasor plot. In *PAM* the user can (un)select individual pixels, so that only valid pixels are then used to generate the phasor histogram. To keep the full image information, but still differentiate different regions, the unselected pixels are indicated with an inverted color-scheme (effectively 1-RGB), as is shown in Figure 4.18.
For a narrow distribution in the phasor plot, several hundreds of photons per pixels need to be recorded. Measurements where such a high numbers cannot be achieved due to limitations in acquisition time (e.g. for dynamic processes) or maximum photon yield (e.g. in case of photobleaching) suffer from decreased accuracy in determining the lifetime. To deal with this problem, the user can select to apply a spatial moving average of 3×3 pixels to the phasor data, weighted by their photon counts. As is shown in Figure 4.19, this strongly decreases the spread in the phasor plot, but at the same time reduces the spatial lifetime resolution. The intensity image, however, is not affected by this.

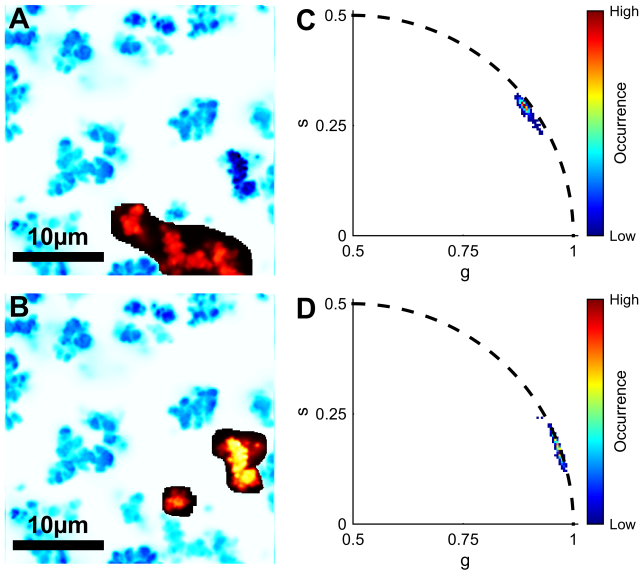

Figure 4.18: Image region selection in the *Phasor* program. A and B) Intensity images of the same measurement as shown in previous figures, with different selected regions. The active pixels are displayed in the Hot color-map (from black over red to yellow and white) and a complimentary color-scheme for unselected regions (white over cyan to blue and black). C and D) Phasor histograms showing only the selected pixels of images A) and B), respectively.

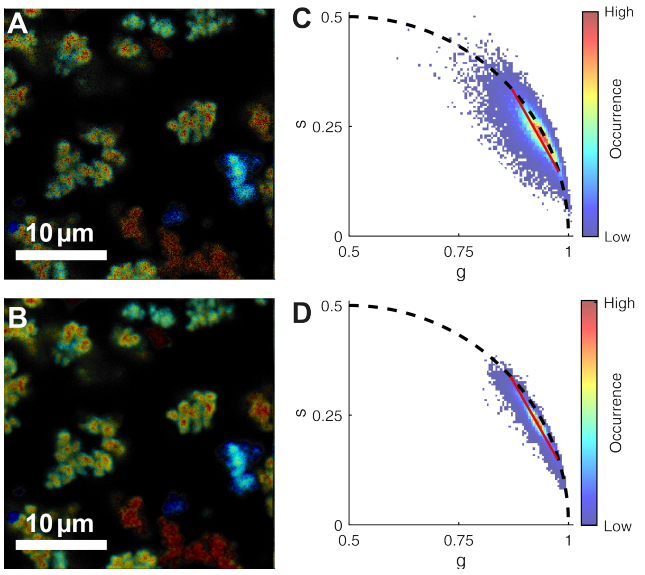

Figure 4.19: Image and phasor plots of the same measurement as shown in previous figures. A and B) Intensity images without (A) and with (B) moving average applied. C and D) Phasor histograms for images A) and B), respectively, showing a decreased spread when a moving average was used (D). To better illustrate the effect of the moving average, the spread in the phasor plot was increased by decreasing the the photon counts per pixel.

4.7 Simulation in PAM

A quick and reliable method of validating new techniques, approaches or fit models is to apply them to measurements where all the relevant parameters are well known. The simplest way to ensure the later is to use simulated data. To acquire these, one needs a program that can generate simulations suitable for the various applications of PAM.
Just like with PAM in general, the focus of the simulation subroutine lies on the random diffusion of particles and FRET between them, as observed with a confocal microscope. Often, such calculations need to be performed multiple times with slightly changed parameters. At the same time, each measurement might contain different species with different particles. Simulating each one of these individually and then combining them requires a lot of user input. Therefore, this process is mainly automated in PAM so that, even for long calculation times, the time invested by the user is short.

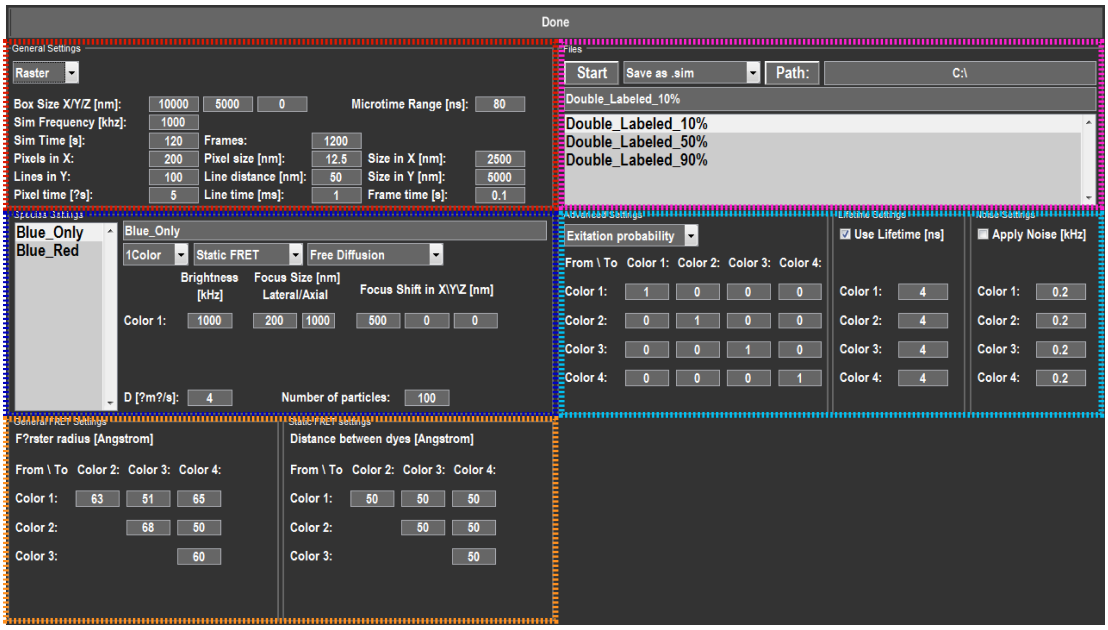

Figure 4.20: Screenshot of the *Simulation* sub-program of *PAM*.

In a first step for each simulated experiment, the general measurement parameters are given (*General Settings*, red box in Figure 4.20), including the measurements time and scanning settings. These parameters are completely independent of the type of particles simulated and are applied to all species. The second tier of settings are particle specific parameters. The user creates a species for each type of particles and defines their individual settings. The later include values that directly depend on the particle type, like their number, their diffusion coefficient or how many different dyes (up to four colors) are attached to them (*Species Settings*, blue box

in Figure 4.20). However, also other experimental conditions might vary between species, like excitation and detection efficiencies (*Advanced Settings* and *Lifetime Settings*, cyan box in Figure 4.20). Furthermore, the program includes an algorithm to simulate static FRET and interactions with the spatial environment via diffusion barriers or local quenching (orange box in Figure 4.20).
Several such experiments can be pre-programed and are simulated one after another (magenta box in Figure 4.20)). The simulation itself is performed sequentially for each particle, parallelized over multiple CPU cores to speed up the process. To decrease memory usage and time, the main calculations are written and executed in C^{++}. The actual algorithm is based on a Monte Carlo approach and consists of several steps. The pseudorandom numbers required are generated using the Mersenne Twister Engine.
The individual steps are:
Particle Movement: A random step for the particle is simulated, based on the diffusion coefficient, the dimensionality and the restraints of the simulation box. At this point, spatial restrictions on the movement are implemented (if applicable). This might lead to the particle entering an invalid region. In this case, new steps are generated from the original position until a valid resting point is reached.
The movement might also cause the particle to exit the predefined simulation box. When this happens, it is moved to the opposite end of the box. At the same time, its properties are reset to their original value (e.g. bleaching is reversed). Setting the size of the box to zero for the z-dimension reduces the particle behavior and all further calculation to two dimensions.
Focus Movement: In the next step, the deterministic focus position relative to the confinement is calculated. There are four different types of movement possible: A stationary focus, a raster scan, line scan or circular scan.
Excitation: Once the relative positions of the particle and the focus are established, the algorithm checks if the particle is excited. This and all following steps are repeated for all active colors, both for the excitation laser and the excited dye (i.e. direct excitation). Considering up to four colors, this means, these steps are executed for a maximum of 16 times. Generally, the excitation probability of a dye with a laser with a wavelength that is much longer than the optimal is negligible. Therefore, only 10 cases need to be checked for a normal four color experiment. Hereby, the excitation probability is calculated (based of a 3D Gaussian profile). If a spatial quenching map is used, it is applied at this stage, mimicking an immediate de-excitation by the quencher.
To generate a random and non-deterministic excitation, the resulting probability is then compared to a uniformly distributed random number. If the probability is the higher value, the particle is assumed to be excited. Otherwise, the following steps are skipped and the next color checked. Since the random number generation is a very time consuming process, it is only executed, if the total probability exceeds 0.01% and no excitation is assumed for lower values.
FRET: Next, the emitting dye is determined. For this, the algorithm uses a random number to check if FRET takes place and to which dye, in a similar fashion as for

the excitation. To simulate FRET cascades over multiple fluorophores, this process if repeated, until no transfer occurs. In the program, FRET is strictly a downward process and energy cannot be transfered back to the donor.
If enabled, this is also the stage when the fluorescence lifetime or rather the micro-time of the photon is determined. At each step during the cascade, a geometrically distributed random number, based on the (FRET modified) fluorescence lifetime of the corresponding dye, is added to the photon's micro-time. This resulting micro-time distribution is a convolution of the lifetime of all involved dyes. This is exactly what is theoretically expected for a FRET cascade. To simulate PIE, the micro-time is additionally shifted by a value corresponding to the delay of the excitation laser.
Bleaching: Before photon emission, the program analyzes whether bleaching takes place. Since this is done after the emitting dye is determined, only that fluorophore can also bleach. Therefore, FRETing donor dyes have an increased stability. Bleaching is again simulated using a random number check. If a fluorophore bleaches, no photon is emitted and it can no longer be excited, neither directly nor via FRET.
Crosstalk and Detection: Lastly, the detection of the photon is probed. Hereby, a random number is used to check which detector channel the photon falls into. This process is supposed to emulate spectral crosstalk. A second random number then determines, whether the photon is actually registered, based on the channel's detection efficiency. A detected photon is then assigned a macro-time (cycle step) and a micro-time, as well as an 8 bit identifier. The later consists of 2 bits each for the excitation laser, the excited dye, the emitting dye and the detector channel. This can later be used to determine the photons exact origin.
Once the program has gone through all these steps, it moves to the next time point and cycles through them again, until the maximal simulation time has been reached. This is repeated for all particles and then species. At the very last stage, random noise can be added to the photon stream.
The data can either be saved as a photon file (.sim), to be analyzed in PAM, or directly as a TIFF, in the case of a raster scanned image. After saving, the next pre-programed simulation experiment is started.

4.8 Application of PAM

Some of the presented functionalities and sub-programs were used in analyzing data that will be presented in the following chapters. There are also a number of collaborations with other groups and coworkers that relied on the program. Since the main part of the experiments and analyses was not performed by myself in these cases, they will not be described here in detail but only briefly introduced.

4.8.1 Organization and Dynamics of Myelin Proteins

In the publication "The Lateral Membrane Organization and Dynamics of Myelin Proteins PLP and MBP Are Dictated by Distinct Galactolipids and the Extracellular Matrix" by Ozgen *et al.*, published in *PLoS ONE*,[96] various correlation functionalities of PAM were used for analyzing RICS data and scanning FCS data. Together with other biophysical and -chemical methods these data helped to determine the effect of myelin typical galactolipids galactosylceramide (GalC) and sulfatide, as well as of the extracellular matrix on the distribution and dynamics of the myelin basic protein (MBP) and the myelin proteolipid protein (PLP) in the oligodendrocyte cell line OLN-93. RICS and z-scan point FCS experiments revealed that MBP diffusion rates increased in GalC expressing cells. Furthermore, scanning FCS was used to show that, on an inert or a myelination-promoting laminin-2 surface, PLP exhibited a decreased mobility in sulfatide containing cells while its diffusion coefficient increased when the cells were grow on fibronectin, a myelination-inhibiting substrate. Supported by additional biochemical measurements, these differences in lateral mobility can be attributed to their biophysical properties, like their specificity for association with lipid rafts.

4.8.2 Protein-Specific Glycosylation in Living Cells

In "Visualization of Protein-Specific Glycosylation inside Living Cells" by Doll *et al.*, published in *Angewandte Chemie International Edition*,[97] a novel method for measuring the glycosylation state of specific proteins in living cells is introduced and demonstrated for several different proteins. Hereby, the frequency domain phasor part of PAM was used to measure FLIM. By monitoring the lifetime decrease of eGFP coupled to the target protein, FRET to a glycan-anchored fluorophore was detected. Since FRET can only occur over short distances, donor quenching is only observed in the case that the protein of interest is also labeled with the acceptor dye. Since the acceptor fluorophore is attached to a carbohydrate via a bioorthogonal Diels-Alder reaction, only glycosylated proteins exhibit a noticeable FRET signal, making the method both sensitive and specific.

4.8.3 Dynamics and Oligomerization of Cytosolic HIV-1 Gag

The mobility, interactions and oligomerization state of cytosolic HIV-1 Gag was studied in "Live-cell observation of cytosolic HIV-1 assembly onset reveals RNA-interacting Gag oligomers" by Hendrix *et al.*, published in *The Journal of Cell Biology*.[98] In this publication a wide variety of complimentary fluctuation imaging techniques were employed to reveal the oligomerization state of cytosolic Gag. By analyzing the diffusion behavior, cross-correlation and stoichiometry of the wild-type protein and of several mutants, two species of cytosolic Gag were identified. The first was attributed to monomeric Gag, as no cross-correlation was observed

for this species. From the effect of mutations in the nucleocapsid domain of Gag on its diffusion it was shown that the protein interacts transiently with RNA. The second observed species exhibits a strongly decreased mobility and oligomerizes in a concentration dependent manner.

4.9 Discussion and Outlook

In its current form, *PAM* already contains a wide variety of different methods for advanced fluorescence spectroscopy ranging from fluorescence fluctuation over lifetime to single molecule FRET analysis. Hereby, applications that are used extensively are more developed and refined than those that are not that much in the focus of our lab. However, the goal for *PAM* is to become a program that is used by a large number of research groups and applied to a broad spectrum of different methods and topics. For this to happen, especially two aspects of *PAM* need to be extended.
The first issue is the compatibility with different data types. Almost every supplier of microscopy devices has its own file format for saving measurement data. While the most common TCSPC formats are already implemented, a large number of commercial microscopes are still not supported.
The second area that needs improvement is the exporting of the analyzed data. Currently, most implemented export functions require the Matlab development environment. Since *PAM* is designed to also be used as a compiled standalone program, these functions would not work in such a case and the data would not be accessible. Therefore, the export capabilities need to be extended to common file formats, e.g. simple text and image files. In the near future, *PAM* will be published and made available for a larger group of people. The feedback from the new group of users will help to improve current features and implement new applications.

5. Fluorescence Lifetime and Intensity Imaging of Metal-Organic Frameworks

Metal-organic frameworks (MOFs) are a class of crystalline materials consisting of metal ions or metal containing units (called secondary building units, SBUs) that are connected via organic linkers, forming a three-dimensional lattice. They have emerged as an interesting new class of porous materials with potential applications in various fields (e.g. catalysis, gas adsorption or molecular sensors)[99–102] due to the following three important characteristics:

Porosity: The ball-and-rod assembly can create large cavities in the crystal, resulting in a high permanent porosity (>50% of the MOF volume). This leads to a very high active surface area, typically in the range of 1000–10 000 $m^2\,g^{-1}$, thus exceeding those of traditional porous materials such as zeolites and carbons. This makes MOFs especially interesting for applications in gas and fuel storage, molecular sieving and sorting, or heterogeneous catalysis.

Tunability: Since MOFs are constructed from individual building blocks, one can achieve a huge number of different materials just by mixing and matching. By varying the organic linker or the SBU, almost any property (e.g. pore size and shape, or catalytic activity) can be changed and adjusted to satisfy the particular need of the application. The large diversity of both the linkers and the SBUs has allowed for the synthesis of a large number of different MOFs, with currently more than 20,000 reported structures. MOFs are therefore a good candidate for the concept of designed materials.

Functionalization: The versatility of MOFs is not only limited to their scaffold and structure, but also to the incorporation of different functionalities. Especially modification of the organic linkers allow for the introduction of functional sided groups that do not interfere with the formation of the scaffold. This functionalization is not only possible during synthesis of the MOF, but can also be performed after the formation of the framework is complete. The large pore volume allows molecules to diffuse deep into the MOFs and react with either unsaturated metal sites or moieties on the organic linker, resulting in post-synthetic modifications (PSM).[103,104] Another way of changing the properties of a MOF is done by exchanging whole building blocks. Hereby, the organic linkers[105,106] or cations[107] of a MOF are exchanged between neighboring crystals or with the solutions. Thus, various new capabilities and functions can be added to a MOF scaffold, including catalytic activity and applications in molecular sensing[108] without affecting the overall structure.

One topic that is currently attracting a lot of attention in the MOF field is the concept of multivariate (MTV) functionalities.[109,110] Hereby, multiple different

functional groups are incorporated into a MOF scaffold at once. This is usually done by slightly modifying the organic linkers with functional side groups (e.g amines or halides) that do not interfere with the formation of the scaffold. In 2010, a study showed synergistic effects of such multiple functionalities even when randomly distributed in the material.[110] Here, a variety of MTV-MOFs where synthesized and characterized. Interestingly, MOFs with certain combinations of linker side groups exhibited increased performance in H_2 uptake or CO_2 selectivity compared to the materials with just a single moiety, demonstrating that for MOFs the total is greater than the sum.
A different point of interest focuses on heterogeneities in MOFs and their influence on function and performance.[111] Even for materials with identical composition and crystal structure, the distribution of defects might vary from batch to batch. They can be small irregularities and mismatches in the lattice, but also on a larger scale like in the case of crystal edges, whose type and abundance strongly depends on particle size and morphology. Although these heterogeneities only compose a small fraction of the total material, they have vastly different properties from the bulk matter and can dramatically alter its behavior and performance.
One aspect common to these two topics is that they are both strongly influenced by the spatial distribution, either of the different functional groups or the defects. In both cases, the effect of heterogeneities will be different when they are homogeneously distributed throughout the material from when they are localized in individual phases. Therefore, measuring and controlling this spatial distribution plays a key role in optimizing the performance of MOFs.
In this work, two different MOF structures were investigated. On the one side, the correlation between morphology and fluorescence lifetime of fluorescein modified MIL-101(Al)-NH_2 was studied. This work was done in a collaboration with the group of Dr. Wuttke and was published in *Small* under the title "Investigation of the Co-dependence of Morphology and Fluorescence Lifetime in a Metal-Organic Framework".[112] The second investigation focused on the interplay between functional modifications and the scaffold of the MOF UiO-67 under different synthesis and functionalization conditions. This study was conducted together with the groups of Prof. Yaghi in Berkeley and Dr. Wuttke at the LMU. For both studies, fluorescence intensity and lifetime microscopy were the primary analysis methods.

5.1 Correlating Fluorescence Quenching and Morphology in MIL-101(Al)-NH_2

The original MIL-101 (MIL standing for Material of Institut Lavoisier) framework is a chromium based MOF with terephtalate linkers.[113] In the years following the first report, equivalent structures with other trivalent metals and modified linkers were reported,[114] among these the aluminum based MIL-101(Al)-NH_2.[115,116] Here, four trimeric aluminum octahedra (Figure 5.1 A) are connected by six 2-amino terephtalate linkers (Figure 5.1 B) forming a super-tetrahedron structure (ST,

Figure 5.1 C). Like with all MIL-101 MOFs, these tetrahedra assemble to a larger structure consisting of two types of cages. The smaller ones (29 Å, Figure 5.1 D) are build up of 20 STs arranged in a dodecahedron, while the larger cages (34 Å, Figure 5.1 E) consist of 28 STs forming both pentagonal (12 Å) and hexagonal openings (16 Å). With a ratio of 2:1, these cages are connected to a Mobil Thirty-Nine (MTN) zeotype topology.

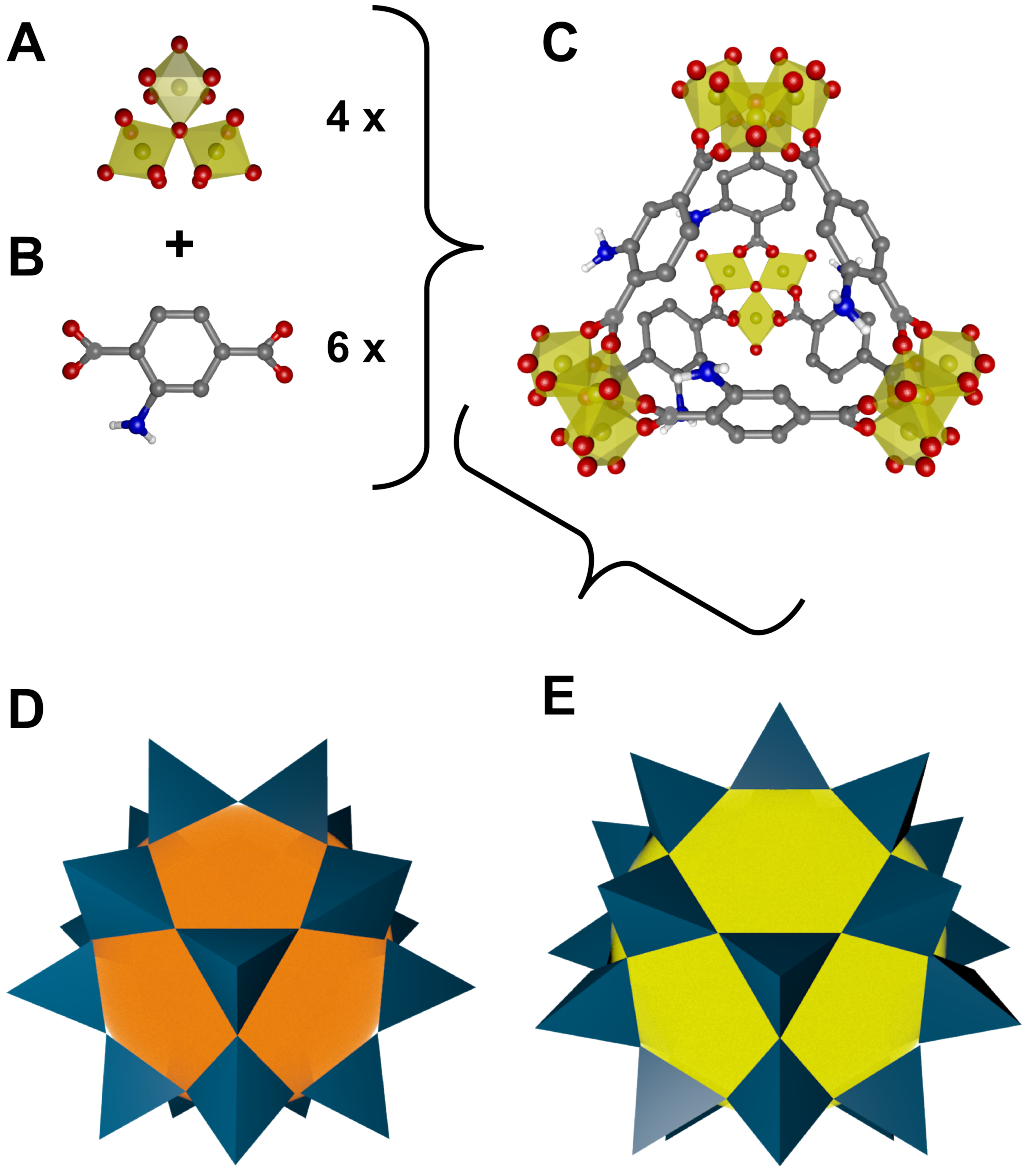

Figure 5.1: Structure of the MIL-101(Al)-NH_2 framework. Four trimeric aluminum octahedra (A) and six 2-amino terephtalate linkers (B) constitute the vertices and edged of a super-tetrahedron (ST) (C), respectively. The STs, in turn, form the vertices of two types of cages. D) In the smaller cages, 20 STs are arranged in a dodecahedron. E) The larger enclosure consists of 28 STs forming both hexagonal and pentagonal windows.

The aromatic amines are not directly involved in forming the framework and are therefore available for covalent PSM with amine selective reagents. Together with the MOF's high thermal and chemical stability as well its high porosity (specific BET surface of $\approx 3000\,m^2\,g^{-1}$), this fact makes MIL-101(Al)-NH_2 very interesting for applications in catalysis, drug delivery and chemical sensing. With respect to chemical sensing, it has been shown that fluorescein isothiocyanate (FITC) modified MIL-101(Al)-NH_2 can be used to very sensitively and selectively detect fluoride ions in aqueous solutions.[108] In this case, the light emission of fluorescein is strongly quenched when bound to the MOF. However, when subjected to fluoride, the framework is decomposed, releasing the dye and recovering the fluorescence. The resulting increase in fluorescence signal can be measured very accurately to detect fluoride concentrations as low as 15 ppb.
Although fluorescence suppression was clearly observed, the exact mechanism of quenching was not known. In order to investigate whether it is based on auto-quenching from dye-dye interactions or on a photoinduced electron transfer type mechanism caused by unreacted amino groups,[117] fluorescence lifetime imaging microscopy was employed. Virtually all quenching types shorten the fluorescence lifetime of a dye, making it an ideal property to quantify the quenching amount and, by varying certain other parameters, deduce the involved mechanism. When combined with imaging, this additionally provides information about the spatial heterogeneity.

5.1.1 FITC Self-Quenching in MIL-101(Al)-NH_2

The first potential quenching mechanism that was investigated is self-quenching of fluorescein. If the dye concentration in the framework is too high, multiple fluorophores are in close proximity and can interact with each other. Depending on the exact type of dye-dye interactions, this might lead to a decrease in fluorescence signal coinciding with a shortened lifetime. To check this hypothesis, samples containing varying amounts of FITC (1.23 nmol, 2.46 nmol and 12.3 nmol per 100 mg MOF) were synthesized and their fluorescence lifetime measured (see chapter 5.3). Although the dye concentration was changed by a factor of 10, the photon arrival time histograms for all samples look very similar (Figure 5.2). Minor differences are only noticeable for times longer than 5 ns after the laser pulse, with the lower concentration samples showing a higher amount of a long lifetime component (Figure 5.2 B). This indicates that dye-dye interactions are, at most, just a very minor contribution to FITC quenching. The differences at long lag times are most likely caused by the inherent luminescence of the MIL-101(Al)-NH_2 framework (described in more detail in chapter 5.1.4), contributing more to the signal at lower dye concentrations.

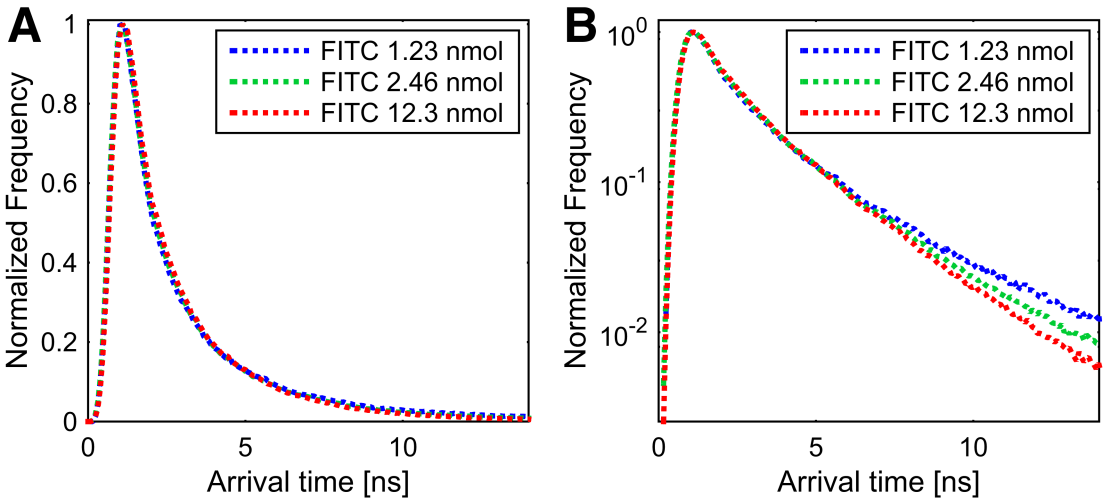

Figure 5.2: Photon arrival time histograms for three MIL-101(Al)-NH_2-FITC samples with 1.23 nmol, 2.46 nmol and 12.3 nmol FITC per 100 mg MOF, plotted on a linear (A) and logarithmic (B) ordinate.

5.1.2 FITC Quenching via Unmodified Amino Groups in MIL-101(Al)-NH_2

As self-quenching is not the main cause of the decreased fluorescence in MIL-101(Al)-NH_2-FITC, other sources were investigated. One likely candidate is the amino groups on the organic linker. The amount of FITC used for modifying the MOF was significantly lower than the available reaction sides, even when assuming a 100% labeling efficiency. This leaves a lot of unmodified NH_2 groups in close proximity to the dye. It is well known that amino groups can quench fluorophores via photoinduced electron transfer (PET) and such a process has even been shown in dye functionalized MOFs.[117] Although PET only works over very small distances (≈1 nm), it is still very likely when considering the structure of MIL-101 (Figure 5.1) and the high density of linkers.
To test this hypothesis, two batches of MIL-101(Al)-NH_2-FITC were synthesized with higher FITC content (15.5 nmol per 100 mg MOF) to minimize autoluminescence contributions. Parts of both samples were further modified in a reaction with pivaloyl anhydride (chapter 5.3).[118] In this way, the remaining amines were transformed to amides, altering their redox properties and decreasing PET type quenching. The bulky *tert*-butyl group additionally constitutes a sterical hindrance, further reducing the interactions with the dye. To determine how this capping affects the fluorescence lifetime as well as how this influence is distributed spatially, both untreated (MIL-101(Al)-NH_2-FITC) and modified (MIL-101(Al)-NH_2-FITC/P) samples were analyzed with phasor FLIM.
As can be seen in Figure 5.3, the samples with free amino groups (Figure 5.3 B-E) exhibit a significantly shorter average lifetime than their capped counterparts (Figure 5.3 F-I). This strongly suggests that PET is the main quenching mechanism

in this MOF. However, there is also evidence that other quenching sources are involved. The first indication is the fact that, even with capped amines, the lifetime is still significantly lower than the value expected for unaffected fluorescein (4.0–4.1 ns),[119], suggesting that the fluorescence quantum yield is still decreased. The second observation suggesting additional quenching mechanisms is the difference in lifetime between the two batches, both for pivaloyl treated and untreated samples. In the first batch (Figure 5.3 B, C, F and G), the lifetime is generally longer than in the corresponding sample of the second synthesis lot (Figure 5.3 B, C, F and G). Especially in the case of MIL-101(Al)-NH_2-FITC this cannot be explained by differences in the amount or distribution of the amino groups, since both samples show the same chemical composition. Therefore, these discrepancies must be caused by other factors like variations in the MOF structure or morphology at the nano-scale.

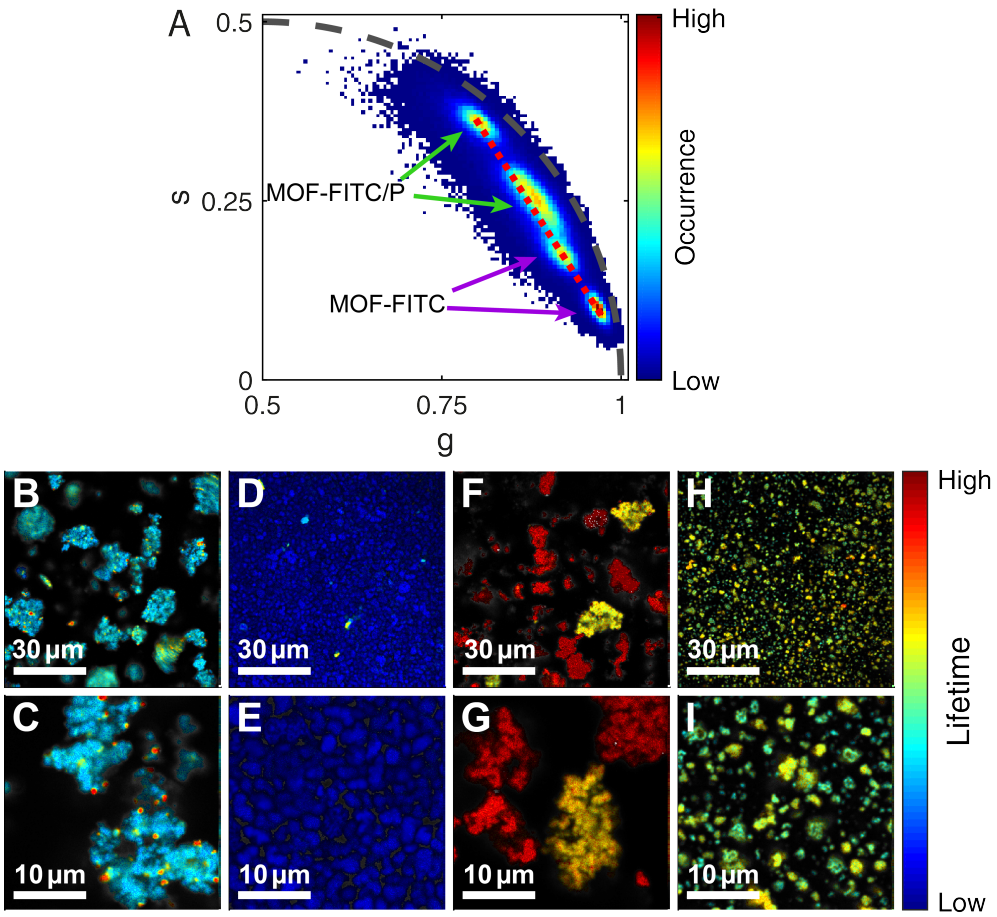

Figure 5.3: Phasor FLIM histogram and images of MIL-101(Al)-NH_2-FITC samples. The color of the images corresponds to the pixel position on the red dotted line in the phasor plot (A). Long lifetimes are positioned on the top left and correspond to a red and orange hue, while short lifetimes lie at the bottom right and are color coded with blue and cyan. Intermediate values in the center are displayed in green and yellow. The images show MIL-101(Al)-NH_2-FITC batches one (B and C) and two (D and E), as well as MIL-101(Al)-NH_2-FITC/P for batches one (F and G) and two (H and I).

5.1.3 Correlation of Morphology and Fluorescence Lifetime in Fluorescein Modified MIL-101(Al)-NH_2

From the observation that the amino groups cannot be the only major mechanism of quenching in MIL-101(Al)-NH_2-FITC, the question arises what other sources and parameters affect the dye's fluorescence. For both batches, the PXRD spectra and nitrogen adsorption isotherms do not show significant differences (see Appendix B), indicating that the overall structure and composition is identical for the different samples. However, these methods probe the bulk properties while heterogeneities and minor populations might not be resolved. Fluorescence, on the other hand, is much more sensitive to sporadic differences and heterogeneities. Rare defects, like under-coordinated metal ions, will not affect the overall crystal structure, but they can interfere with many fluorophores in their vicinity, significantly altering the fluorescence lifetime.

In order to identify heterogeneities in and the morphology of the materials and to link these to the differences in lifetime, correlative FLIM and SEM was performed. For this, samples were first measured with the confocal microscope. Afterwards, the same regions were identified and imaged with SEM (see chapter 5.3.1). Fluorescence microscopy reveals the spatial lifetime distribution, but it is limited to a resolution determined by the diffraction limit of light Therefore, structures below 200 nm are not resolvable. Electron microscopy, on the other hand, can resolve much smaller details, but is insensitive to the molecular composition and the detailed nanoscopic environment. Imaging the same region with both methods extracts the maximal amount of information and can establish correlations between morphology and quenching.

It must be noted that the samples had to be dried before imaging. Fluorescence lifetime, however, is a property that is strongly dependent on the solvation state of the fluorophore. Therefore, the phasor histograms are shifted as compared to the same samples measured in water. As evaporation, especially inside a highly porous material, is very hard to control, different samples might be affected differently by the drying process and the resulting lifetimes cannot be compared directly. Although the phasor position is shifted, the general shape and outline of the distribution are comparable for dried and hydrated samples, suggesting that the observed heterogeneities are due to intrinsic differences in the material and not due to variances in solvation.

Both the unmodified samples (Figure 5.4), as well as those capped with pivaloyl (Figure 5.5) show strong differences in morphology between batches one and two. The first morphology, called Type I, consists of aggregates of round particles with diameters of a few hundred nanometers and a fairly smooth surface (Figures 5.4 A and 5.5 A). Type II, on the other hand, exhibit a much rougher morphology (Figures 5.4 B and 5.5 B). Here, the aggregates are covered with significantly smaller crystals, often with diameters below 100 nm, and show more edges and breaks.

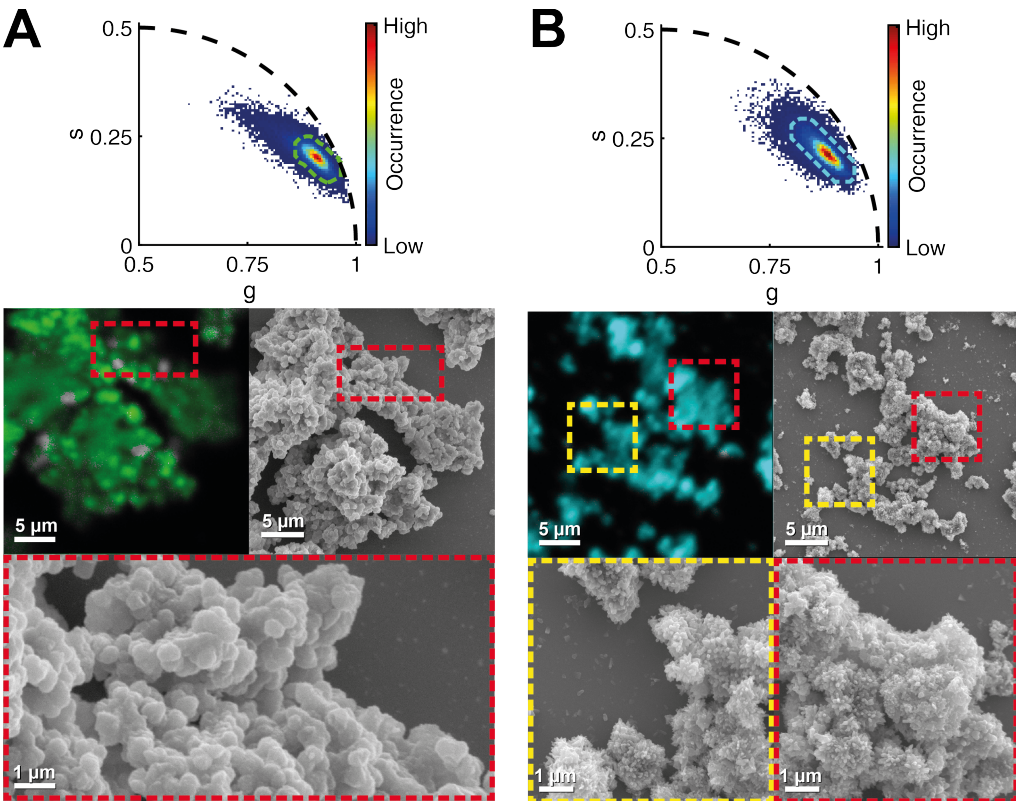

Figure 5.4: Comparison of FLIM and SEM images for MIL-101(Al)-NH_2-FITC of Type I (A) and Type II (B). The hue in the fluorescence images represent regions of interest selected in the phasor plot (green and cyan ellipsoids). The red and yellow rectangles in the FLIM and SEM images highlight the regions imaged with higher magnification.

It is very likely that this difference in morphology between batches one and two is also the cause for the changes in the fluorescence lifetime, either directly or indirectly. It is not possible to determine exactly how the morphologies affect the lifetime, but the most obvious difference between the two structures is the outer surface area. The larger and smoother particles of Type I have a significantly smaller outer surface-to-volume ratio than the small and jagged fragments of Type II. These edges always constitute breaks in the crystal structure and result in changed properties as compared to the bulk material.
It stands to reason that these defects might quench FITC, which would explain the lower lifetime observed for Type II samples. Although the influence of the outer surface will most likely not penetrate more than a few nanometers into the material, it can still significantly alter the overall lifetime. On the one hand, the distribution of the fluorophores may not be homogeneous within the MOF. Although the pores allow the dye to move in the framework, diffusion is nonetheless hindered. This makes it more likely for the dye to react with sites close to the surface. Since the crystallite size is on the order of the resolution limit, this gradient, if present, cannot be observed with a confocal microscope. On the other hand, it is also possible that the morphology is a symptom, not the cause. If Type II MOFs crystallize with more

defects, it makes them more prone to irregularities and fragmentation, leading to a formation of smaller particles. Thus, it is valid to attribute the second quenching mechanism to defects, either caused by external surfaces or interior lattice breaks.

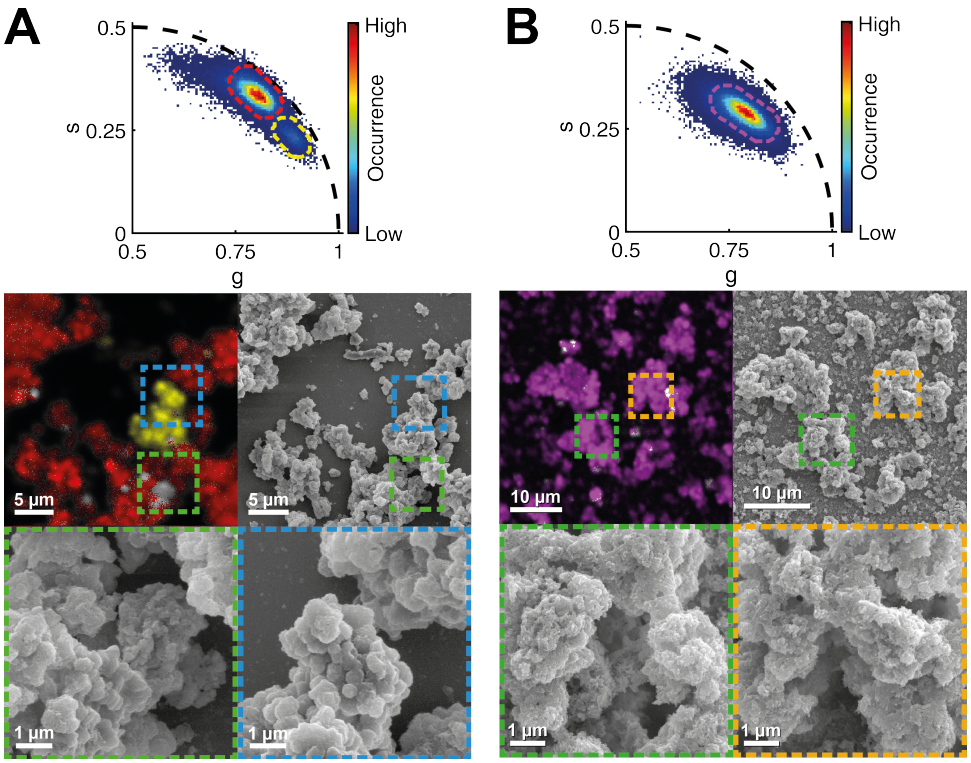

Figure 5.5: Comparison of FLIM and SEM images for MIL-101(Al)-NH_2-FITC/P of Type I (A) and Type II (B). The hue in the fluorescence images represent regions of interest selected in the phasor plot (red, magenta and yellow ellipsoids). The colored squares in the FLIM and SEM images highlight the regions imaged with higher magnification.

5.1.4 Correlation of Morphology and Auto-Luminescence Lifetime in Unmodified MIL-101(Al)-NH_2

While the FITC bearing samples show two vastly different morphologies, it was not clear in what way the dye influences the crystal shape and size. To test this, samples not bearing any dye were synthesized and measured using FLIM and SEM. The framework itself exhibits significant auto-luminescence so the lifetime can still be quantified. The excitation intensity, however, had to be increased to 5–10 µW, showing that its contribution to the dye labeled samples was very small, not significantly affecting the previous measurements.
As with the FITC samples, both the pure and the pivaloyl capped MOF show the two morphology types, in this case also within the same sample and even image (Figure 5.6). Contrary to FITC, which is more strongly quenched for the Type II morphology, the MOF's fluorescence lifetime is lower for Type I, and Type II regions

appear slightly brighter. Since none of the populations in the phasor plot lie on the universal circle, at least two different emitting states must be present for both types. At least one of these is linked to the morphology. Changes in the particle shape then result in variations of the contribution of the different lifetime species for the two morphologies.

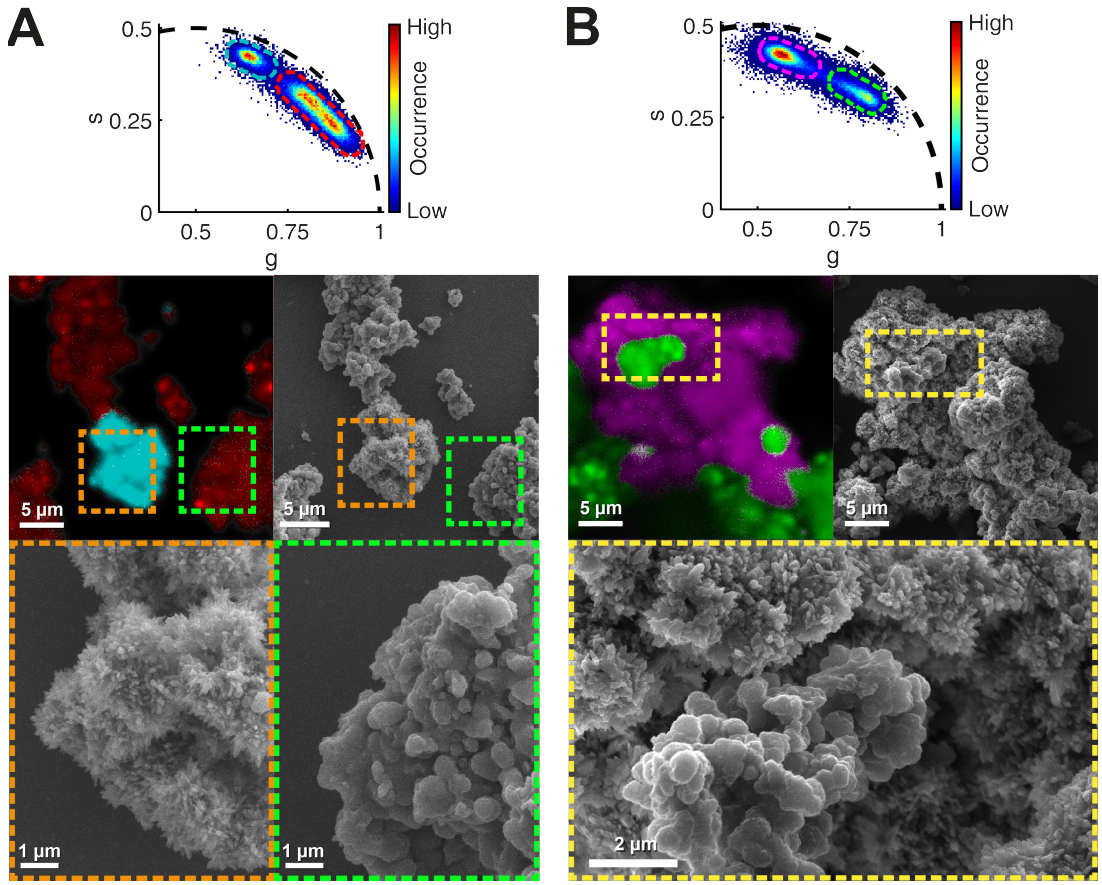

Figure 5.6: Comparison of FLIM and SEM images for MIL-101(Al)-NH_2 (A) and MIL-101(Al)-NH_2-P (B). The hue in the fluorescence images represent regions of interest selected in the phasor plot (cyan, red, magenta and green ellipsoids). The colored squares in the FLIM and SEM images highlight the regions imaged with higher magnification.

5.1.5 Quantification of Quenching in FITC Modified MIL-101(Al)-NH_2

Analyzing the fluorescence lifetime can not only be used to identify different quenching mechanisms in a qualitative way, but also to quantify their different contributions and elucidate the exact way the dyes are affected. The most obvious aspect in the phasor plot is that none of the observed populations fall on the universal circle. According to the rules of phasor space, this means that all samples consist of at least two fluorophore species with different lifetimes. A careful analysis

reveals that only three species are needed to explain and assign all measured samples (Figure 5.7).
The first lifetime of 3.8 ns corresponds to unquenched fluorophores and can also be observed when adding fluoride ions to the solution. This results in a decomposition of the MOF, releasing the dye and disrupting interactions responsible for quenching. The lifetime is still shorter than the value expected for free FITC (4.0–4.1 ns), indicating a slight quenching caused by the organic linker to which the fluorophore is still bound. Since all dye molecules are now identical, only a single species remains, resulting in a phasor population lying on the universal circle (Figure 5.7 dark gray ellipsoid).
The two remaining species are connected to the two quenching mechanisms. For samples modified with pivaloyl, three different populations are observed, two for Type I (Figure 5.7 red and yellow ellipsoids) and one for Type II (Figure 5.7 purple ellipsoid). All three are positioned on a straight line connecting the unquenched species to a species with a mono-exponential lifetime of 0.8 ns. Since the amino groups are capped, they no longer interfere with the emission and the 0.8 ns can therefore be attributed to quenching caused by defects.

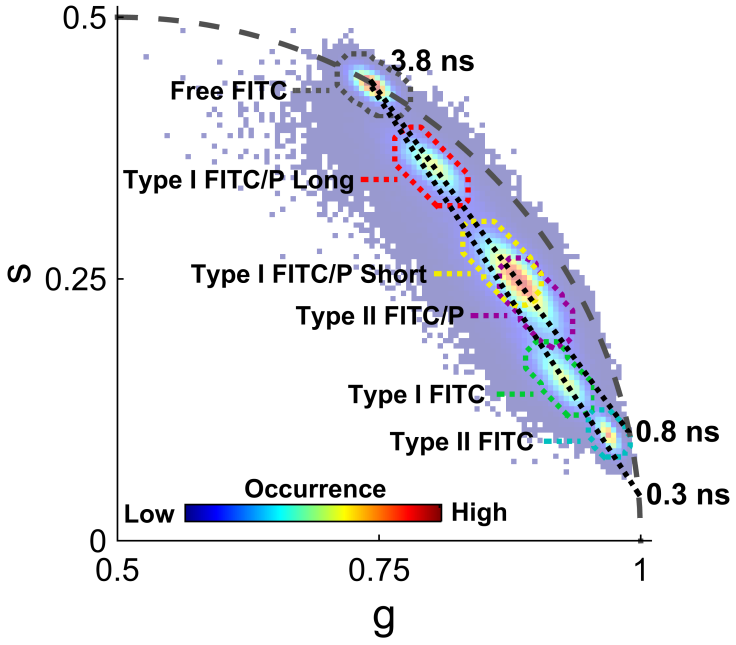

Figure 5.7: Phasor histogram for all fluorescein modified MIL-101(Al)-NH_2 measured in water. The black dotted lines indicate the mixture trajectories for the unquenched 3.8 ns and the two quenched (0.8 ns and 0.3 ns) species. The different populations for the individual samples are highlighted by colored ellipsoids.

If one assumes that, in Type I MIL-101(Al)-NH_2-FITC environments (Figure 5.7 green ellipsoid), quenching via defects is negligible compared to the contribution of the amino groups, it is possible to draw a second line that yields a third species with a lifetime of 0.3 ns. In Type II structures (Figure 5.7 cyan ellipsoid), this is

the main quenching source, but more defects are present, so that the distribution in the phasor plot is shifted closer to the 0.8 ns line.
The fact that all species lie on straight lines instead of following a curved trajectory suggest an all-or-nothing quenching mechanism. Hereby, a particular fluorophore is either unaffected (3.8 ns), or quenched (0.3 ns for the amino groups or 0.8 ns for defects), but no intermediate quenching is present. The fraction of fluorophores in the three states then determines the exact phasor position for the different samples, while slight fluctuations between pixels cause the distributions to be elongated along the quenching lines. This can also be used in reverse, calculating the contributions from the mean phasor, summarized in Table 5.1.

Table 5.1: Fractional contributions of the unquenched (3.8 ns), as well as the amino (0.3 ns) and defect (0.8 ns) quenched lifetime species.

	MIL-101(Al)-NH_2-FITC		**MIL-101(Al)-NH_2-FITC/P**		
Lifetime Component	**Type I**	**Type II**	**Type I Long**	**Type I Short**	**Type II**
3.8 ns	3%	<1%	43%	17%	13%
0.3 ns	97%	90%	NA	NA	NA
0.8 ns	NA	9%	57%	83%	87%

5.1.6 Spatial Heterogeneities in FITC Modified MIL-101(Al)-NH_2

So far, all the analyses concentrated on the main populations and effects on the average lifetime in the different samples and morphologies. Both FLIM and SEM, however, are imaging techniques. Unlike bulk methods where the results are an average over the whole sample, imaging can actually resolve heterogeneities spatially even when their relative contribution is very small. Indeed, most MOF samples showed some additional populations that deviated significantly from the main distributions. In many cases, these heterogeneities were only a tiny fraction of the whole sample and did not have a noticeable effect on the average lifetime.
The most significant of these heterogeneities is a minor population of particles in Type I MIL-101(Al)-NH_2-FITC/P (yellow regions in Figures 5.3 F-G and 5.5 A), constituting approximately 20% of the total sample (based on the number of pixels). Although it shows the same morphology as the main population, the lifetimes differ strongly (Figure 5.5 A). In this subpopulation, the fraction of unquenched fluorophores is much lower and even closer to that of the Type II morphology. The data does not allow the source of this deviation to be determined. One can speculate that these particles are an intermediate species between Types I and II, where the number of defects in the framework is increased, but not enough to effect a change to the rough morphology.

The second type of heterogeneities are individual, small (≈1 µm) particles observable for all Type I samples and populations (Figure 5.8). Unlike the short lifetime species of MIL-101(Al)-NH_2-FITC/P, these do no form separate aggregates, but are situated on top of the main population and make up <5% of the pixels. Again, these heterogeneities cannot be distinguished via morphology (gray regions in the phasor images of Figures 5.4 A and 5.5 A), but show a clear deviation in lifetime.

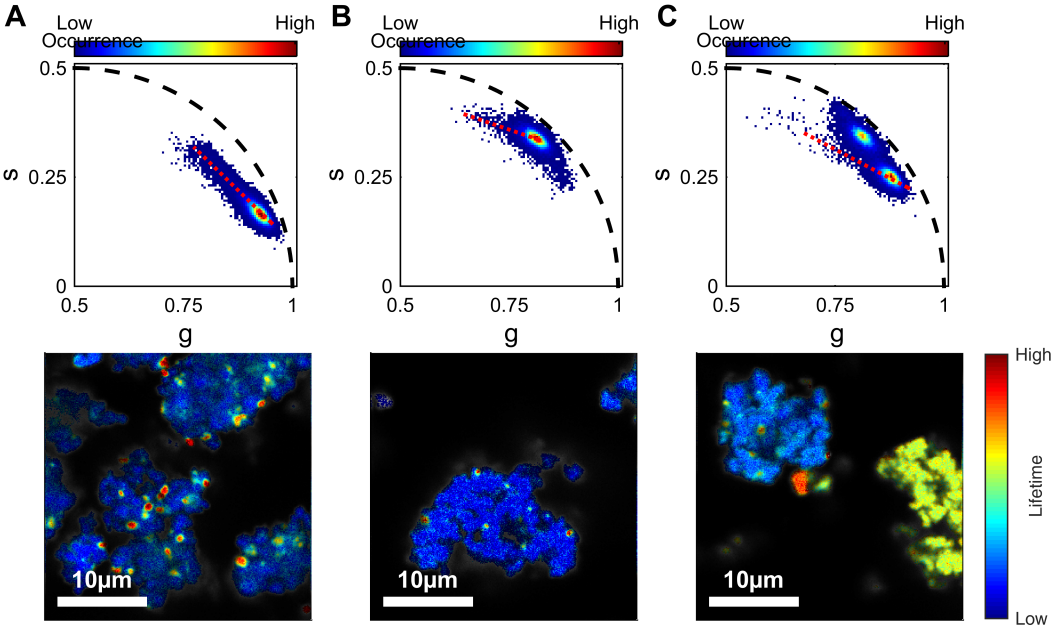

Figure 5.8: Phasor histograms and images showing the additional population on top of the Type I morphology for MIL-101(Al)-NH_2-FITC (A), as well as the short (B) and long (C) MIL-101(Al)-NH_2-FITC/P species. The red dotted lines show the axes used for color coding the images. The bottom left corresponds to blue, the top right to red and the middle to yellow and green.

5.1.7 Discussion and Conclusion

A careful analysis of the fluorescence lifetime in FITC modified MIL-101(Al)-NH_2 revealed two major types of quenching mechanisms in the MOF. One of these is mediated via photoinduced electron transfer to the unreacted amino groups, while the second type of quenching originates from the defects in the framework or the external surface of the MOF crystallites. The phasor plots additionally show that both of these quenching types follow an all-or-nothing mechanism. At any given moment a fluorophore is either quenched to the full extend (0.3 ns or 0.8 ns for the two mechanisms) or completely unaffected (3.8 ns). Thus, the resulting fluorescence lifetime is only determined by the fraction of molecules in the different states, but not by the degree of quenching of the individual fluorophores.
Furthermore, two different morphological groups were observed in both dye modified and pure MIL-101(Al)-NH_2. The first one, denoted as Type I, consists of

aggregates of smooth, round particles with a diameter of a few hundred nanometers. Type II, on the other hand, forms a more rugged, almost needle-like surface with significantly smaller crystallites. Using correlative FLIM and SEM microscopy, we could establish a clear relationship between the morphology and the fluorescence lifetime of the two types. The changes in lifetime between the different morphologies are linked to the quenching mechanism via defects. In the Type II morphology, the smaller and rougher crystals also result in a higher amount of defects, increasing their contribution in quenching and leading to a shorter lifetime.
This project did not only identify and quantify the different mechanism involved in FITC quenching in the MOF, but it also demonstrates the power and potential of FLIM for investigating porous materials, especially when combined with SEM. Correlative light and electron microscopy is a fairly new technique originating from the life sciences. It combines the high resolution power of the electron microscope with the sensitivity and selectivity of fluorescence, revealing new information not available from the individual techniques alone. This potential is evidenced by the increase of commercially available integrated light and electron microscopes. Although a few studies have already been published,[120,121] this approach is still mostly unexplored in the field of material science. Likewise, FLIM is only rarely, if at all, used to study solid state materials, although it is a well established technique in biophysical and medical research. It is usually applied for detecting analytes or studying interactions between biomolecules in cells or even whole organisms.
Only by combining these two methods was it possible to identify all the relevant contributions to the FITC quenching. While in this project the aim was to investigate the influence of the morphology and composition on the lifetime, the reverse approach is also possible and even more promising. Hereby, heterogeneous catalysis can be of particular interest. The active centers of a catalyst are very likely to affect a fluorophore. Thus, the lifetime can be used as a parameter to detect these centers and to study their spatial distribution, while the fluorescence intensity in combination with the electron image probe the structure and accessibility of the material.

5.2 *De novo* and Linker Exchange Functionalization of UiO-67

One important aspect for the use of porous materials in industrial processes is their stability.[102] Although many metal-organic frameworks show excellent performances in catalysis, selective sorting or gas adsorption, their large scale application is still hindered by their fast degradation. A group of MOFs that show a high stability both against temperature as well as chemical decomposition (especially water) is the isoreticular series of UiO-66, -67 and -68 (UiO as an acronym for Universitetet i Oslo).[122–125] Here, the secondary building units consist of zirconium octahedra with four μ_3-O and four μ_3-OH groups capping the eight faces (Figure 5.9 A). The octahedron's edges are bridged by carboxyl groups of the organic linker (transparent

structures in Figure 5.9 A), leading to a zirconium coordination of eight. This results in a total of twelve connections per cluster. Together with the linear linkers (Figure 5.9 B), they form a face-centered cubic unit cell (Figure 5.9 C) with octahedral and tetrahedral pores (Figure 5.9 D). The size of the pores and windows depends on the linker used for synthesis. For one (1,4-benzenedicarboxylate, UiO-66), two (biphenyl-4,4'-dicarboxylate, UiO-67) and three (*p*-terphenyl-4,4"-dicarboxylate, UiO-68) benzyl rings, the openings are 6, 8 and 10 Å in diameter, respectively.

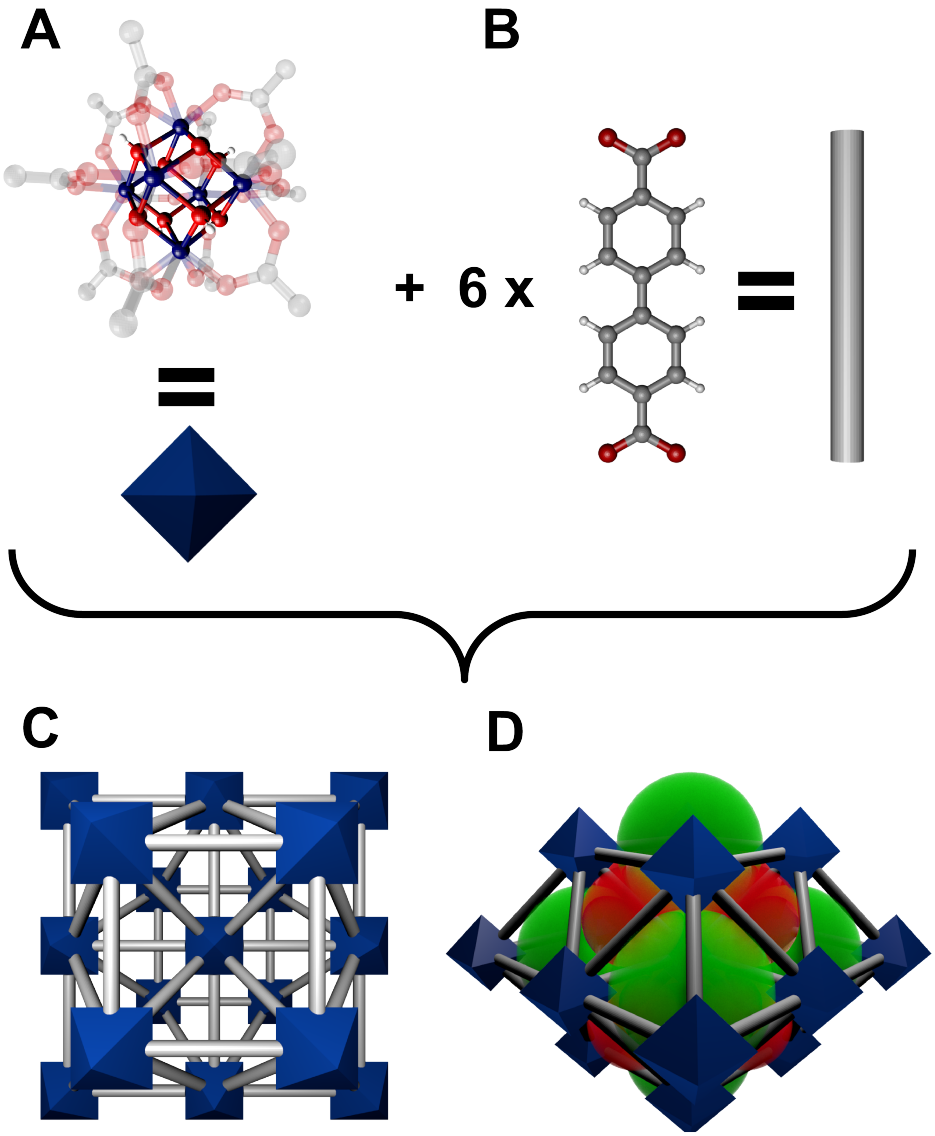

Figure 5.9: Schematic structure of the UiO-67 framework. A) $Zr_6O_4(OH)_4(R\text{-}CO_2)_{12}$ cluster forming the SBUs of UiO-67. The faces of the zirconium octahedron are capped by four μ_3-O and four μ_3-OH groups. The transparent atoms represent the attachment positions of the carboxyl groups of the biphenyl-4,4'-dicarboxylate linker (B). C) Simplified model showing the face-centered cubic crystal structure of UiO-67. D) Octahedral and tetrahedral pores of UiO-67 depicted with green and red spheres, respectively.

The high stability of these MOFs is to large extend due to the zirconium cluster and its high coordination. During thermal degradation (at 540 °C), the bond between the phenyl ring and the carboxyl group is broken first, showing the weakest point is not the connection between the inorganic SBUs and the linker, but rather the organic linker itself. Before final decomposition, dehydration of the MOF's SUBs takes place at 250–300 °C. The $Zr_6O_4(OH)_4$ clusters lose two molecules of water to form Zr_6O_6 with a reduced zirconium coordination of seven. The framework can withstand this rearrangement without breaking down and the whole process is reversible.
Another usefull feature of UiO-66/67/68 is the possibility of incorporating linkers with active groups into the framework without affecting its stability and crystallinity. This can be done both during *de novo* synthesis,[124,126,127] as well as via solvent-assisted linker exchange (SALE).[105,126,128] In the later, individual linkers in the framework are replaced by modified linkers provided in excess in the solvent. For UiO-66, such an exchange has been shown for unmodified linker (1,4-benzenedicarboxylate, BDC) and linkers bearing amino (2-amino-1,4-benzenedicarboxylate) or bromium (2-bromo-1,4-benzenedicarboxylate) groups.[128] For all combinations of these linkers, significant exchange efficiencies (≈40-80%) between the MOF scaffold and the solvent have been shown, with the substitution degree being affected by a variety of parameters like donor ability, sterics, and solubility.
The big advantage of SALE is that it opens up a large number of new functionalized MOFs. In a *de novo* synthesis route, the introduction of substituents to the linker often interferes with the MOF formation. This requires the optimization of the synthesis conditions for each new group or, in the worst case, prohibits framework formation completely. For linker exchange, on the other hand, lower temperatures and gentler environments can be used. This means that the conditions are not so harsh as to alter the structure of MOFs, but they are sufficient to achieve linker incorporation.
In previous studies, mostly relatively small substituents were used both for *de novo* synthesis and SALE. However, many applications might require larger and more complex functionalities. Furthermore, only the degree of exchange was analyzed, but not the mechanisms and kinetics defining this process or the spatial distribution of the exchanged linkers. Especially the last aspect is of high importance, as the position of different groups relative to each other strongly affects their performance.
In this project, we studied the incorporation of FITC and rhodamine B isothiocyanate (RITC) modified linkers into UiO-67 via direct synthesis and via linker exchange and compared the effect of the dyes on the MOF in these two processes. UiO-67 was chosen due to its larger pores and windows to allow room for the large fluorophores. The dyes, on the other hand, are representatives for large, complex substituents. At the same time, they can function as a readout for their distribution in the MOF.
Additionally, two different methods (denoted as method 1 and method 2) of synthesizing UiO-67 were used, showing different features that were advantageous

or problematic for investigating the various aspects. The main difference in the synthesis conditions between the two protocols is that for method 1 equal stoichiometric amounts of the zirconium salt and the organic linker are used, while in method 2 the linker is added in excess. The second important difference is the amount and type of acid used (hydrochloric acid for method 1 and glacial acidic acid for method 2). The solvent (dimethylformamide), reaction temperature (90 °C) and incubation time (24 h) were identical for both methods.
Method 1 results in small particles that have rounded edges and form stable aggregates (Figure 5.10 A and B).[129] This protocol was mainly used for *de novo* functionalization, as it shows a high yield in MOF formation, which results in lower material consumption and thus allowed us to use higher concentrations of dye modified linkers. The second synthesis protocol (denoted here as method 2), on the other hand, leads to larger crystals with sharp edges (Figure 5.10 C and D).[130] This made it possible to resolve individual particles with the fluorescence microscope and thus to study the spatial distribution of the dyes in the crystals. This was especially important for linker exchange studies.
For the purpose of brevity, the two functionalization methods will be abbreviated with DN and LE for *de novo* and linker exchange, respectively, while the synthesis methods will be denoted by M1 and M2.

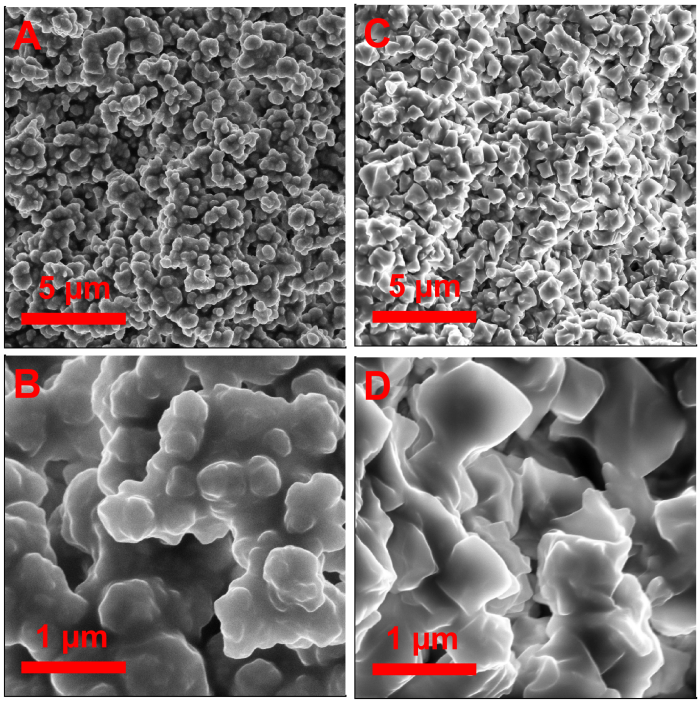

Figure 5.10: SEM images of UiO-67 synthesized with method 1 (A and B) and method 2 (C and D).

5.2.1 *De Novo* Functinalization with Fluorescein and Rhodamine B

To investigate the incorporation of the fluorophore modified linkers during MOF formation, samples were synthesized from reaction mixtures containing different percentages of dye-bound linker, ranging from 0.1% to 2% for both fluorescein and rhodamine B. Hereby, synthesis method 1 (see chapter 5.3.2) was used, as this allowed us to use higher concentrations of dye labeled linkers. Additionally, method 2 was used for a sample with 0.1% FITC to be able to compare the two synthesis procedures.
Due to their size or solubility, the fluorophore modified linkers have a decreased probability of incorporation. The actual dye content was determined via fluorescence of UiO-67 dissolved in a fluoride solution. The incorporation efficiency for FITC was 17-27% for M1 and 54% for M2. This implies an almost twofold better dye insertion when using method 2. For RITC, the incorporation percentage was significantly lower at only 2-4% (Table 5.3). As this trend is systematic, the lower yield of rhodamine B is most likely due to the chemical differences of the two dyes, including their steric, electrostatic and hydrophobic/hydrophilic properties.

Table 5.2: Fraction of dye modified linkers incorporated into the FITC and the RITC modified UiO-67 samples.

FITC Samples (Method 1)

set [ppm]	1,000	3,000	7,000	20,000
measured [ppm]	256	808	1624	3,511

FITC Samples (Method 2)

set [ppm]	1,000
measured [ppm]	542

RITC Samples (Method 1)

set [ppm]	1,000	3,000	7,000	20,000
measured [ppm]	38	89	220	410

Fluorescence imaging of the DN-M1 samples revealed that the MOFs consisted of aggregates of sub-micrometer sized particles of fairly homogeneous brightness (Figures 5.11 and 5.12). For low percentages of incorporated dye, the fluorescence signal increased with the dye content. At high concentrations, however, the brightness stagnated or even decreased.
Besides the fluorescence intensity, also the fluorescence lifetime of the MOFs was analyzed using the phasor approach. For both fluorophores, the average lifetime decreased with rising dye concentration. This quenching effect is slightly stronger

for fluorescein, probably due to the higher incorporation efficiency. Although pure UiO-67 exhibits significant autofluorescence (see Appendix C), the brightness is 100–1000 times lower than in samples modified with fluorophores. Therefore, the influence of autofluorescence on the lifetime measurements can be neglected.
The increased quenching is in good agreement with the observations of the particle brightness. For low amounts of the dyes, the rising fluorophore concentration outweighs the reduction in quantum yield, so that the particles appear brighter. For higher dye densities, on the other hand, the quenching increases faster than the fluorophore number, decreasing the total signal.

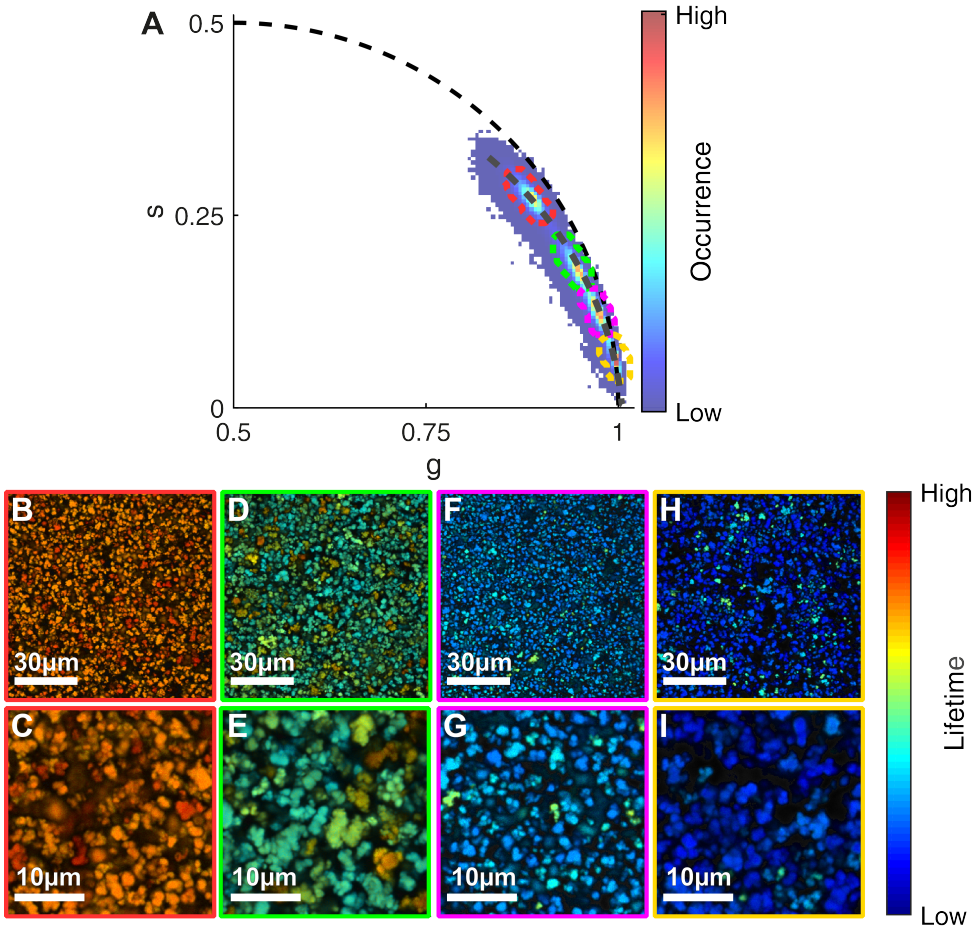

Figure 5.11: Phasor FLIM histogram and images of UiO-67 samples with FITC labeled linker. The phasor positions of the different concentrations are indicated by an ellipsoid (0.1% red, 0.3% green, 0.7% magenta and 2% yellow). The color of the images corresponds to the pixel position on the light gray dotted curve in the phasor plot (A). Hereby, long lifetimes are positioned on the top left and correspond to a red and orange hue, while short lifetimes lie at the bottom right and are color coded with blue and cyan. Intermediate values in the center are displayed in green and yellow. The images show samples synthesized from reactants containing 0.1% (B and C), 0.3% (D and E), 0.7% (F and G) and 2% (H and I) of labeled linker.

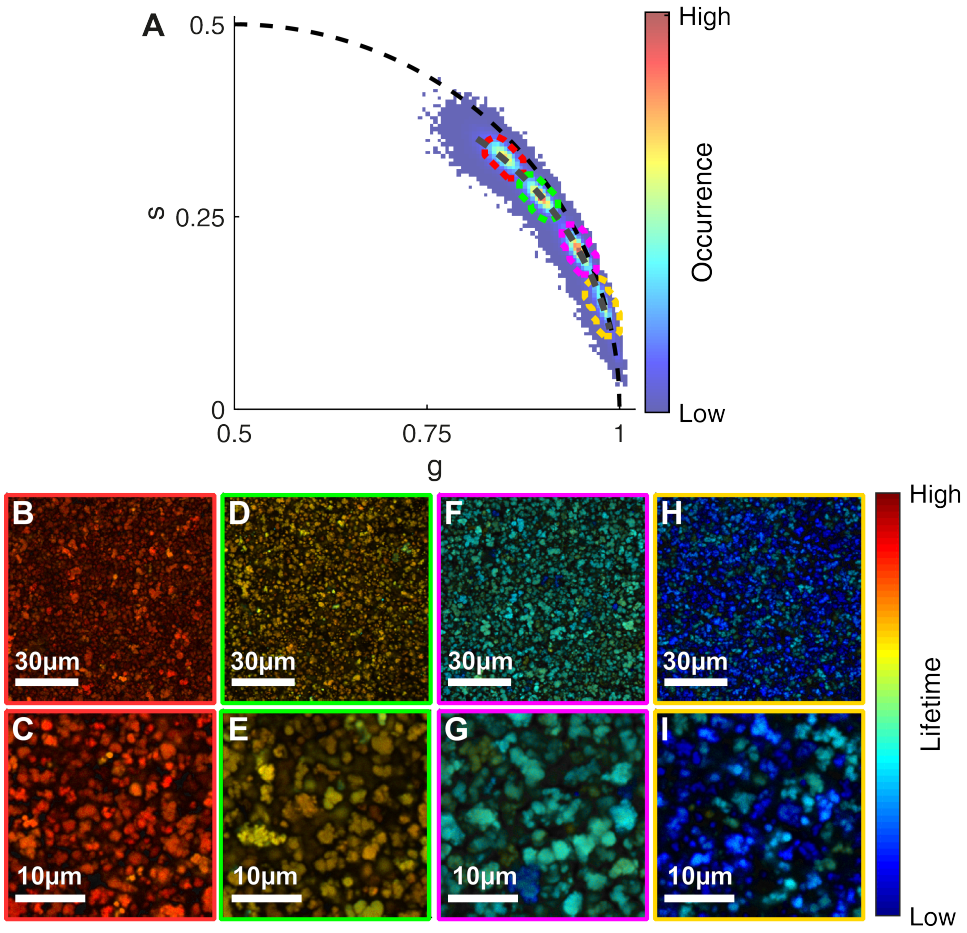

Figure 5.12: Phasor FLIM histogram and images of UiO-67 samples with RITC labeled linker. The phasor position of the different concentrations are indicated by an ellipsoid (0.1% red, 0.3% green, 0.7% magenta and 2% yellow). The color of the images corresponds to the pixel position on the light gray dotted curve in the phasor plot (A). Hereby, long lifetimes are positioned on the top left and correspond to a red and orange hue, while short lifetimes lie at the bottom right and are color coded with blue and cyan. Intermediate values in the center are displayed in green and yellow. The images show samples synthesized from reactants containing 0.1% (B and C), 0.3% (D and E), 0.7% (F and G) and 2% (H and I) of labeled linker.

The fluorescence decay for both fluorophores in UiO-67 is multi-exponential, as the phasor positions of all samples lie within the universal circle. Furthermore, the quenching follows a curved trajectory, meaning that the lifetime components change between different samples. The most likely explanation is that each fluorophore is quenched to a slightly different degree, resulting in a distribution of lifetimes and a multi-exponential decay. With increasing dye content, the average quenching increases, shifting this distribution to lower lifetimes.
There are two possible causes for the increase of quenching with the dye concentration, direct dye-dye interactions via self-quenching of the fluorophores, and dye induced changes in the structure of the crystals. Self-quenching only occurs at

very close distances that depend on the exact type of quenching. For mechanisms involving π-stacking or electron transfer the dyes practically have to be in direct contact with each other, and even for long range self-quenching, observed for homoFRET, inter dye distances less then 40–50 Å are needed. The later has been shown to be an important self-quenching process for fluorescein and related dyes. However, homoFRET on its own does not result in quenching, as the energy is merely transfered between molecules with identical photophysical properties. A decrease in fluorescence intensity and lifetime is only observed when non-radiative traps acting as energy sinks (e.g. dyes quenched in other ways) are present in the population. Therefore, effective quenching will only happen at significantly higher dye concentrations then measured in the samples.
The more likely explanation is that the fluorophores interfere with the formation of the MOFs and introduce defects into the crystals. These defects, in turn, quench the dyes, reducing the observed lifetime. Since these disruptions in the structure can induce new cracks and flaws, they will propagate and an effect is visible even at low fluorophore densities. Depending on the extent of a defect or a fluorophores distance to it, the degree of quenching varies. Therefore, a distribution of lifetimes is observed that shifts with the dye concentration, consistent with a curved trajectory.

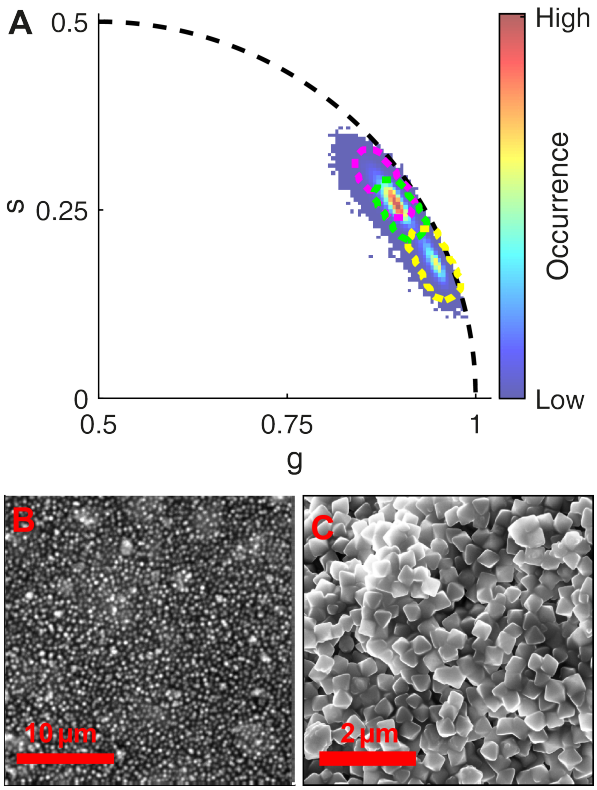

Figure 5.13: Effect of the different synthesis methods for UiO-67 on the FITC lifetime. A) Phasor histogram for a 0.1% FITC DN-M2 sample (green ellipsoid), and two DN-M1 samples with 0.1% (magenta ellipsoid) and 0.3% (yellow ellipsoid) FITC, respectively. B) Fluorescence intensity image of DN-M2. C) SEM image for DN-M2.

In order to investigate the influence of the synthesis method on the fluorophore, the DN-M2 sample was analyzed in the same way (Figure 5.13). Here, the lifetime lies between those measured for DN-M1 samples synthesized from 0.1% and 0.3% FITC solutions. This phasor position corresponds well to the actual FITC content incorporated into the MOF (Table 5.2), suggesting that, for *de novo* functionalization, the fraction of modified linkers incorporated plays a bigger role than the synthesis method.
SEM images of the different samples were recorded to determine whether increased incorporation of functionalized linkers has an effect on the morphology of the MOF. As can be seen in Figure 5.14, the shape and surface structure of the DN-M1 particles did not change noticeably between the unfunctionalized sample dyes and those containing dyes. This is not surprising as even the highest concentration of fluorophore was less than 4‰. This low functionalization is high enough to result in local changes and defects, but not to effect large scale changes. The crystal shape of the DN-M2 sample (Figure 5.13 C) also corresponds well to the one observed for the unmodified method 2 UiO-67 (Figure 5.10 C and D). Although the individual crystals are smaller that in the pure MOF, this difference is probably due to fluctuations in the synthesis conditions rather than due to the dye, as such variations were also observed for different batches of unmodified UiO-67.

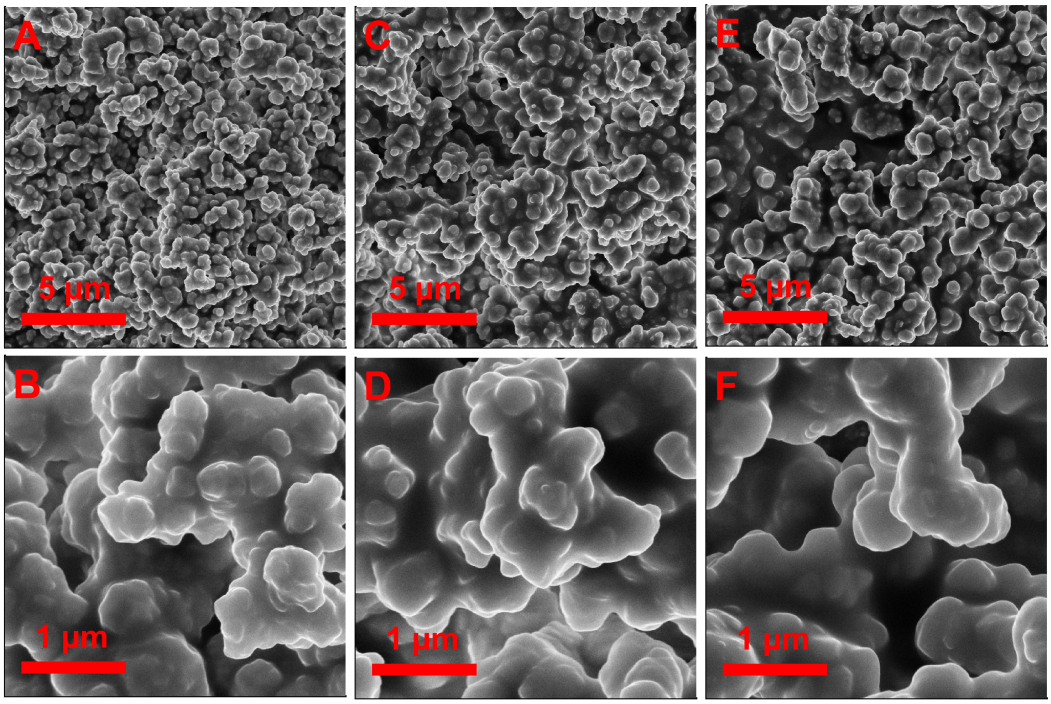

Figure 5.14: SEM images of UiO-67 synthesized with method 1 with 0% (A and B), 0.1% (C and D) and 2% (E and F) FITC modified linker.

5.2.2 Multivariate Functionality Distribution in UiO-67

For studying how different functionalities interfere with each other and how they are distributed within the MOF, UiO-67 samples were synthesized from linkers bearing both FITC and RITC. Synthesis method 1 was used for the same reasons as for the single dye labeled samples. Two different aspects were analyzed, the distribution and colocalization of the two dyes, and possible FRET between fluorescein as donor and rhodamine B as acceptor.
In all samples, the amount of FITC was kept constant at 0.1% while RITC varied between 0.01% and 1%. As with the single dye MOFs, the actual percentage of incorporated dye-linkers was lower than the set value. For FITC, the incorporation efficiency was around 21-27%, while RITC again showed lower values with 4-7%.

Table 5.3: Fraction of dye modified linkers incorporated into two color UiO-67 samples.

set **RITC** \ **FITC** [ppm]	100 \ 1,000	300 \ 1,000	1,000 \1,000
measured **RITC** **FITC** [ppm]	7 \ 212	21 \ 264	64 \ 238
set **RITC** \ **FITC** [ppm]	3,000 \ 1,000	10,000 \ 1,000	
measured **RITC** \ **FITC** [ppm]	134 \ 212	529 \ 212	

The fluorescence lifetime of FITC is strongly affected by the concentration of RITC in the MOF (blue curve in Figure 5.15 L). At the same time, the red signal after 475 nm excitation increases (red curve in Figure 5.15 L). A correlation of these two parameters is not only noticeable from the average values, but it is also apparent in the individual images, where particles with exceptionally high red signal coincide with lower FITC count rate and lifetime (Figure 5.15 B-K).
Almost all pixels and particles show significant intensity in both channels, indicating a very high colocalization between FITC and RITC. This colocalization shows that both dyes must be present within the point-spread function (ca. 200–300 nm).
Just as in the single color samples, the concentration for both FITC and RITC fluctuates between different particles, but is homogeneous within a single aggregate (see Figure 5.15 F and G). The decrease in green fluorescence signal with increasing rhodamine B concentrations indicates a competition of the two dyes for incorporation into the MOF. However, particles with high RITC content also show strong quenching. It is therefore likely that the lower green fluorescence signal is caused by increased quenching rather than by displacement by RITC, especially since no significant decrease in FITC concentration is observed in the bulk measurements (see Table 5.3).

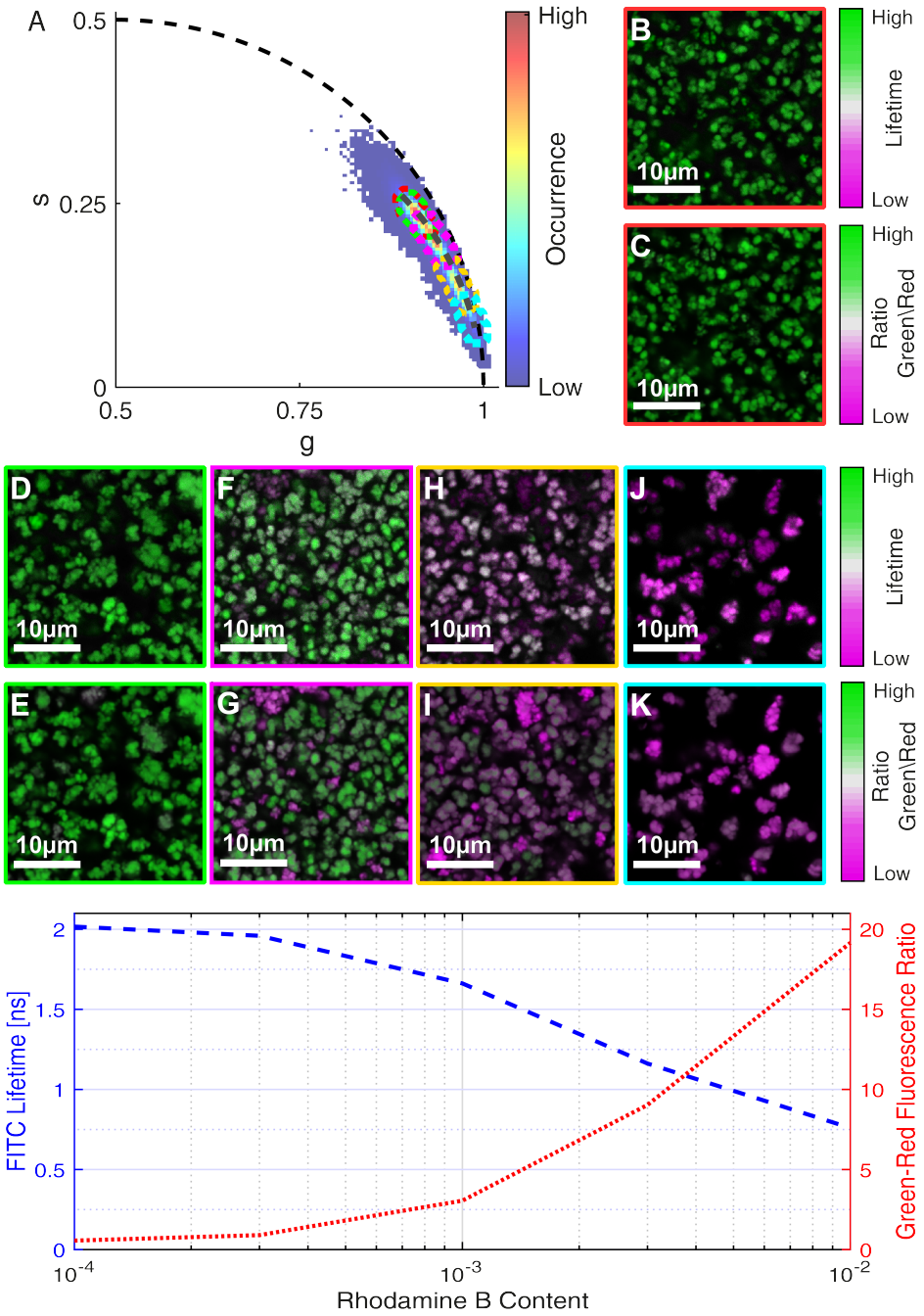

Figure 5.15: UiO-67 samples with both FITC and RITC labeled linkers. The FITC content was 0.1%, with 0.01% (B and C, red ellipsoid in A), 0.03% (D and E, green ellipsoid in A), 0.1% (F and G, magenta ellipsoid in A), 0.3% (H and I, yellow ellipsoid in A) and 1% (J and K, cyan ellipsoid in A) of RITC. The color of the lifetime images in the upper rows (B, D, F, H and J) corresponds to the pixel position on the light gray dotted curve in the phasor plot (A), with green representing long and magenta short lifetimes. The lower images (C, E, G, I and K) display the intensity ratio between the red and the green channels after excitation with a 475 nm laser. To optimize the contrast, the green signal was increased by a factor of 5 compared to the red channel. The average lifetime (blue dashed line) and ratio (red dotted line) are shown in panel L.

Both a decrease in lifetime as well as a rise in red signal are indications of FRET. However, a careful analysis revealed that, in this case, the observed changes are not caused by FRET. Three different processed lead to an acceptor signal after donor excitation. The first two are spectral crosstalk from the donor and direct excitation of the acceptor. Both of them result in an observed lifetime equal to the corresponding dye. The third process is FRET and the resulting fluorescence lifetime is a convolution of the donor and acceptor decays, thus longer than either one. For the UiO-67 samples labeled with both FITC and RITC, the fluorescence lifetime in the red channel after blue (475 nm) or yellow excitation (565 nm) are identical (Figure 5.16). This suggests, that the acceptor signal is caused solely by direct excitation and no significant FRET contribution is present.

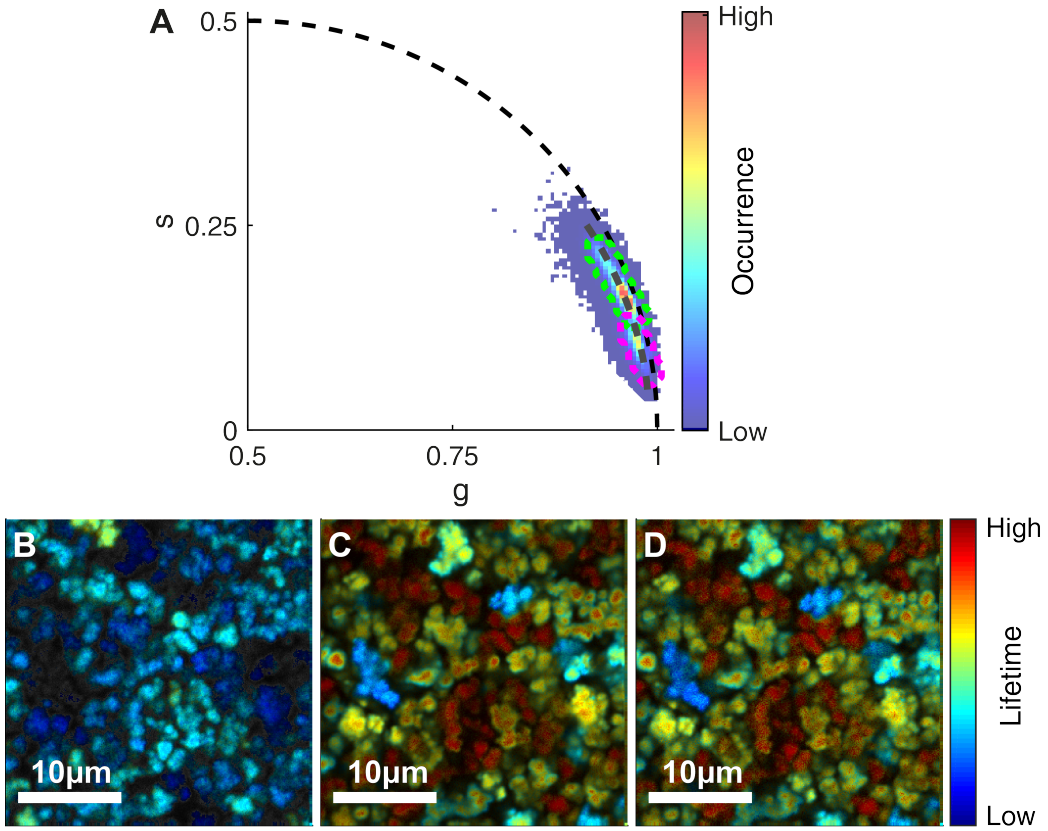

Figure 5.16: Phasor FLIM histogram and images of UiO-67 samples with 0.1% FITC and 1% RITC labeled linkers. A) Phasor plot of the lifetime decay in the green FITC (green dotted ellipsoid) and the red RITC channel, both for 475 nm and 565 nm excitation. The color of the images corresponds to the pixel position on the light gray dotted curve in the phasor plot (A). Hereby, long lifetimes are positioned on the top left and correspond to a red and orange hue, while short lifetimes lie at the bottom right and are color coded with blue and cyan. Intermediate values in the center are displayed in green and yellow. The images show the green FITC signal (B), as well as the red signal after blue excitation (C) and after yellow excitation (D).

These results are further substantiated by the low acceptor concentration. Although FRET extends over much longer distances (up to 100 Å) than self-quenching, this is still not enough to result in significant energy transfer in the measured samples. Considering the 24 linkers per unit cell of UiO-67 ($a = 26.783$ Å), a 100 Å large sphere therefore contains 654 possible dye positions. Even for the highest rhodamine B concentration (529 ppm) this results in an average of only about 0.3-0.4 acceptors per sphere, too few to cause a significant FRET signal. These assumptions are only valid for a completely random distribution of dyes within the MOF crystals. If the fluorophores showed strong clustering (e.g. at the surface), the average distance to the nearest neighbor would decrease and result in a measurable FRET signal. Since this is not the case, it can be concluded that the dyes are distributed homogeneously throughout the crystals.
The absence of FRET supports the assumptions that fluorescence quenching is caused by defects in the MOF structure and not by direct dye-dye interactions. While no energy transfer is observed, both dyes can still introduce defects to the MOF framework resulting in an indirect quenching of FITC by RITC.

5.2.3 Linker Exchange Mechanisms of UiO-67

Instead of incorporating dye modified linkers into the MOF during synthesis, it is also possible to add the functionalization after the formation of the scaffold is complete using linker exchange. As the name suggests, individual linkers within the MOF are exchanged with those added in excess to the solvent. By using modified linkers, a dye can be incorporated into a previously unmodified MOF. Studies have shown that linker exchange in possible for zirconium MOFs, but the mechanism and spatial distribution within the framework are still unknown. To investigate these aspects, unfunctionalized UiO-67 was synthesized and subsequently subjected to a linker exchange with FITC modified biphenyl-4,4'-dicarboxylate (see chapter 5.3.2). In order to be able to study the spatial distribution of the dye in the MOF, homogeneous and regular crystals that are significantly larger than the resolution limit are needed. To achieve this, synthesis method 2 (chapter 5.3.2) was employed. This procedure results in MOF crystals with a size of around one micrometer and sharp edges. The low yield of the method was not a big issue in this case, since only unmodified linker was used. Starting from a batch of unfunctionalized UiO-67, samples were subjected to linker exchange at different temperatures (25–100 °C) for varying amounts of time (1 h to 7 d).
As is shown in Figures 5.17 B and 5.18 A, already after one hour at room temperature, a significant amount of FITC modified linker was incorporated into the MOF. The edges of all crystals are significantly brighter than the interior, indicating that the initial exchange or binding happens primarily on the outside of the MOFs. Since the resolution of the fluorescence microscope is limited to around 200 nm, it is impossible to determine the exact depth the dye penetrated into the crystals. However, the sharpness of the bright zones suggests that the binding is limited to a very narrow region, probably just the very surface and the first few nanometers.

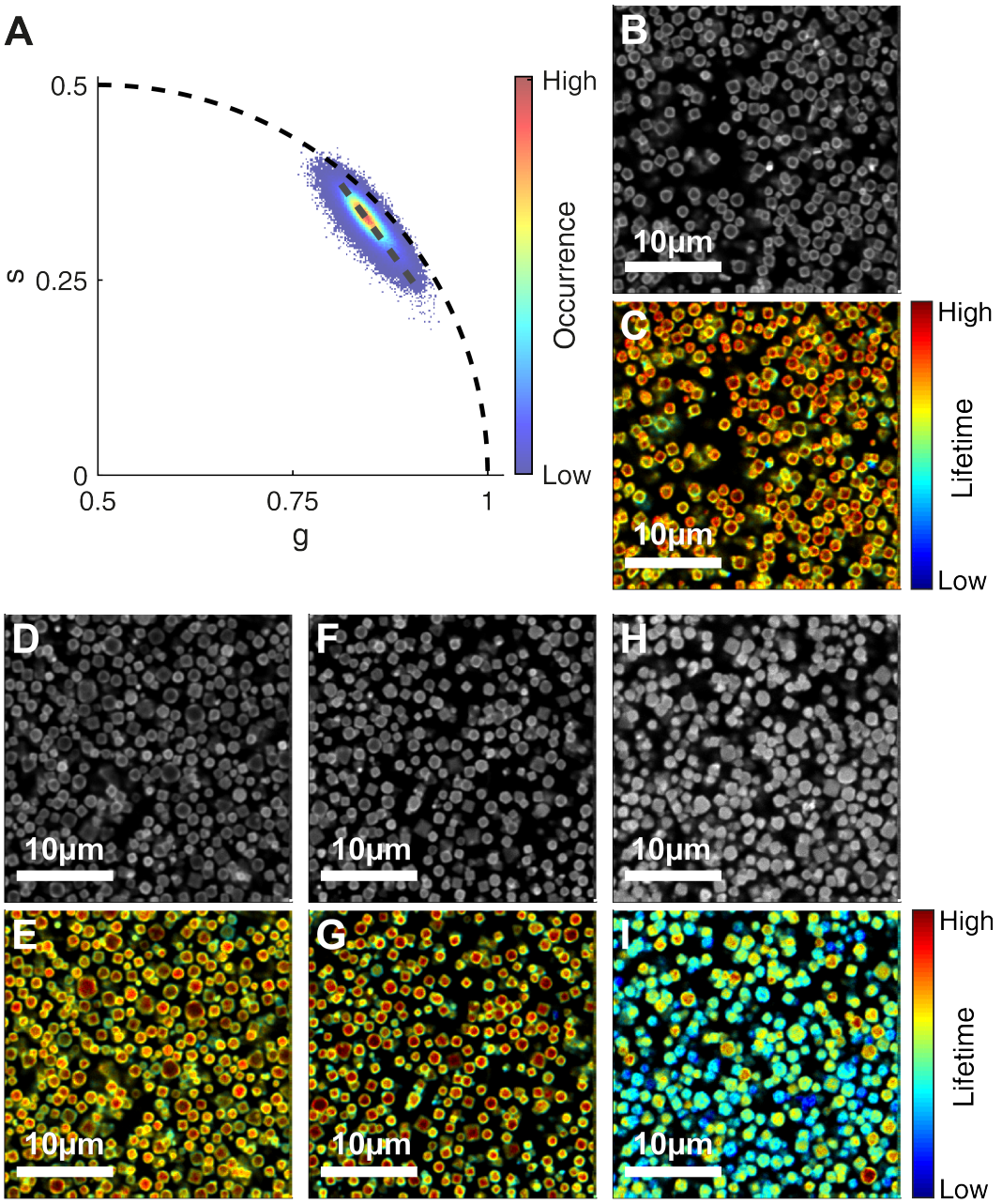

Figure 5.17: FLIM of UiO-67 (Method 2) after linker exchange with FITC modified biphenyl-4,4'-dicarboxylate for 1 h at 25 °C (B and C), 1 d at 65 °C (D and E), 1 d at 100 °C (F and G) and 7 d at 100 °C (H and I). A) Phasor histogram of the four samples. The grayscale images (B, D, F and H) show the fluorescence intensity images for the different samples. The false color images (C, E, G and I) show the fluorescence lifetime of the individual pixels. The color of the FLIM images corresponds hereby to the pixel position on the light gray dotted line in the phasor plot (A). Long lifetimes are positioned on the top left and correspond to a red and orange hue, while short lifetimes lie at the bottom right and are color coded with blue and cyan. Intermediate values in the center are displayed in green and yellow. A running mean of 3×3 pixel was used to smooth the phasor data.

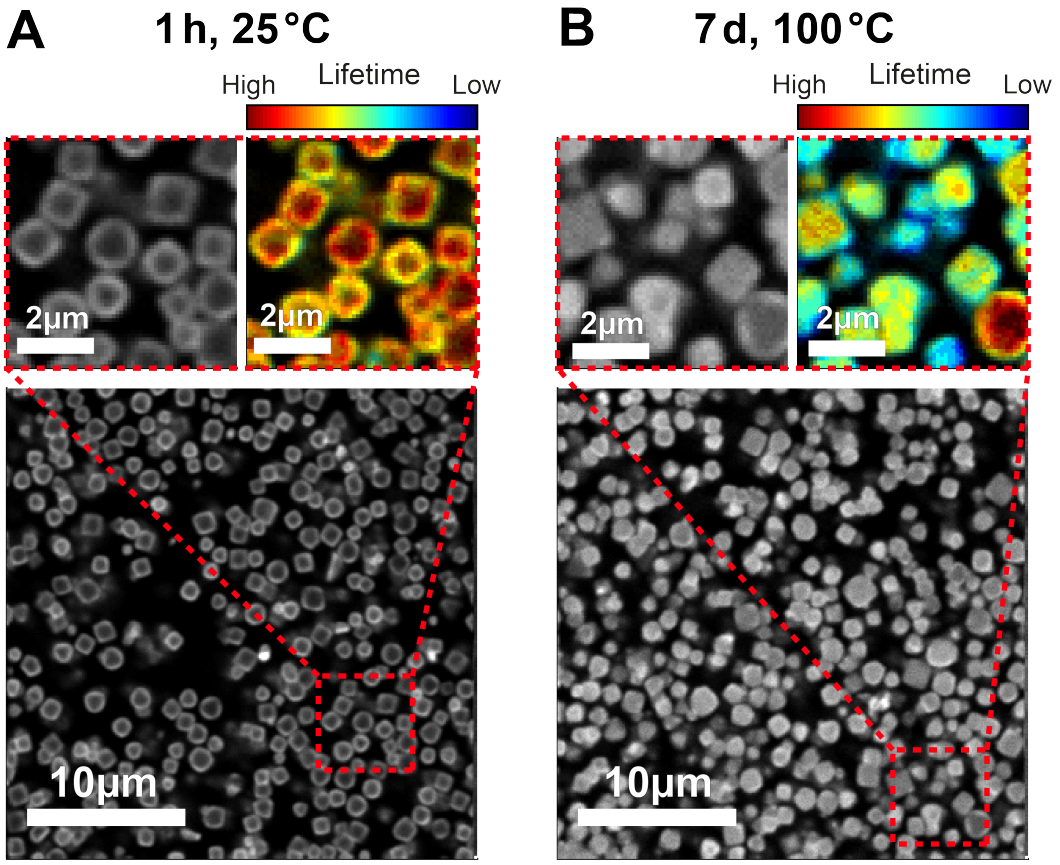

Figure 5.18: Fluorescence intensity and lifetime images of UiO-67 (Method 2) after linker exchange with FITC modified biphenyl-4,4'-dicarboxylate for 1 h at 25 °C (A) and 7 d at 100 °C (B). The upper images show higher magnification intensity (left) and lifetime (right) images of the region indicated by the red boxes.

In the fluorescence images, the center of a crystal is not completely dark. One possible source of these photons is out-of-focus light. Due to the lower axial resolution of a confocal microscope (≈1 µm), light from the surfaces slightly above and below the focal plan is also recorded, resulting in residual brightness inside the MOF crystals. However, phasor analysis showed that the fluorescence lifetime at the center is slightly, but noticeably longer than at the surface (Figure 5.17 C). Since out-of-focus light does not change the lifetime, it means that there is an additional population of fluorophores. The dyes that have permeated deep enough into the crystals are not affected by the surface, thus exhibiting a different lifetime. This further substantiates the theory that initial binding happens at the very crystal surface. Since the fluorescence lifetime only senses the immediate surroundings, solely dyes that are bound at or close to the surface are affected by it.
Increasing the duration and temperature of the linker exchange reduced the difference in fluorescence intensity between the center and the surface (Figure 5.17 B, D, F and H, and Figure 5.18). After 7 d at 100 °C, the linker exchange has progressed so far that the fluorescence intensity is mostly homogeneous throughout the

MOF's cross section (Figure 5.18 B). Moreover, the uniformity in the fluorescence intensity also correlates well with the spatial homogeneity in the observed lifetime. Particles still showing a pronounced border (bottom left particle in the zoom-in of Figure 5.18 B) have a long lifetime at the center and a faster fluorescence decay at the edges. Crystals exhibiting a more uniform fluorescence, on the other hand, also show a homogeneous lifetime distribution.
This two different binding kinetics - a fast binding at the surface and the slower homogeneous intensity increase - suggest two independent mechanisms. Hereby, the slow, spatially homogeneous binding corresponds well to the linker exchange described previously, especially in the required reaction time and temperatures. Additionally, the high exchange yields reported for this mechanism imply a homogeneous substitution throughout the crystal and not just close to the surface, consistent with out results. The fact that the intensity increases uniformly in space shows that movement of the dye modified linkers is not the rate limiting step, but rather that the actual substitution of the original linker determines the reaction velocity.
The second mechanism, however, was previously not observed. The very fast binding in less than an hour even at 25 °C suggests a low activation energy for the reaction. This makes it very unlikely that a real linker exchange is involved. The later involves an initial dissociation of the original linker, a process requiring a substantial amount of energy. It is far more likely that the organic linker binds to the MOF in an unspecific manner, or that it reacts with weakly or uncoordinated metal sites on the surface.
For both mechanisms, the linker binds very tightly, as extensive washing (see chapter 5.3.2) did not remove the dye. Even after treatment with the lewis base pyridine, a significant amount of dye remains bound to the outer MOF surface (Table 5.4, Figure 5.19).
The amount of incorporated dye increased within the first day of exchange, but no significant changes were observed for longer incubation times and higher temperatures (Table 5.4). This trend suggests that an equilibrium is reached very quickly, were the total dye content stays constant over time, but is redistributed within the crystals.

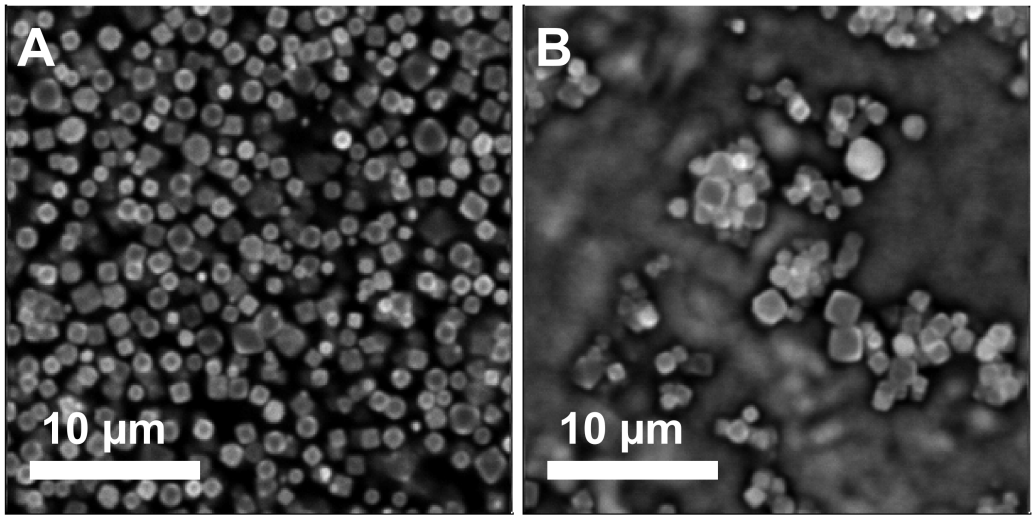

Figure 5.19: Fluorescence intensity image of UiO-67 after linker exchange with FITC modified biphenyl-4,4'-dicarboxylate for 1 d at 65 °C before (A) and after (B) treatment with pyridine. The blurry regions in (B) were caused by particles that were not settled and moved during the acquisition

Table 5.4: Fraction of FITC modified linkers incorporated via linker exchange into UiO-67 samples.

Linker exchange (Method 2)

exchange conditions	1 h, 25 °C	1 h, 65 °C	1 d, 65 °C	7 d, 65 °C
FITC content [ppm]	549	425	,1670	1,963

exchange conditions	1 d, 100 °C	7 d, 100 °C	1 d, 65 °C, pyridine treated
FITC content [ppm]	1,274	1,510	618

Linker exchange (Method 1)

exchange conditions	1 h, 65 °C	6 h, 65 °C	24 h, 65 °C
FITC content [ppm]	8,188	7,212	9,561

SEM Analysis shows no adverse effect on the regularity of the crystals by the treatment (Figure 5.20). The octahedral shape seems to actually improve and become more regular with increasing temperature and duration of the exchange. Since all samples originate from separate synthesis batches, the most obvious explanation for this behavior are slight variations in the synthesis conditions, which then resulted in the differences in crystal qualities.

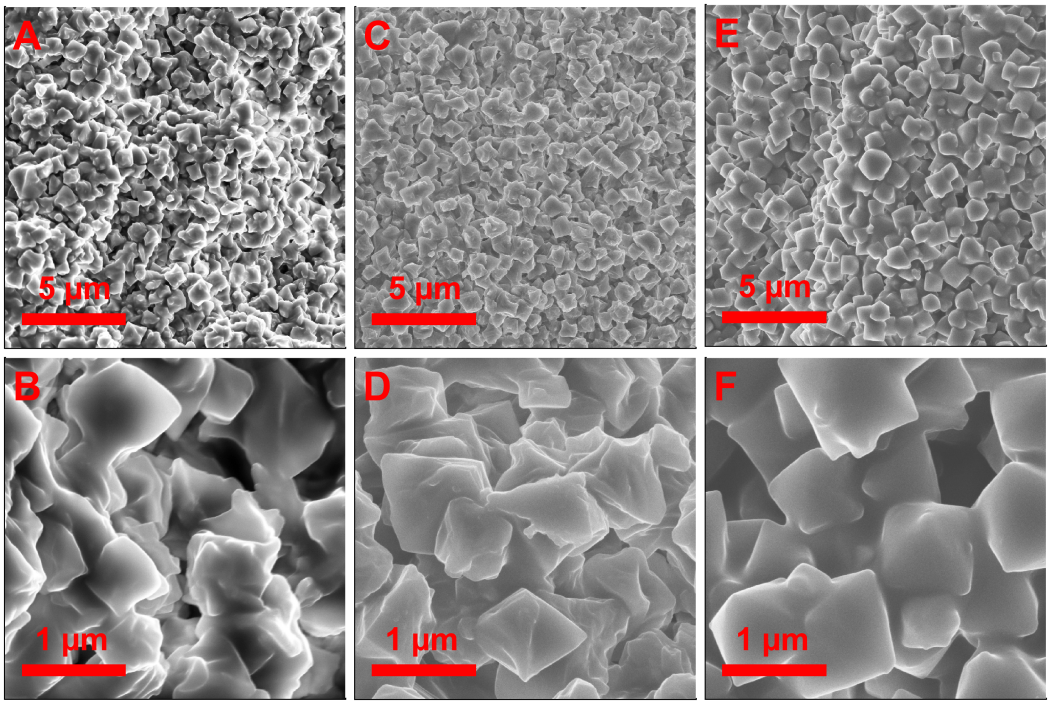

Figure 5.20: SEM images of UiO-67 synthesized with method 2 without linker exchange (A and B), as well as after linker exchange with FITC modified linker for 1 h at room temperature (C and D) and for 7 d at 100 °C(E and F).

When performing linker exchange with M1 samples, a similar behavior was observed. In the fluorescence intensity images, ringlike structures are visible, showing again that the initial binding happens primarily on the external surface, even though this heterogeneity is not as obvious as for method 2 due to the crystal size and morphology. But unlike in LE-M2, the fluorescence lifetime decreased significantly with the duration of the linker exchange (Figure 5.21 A, C, E and G), even though the dye incorporation stayed constant (Table 5.4). This implies that prolonged exposure to dye modified linkers at higher temperatures has an adverse effect on the MOFs' structure and increases defect formation. However, considering the high dye incorporation (Table5.4), quenching is much lower then in DN-M1 samples with comparable dye concentrations (Figure 5.10). Thus, while linker exchange influences the MOF scaffold, it affects it to a much lesser degree than *de novo* synthesis.

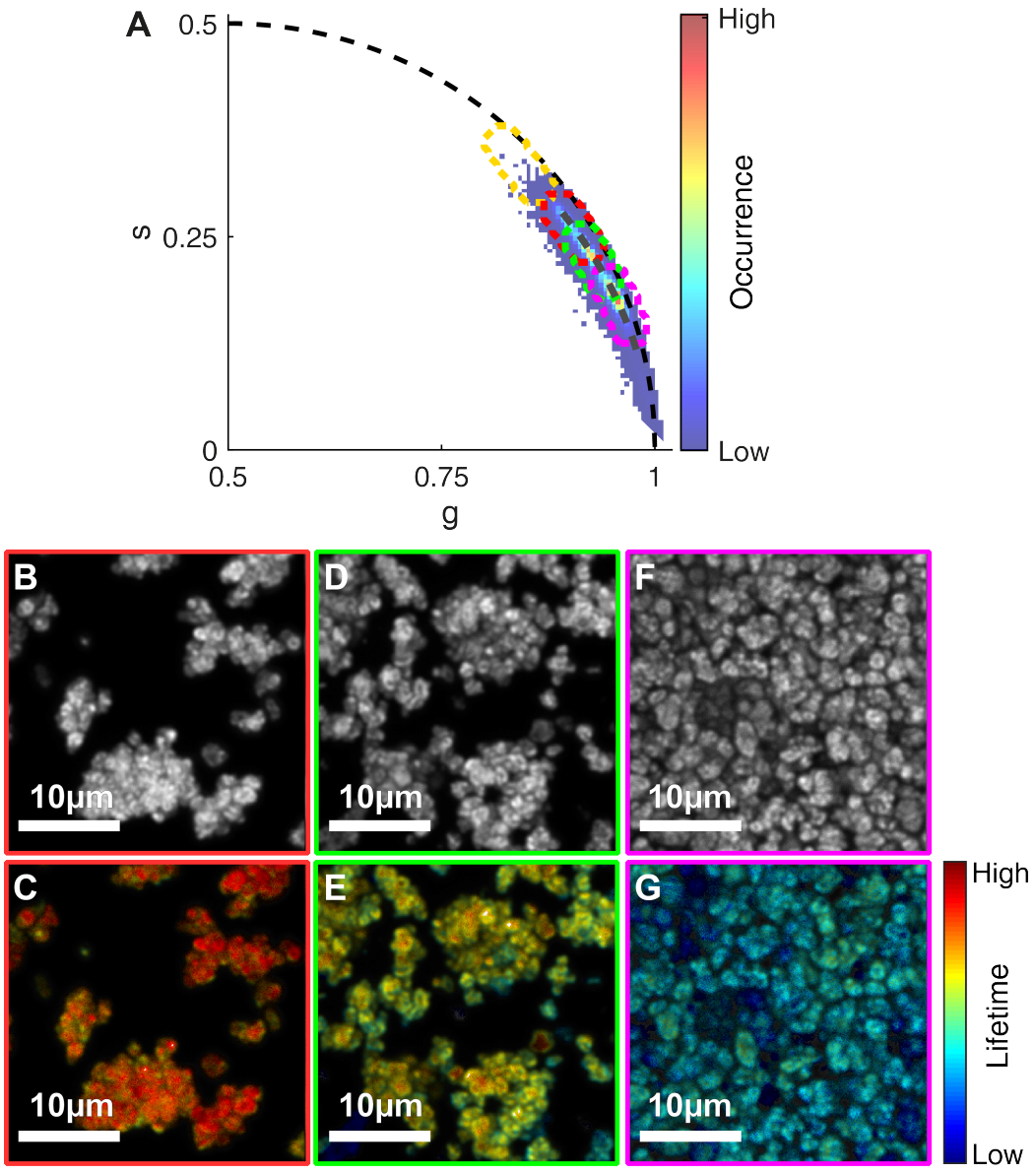

Figure 5.21: FLIM of UiO-67 samples (Method 1) after linker exchange with FITC modified biphenyl-4,4'-dicarboxylate for 1 h (B and C), 6 h (D and E) and 24 h (F and G) at 65 °C. A) Phasor histogram of the three samples. The dotted ellipsoids indicate the different incubation times of 1 h (red), 6 h (green) and 24 h (magenta). The yellow ellipsoid shows the phasor position of the linker exchange samples synthesized with method 2. The grayscale images (B, D and F) show the fluorescence intensity images for the different samples. The false color images (C, E and G) show the fluorescence lifetime of the individual pixels. The color of the FLIM images corresponds hereby to the pixel position on the light gray dotted line in the phasor plot (A). Long lifetimes are positioned on the top left and correspond to a red and orange hue, while short lifetimes lie at the bottom right and are color coded with blue and cyan. Intermediate values in the center are displayed in green and yellow.

5.2.4 Discussion and Conclusion

Our results clearly show that both *de novo* as well as solvent assisted linker exchange functionalization can be used to integrate fluorescent dyes, or similarly big and complex functional groups, into the scaffold of UiO-67. However, since the dyes are of a similar size (≈14–16 Å) as the pores, their incorporation shows a much reduced efficiency. During *de novo* functionalization of method 1 MOFs, the maximal yield was 27% for FITC and 7% for RITC. The fourfold lower efficiency of rhodamine B is caused by the side groups of the fluorophore (Figure 5.24), showing how critical the size and chemical properties of the functionalization are for efficient integration into the framework. Moreover, even the dyes that were integrated into the structure affected the MOF scaffold by introducing defects into the structure. An increase of the fluorophore content strongly enhanced quenching. While self-quenching is a possible source of the observed lifetime decrease, the low concentrations and high distances between fluorophores make it highly unlikely. The other, more probable explanation is an interaction between the dye and the MOF. Adding a dye modified linker into the framework creates a steric hindrance around it, so that crystal growth is disturbed at that position. This results in defects in the structure that can propagate and, in turn, quench nearby fluorophores.
By adding two different fluorophores at the same time, we could further show that they colocalize on the scale of the PSF (≈ 200 nm). Moreover, the absence of FRET suggests that no clustering of dyes occurs, but rather that they are randomly distributed throughout the crystals.
The dye induced disruption of the MOF structure is much weaker for functionalization via linker exchange. For MOFs synthesized with method 2, the fluorescence lifetime was significantly longer than in *de novo* functionalized samples with a similar dye concentration and it was not affected by the exchange procedure. Method 1 MOFs, on the other hand, showed an increase in FITC quenching with the linker exchange reaction duration. Therefore, the larger and more regular crystals obtained by method 2 seem to be more stable and resilient to the effects of the dye modified linkers on the structure than the irregular particles of method 1 MOFs. However, quenching was still much lower than with *de novo* dye modified samples, showing that, in this case, linker exchange is the gentler approach for MOF functionalization.
Additionally, spatially resolved analysis revealed two different mechanisms that happen during linker exchange (Figure 5.22). Initially, dye modified linkers bind primarily to the crystals' exterior. The spatial distribution, speed of the reaction and the strength of the adsorption point towards a binding to under-coordinated metal sites, predominantly found on the outer crystal surface. This is substantiated by the higher exchange efficiency of method 1, where the smaller and more irregular particles exhibit a higher relative surface area and more defects in the structure, thus allowing more dyes to bind.
The second mechanism is the actual linker exchange. Since this exchange happens homogeneously throughout the whole crystal, the movement must be significantly faster than the actual binding of the dye modified linker. This fact is quite surpris-

ing, as the dyes are larger (minimal diameter of 14 Å for FITC and 16 Å for the RITC modified linkers) than the window size of UiO67 (8 Å) and should therefore not be able to simply diffuse through the scaffold. However, one should not assume MOFs to be a completely static and rigid structure. The high porosity and the long organic linkers allow for quite a lot of flexibility. The fact that linker exchange can happen at all shows that individual bonds between the inorganic clusters and the organic linker can open even though the structure as a whole is remarkably stable. At the high temperatures used for the exchange procedure, transient one-sided detachment of the linkers might occur, opening up the windows and allowing the dyes to move through the MOF. Exchange, on the other hand, requires the original linker to detach completely, a process that is less likely and therefore also slower. All experiments presented here were performed on samples that were extensively washed to remove excess dye, so that no direct observations about diffusion in the scaffold were made. Therefore, a logical future experiment is to add fluorophore solution to the MOFs and directly observe with the microscope how and under what conditions diffusion happens in UiO-67.

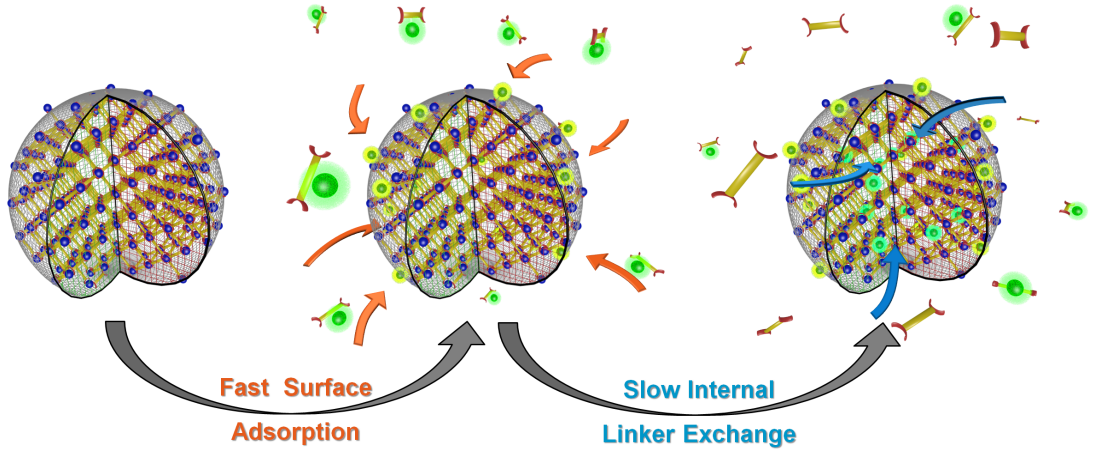

Figure 5.22: Illustration of the two linker exchange mechanisms in UiO-67 with a fast initial adsorption at the surface (center) and a slower, spatially homogeneous linker exchange (right).

5.3 Synthesis, Post-Synthetic Modification and Characterization Methods

The project with MIL-101(Al)-NH_2 was performed in collaboration with the group of Dr. Stefan Wuttke. Synthesis of MIL-101(Al)-NH_2, the subsequent modification with fluorescein isothiocyanate and pivaloyl anhydride, as well as bulk characterization of the samples (x-ray diffraction, N_2-sorption and mass spectrometry) were performed by Dr. Stefan Wuttke and Patrick Hirschle. The investigations of the functionalization of UiO-67 were performed in collaboration with the groups of

Dr. Stefan Wuttke and Prof. Omar Yaghi. UiO-67 samples were synthesized by Juncong Jiang. He also performed the linker exchange experiments and the bulk characterization of the samples (x-ray diffraction, N_2-sorption and thermo gravimetry). Scanning electron microscopy images were taken by Dr. Ramona Hoffmann. Patrick Hirschle measured the amount of fluorescent dyes incorporated in the MOFs. These methods are mentioned here for completeness.

5.3.1 Methods for MIL-101(Al)-NH_2

Synthesis of MIL-101(Al)-NH_2

MIL-101(Al)-NH_2 synthesis was performed following a slightly modified procedure of Hartmann and co-workers:[116] 2-amino terephthalic acid (680.1 mg, 3.75 mmol) was dissolved in dimethylformamide (150 mL) and heated to 110 °C while stirring. A total of 3.75 mmol $AlCl_3 \cdot 6H_2O$ (1809.9 mg) was added to the solution in seven equal portions in intervals of 15 min. The solution was further stirred for 3 h and afterwards kept in a closed glass container at 110 °C for another 17 h. After cooling the reaction to room temperature, the yellow powder, that had formed during the reaction, was removed via filtration and washed with dimethylformamide and ethanol (both 60 mL) and afterwards further purified by soxhlet extraction in ethanol (175 mL) for 18 h. The resulting pale yellow powder was dried and stored under N_2-atmosphere.

Post-Synthetic Modification

Post-synthetic modification with fluorescein isothiocyanate (FITC) was done according the procedure reported by Bein and co-workers:[108] FITC (varying amounts, depending on the sample; usually 6.0 µg, 15.5 nmol) was dissolved in absolute ethanol (both 50 mL) and MIL-101(Al)-NH_2 (100 mg) was added to the solution. After leaving the suspension on the orbital shaker for 48 h, the powder was removed via filtration and repeatedly washed with ethanol. In the end, the sample (labeled MIL-101(Al)-NH_2-FITC) was dried and kept under N_2-atmosphere.
Both MIL-101(Al)-NH_2 and MIL-101(Al)-NH_2-FITC were further modified by capping the unreacted amino groups with pivaloyl. Hereby, 75 mg of each sample was preheated in an oil bath to 100 °C. Afterwards, 4 mL pivaloyl anhydride was added to the round bottom flask via a septum. After 12.5 min, the powder was filtered, washed five time with acetone (20 mL), and finally dried and kept under N_2-atmosphere. The resulting samples were labeled MIL-101(Al)-NH_2-P and MIL-101(Al)-NH_2-FITC/P, respectively.

Fluorescence Lifetime Imaging and Scanning Electron Microscopy

A JEOL JSM-6500F equipped with a field emission gun was used to acquire scanning electron microscopy (SEM) images, operated at 5 kV acceleration voltage and a distance of 10 mm. Before the measurements, the samples were coated with a

thin carbon layer using an Oerlikon Leybold Vacuum UNIVEX 350 sputter coater system. A base pressure of 1×10^{-6} mbar and an Argon pressure of 1×10^{-2} mbar were set, with a power of 25 W over 5 min.
All fluorescence intensity and lifetime measurements were performed on the microscope described in chapter 2.6. If no further SEM measurements were planned, 20–30 µL of a suspension containing 1–10 µg mL^{-1} MOF were put on an 8-Well LabTek I (VWR) slide. Once the particles were sedimented, the surface was imaged using a 60× 1.27 NA water immersion objective (Plan Apo IR 60x WI, Nikon). In cases when the sample was further used in electron microscopy, a drop of the suspension was put on a glass slide. After the water evaporated completely, fluorescence images were acquired with a 20× 0.6 NA air objective (Plan Apo Lambda 20x, Nikon). In this case the samples were imaged not through the glass, but from above to make it consistent with electron microscopy. For all measurements a region of interest was scanned with a resolution of 300×300 pixels for a total of 250–500 s. In order to avoid artifacts from too high count rates while ensuring a good signal-to-noise ratio, a total pixel count of 200–3000 photons is optimal. To achieve this, the excitation power was adjusted for each individual experiment, ranging between 100 nW and 1 µW as measured before the objective.
In order to correlate fluorescence lifetime to morphology, the same region imaged with a fluorescence microscope was also recovered and measured with SEM. To facilitate and speed up this process, a black marker spot, recognizable with both imaging methods, was placed in the center of the sample, creating a navigational guidepost. All measurement were then performed close to this spot to further limit the search space. The fine mapping, in the end, was done using distinct topological patterns in the sample, as is illustrated in Figure 5.23.

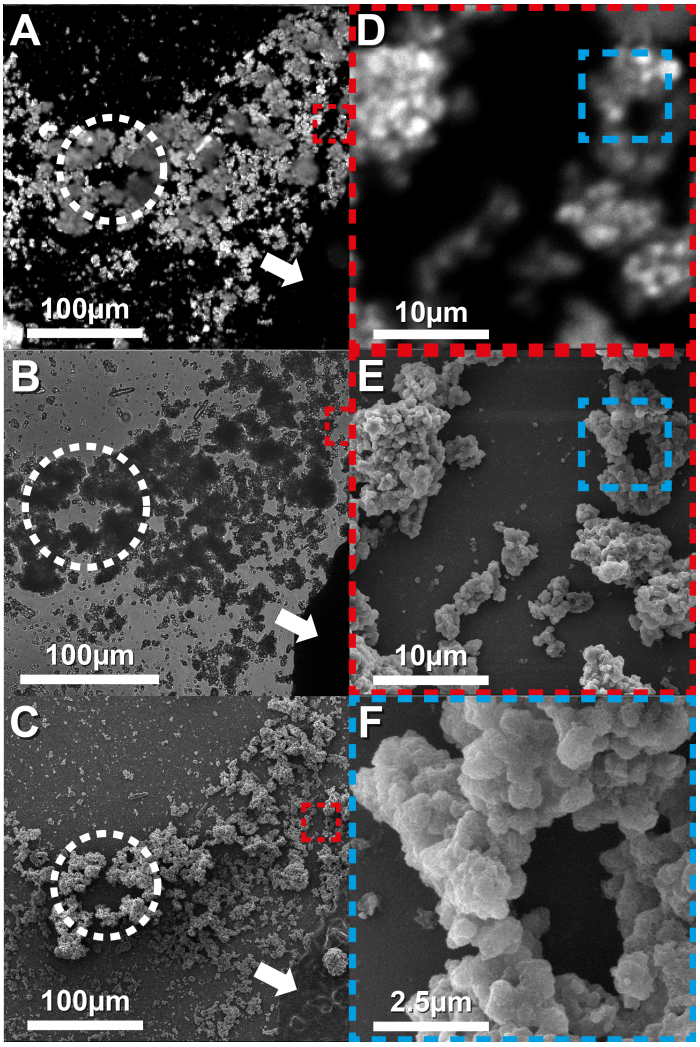

Figure 5.23: Colocalizing FLIM and SEM images. An overview image of an area close to the black marker spot (indicated with the white arrow) was recorded with a fluorescence (A), a bright-field (B) and an electron (C) microscope. Using distinct topological features (dotted white circle), identical regions of interest (red dotted squares) where identified in both fluorescence (D) and electron (E) microscopy images. To better resolve the morphology, the regions indicated with the blue dotted square in (D) and (E) were imaged in SEM with a higher magnification (F).

5.3.2 Methods for UiO-67

Synthesis of UiO-67 with Method 1

Biphenyl-4,4'-dicarboxylic acid (H_2BPDC), functionalized linker (see Table 1), and zirconium chloride (18.2 mg, 78.1 µmol) were mixed in a 4 mL scintillation vial. The functionalized linker was 2-amino-biphenyl-4,4'-dicarboxylic acid modified with either fluorescein isothiocyanate (FITC-H_2BPDC, Figure 5.22 A) or rhodamine B isothiocyanate (RITC-H_2BPDC, Figure 5.22 B). A solution of dimethylformamide (2 mL) and hydrochloric acid (0.1 mL, 37%) was added to this mixture. After sonication for 20 min, the vial was heated at 90 °C for 24 h yielding functionalized UiO-67. The sample was then immersed in 4 mL of anhydrous DMF for three days, during which time the DMF was replaced five times per day. The same procedure was subsequently repeated with anhydrous methanol. The methanol exchanged sample was then evacuated at room temperature under vacuum for 24 h.

Table 5.5: Synthesis details for dye-functionalized UiO-67.

Name	**H_2BPDC [mg]**	**FITC-H_2BPDC [mg]**	**RITC-H_2BPDC [mg]**
UiO-67	18.8	-	-
UiO-67-0.1% FITC	18.8	0.0502	-
UiO-67-0.3% FITC	18.7	0.1506	-
UiO-67-0.7% FITC	18.7	0.3514	-
UiO-67-2% FITC	18.4	1.004	-
UiO-67-0.1% RHO	18.8	-	0.0638
UiO-67-0.3% RHO	18.7	-	0.01914
UiO-67-0.7% RHO	18.7	-	0.4466
UiO-67-2% RHO	18.4	-	1.276
UiO-67-0.1% FITC, 0.01% RHO	18.8	0.0502	0.00638
UiO-67-0.1% FITC, 0.03% RHO	18.8	0.0502	0.0191
UiO-67-0.1% FITC, 0.1% RHO	18.8	0.0502	0.0638
UiO-67-0.1% FITC, 0.3% RHO	18.7	0.0502	0.191
UiO-67-0.1% FITC, 1% RHO	18.6	0.0502	0.638

Synthesis of UiO-67 with Method 2

H_2BPDC (40.0 mg, 165 µmol) and zirconium oxychloride octahydrate (18.0 mg, 55.8 µmol) were mixed in a 10 mL scintillation vial. For the functionalized sample, 0.1% of the H_2BPDC were substituted by FITC modified linker (0.1 mg, 0.16 µmol). A solution of dimethylformamide (8 mL) and glacial acetic acid (0.87 mL) was added to this mixture. After sonication for 10 min, the vial was heated at 90 °C for 24 h to yield UiO-67 as a white powder. The sample was then immersed in 20 mL of anhydrous DMF for three days, during which time the DMF was replaced five times per day. The same procedure was subsequently repeated with anhydrous methanol.

The methanol exchanged sample was then evacuated at room temperature under vacuum for 24 h.

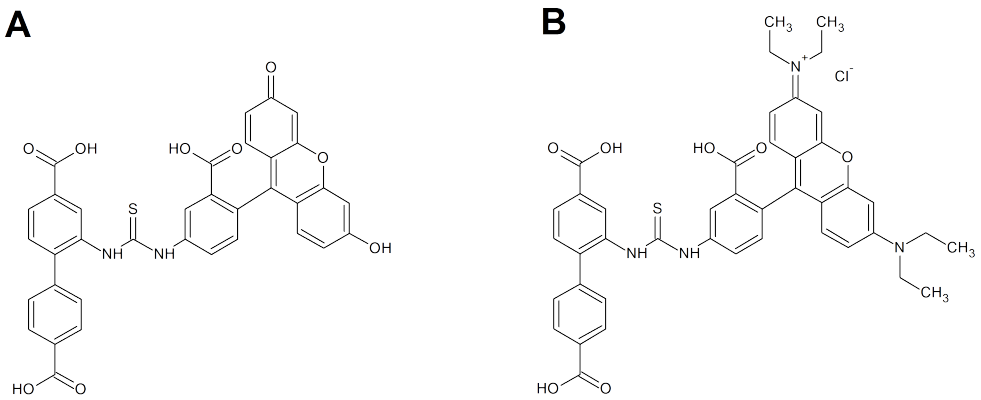

Figure 5.24: Chemical structure of FITC (A) and RITC (B) modified 2-amino-biphenyl-4,4'-dicarboxylic acid.

Linker Exchange

For linker exchange measurements, several 20 mL scintillation vials each containing 12.5 mg of UiO-67 (synthesized with either method 1 or method 2) were prepared. To each of them a solution of FITC-H_2BPDC (2.0 mg, 3.1 µmol) in DMF (20 mL) was added. The vials were heated to different temperatures (25–100 °C). At certain time points (1 h, 6 h, 1 d, 7 d), samples (2 mL) of the suspension were removed. The solid was separated by centrifuge and subsequently washed with anhydrous DMF (10 times, 4 mL each) and anhydrous methanol (10 times, 2 mL each). The methanol washed samples were then evacuated at room temperature under vacuum for 24 h.

Dye Concentration Measurements

For determining the concentration of dye modified linkers, an aliquot of the respective samples (0.3–0.6 mg) was suspended in 4 mL of a digestion mixture comprised of cesium fluoride (137.2 mg, 0.90 mmol) in a mixture of water (1.43 mL) and DMSO (2.57 mL). The suspension was sonicated for 10 min and subsequently incubated at room temperature for 2 h. After a second sonication for 10 min, fluorescence intensity measurements were conducted on the resulting clear solutions.
The undiluted stock solutions (3 mL) were measured in PMMA capillaries on a fluorescence system consisting of a 814 Photomultiplier Detector, a LPS220B Lamp Power Supply, a PTi–MD3020 Motor Drive (all Photon Technology International, PTI) and a TC125 Temperature control (Quantum Northwest). The calibration curves necessary for the dye-calculations were determined by dissolving raw modified linker molecules in the digestion mixture and measuring the fluorescence signal at different dilutions. This data was then fitted with a linear function.

Fluorescence Lifetime Imaging and Scanning Electron Microscopy

All fluorescence intensity and lifetime measurements were performed on the microscope described in chapter 2.6. A suspension (20–30 µL) containing 1–10 mg mL^{-1} MOF were put on an 8-Well LabTek I (VWR) slide. Once the particles were sedimented, the surface was imaged using a 60× 1.27 NA water immersion objective (Plan Apo IR 60x WI, Nikon). For all measurements, a region of interest was scanned with a resolution of 300 × 300 pixels for a total of 250–500 s. Full pixel size ranged from 100 nm (30 µm total image size) to 1 µm (300 µm. In order to avoid artifacts from too high count rates while ensuring a good signal-to-noise ratio, a total pixel count of 200–3000 photons is optimal. To achieve this, the excitation power was adjusted for each individual experiment, ranging between 1 nW and 20 nW as measured before the objective.
For SEM imaging, a Zeiss NVision40 microscope was used. Secondary electron images were acquired using the InLens detector at a low acceleration voltage of 5 kV. In order to avoid charging effects, the samples were coated with a thin carbon film before the measurements. The carbon deposition was performed using a BAL-TEC coating system.

6. Influence of Chrome Barriers on Diffusion in Lipid Bilayers

The plasma membrane is not simply a barrier that separates the inside of the cell from its surroundings, but it is also the cell's primary mode of interaction with its neighbors and the environment. These functions require an extraordinary degree of complexity in composition, for both lipids and membrane proteins, as well as in its spatial organization. External stimuli often result in a response of the cell. In most cases, these responses takes place mainly within the cell, e.g. via signaling cascades. Some stimuli, however, primarily result in spatial reorganization of membranes.[131–134] This can be a redistribution of lipids to a new equilibrium state or a recruitment of receptors to a binding site. In all cases, the mobility of the membrane's components is crucial for a well functioning feedback, regardless of whether the rearrangement if brought about via active transport or passive diffusion.

Recent studies have shown that movement in the plasma membrane is far from being "free".[135–140] Depending on the investigated biomolecule or organelle, the experimental conditions and the relevant distances, their diffusion can be described as slightly anomalous or as compartmentalized. Especially the later case, caused by different lipid phases (e.g. lipid rafts) or interactions with the cytoskeleton, is particularly interesting, but not well understood. For example, Fujiwara *et al.*[135] showed for unsaturated phospholipids in rat kidney fibroblast membranes confined diffusion on short timescales ($\approx 10\,\mathrm{ms}$) with hopping between the 200 nm sized compartments. They also identified a higher level of compartmentalization into 750 nm large partitions in which the phospholipids were confined for 0.33 s on average. While the diffusion on small time and spatial scales was observed to correspond well to movement in simple reconstituted lipid membranes. the confinement resulted in a much reduced apparent mobility for longer observation times.

This high complexity of the plasma membrane organization and the cell as a whole contributes to out the lack of understanding of the general principles involved. Due to the high number of different properties and interaction partners influencing the substrate's movement, it is almost impossible to establish a clear cause-and-effect relationship. Moreover, the obtained parameters highly depend on the investigated substance so that insights gained in one study cannot be simply extrapolated to a different system.

A way to deal with this is to use a bottom up approach. Instead of trying to disentangle the complexity of the full system, it is often easier to investigate the governing influences individually in a simplified model and use the obtained information to understand the big picture. Reconstituted lipid bilayers are the simplest model systems for studying plasma membranes in which both the environment and composition can be precisely controlled. Substrates can be patterned in such a way that the altered surfaces prohibit the formation of lipid bilayers or disrupt their

mobility. Arranging these barriers in different ways allows one to gain information about their influence on membranes.[141–144]
For this project, we used glass coated with a chrome pattern as a substrate for supported lipid bilayers in order to investigate how barriers and obstacles influence diffusion in membranes. It is believed that chrome surfaces prohibit lipids from crossing them. Unlike some other substrates, chrome allows formation of bilayers on top of it while prohibiting mixing with the surrounding regions, either because the membranes are not connected or because the layer on top of the metal is not fluid.[145,146] These barriers are then arranged in a special pattern using a procedure developed by Lohmüller *et al.*[147] Here, a monolayer of polystyrene beads (diameter $\approx 1\,\mu m$) is used as a shadow mask for chrome evaporation, resulting in a hexagonal distribution of chrome triangles extending over millimeters. By using plasma treatment, the beads can be partially etched prior to chrome evaporation, leading to a decrease of their size. Since they do not move during the procedure, this leads to larger spacing between the particles and consequently to larger metal patches and smaller gaps between different compartments (Figure 6.1). By adjusting the etching time, these parameters are precisely controlled and thus their influence on diffusion can be studied.

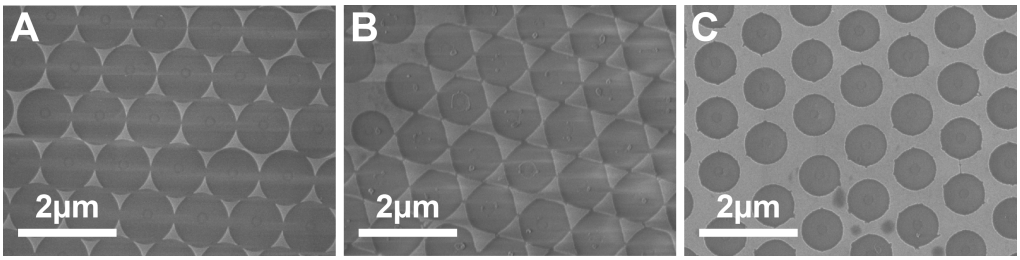

Figure 6.1: SEM images of the hexagonal chrome pattern without etching (A), as well as with 200 s (B) and 450 s (C) plasma treatment. Increased etching time results in an increased area covered with metal, thus decreasing the gap size between compartments. For very long etching times (C), the compartments are completely closed.

Fluorescence pair-correlation is a technique that is well suited to investigate the influence of obstacles and compartmentalization. Here, the temporal cross correlation between different points on a line is calculated. Since only the same particle observed at two different points results in a positive correlation amplitude, the probability and time for crossing that space can be determined. Comparing these parameters for two points within the same region with those located in different compartments can reveal how these barriers affect the diffusion.

6.1 Sample Characterization

To determine how the gap and the barrier sizes affect the mobility of lipids in membranes, patterns with five different etching times (0 s, 150 s, 200 s, 300 s, 450 s), but identical bead diameter (950 nm) and metal thickness (6 nm) were produced

(chapter 6.6). As can be seen in the SEM images in Figure 6.2, increased etching times resulted in larger chrome regions and smaller gap sizes. The metal covered 10% of the total area for the unetched samples, closely corresponding to the packing efficiency of circles (90.7%). For etched samples, the coverage was 22% (150 s), 30% (200 s), 44% (300 s) and 50% (450 s). Consequently, the average gaps size decreased from around 130 nm to 55 nm and 40 nm for samples treated for 150 s and 200 s, respectively (Figure 6.3), resulting in more connections being completely closed off. All compartments were completely isolated in samples etched for 300 s or more.

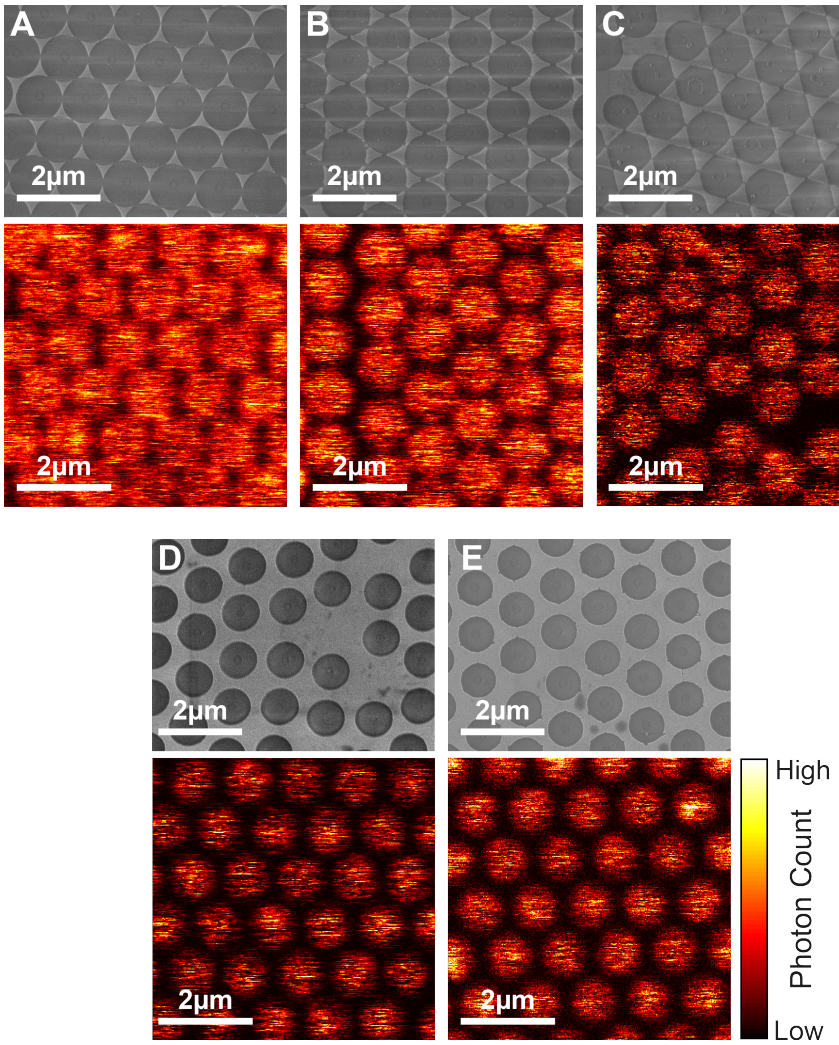

Figure 6.2: SEM (grayscale) and fluorescence (hot color map) images of the hexagonal chrome pattern without etching (A), as well as with 150 s (B), 200 s (C), 300 s (D) and 450 s (E) etching. The chrome covered regions appear darker in the fluorescence images. The thick dark lines are caused by defects in the polystyrene bead monolayers and were excluded from measurements. The SEM and fluorescence images were taken at different position of the respective samples.

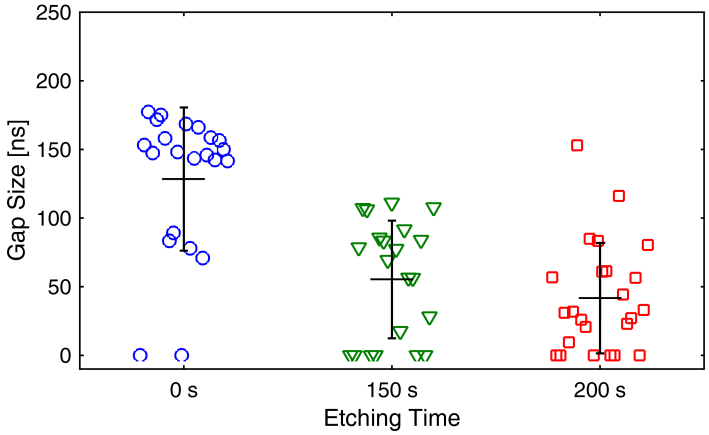

Figure 6.3: Gap size distribution for samples that were plasma treated for 0 s, 150 s and 200 s. The black lines indicate the mean and standard deviation.

A supported 1,2-Dioleoyl-sn-glycero-3-phosphocholine (DOPC) bilayer, spiked with a small amount of fluorescent labeled lipids, was placed on top of the patterned surfaces. Confocal scanning fluorescence images (Figure 6.2 bottom rows) revealed two important aspects. First of all, the chrome covered regions appeared darker than the glass surfaces. The main reason for this is quenching of the dyes due to their close proximity to the metal surface, evidenced by the decrease of the fluorescence lifetime close to the chrome (Figure 6.4). Furthermore, the reflective nature of the chrome layer results in a decreased brightness of the chrome covered regions. Some of the light is blocked by the metal, decreasing both the excitation intensity, as well as the photon collection efficiency. This, however, is at most a minor contribution, since the same dark regions are observed when illuminating and imaging samples from the top or from the bottom.

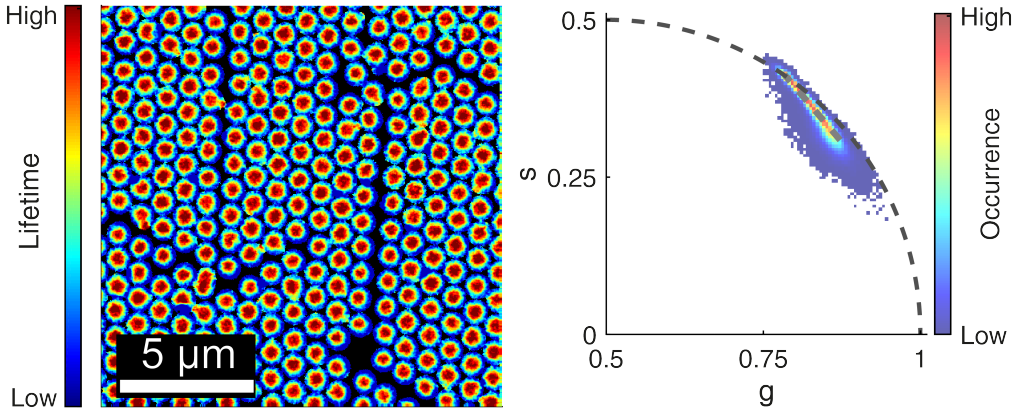

Figure 6.4: FLIM image (left) with corresponding phasor plot (right) for a chrome patterned surface. The color code in the FLIM image corresponds to the pixel position along the gray line in the phasor histogram, with red representing long, blue short, and green and yellow intermediate lifetimes. To decrease noise fluctuations, a spatial sliding average of 3×3 pixels was applied to the phasor data.

The short horizontal lines observed in the image (see Figure 6.2) are a consequence of the raster scanning procedure in combination with the low concentration of fluorophores. Horizontal scanning is two to three orders of magnitude faster than the vertical, so that diffusing particles are more likely to stay in focus during a line scan than between two lines. Since this is only observed when the fluorophores are moving, it is a good way to check the fluidity of the membrane.

6.2 Dependence of Diffusion on Gap and Barrier Size

To measure the diffusion of dye labeled lipids between different compartments, fluorescence pair-correlation analysis was used. A 3 µm long line was repeatedly scanned over the sample. The line scan was placed to cover three compartments and either the two gaps or chrome barriers connecting them. Since scanning and detection are synchronized, the exact detection time was then used to assign the individual photons to the corresponding positions on this line, yielding the fluorescence intensity as a function of time for each spatial bin (Figure 6.5 A).

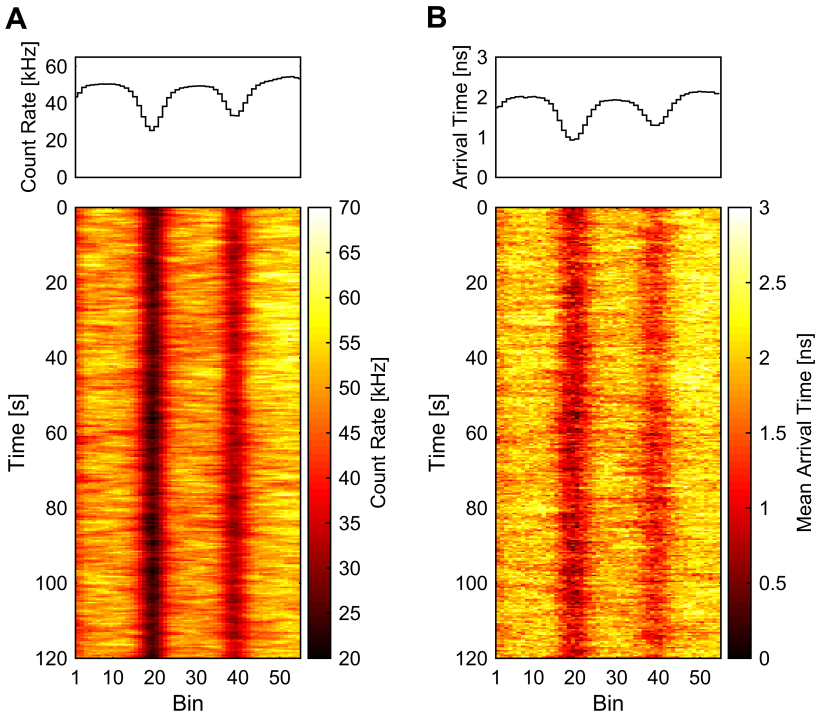

Figure 6.5: Fluorescence intensity (A) and mean arrival time (B) kymographs of a 3 µm line scan with 1 kHz repetition rate across two chrome barriers of an unetched sample. The whole line was divided into 60 bins of 50 nm size. Bins containing the retraction of the focus were removed. The upper graphs display the time-averaged count rate (A) and the mean arrival time (B) per bin.

Additionally, the TCSPC detection provided us with the photon arrival times relative to the individual laser pulses, which were then used to visualize the respective fluorescence lifetimes (Figure 6.5 B). Due to quenching, both mean intensity and arrival time on the barriers were reduced (Figure 6.5). This made it possible to assign each spatial bin to either a barrier or one of the compartments.
For the actual pair correlation analysis, a temporal cross-correlation between different positions was calculated, resulting in a correlation carpet for each bin distance (Figure 6.6). In most cases, a spatial lag of 500 nm was used for the analysis, a compromise between the minimal overlap and the maximal signal. Using the mean intensity and arrival time profile, individual correlation curves were sorted into two categories and averaged. The first consisted of all data points situated within the same compartment (Figure 6.6 green region). If the two position on the line belong to different compartments, they are assigned to the second category (Figure 6.6 magenta regions). The remaining curves contained the laser retraction and position directly on top of a barrier or gap. Due to difficulties in analyzing these curves, they were discarded from all further analyses.

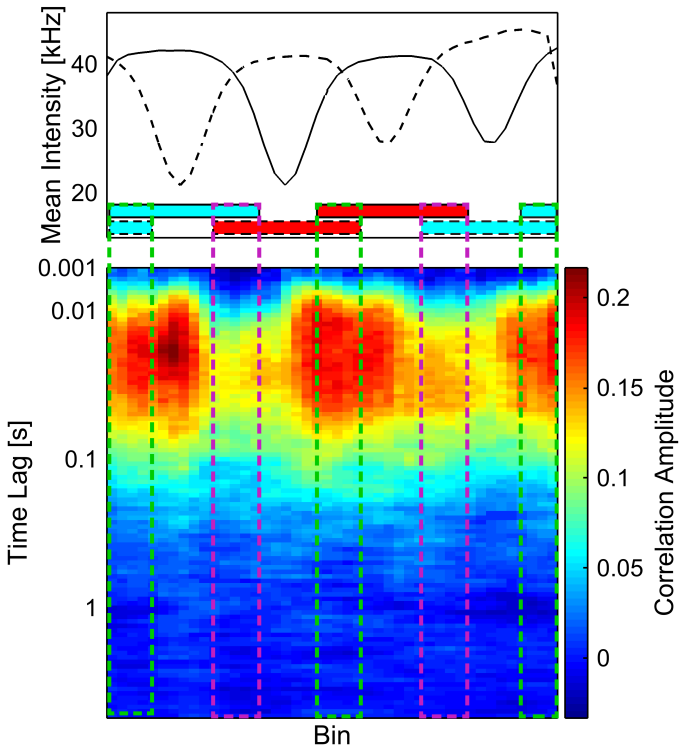

Figure 6.6: Pair-correlation carpet of 500 nm spatial lag for an unetched chrome patterned surface. Using the mean intensity profile of i (solid curve in the top plot) and j (dashed curve in the top plot) of the $i \times j$ cross correlation, bins are assigned to the different compartments (cyan and red bars in the top plot). The individual correlation curves are then divided into those regions, where the ith and jth bins are in the same compartment(green areas), and those where they are in neighboring compartments (magenta regions).

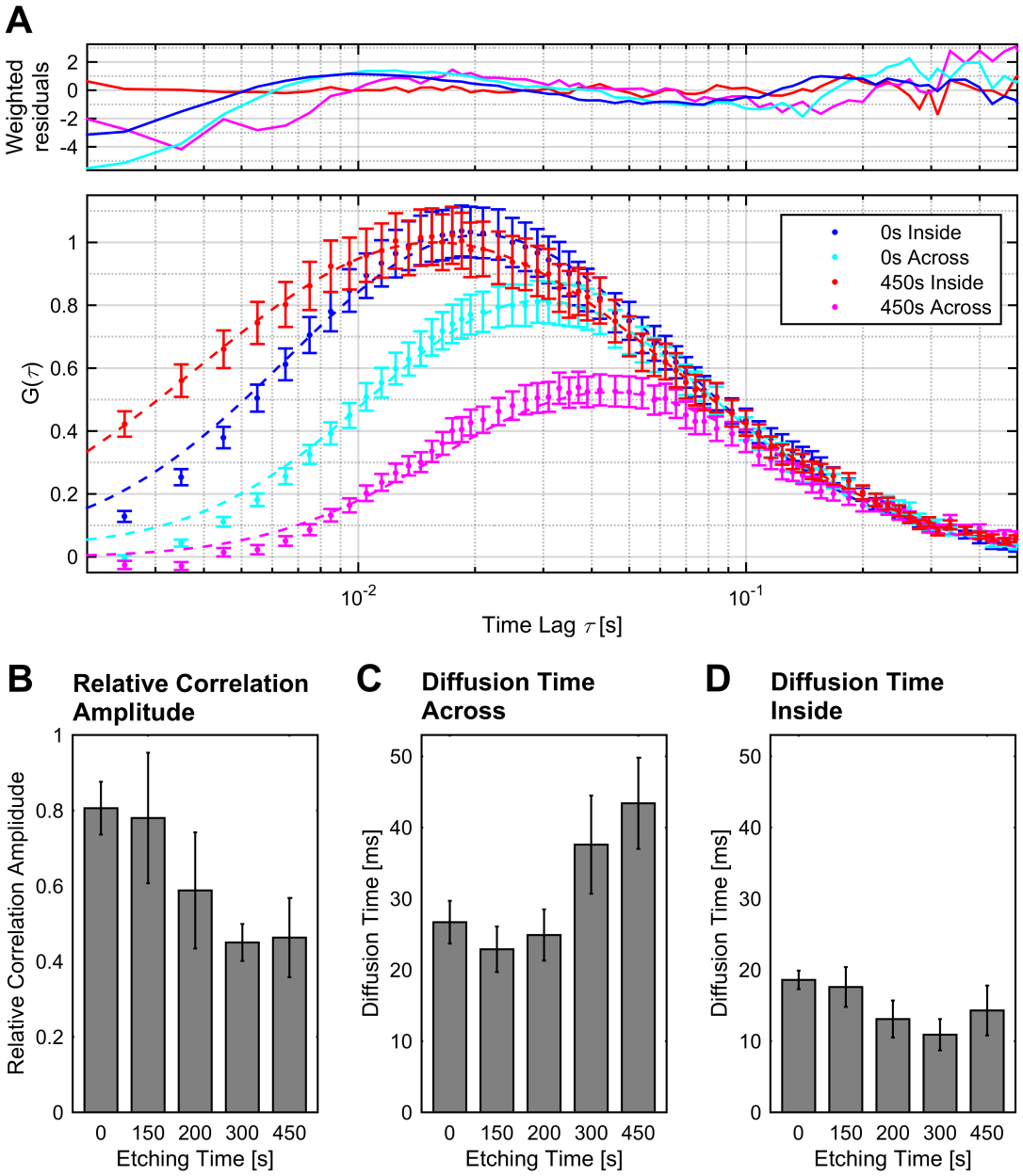

Figure 6.7: Results of the pair correlation analysis for different etching times. A) PCF curves inside and across compartments for unechted and 450 s etched samples. Dashed lines represent the fits with a lognormal distribution. The amplitudes were normalized to the maximal amplitude of the curves inside a compartment. The upper graph shows the weighted residuals of the fit. B) The relative correlation amplitude, calculated from the ratio of the maximal correlation amplitude of two bins in neighboring compartments and the value for two bins inside the same compartment. C) Diffusion time across a barrier between two compartments. D) Diffusion time within a single compartment. The error bars represent the standard deviation.

Since, in this case, the diffusion behavior is governed by the complex interplay of a variety of parameters, an exact analytical description of the pair-correlation function was not possible. Therefore, a logarithmic Gaussian function was used to fit the data as it described the general shape of the data very well:

$$G(\tau) = A \cdot exp\left(- \frac{lg^2\left(\frac{\tau}{\tau_{mode}}\right)}{2\sigma^2} \right) + G(\infty) \tag{6.1}$$

Where A describes the correlation amplitude at the maximum of the curve, τ_{mode}, and σ is the Gaussian root mean square width. $G(\infty)$ is an offset to better describe curves that did not completely decay to zero.
The time lag at the maximum is related to the average time it takes a molecule to diffuse the distance between the two spatial positions. Therefore, it can be used to quantify how much lipids are slowed down when they cross the gaps compared to free diffusion inside a compartment. The correlation amplitude, on the other hand, is related to both the number of observed particles, as well as to the probability of a fluorophore to diffuse from the first position to the second. Changes in concentration affect all correlations in the carpet the same. The probability of crossing the distance, however, depends heavily on the local conditions and the path a particle has to take. By looking at the amplitude of a correlation between different compartments relative to the amplitude within a single compartment, the effect of concentration fluctuations is removed, thus reflecting the influence of obstacles a particle encounters.
As expected, an increase in etching times reduced the average relative correlation amplitude (Figure 6.7 B). However, even for completely closed gaps, the value did not decrease to zero, but stayed at around 0.4–0.5 Even when taking into account occasional open gaps, noise or other sources that could contribute a correlation, these high values could not be explained, assuming that the lipids do not cross the chrome barrier. Rather, this observation proofs that, in some cases, the metal barriers only hinder, but do not completely stop lipid diffusion. This argument is also supported by the fact that the fluorescence intensity did not significantly decrease during line scans (Figure 6.8). Considering the laser power and long measurements times of up to 10 min, a large number of fluorophores would bleach during scanning if the compartments where closed. Due to the small size of compartments and low concentration of dyes, this must notably reduce the measured count rate in case of isolated areas. Only when individual compartments are connected to a much larger reservoir, can the bleached fluorophores be replenished and a constant steady state fluorescence signal can be maintained. Therefore, a constant intensity during measurements suggests a rapid exchange even over chrome barriers.
Not only the correlation amplitudes, but also the diffusion times were affected by changing the size of gaps and barriers. For patterns showing gaps (0–200 s etching), the time to diffuse between two compartments stayed at around 25 ms, but increased by more than 50%, when the gaps were closed (Figure 6.7 C). One possible way to explain the data is that, as long as two regions are still connected, diffusion is

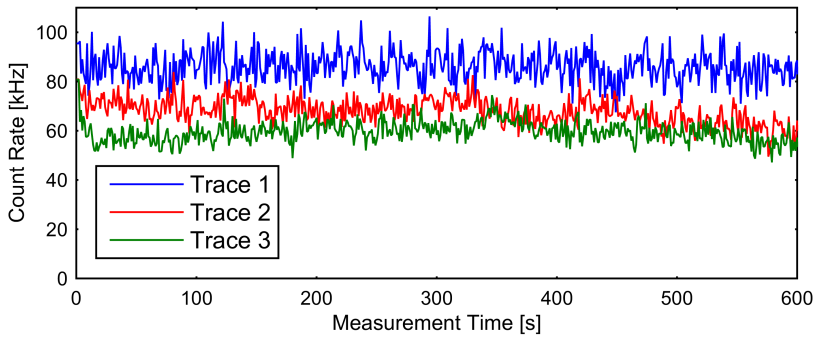

Figure 6.8: Fluorescence intensity traces for three different line scans of a 450 s etched chrome pattern. Although the intensity fluctuates over the course of the measurement, no significant decrease of intensity is observed with time.

fairly fast and only slightly affected by the gap size. For isolated compartments, lipids must diffuse over barriers and are thus slowed down. However, these results show that lipids can move over metal covered areas. Therefore, this path should always contribute to the lipid crossing, significantly increasing diffusion times even for shorter etched samples.
A more likely interpretation is that the diffusion time does not depend on the gap size or even the presence of gaps, but rather on the width of the chrome barriers. As it be seen from the SEM images in Figure 6.2, the amount of chrome obstructing the paths between compartments changes only slightly from the unetched samples to the ones etched for 200 s. However, it increases dramatically when the samples were etched for 300 s or 450 s. Thus, the largest change in the diffusion time is observed between the 200 s and 300 s etched samples, consistent with our data. This argument is also supported by the fact that the diffusion time inside a compartment (Figure 6.7 D) is lower than between them (Figure 6.7 C), even for the unetched pattern. Since in all samples the path is significantly blocked by chrome, slower crossing is expected in all cases.
The effect of the etching time on the diffusion time within a compartment was not as pronounced as the change in crossing time or the relative amplitude, but still noticeable (Figure 6.7 D). The diffusion time actually decreased slightly for long etched samples. This is most likely an effect of the decrease in compartment size from the larger chrome patches. Since diffusion over the chrome barriers is hindered, the particles are temporarily confined to the compartments. As the area a particle can freely explore decreases, the probability of moving to the over focus increase. Thus, the maximum of the correlation function shifts to shorter lag times. This decrease in diffusion time within individual compartments was also observed in Monte Carlo simulations. Here, two dimensional diffusion inside a hexagonal compartment was assumed, while movement between them was only possible through 100 nm large gaps. As is shown in Figure 6.9, the diffusion time shows a strong dependence of the compartment size, similar to the observations of diffusion on chrome patterned surfaces.

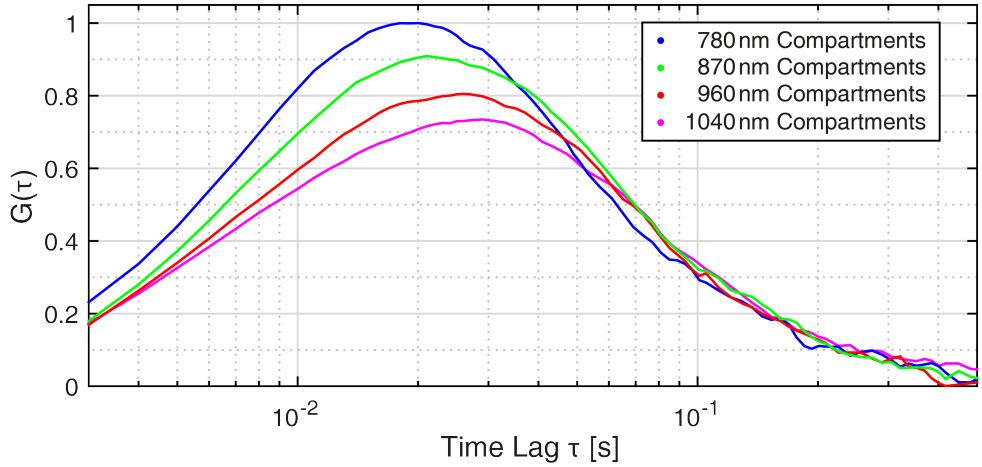

Figure 6.9: Pair-correlation functions for simulated diffusion inside of separate compartments connected by 100 nm large gaps as a function of compartment size.

6.3 Influence of Fluorescence Quenching on the Pair Correlation Results

The effect of quenching on the resulting pair correlation function have not been taken into account so far. The fluorescence signal decreases close ($\approx$ 10 nm) to the chrome areas, changing the PSF and shifting its center away from the quenched regions (Figure 6.10). This means that, for two positions inside a compartment, the observed distance is actually shorter than expected. On the other hand, measurements across a barrier increase the apparent distance. The discrepancies between the assumed and the observed spatial lag, in turn, cause effects on the pair correlation function consistent with the observations for the chrome patterns.

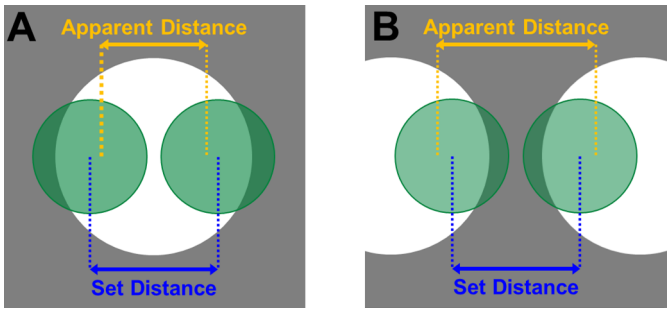

Figure 6.10: Effect of quenching on the apparent focal distance. A) Two foci within the same compartment are quenched on the outside, decreasing the effective distance. B) Two foci on the opposite sides of a barrier are quenched on the inside and therefore appear further apart.

To estimate how much and under which conditions quenching would influence the pair correlation function, Monte Carlo simulations were performed and analyzed

in the same way as in the actual experiments. Specifically, free, two dimensional diffusion was assumed. Whenever a particle resided in a region corresponding to the chrome areas, its fluorescence was completely quenched.
These simulations show that quenching does affect correlations (Figures 6.11 and 6.12), however, less than what was observed for the experiments. Even for 300 nm wide barriers, the decrease in amplitude and increase in diffusion time across the barrier are still below the experimental values. Although a larger focus also shows larger effects, a barrier and focus far exceeding the measured parameters are required to emulate the experiments *in silico*.

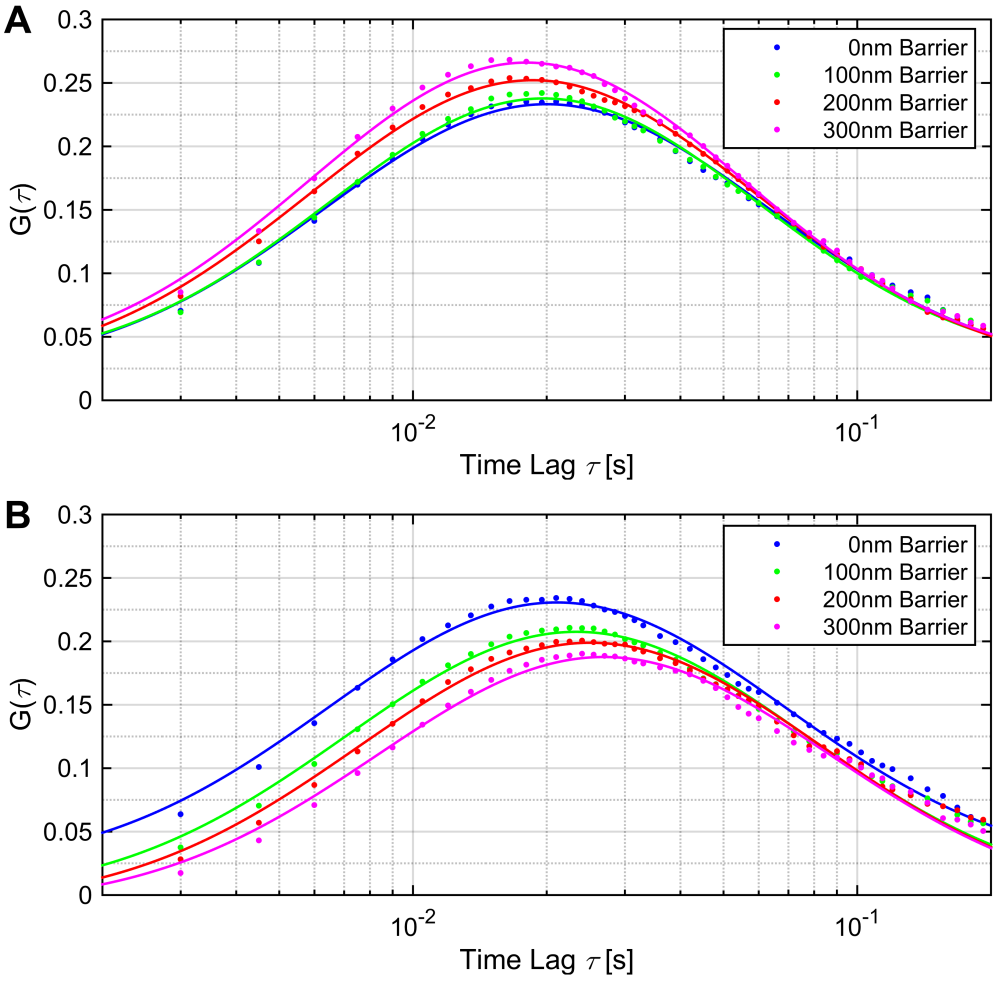

Figure 6.11: PCF curves of simulated data for different barrier widths. A) For positions within a single compartment, the maximum amplitude increases while the correlation time decreases with increasing barrier width. B) In contrast, correlations across a barrier show the opposite behavior with increasing diffusion time and decreasing amplitude.

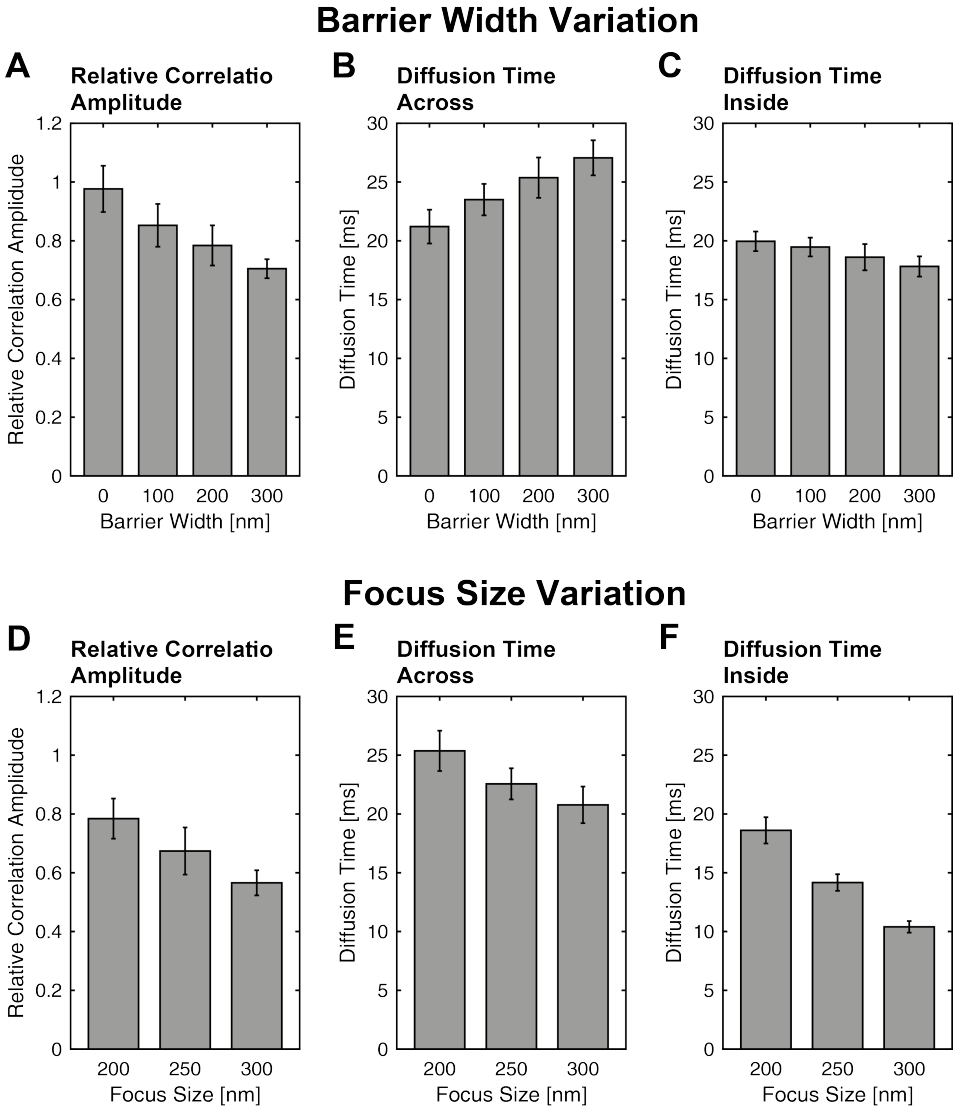

Figure 6.12: Results of the PCF simulation. A-C) Apparent relative correlation amplitude (A), as well as diffusion times across a barrier (B) and inside a compartment (C) as a function of barrier width for a focus size of 200 nm. D-F) Apparent relative correlation amplitude (D), as well as diffusion times across a barrier (C) and inside a compartment (D) as a function of the focus size for a barrier width of 200 nm.

Another way of checking the influence of quenching on the correlation functions is to compare bins close to the chrome to those, located farther away. As shown in Figure 6.13, by selecting spatial bins right at the edge of the barriers, where quenching is very strong, the relative correlation amplitude and the diffusion time inside a compartment changes only slightly, while the time to cross a barrier remains unaffected. However, these observed differences are minor compared to the changes seen for increasing etching times and the edge bins are usually discarded during analysis.

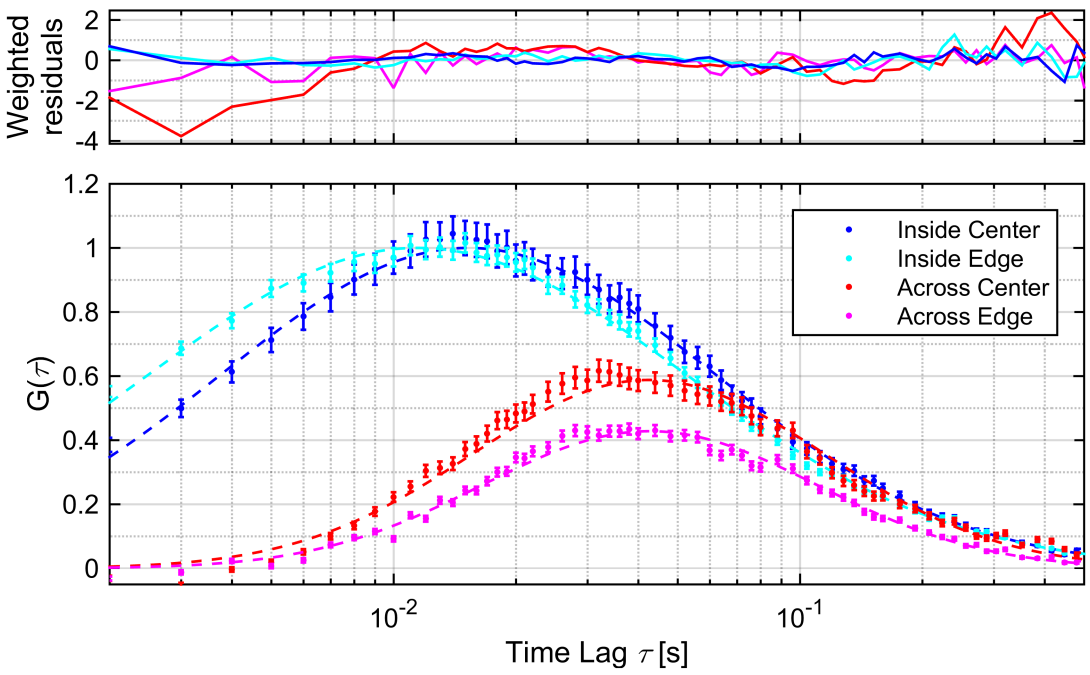

Figure 6.13: PCF curves of the 450 s etched sample for spatial bins in the center of compartments (blue and red curves), and those close to the edge of quenched regions (cyan and magenta curves). Dashed lines represent the fits with a lognormal distribution. The amplitudes were normalized to the maximal amplitude of the curves inside a compartment. The upper graph depicts the weighted residuals of the fit.

Together with the simulated data, these results strongly suggest that quenching influences the correlation function to a certain degree. However, this effect is much smaller than the observed changes with etching time, indicating that a second mechanism affecting the diffusion behavior is present.

6.4 Influence of the Barrier Height and Width

A variety of methods have been used previously to show that chrome forms a complete barrier and that no crossing is possible. However, our data clearly show, that fluid lipid layers can form on top of chrome regions, connecting compartments and thus allowing diffusion across these compartments. Moreover, we observed that the metal surface affects mobility of lipids diffusing across the barriers. So what are the parameters determining whether diffusion takes place?
The most obvious parameter is the width of the barrier. As shown in chapter 6.2, larger chrome diameters hinder diffusion of lipids, decreasing the correlation amplitude and increasing the crossing time. Therefore, it is quite likely that a further increase of the width may result in a complete abrogation of mobility between compartments. Secondly, the thickness of the metal layer will also affect the mobility.

As the height of the barriers increases, the curvature of the lipid layer at the edge also needs to adapt. A further increase in barrier height results in a disruption of the lipid layer. Therefore, the lipids on the glass and on the chrome are no longer connected and diffusion is prevented (Figure 6.14).

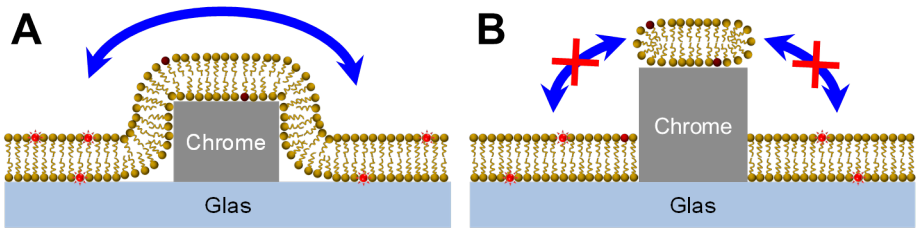

Figure 6.14: Influence of the metal height on lipid mobility. A) For thinner chrome layers, the lipid bilayer spans the chrome barriers, allowing diffusion between compartments. B) For high barrier heights, bilayers are no longer connected, preventing diffusion between the two sides.

To test these hypotheses, additional samples of varying thickness of the chrome layer (6 nm, 18 nm and 37 nm) were synthesized. 1280 nm large polystyrene beads were plasma treated for 400 s and then used to form closed-off compartments with an average barrier width of 160 nm. During chrome coating, an additional mask was used to create a grid on the sample. This mask was used to identify exact positions in the sample, thus allowing us to perform confocal fluorescence and scanning electron measurements on the same regions. This correlative approach was used to investigate the influence of the width of the barriers.

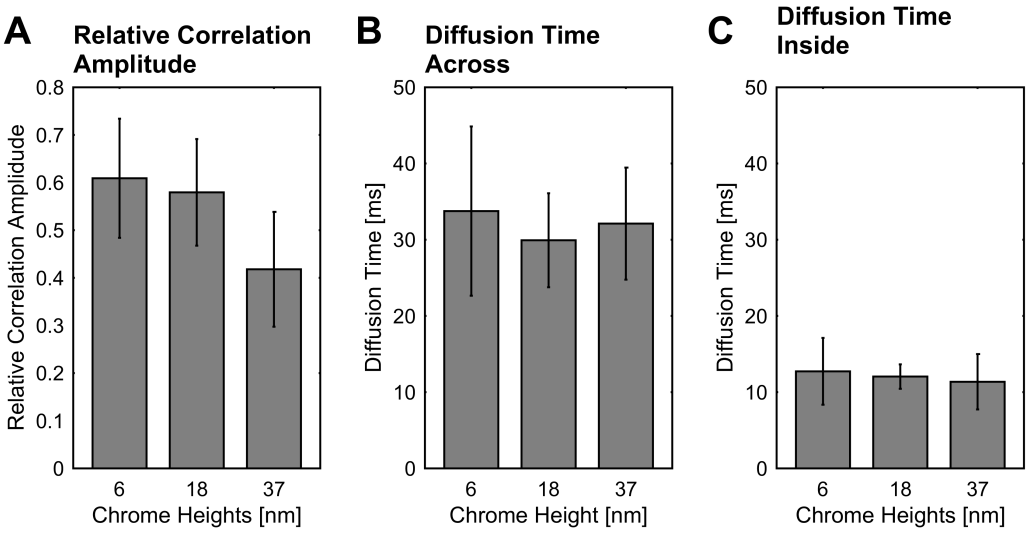

Figure 6.15: Results of the pair correlation analysis for different chrome heights. A) Relative correlation amplitude. B) Diffusion time across a barrier between two compartments. C) Diffusion time within a single compartment. The error bars represent the standard deviation.

A PCF analysis revealed that the chrome layer thickness has only a minor effect on diffusion (Figure 6.16). The 6 nm and 18 nm samples showed almost identical results. Only at the highest thickness of 37 nm were some changes noticeable, with the amplitude dropping from around 60% to 42% (Figure 6.16 A). However, the diffusion times were not affected (Figure 6.16 B and C).
Analysis of SEM images of different samples has revealed another possible cause of changes observed with 37 nm high barriers. While lower chrome thicknesses resulted in relatively smooth metal surfaces, synthesis of higher layers has produced less regular metal coating (Figure 6.16). For a chrome height of 37 nm, the metal seems to form two slightly shifted layers in some regions. This structure may change the properties of lipid layers, while the actual metal height may have very little effect.

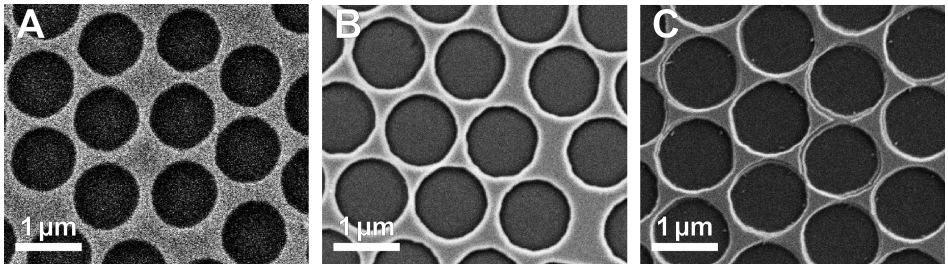

Figure 6.16: Scanning electron microscopy images of samples with 6 nm (A), 18 nm (B) and 37 nm (C) high chrome layers.

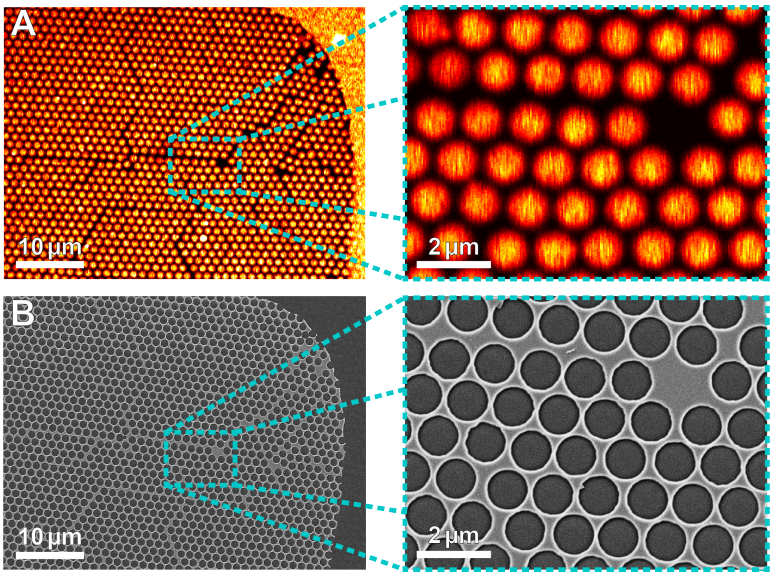

Figure 6.17: Correlative fluorescence and electron microscopy of a 6 nm high chrome sample. A region was first measured with a confocal fluorescence microscope (A). Using the grid and defects in the structure for identification, the same area was then imaged using the SEM (B).

To determine the influence of the barrier width, individual regions were first analyzed with pair-correlation. Afterwards, the same regions were imaged with SEM in order to precisely measure the barrier width (Figure 6.17). The results of these measurements show no significant correlation between the amplitude, diffusion time and the barrier width (Figure 6.18). However, the distribution of barrier sizes was very narrow, with most values ranging from 100 nm to 200 nm, with only a few values above that range. Due to fluctuations and the noise of the pair correlation data, the small dependence of the barrier width might be hidden and only visible for larger barriers. Wider obstacles, however, are problematic to measure with PCF, since quenching and a lower signal-to-noise ratio reduce data quality.

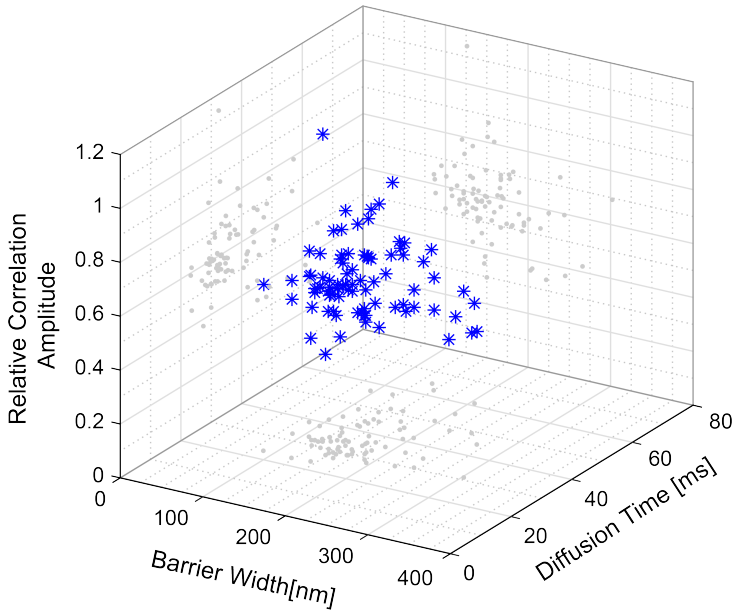

Figure 6.18: Scatter plot of the relative pair correlation amplitude and the diffusion time between two compartments as a function of barrier width. The blue stars represent the 3D positions, while the gray dots show the three 2D projections.

In most cases, the fluorescence intensity did not decrease during PCF measurements. However, using high laser powers to illuminate certain areas with exceptionally many defects or wide barriers resulted in a reduced intensity (Figure 6.19). This bleaching was not confined to the directly illuminated compartment, but extended beyond it and resulted in bleached areas with irregular shapes, with the illuminated spot usually not directly in the center (see gray, green and purple circles in Figure 6.19). In many cases, the borders of these regions coincided with defects in the pattern, visible as thick black lines (indicated by blues lines in Figure 6.19 A). These observations suggest that most compartments are connected to their neighbors, with some barriers being completely closed off. None or only very slow fluorescence recovery events were observed when a section of the border was cut off. Since these impenetrable borders are often formed by extremely wide barriers, these results indicate that the absence of diffusion between compartments correlates with

the barrier width. Unfortunately, pair-correlation is not able to reliably measure diffusion for such large barrier width. Bleaching experiments, on the other hand, do not contain information about the directionality of the diffusion. This means that absolute barriers may only be observed for extended defects, while the dyes can diffuse around individual wide barriers, and therefore no bleaching is observed.

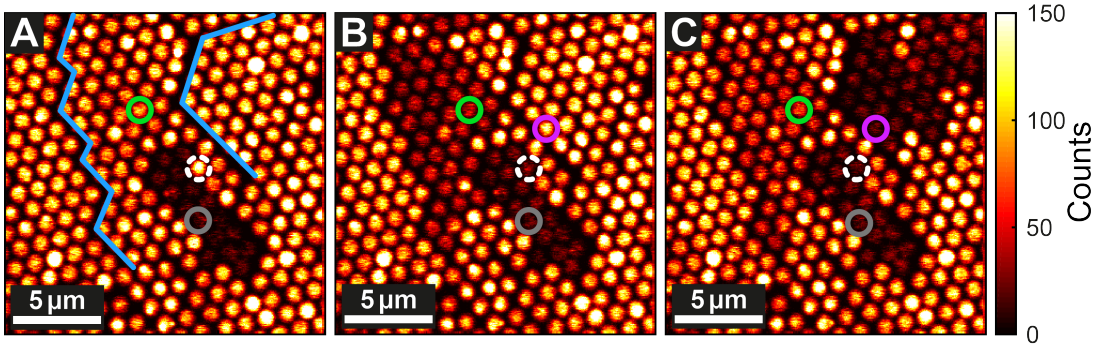

Figure 6.19: Images from fluorescence bleaching experiments on a sample with 18 nm high chrome barriers. A) Fluorescence image after illumination of the region marked with the gray circle for 2 min with 30 µW of the 635 nm laser. The blue lines show particularly thick barriers caused by defects in the polystyrene beads monolayer during pattern synthesis. B) Image after additional illumination of the region marked with the green circle for 4 min. The white dotted circle indicates a compartment that merged with the darker region next to it between images A) and B), slightly increasing the average intensity of the region. C) Image after an additional illumination of the compartment indicated by the purple circle for 7 min. The fluorescence intensity of the region bleached between images A) and B) partially recovered in C).

While most experiments showed some correlation amplitude across a barrier, such behavior was not uniform throughout the whole sample. Some regions (extending over several tens to hundreds of micrometers) showed a much lower connectivity between compartments. Here, no direct diffusion was observed between the majority of compartments, accompanied by increased bleaching (Figure 6.20). Even in these areas, the compartments were not completely isolated. Judging from the PCF data and the bleached patterns (Figure 6.20 B), on average about two to three out of six sides allowed diffusion. This was enough to form larger connected regions that were, however, completely isolated from the neighboring regions. Over the course of the experiment, this resulted in various degrees of bleaching, depending on the size of the region and the duration it was illuminated (Figure 6.20 B). Interestingly, the degree of connectivity of the area was maintained even when the sample was cleaned and a new lipid bilayer formed (Figure 6.20 C). The exact barriers allowing or impeding diffusion, however, were different each time, indicating some degree of variation and probabilistic behavior.

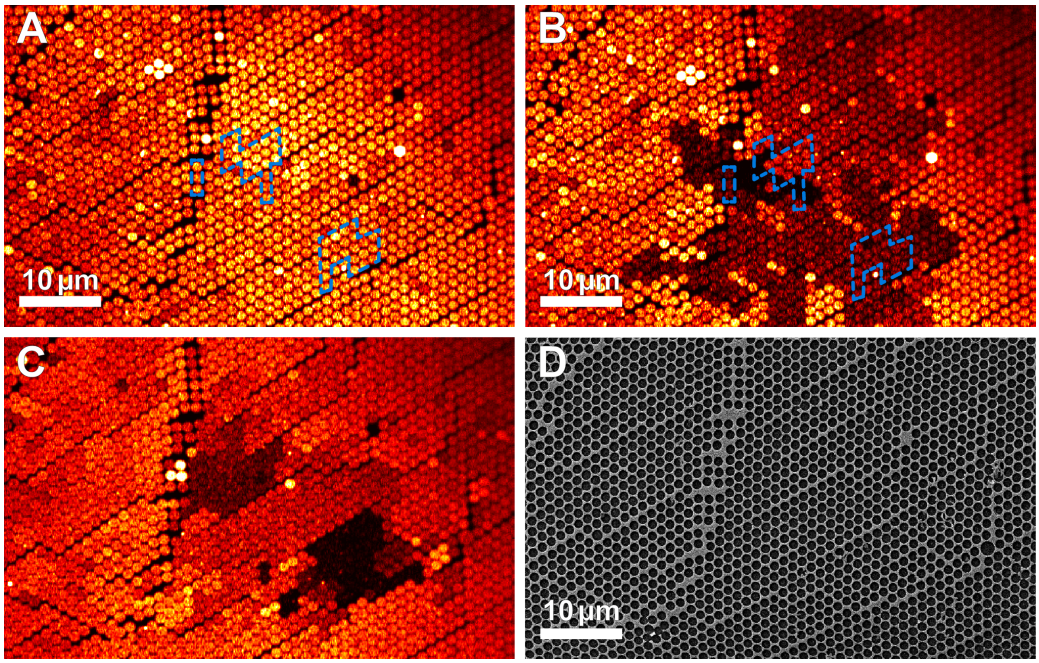

Figure 6.20: Fluorescence and electron microscopy images of a region showing low compartment connectivity on a sample with 18 nm chrome layer. A) Fluorescence image before pair correlation measurements. B) Image of the same region after the pair-correlation measurements were performed. The blue dotted lines indicate regions that were illuminated during the scans. In this case, scans were performed along the y-axis. C)Fluorescence image of the same area as in A) and B) for a new, freshly prepared lipid bilayer. To test quenching, similar regions as in B) were illuminated. D) SEM image of the same area as in A-C).

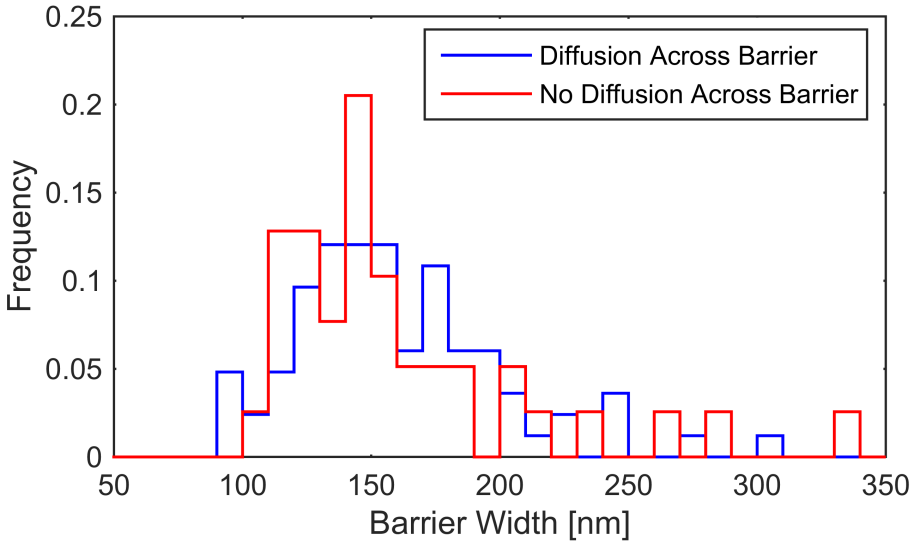

Figure 6.21: Width distribution for barriers which allow diffusion (blue, $n = 83$) and prevent it (red, $n = 39$).

Although these data were not used for the pair correlation analysis, the regions were still imaged with SEM to determine the barrier width (Figure 6.20 C). No obvious differences to areas allowing diffusion were detected when viewed by electron microscopy. Even the barrier size distribution is the same, with most barriers widths being around 100–200 nm (Figure 6.21). However, the low conductivity of the sample, even after evaporation of a carbon layer, prohibited recording of higher resolution images. Therefore, other features that might affect diffusion behavior, such as surface properties or the steepness of the barriers, could not be resolved.

6.5 Discussion and Conclusion

According to literature, chrome surfaces are believed to form clear and absolute borders for fluid lipid layers, preventing any diffusion across them.[145,146] Here, however, we unambiguously show that under certain conditions, the mobility of lipids on top of the chrome can still be maintained. While bleaching experiments established that individual compartments are connected, pair correlation analysis combined with electron microscopy has revealed that lipid bound dyes move directly across the metal barriers. Although pair correlation could not show a direct relationship between the diffusion behavior and barrier width and height, it revealed a decrease in diffusion as a result of an increased plasma etching time and, therefore, the chrome coverage. Furthermore, wide metal barriers (caused by defects in the monolayer of the polystyrene beads) often formed the borders of patterns created during fluorescence bleaching experiments. This strongly suggests that the barrier size is a key factor controlling diffusion. Moreover, the presence of areas exhibiting low connectivity, even for similar barrier width distributions when compared to better connected regions, indicate that other contributions must be also considered. These areas maintained their degree of connectivity throughout several measurements and cleaning cycles, albeit with variations in the fine structure. This suggests that certain randomness aspects are present and that it is the probability of a connection between compartments that depends on the barrier width.
Many of our results are in good agreement with the results reported by *Tsai et al.* in 2008.[148] The authors described the synthesis of long, parallel spacers of chrome and titanium, which were used for forming supported lipid bilayers. Using fluorescence recovery after photobleaching, they investigated the influence of these spacers and of the size of gaps on the diffusion parallel and perpendicular to these barriers. Although no crossing was observed for continuous chrome spacers, titanium still allowed diffusion across barriers without any gaps. The study further showed that complete fluorescence recovery was possible even for a square pattern forming individual compartments, as long as the duration of light exposure was short. Longer photobleaching resulted in broken patterns and fragmentation, similar to our observations in some regions (Figure 6.20). However, when the width of the titanium spacers was increased from 50 nm to 100 nm, the mobility across the metal was prevented completely.

In contrast to our results, the mobility was only observed on titanium and not on the chrome, and the cutoff barrier width was significantly smaller. These discrepancies, however, are most likely caused by the different methods used to form the lipid bilayers. While *Tsai et al.* used egg phosphatidylcholine unilamellar vesicles generated by extrusion through 50 nm pores, our preparation method used 200 nm sized unilamellar vesicles consisting of DOPC. The difference in diameter of vesicles is important if one assumes that the lipid bilayer requires interactions on both sides of the barrier to form a connection, as was discussed by *Tsai et al.*. Larger vesicles can therefore bridge wider barriers while still having a maximum span. For a diameter of 50 nm, the cutoff is somewhere in the range of 50–100 nm. Assuming a linear dependence, the maximal barrier width for 200 nm large vesicles would be somewhere between 200 nm and 400 nm. These values correspond very well both to the 200–300 nm wide barriers still allowing diffusion (Figure 6.21), as well as to the width of defects (typically >400 nm) that prohibit mobility.
A variety of different factors may have contributed to the distinct behavior of chrome in our case, including the method of generating the patterns, the surface roughness and barrier steepness, the lipids used, as well as the concentration and type of dye. Chrome may have a lower propensity for allowing lipid bridges to form compared to titanium, thus requiring larger vesicles for the same barrier width.
In conclusion, our experiments clearly demonstrate that chrome is not always an absolute barrier for lipid diffusion and that connections over the metal are possible. These connections allow lipids to cross the barriers, albeit at a slower rate. These results strongly suggest that the interplay between the barrier and the vesicle size is essential in determining this behavior.

6.6 Sample Preparation and Experimental Conditions

The chrome patterned substrates were synthesized and characterized by Dr. Paul Kühler and Anastasia Babynina in the Group of Dr. Theobald Lohmülller. SEM experiments for correlative microscopy were performed together with Anastasia Babynina. These methods are mentioned here for completeness.

Chrome Pattern Generation

Colloidal lithography was used for the fabrication of chrome nano-triangle patterns.[147] In a first step, a hexagonal monolayer of polystyrene beads (950 nm or 1280 nm diameter) was self-assembled on a water surface. It was deposited on borosilicate glass substrates by slowly pumping out the water. Samples were subsequently etched with an oxygen plasma (Plasma System FEMTO equipped with a RIE electrode, Diener Electronic). Different times of etching (100–450 s for 950 nm sized beads and 400 s for 1280 nm sized beads) were selected to adjust gap size and barrier width. A group of patterns were not etched to achieve the

largest gap sizes. For patterns with 950 nm diameter 6 nm thick chrome layer was evaporated at a pressure of 2×10^{-6} mbar with a rate of $2\,\text{Å}\,\text{s}^{-1}$ using an Edwards Auto 306 Turbo thermal evaporator (Edwards). The metal height was set to 6 nm, 18 nm or 37 nm for 1280 nm sized samples using the same conditions. Finally, the polystyrene beads were removed with a sticky tape.

Scanning Electron Microscopy

High resolution images were recorded with a Gemini Ultra Plus field emission scanning electron microscope (Zeiss). Acceleration voltage was set either to 1 kV or 3 kV. The working distance ranged between 4.0 mm and 5.9 mm. Both values were adjusted to achieve optimal image quality for each individual sample.

Vesicle Preparation

For preparing vesicles, 30 µL of a DOPC solution in chloroform ($10\,\text{mg}\,\text{mL}^{-1}$) was added to a test tube and dried with a nitrogen stream. After complete evaporation of the chloroform, the test tube were further dried for 2 h in an exicator. The same procedure was also performed with a solution containing an additional $5\,\text{µg}\,\text{mL}^{-1}$ of Atto647N labeled 1,2-dipalmitoyl-sn-glycero-3-phosphoethanolamine (Atto647N-DPPE), resulting in 0.05 wt % of dye modified lipids. The test tubes were sealed off with parafilm and stored at −20 °C for up to a month.
Before each experiment, 400 µL of 5× phosphate buffered saline solution (5×PBS, 685 mM NaCl, 13.5 mM KCl, 50 mM Na_2HPO_4, 9 mM KH_2PO_4) was added to the test tubes. The lipids were resuspended using a vortexer, creating multilamellar vesicles. Large unilamellar vesicles (LUVs) were formed via extrusion of multilamellar vesicles through a membrane with 200 nm large pores (LiposoFast, Sigma Aldrich) for a total of 30 times. Atto647N-DPPE spiked and pure DOPC LUV solutions were mixed in a 1:10 ratio, resulting in 5 ppm of labeled lipids.

Generation of the Lipid Bilayer

Before applying the lipid bilayer to the patterned surfaces, the chrome substrates surface was cleaned and activated for 30–45 min with a plasma cleaner (Plasma System Zepto, Diener Electronic) under air atmosphere. After adding a drop of LUV solution, it was placed face down on a petri dish, forming a thin water layer between the two surfaces. Afterwards, the whole petri dish was submerged in 50–100 mL of deionized water to make the vesicles burst. Keeping the sample under water, a cover glass was attached. A thin spacer (a double sided tape or clear nail polish) on the glass created a small chamber ensuring that the lipid bilayer was kept hydrated during the measurements. Only after sealing the chamber was the sample removed from the water bath, dried externally and used for experiments.
After fluorescence measurements, the sample was submerged in chloroform for a few hours to remove the tape or nail polish and the lipids. Afterwards it was rinsed

extensively with ethanol followed by deionized water, then dried and stored until further experiments.

Confocal Fluorescence Microscopy

All fluorescence experiments were performed on the confocal microscope described in chapter 2.6 using a 1.49 NA 100× oil immersion objective. The sample was positioned to allow all the individual compartments to form a straight line along either the x- or the y-axis. To keep the lipid membrane in focus, a perfect focus system was employed during the experiments.
For pair-correlation experiments, a 3 µm long line was repeatedly scanned across two barriers and three compartments. Each measurement lasted for 2 min and was repeated 5 times, resulting in a total duration of 10 min. The long measurement time ensured a high signal-to-noise ratio while repeated experiments allowed simpler correction of a small axial drift during the analysis. The 635 nm excitation laser power was kept at 3–5 µW measured before the objective. When correlative SEM measurements were performed, a fluorescence image at maximal range (60 µm×60 µm) was recorded. Additionally, bright field images of the area were taken, using the 100× oil immersion and a 30× air objective. This facilitated identification of the same region that was subsequently measured by electron microscopy.
For bleaching experiments, individual compartments were illuminated with higher laser power (30–200 µW) for several minutes. Images were recorded before and after bleaching.

7. Summary and Outlook

The central aspect of this thesis is the development of software for analyzing advanced fluorescence spectroscopy data and the subsequent application of these algorithms to current research topics. The goal during the design and optimization of the program, called *PIE Analysis in Matlab* (*PAM*), was to create a platform that is both versatile by supporting a multitude of different data types and analysis methods, as well as flexible by allowing the adjust the underlying algorithms to the needs of the current project. To achieve these two aims, *PAM* is structured as a core program that branches into semi-independent applications for the different analysis methods. This modular setup minimizes the direct interactions between the individual parts of the program, simplifying the implementation of new functionalities and the modification of existing algorithms.
Currently, the capabilities of *PAM* include, among others, auto-, cross- and pair-correlation analysis (FCS, PCF), various image fluctuation techniques (RICS, STICS, etc.), fluorescence lifetime analysis (Phasor FLIM) and burst-wise FRET analysis (programed by Anders Barth). This broad spectrum of analysis methods is one of the main strengths of *PAM*. While a variety of other software packages for quantitative fluorescence data analysis have been developed and published, most of these programs focus on just a single analysis technique (e.g. FCS[149], stochastic reconstruction microscopy[150]), limiting the amount information that can be extracted from the data. The second big advantage of *PAM* is its utilization of pulsed interleaved excitation (PIE) data. Although several other programs are equipped to use PIE,[151] *PAM* is unique in putting PIE into the center of its design concept, optimizing its potential for multi-color analysis.
PAM's capabilities were utilized for two projects concerning metal-organic frameworks (MOFs). MOFs consist of inorganic clusters that are cross-linked by organic linkers forming extended crystalline structures. This versatility in composition and the high porosity make MOF potential candidate for a variety of industrial applications. In the first project, fluorescence quenching of fluorescein in the MIL-101(Al)-NH_2 was investigated. For the MOF, two morphological groups were identified, one consisting of aggregates of smooth round particles, while the second morphology showed a rougher needle-like structure. The differences in morphology are linked to differences in fluorescein quenching mediated via defects in the crystal structure. Furthermore, a second all-or-nothing quenching mechanism was attributed to unmodified amino groups.
In the second project, *de novo* and solvent assisted linker exchange functionalization mechanisms in the MOF UiO-67 were investigated. Detailed fluorescence lifetime analysis revealed that the fluorophores are incorporated homogeneously throughout the crystals during synthesis. However, the incorporation of the large complex functional groups introduces defects into the structure. The introduction of the dye into the scaffold via linker shows less effect on the lattice. Here, the fluorophores

modified linkers bind in two distinct mechanism to the crystals. Initially, the linkers attach to under-coordinated metal sites at the outer surface. In the second mechanism, requiring more time and elevated temperatures, individual linkers are exchanged homogeneously throughout the crystals. The data further proved that linker exchange is based on substitution and not on dissolution/recrystallization.
In a third application, pair-correlation analysis and fluorescence bleaching were used to study the influence of chrome nano barriers on the diffusion in supported lipid bilayers. Such nano-scaled chrome patterns are frequently used to separate reconstituted membranes into non-connected compartments. Our results prove that, contrary to the previous understanding, these chrome structures do not necessarily constitute absolute barriers that prohibit diffusion between individual compartments. Rather, the presence or absence of mobility across chrome structure is determined by the width of the barrier.

Currently, a clear trend that goes towards a more quantitative analysis of fluorescence image data is noticeable in the life sciences. This is accompanied by an increase in the number of scientists who are working with advanced fluorescence techniques and using the analysis software. Given their background, these new users are more likely to be experts in the field of biology or biochemistry rather than specialists in fluorescence applications. This means that the software tools need to be adjusted to this new group of lay users. In its current state, *PAM* is targeted more towards experts in the individual methods. While the better established approaches, such as FCS, are implemented in a straightforward and easy-to-use way, the more advanced techniques, e.g. image fluctuation analysis, still require considerate expertise in their application. One challenge in the future development of *PAM* will be to create a balance between these two sides: Being simple and accessible enough for casual users, but at the same time allowing the specialist to use a variety of techniques and approaches.
Another consequence of the increased popularity of quantitative fluorescence methods is the development of new approaches and applications. In the last decade, the number of different advanced fluorescence techniques has grown considerably (see chapter 3) and the variety is bound to increase further in the future. Moreover, the applicability of these methods is not only limited to the biophysical field. As I have shown in chapter 5, fluorescence spectroscopy and microscopy can also be utilized in material science where they are still rarely used. Combining the established techniques with fluorescence application can be a powerful tool to investigate the properties of and processes in solid-state materials.

References

[1] The nobel prize in chemistry 2008. Nobelprize.org. Nobel Media AB 2014. http:\\www.nobelprize.org\nobel_prizes\chemistry\laureates\2008\index.html Accessed: 25 May 2016.

[2] The nobel prize in chemistry 2014. Nobelprize.org. Nobel Media AB 2014. http:\\www.nobelprize.org\nobel_prizes\chemistry\laureates\2014\index.html Accessed: 25 May 2016.

[3] Marvin Minsky. Microscopy apparatus, December 19 1961. US Patent 3,013,467.

[4] Wolfgang Becker. *Advanced time-correlated single photon counting techniques*. Number 81 in Springer series in chemical physics. Springer, Berlin ; New York, 2005.

[5] Desmond V. O'Connor and David Phillips. Einzelphotonenzählung: Time-Correlated Single Photon Counting. *Nachrichten aus Chemie, Technik und Laboratorium*, 33(10):896–896, April 1985.

[6] Barbara K. Müller, Evgeny Zaychikov, Christoph Bräuchle, and Don C. Lamb. Pulsed Interleaved Excitation. *Biophysical Journal*, 89(5):3508–3522, November 2005.

[7] Jelle Hendrix, Waldemar Schrimpf, Mathias Höller, and Don C. Lamb. Pulsed Interleaved Excitation Fluctuation Imaging. *Biophysical Journal*, 105(4):848–861, August 2013.

[8] Volodymyr Kudryavtsev, Martin Sikor, Stanislav Kalinin, Dejana Mokranjac, Claus A. M. Seidel, and Don C. Lamb. Combining MFD and PIE for Accurate Single-Pair Förster Resonance Energy Transfer Measurements. *ChemPhysChem*, 13(4):1060–1078, March 2012.

[9] Elke Haustein and Petra Schwille. Fluorescence Correlation Spectroscopy: Novel Variations of an Established Technique. *Annual Review of Biophysics and Biomolecular Structure*, 36(1):151–169, June 2007.

[10] Sergey Tetin. *Fluorescence fluctuation spectroscopy (FFS)*, volume 519. Academic Press, 2012.

[11] Oleg Krichevsky and Grégoire Bonnet. Fluorescence correlation spectroscopy: the technique and its applications. *Reports on Progress in Physics*, 65(2):251–297, February 2002.

[12] Nirmalya Bag and Thorsten Wohland. Imaging Fluorescence Fluctuation Spectroscopy: New Tools for Quantitative Bioimaging. *Annual Review of Physical Chemistry*, 65(1):225–248, April 2014.

[13] Rudolf Rigler and Elliot S. Elson. *Fluorescence Correlation Spectroscopy Theory and Applications*. Springer Berlin Heidelberg, Berlin, Heidelberg, 2001.

[14] Wolfgang Becker. Fluorescence lifetime imaging - techniques and applications: FLUORESCENCE LIFETIME IMAGING. *Journal of Microscopy*, 247(2):119–136, August 2012.

[15] Yi-Chun Chen and Robert M. Clegg. Fluorescence lifetime-resolved imaging. *Photosynthesis Research*, 102(2-3):143–155, December 2009.

[16] Todd French, Peter T. So, Chen Y. Dong, Keith M. Berland, and Enrico Gratton. Fluorescence lifetime imaging techniques for microscopy. *Methods in Cell Biology*, 56:277–304, 1998.

[17] Erik B. van Munster and Theodorus W. J. Gadella. Fluorescence Lifetime Imaging Microscopy (FLIM). In Jens Rietdorf, editor, *Microscopy Techniques*, volume 95, pages 143–175. Springer Berlin Heidelberg, Berlin, Heidelberg, May 2005.

[18] Theodor Svedberg and Katsuji Inouye. Eine neue methode zur prüfung der gültigkeit des boyle-gay-lussacschen gesetzes für kolloide lösungen. *Zeit Phys Chem*, 77:145–191, 1911.

[19] Douglas Magde, Elliot L. Elson, and Watt W. Webb. Fluorescence correlation spectroscopy. II. An experimental realization. *Biopolymers*, 13(1):29–61, 1974.

[20] Yan Chen, Joachim D. Müller, Peter T.C. So, and Enrico Gratton. The photon counting histogram in fluorescence fluctuation spectroscopy. *Biophysical journal*, 77(1):553–567, 1999.

[21] Peet Kask, Kaupo Palo, Dirk Ullmann, and Karsten Gall. Fluorescence-intensity distribution analysis and its application in biomolecular detection technology. *Proceedings of the National Academy of Sciences*, 96(24):13756–13761, 1999.

[22] Joachim D. Müller. Cumulant Analysis in Fluorescence Fluctuation Spectroscopy. *Biophysical Journal*, 86(6):3981–3992, June 2004.

[23] Douglas Magde, Elliot Elson, and Watt W. Webb. Thermodynamic fluctuations in a reacting system—measurement by fluorescence correlation spectroscopy. *Physical Review Letters*, 29(11):705, 1972.

[24] Elliot L. Elson and Douglas Magde. Fluorescence correlation spectroscopy. I. Conceptual basis and theory. *Biopolymers*, 13(1):1–27, 1974.

[25] H. Jeff Kimble, Mario Dagenais, and Leonard Mandel. Photon antibunching in resonance fluorescence. *Physical Review Letters*, 39(11):691, 1977.

[26] Peet Kask, Peeter Piksarv, and Ülo Mets. Fluorescence correlation spectroscopy in the nanosecond time range: photon antibunching in dye fluorescence. *European Biophysics Journal*, 12(3):163–166, 1985.

[27] W. Patrick Ambrose, Peter M. Goodwin, Jörg Enderlein, David J. Semin, John C. Martin, and Richard A. Keller. Fluorescence photon antibunching from single molecules on a surface. *Chemical Physics Letters*, 269(3-4):365–370, May 1997.

[28] Jan Sýkora, Karin Kaiser, Ingo Gregor, Wolfgang Bönigk, Günther Schmalzing, and Jörg Enderlein. Exploring Fluorescence Antibunching in Solution To Determine the Stoichiometry of Molecular Complexes. *Analytical Chemistry*, 79(11):4040–4049, June 2007.

[29] Måns Ehrenberg and Rudolf Rigler. Rotational brownian motion and fluorescence intensify fluctuations. *Chemical Physics*, 4(3):390–401, June 1974.

[30] Peet Kask, Peeter Piksarv, Ülo Mets, M. Pooga, and E. Lippmaa. Fluorescence correlation spectroscopy in the nanosecond time range: rotational diffusion of bovine carbonic anhydrase B. *European Biophysics Journal*, 14(4):257–261, 1987.

[31] Peet Kask, Peeter Piksarv, M. Pooga, Ülo Mets, and E. Lippmaa. Separation of the rotational contribution in fluorescence correlation experiments. *Biophysical journal*, 55(2):213, 1989.

[32] Christoph M. Pieper and Jörg Enderlein. Fluorescence correlation spectroscopy as a tool for measuring the rotational diffusion of macromolecules. *Chemical Physics Letters*, 516(1-3):1–11, November 2011.

[33] Jerker Widengren, Rudolf Rigler, and Ãœlo Mets. Triplet-state monitoring by fluorescence correlation spectroscopy. *Journal of Fluorescence*, 4(3):255–258, 1994.

[34] Jerker Widengren, Uelo Mets, and Rudolf Rigler. Fluorescence correlation spectroscopy of triplet states in solution: a theoretical and experimental study. *The Journal of Physical Chemistry*, 99(36):13368–13379, 1995.

[35] Jerker Widengren. Photophysical Aspects of FCS Measurements. In F. P. Schäfer, J. P. Toennies, and W. Zinth, editors, *Fluorescence Correlation Spectroscopy*, volume 65, pages 276–301. Springer Berlin Heidelberg, Berlin, Heidelberg, 2001.

[36] Andreas Schönle, Claas Von Middendorff, Christian Ringemann, Stefan W. Hell, and Christian Eggeling. Monitoring triplet state dynamics with fluorescence correlation spectroscopy: Bias and correction: MONITORING DARK STATE DYNAMICS WITH FCS. *Microscopy Research and Technique*, 77(7):528–536, July 2014.

[37] Tedman Torres and Marcia Levitus. Measuring Conformational Dynamics: A New FCS-FRET Approach. *The Journal of Physical Chemistry B*, 111(25):7392–7400, June 2007.

[38] Suren Felekyan, Hugo Sanabria, Stanislav Kalinin, Ralf Kühnemuth, and Claus A.M. Seidel. Analyzing Förster Resonance Energy Transfer with Fluctuation Algorithms. In *Methods in Enzymology*, volume 519, pages 39–85. Elsevier, 2013.

[39] Sören Doose, Hannes Neuweiler, and Markus Sauer. Fluorescence Quenching by Photoinduced Electron Transfer: A Reporter for Conformational Dynamics of Macromolecules. *ChemPhysChem*, 10(9-10):1389–1398, July 2009.

[40] Markus Sauer and Hannes Neuweiler. PET-FCS: Probing Rapid Structural Fluctuations of Proteins and Nucleic Acids by Single-Molecule Fluorescence Quenching. In Yves Engelborghs and Antonie J.W.G. Visser, editors, *Fluorescence Spectroscopy and Microscopy*, volume 1076, pages 597–615. Humana Press, Totowa, NJ, 2014.

[41] Ming Zhao, Lei Jin, Bo Chen, Yao Ding, Hui Ma, and Dieyan Chen. Afterpulsing and its correction in fluorescence correlation spectroscopy experiments. *Applied optics*, 42(19):4031–4036, 2003.

[42] Jörg Enderlein and Ingo Gregor. Using fluorescence lifetime for discriminating detector afterpulsing in fluorescence-correlation spectroscopy. *Review of Scientific Instruments*, 76(3):033102, 2005.

[43] Peter Kapusta, Michael Wahl, Aleš Benda, Martin Hof, and Jörg Enderlein. Fluorescence Lifetime Correlation Spectroscopy. *Journal of Fluorescence*, 17(1):43–48, December 2006.

[44] Suren Felekyan, Stanislav Kalinin, Alessandro Valeri, and Claus A. M. Seidel. Filtered FCS and species cross correlation function. page 71830D, February 2009.

[45] Suren Felekyan, Stanislav Kalinin, Hugo Sanabria, Alessandro Valeri, and Claus A. M. Seidel. Filtered FCS: Species Auto- and Cross-Correlation Functions Highlight Binding and Dynamics in Biomolecules. *ChemPhysChem*, 13(4):1036–1053, March 2012.

[46] Thomas Weidemann and Petra Schwille. Dual-Color Fluorescence Cross-Correlation Spectroscopy with Continuous Laser Excitation in a Confocal Setup. In *Methods in Enzymology*, volume 518, pages 43–70. Elsevier, 2013.

[47] Petra Schwille, Franz-Josef Meyer-Almes, and Rudolf Rigler. Dual-color fluorescence cross-correlation spectroscopy for multicomponent diffusional analysis in solution. *Biophysical journal*, 72(4):1878, 1997.

[48] Kirsten Bacia and Petra Schwille. Practical guidelines for dual-color fluorescence cross-correlation spectroscopy. *Nature Protocols*, 2(11):2842–2856, November 2007.

[49] Yong Hwee Foo, Nikolaus Naredi-Rainer, Don C. Lamb, Sohail Ahmed, and Thorsten Wohland. Factors Affecting the Quantification of Biomolecular Interactions by Fluorescence Cross-Correlation Spectroscopy. *Biophysical Journal*, 102(5):1174–1183, March 2012.

[50] Jörg Enderlein, Ingo Gregor, Digambara Patra, Thomas Dertinger, and U. Benjamin Kaupp. Performance of Fluorescence Correlation Spectroscopy for Measuring Diffusion and Concentration. *ChemPhysChem*, 6(11):2324–2336, November 2005.

[51] Axel Amediek, Elke Haustein, Dag Scherfeld, and Petra Schwille. Scanning Dual-Color Cross-Correlation Analysis for Dynamic Co-Localization Studies of Immobile Molecules. *Single Molecules*, 3(4):201–210, August 2002.

[52] Qiaoqiao Ruan, Melanie A. Cheng, Moshe Levi, Enrico Gratton, and William W. Mantulin. Spatial-Temporal Studies of Membrane Dynamics: Scanning Fluorescence Correlation Spectroscopy (SFCS). *Biophysical Journal*, 87(2):1260–1267, August 2004.

[53] Thomas Dertinger, Victor Pacheco, Iris von der Hocht, Rudolf Hartmann, Ingo Gregor, and Jörg Enderlein. Two-Focus Fluorescence Correlation Spectroscopy: A New Tool for Accurate and Absolute Diffusion Measurements. *ChemPhysChem*, 8(3):433–443, February 2007.

[54] Christoph Pieper, Kerstin Weiß, Ingo Gregor, and Jörg Enderlein. Dual-Focus Fluorescence Correlation Spectroscopy. In *Methods in Enzymology*, volume 518, pages 175–204. Elsevier, 2013.

[55] Michelle A. Digman and Enrico Gratton. Imaging Barriers to Diffusion by Pair Correlation Functions. *Biophysical Journal*, 97(2):665–673, July 2009.

[56] Elizabeth Hinde, Michelle A. Digman, Klaus M. Hahn, and Enrico Gratton. Millisecond spatiotemporal dynamics of FRET biosensors by the pair correlation function and the phasor approach to FLIM. *Proceedings of the National Academy of Sciences*, 110(1):135–140, January 2013.

[57] Elizabeth Hinde, Francesco Cardarelli, Michelle A. Digman, and Enrico Gratton. In vivo pair correlation analysis of EGFP intranuclear diffusion reveals DNA-dependent molecular flow. *Proceedings of the National Academy of Sciences*, 107(38):16560–16565, September 2010.

[58] Francesco Cardarelli and Enrico Gratton. In vivo imaging of single-molecule translocation through nuclear pore complexes by pair correlation functions. *PLoS ONE*, 5(5):e10475, May 2010.

[59] Paul W. Wiseman. Image Correlation Spectroscopy. In *Methods in Enzymology*, volume 518, pages 245–267. Elsevier, 2013.

[60] Michelle A. Digman, Milka Stakic, and Enrico Gratton. Raster Image Correlation Spectroscopy and Number and Brightness Analysis. In *Methods in Enzymology*, volume 518, pages 121–144. Elsevier, 2013.

[61] Radek Machan and Thorsten Wohland. Recent applications of fluorescence correlation spectroscopy in live systems. *FEBS Letters*, 588(19):3571–3584, October 2014.

[62] Niles O. Petersen, Pia L. Höddelius, Paul W. Wiseman, Olle Seger, and Karl-Eric Magnusson. Quantitation of membrane receptor distributions by image correlation spectroscopy: concept and application. *Biophysical journal*, 65(3):1135, 1993.

[63] Mamta Srivastava and Nils O. Petersen. Image cross-correlation spectroscopy: a new experimental biophysical approach to measurement of slow diffusion of fluorescent molecules. *Methods in cell science*, 18(1):47–54, 1996.

[64] Paul W. Wiseman and Nils O. Petersen. Image correlation spectroscopy. II. Optimization for ultrasensitive detection of preexisting platelet-derived growth factor-β receptor oligomers on intact cells. *Biophysical journal*, 76(2):963–977, 1999.

[65] Michelle A. Digman, Parijat Sengupta, Paul W. Wiseman, Claire M. Brown, Alan R. Horwitz, and Enrico Gratton. Fluctuation Correlation Spectroscopy with a Laser-Scanning Microscope: Exploiting the Hidden Time Structure. *Biophysical Journal*, 88(5):L33–L36, May 2005.

[66] Michelle A. Digman, Paul W. Wiseman, Alan R. Horwitz, and Enrico Gratton. Detecting Protein Complexes in Living Cells from Laser Scanning Confocal Image Sequences by the Cross Correlation Raster Image Spectroscopy Method. *Biophysical Journal*, 96(2):707–716, January 2009.

[67] David L. Kolin, Santiago Costantino, and Paul W. Wiseman. Sampling Effects, Noise, and Photobleaching in Temporal Image Correlation Spectroscopy. *Biophysical Journal*, 90(2):628–639, January 2006.

[68] Santiago Costantino, Jonathan W.D. Comeau, David L. Kolin, and Paul W. Wiseman. Accuracy and Dynamic Range of Spatial Image Correlation and Cross-Correlation Spectroscopy. *Biophysical Journal*, 89(2):1251–1260, August 2005.

[69] Claire M. Brown, Benedict Hebert, David L. Kolin, Jessica Zareno, Leanna Whitmore, Alan Rick Horwitz, and Paul W. Wiseman. Probing the integrin-actin linkage using high-resolution protein velocity mapping. *Journal of Cell Science*, 119(24):5204–5214, December 2006.

[70] Carmine Di Rienzo, Enrico Gratton, Fabio Beltram, and Francesco Cardarelli. Fast spatiotemporal correlation spectroscopy to determine protein lateral diffusion laws in live cell membranes. *Proceedings of the National Academy of Sciences*, 110(30):12307–12312, July 2013.

[71] Rooshin B. Dalal, Michelle A. Digman, Alan F. Horwitz, Valeria Vetri, and Enrico Gratton. Determination of particle number and brightness using a laser scanning confocal microscope operating in the analog mode. *Microscopy Research and Technique*, 71(1):69–81, January 2008.

[72] Michelle A. Digman, Rooshin Dalal, Alan F. Horwitz, and Enrico Gratton. Mapping the Number of Molecules and Brightness in the Laser Scanning Microscope. *Biophysical Journal*, 94(6):2320–2332, March 2008.

[73] Michelle A. Digman, Paul W. Wiseman, Colin Choi, Alan R. Horwitz, and Enrico Gratton. Stoichiometry of molecular complexes at adhesions in living cells. *Proceedings of the National Academy of Sciences*, 106(7):2170–2175, 2009.

[74] A. Prasanna de Silva and Saliya A. de Silva. Fluorescent signalling crown ethers; ?switching on? of fluorescence by alkali metal ion recognition and binding in situ. *Journal of the Chemical Society, Chemical Communications*, (23):1709, 1986.

[75] Joseph R. Lakowicz, Henryk Szmacinski, and Michael L. Johnson. Calcium imaging using fluorescence lifetimes and long-wavelength probes. *Journal of Fluorescence*, 2(1):47–62, March 1992.

[76] Kohki Okabe, Noriko Inada, Chie Gota, Yoshie Harada, Takashi Funatsu, and Seiichi Uchiyama. Intracellular temperature mapping with a fluorescent polymeric thermometer and fluorescence lifetime imaging microscopy. *Nature Communications*, 3:705, February 2012.

[77] Tianyu Liu, Xiaogang Liu, David R. Spring, Xuhong Qian, Jingnan Cui, and Zhaochao Xu. Quantitatively Mapping Cellular Viscosity with Detailed Organelle Information via a Designed PET Fluorescent Probe. *Scientific Reports*, 4, June 2014.

[78] Takakazu Nakabayashi and Nobuhiro Ohta. Sensing of Intracellular Environments by Fluorescence Lifetime Imaging of Exogenous Fluorophores. *Analytical Sciences*, 31(4):275–285, 2015.

[79] Takatoku Oida, Yasushi Sako, and Akihiro Kusumi. Fluorescence lifetime imaging microscopy (flimscopy). Methodology development and application to studies of endosome fusion in single cells. *Biophysical journal*, 64(3):676, 1993.

[80] Brian J. Bacskai, Binyamin Hochner, Martyn Mahaut-Smith, Stephen R. Adams, Bong-Kiun Kaang, Eric R. Kandel, and Roger Y. Tsien. Spatially resolved dynamics of cAMP and protein kinase A subunits in Aplysia sensory neurons. *Science (New York, N.Y.)*, 260(5105):222–226, April 1993.

[81] Horst Wallrabe and Ammasi Periasamy. Imaging protein molecules using FRET and FLIM microscopy. *Current Opinion in Biotechnology*, 16(1):19–27, February 2005.

[82] Alan E. W. Knight and Ben K. Selinger. The deconvolution of fluorescence decay curves. *Spectrochimica Acta Part A: Molecular Spectroscopy*, 27(8):1223–1234, August 1971.

[83] Marc. Van Den Zegel, Noël Boens, D. Daems, and Frans .C. De Schryver. Possibilities and limitations of the time-correlated single photon counting technique: a comparative study of correction methods for the wavelength dependence of the instrument response function. *Chemical Physics*, 101(2):311–335, January 1986.

[84] A. S. Verkman, Michael Armijo, and Kiyohide Fushimi. Construction and evaluation of a frequency-domain epifluorescence microscope for lifetime and anisotropy decay measurements in subcellular domains. *Biophysical chemistry*, 40(1):117–125, 1991.

[85] Theodorus W.J. Gadella, Thomas M. Jovin, and Robert M. Clegg. Fluorescence lifetime imaging microscopy (FLIM): Spatial resolution of microstructures on the nanosecond time scale. *Biophysical Chemistry*, 48(2):221–239, December 1993.

[86] Glen I. Redford and Robert M. Clegg. Polar Plot Representation for Frequency-Domain Analysis of Fluorescence Lifetimes. *Journal of Fluorescence*, 15(5):805–815, September 2005.

[87] Michelle A. Digman, Valeria R. Caiolfa, Moreno Zamai, and Enrico Gratton. The Phasor Approach to Fluorescence Lifetime Imaging Analysis. *Biophysical Journal*, 94(2):L14–L16, January 2008.

[88] Takuhiro Otosu, Kunihiko Ishii, and Tahei Tahara. Note: Simple calibration of the counting-rate dependence of the timing shift of single photon avalanche diodes by photon interval analysis. *Review of Scientific Instruments*, 84(3):036105, 2013.

[89] Katrin G. Heinze, Michael Jahnz, and Petra Schwille. Triple-color coincidence analysis: one step further in following higher order molecular complex formation. *Biophysical journal*, 86(1):506–516, 2004.

[90] Holly M. Wobma, Megan L. Blades, Ekaterina Grekova, Dylan L. McGuire, Kun Chen, Warren C. W. Chan, and David T. Cramb. The development of direct multicolour fluorescence cross-correlation spectroscopy: Towards a new tool for tracking complex biomolecular events in real-time. *Physical Chemistry Chemical Physics*, 14(10):3290, 2012.

[91] Michael Wahl, Ingo Gregor, Mattias Patting, and Jörg Enderlein. Fast calculation of fluorescence correlation data with asynchronous time-correlated single-photon counting. *Optics Express*, 11(26):3583–3591, 2003.

[92] Davide Magatti and Fabio Ferri. 25 ns software correlator for photon and fluorescence correlation spectroscopy. *Review of Scientific Instruments*, 74(2):1135, 2003.

[93] Emmanuel Schaub. High countrate real-time FCS using F2cor. *Optics Express*, 21(20):23543, October 2013.

[94] Klaus Schätzel. New concepts in correlator design. In *Inst. Phys. Conf. Ser*, volume 77, page 40, 1985.

[95] Thorsten Wohland, Rudolf Rigler, and Horst Vogel. The standard deviation in fluorescence correlation spectroscopy. *Biophysical journal*, 80(6):2987–2999, 2001.

[96] Hande Ozgen, Waldemar Schrimpf, Jelle Hendrix, Jenny C. de Jonge, Don C. Lamb, Dick Hoekstra, Nicoletta Kahya, and Wia Baron. The Lateral Membrane Organization and Dynamics of Myelin Proteins PLP and MBP Are Dictated by Distinct Galactolipids and the Extracellular Matrix. *PLoS ONE*, 9(7):e101834, July 2014.

[97] Franziska Doll, Annette Buntz, Anne-Katrin Späte, Verena F. Schart, Alexander Timper, Waldemar Schrimpf, Christof R. Hauck, Andreas Zumbusch, and Valentin Wittmann. Visualization of Protein-Specific Glycosylation inside Living Cells. *Angewandte Chemie International Edition*, 55(6):2262–2266, February 2016.

[98] Jelle Hendrix, Viola Baumgartel, Waldemar Schrimpf, Sergej Ivanchenko, Michelle A. Digman, Enrico Gratton, Hans-Georg Krausslich, Barbara Muller,

and Don C. Lamb. Live-cell observation of cytosolic HIV-1 assembly onset reveals RNA-interacting Gag oligomers. *The Journal of Cell Biology*, 210(4):629–646, August 2015.

[99] Hong-Cai Zhou, Jeffrey R. Long, and Omar M. Yaghi (Editors). Theme Issue: Metal-Organic Frameworks. *Chemical Reviews*, 2:673–1268, 2012.

[100] Hong-Cai Zhou and Susumu Kitagawa (Editors). Theme Issue: Metal-Organic Frameworks. *Chemical Society Reviews*, 43:5403–6176, 2014.

[101] Hiroyasu. Furukawa, Kyle E. Cordova, Michael O'Keeffe, and Omar M. Yaghi. The Chemistry and Applications of Metal-Organic Frameworks. *Science*, 341(6149):1230444–1230444, August 2013.

[102] Gerard Ferey. Hybrid porous solids: past, present, future. *Chemical Society Reviews*, 37(1):191, 2008.

[103] Seth M. Cohen. Postsynthetic Methods for the Functionalization of Metal-Organic Frameworks. *Chemical Reviews*, 112(2):970–1000, February 2012.

[104] Jack D. Evans, Christopher J. Sumby, and Christian J. Doonan. Post-synthetic metalation of metal-organic frameworks. *Chem. Soc. Rev.*, 43(16):5933–5951, April 2014.

[105] Olga Karagiaridi, Wojciech Bury, Joseph E. Mondloch, Joseph T. Hupp, and Omar K. Farha. Solvent-Assisted Linker Exchange: An Alternative to the De Novo Synthesis of Unattainable Metal-Organic Frameworks. *Angewandte Chemie International Edition*, 53(18):4530–4540, April 2014.

[106] Pravas Deria, Joseph E. Mondloch, Olga Karagiaridi, Wojciech Bury, Joseph T. Hupp, and Omar K. Farha. Beyond post-synthesis modification: evolution of metal-organic frameworks via building block replacement. *Chem. Soc. Rev.*, 43(16):5896–5912, April 2014.

[107] Carl K. Brozek and Mircea Dinca. Cation exchange at the secondary building units of metal-organic frameworks. *Chem. Soc. Rev.*, 43(16):5456–5467, May 2014.

[108] Florian M. Hinterholzinger, Bastian Rühle, Stefan Wuttke, Konstantin Karaghiosoff, and Thomas Bein. Highly sensitive and selective fluoride detection in water through fluorophore release from a metal-organic framework. *Scientific Reports*, 3:2562–2568, September 2013.

[109] Zhenqiang Wang and Seth M. Cohen. Tandem Modification of Metal-Organic Frameworks by a Postsynthetic Approach. *Angewandte Chemie*, 120(25):4777–4780, June 2008.

[110] Hexiang Deng, Christian J. Doonan, Hiroyasu Furukawa, Ricardo B. Ferreira, John Towne, Carolyn B. Knobler, Bo Wang, and Omar M. Yaghi. Multiple Functional Groups of Varying Ratios in Metal-Organic Frameworks. *Science*, 327(5967):846–850, February 2010.

[111] Hiroyasu Furukawa, Ulrich Müller, and Omar M. Yaghi. "Heterogeneity within Order" in Metal-Organic Frameworks. *Angewandte Chemie International Edition*, 54(11):3417–3430, March 2015.

[112] Waldemar Schrimpf, Giulia Ossato, Patrick Hirschle, Stefan Wuttke, and Don C. Lamb. Investigation of the Co-Dependence of Morphology and Fluorescence Lifetime in a Metal-Organic Framework. *Small*, May 2016.

[113] Gerard Ferey, Caroline Mellot-Draznieks, Christian Serre, Franck Millange, Julien Dutour, Suzy Surble, and Irena Margiolaki. A chromium terephthalate-based solid with unusually large pore volumes and surface area. *Science*, 309(5743):2040–2042, 2005.

[114] Dan Lupu, Ovidiu Ardelean, Gabriela Blanita, Gheorghe Borodi, Mihaela D. Lazar, Alexandru R. Biris, Coldea Ioan, Maria Mihet, Ioan Misan, and Gabriel Popeneciu. Synthesis and hydrogen adsorption properties of a new iron based porous metal-organic framework. *international journal of hydrogen energy*, 36(5):3586–3592, 2011.

[115] Pablo Serra-Crespo, Enrique V. Ramos-Fernandez, Jorge Gascon, and Freek Kapteijn. Synthesis and Characterization of an Amino Functionalized MIL-101(Al): Separation and Catalytic Properties. *Chemistry of Materials*, 23(10):2565–2572, May 2011.

[116] Martin Hartmann and Marcus Fischer. Amino-functionalized basic catalysts with MIL-101 structure. *Microporous and Mesoporous Materials*, 164:38–43, December 2012.

[117] Christian Dietl, Henrik Hintz, Bastian Rühle, Jörn Schmedt auf der Günne, Heinz Langhals, and Stefan Wuttke. Switch-On Fluorescence of a Perylene-Dye-Functionalized Metal-Organic Framework through Postsynthetic Modification. *Chemistry - A European Journal*, 21(30):10714–10720, July 2015.

[118] Henrik Hintz and Stefan Wuttke. Solvent-Free and Time Efficient Post-synthetic Modification of Amino-Tagged Metal-Organic Frameworks with Carboxylic Acid Derivatives. *Chemistry of Materials*, 26(23):6722–6728, December 2014.

[119] Martin Hammer, Dietrich Schweitzer, Sandra Richter, and Ekkehart Königsdörffer. Sodium fluorescein as a retinal pH indicator? *Physiological Measurement*, 26(4):N9–N12, August 2005.

[120] Matthia A. Karreman, Inge L. C. Buurmans, John W. Geus, Alexandra V. Agronskaia, Javier Ruiz-Martinez, Hans C. Gerritsen, and Bert M. Weckhuysen. Integrated Laser and Electron Microscopy Correlates Structure of Fluid Catalytic Cracking Particles to Brönsted Acidity. *Angewandte Chemie International Edition*, 51(6):1428–1431, February 2012.

[121] Matthia A. Karreman, Inge L. C. Buurmans, Alexandra V. Agronskaia, John W. Geus, Hans C. Gerritsen, and Bert M. Weckhuysen. Probing the Different Life Stages of a Fluid Catalytic Cracking Particle with Integrated Laser and Electron Microscopy. *Chemistry - A European Journal*, 19(12):3846–3859, March 2013.

[122] Jasmina Hafizovic Cavka, Soren Jakobsen, Unni Olsbye, Nathalie Guillou, Carlo Lamberti, Silvia Bordiga, and Karl Petter Lillerud. A New Zirconium Inorganic Building Brick Forming Metal Organic Frameworks with Exceptional Stability. *Journal of the American Chemical Society*, 130(42):13850–13851, October 2008.

[123] Sachin Chavan, Jenny G. Vitillo, Diego Gianolio, Olena Zavorotynska, Bartolomeo Civalleri, Soren Jakobsen, Merete H. Nilsen, Loredana Valenzano, Carlo Lamberti, Karl Petter Lillerud, and Silvia Bordiga. H_2 storage in isostructural UiO-67 and UiO-66 MOFs. *Phys. Chem. Chem. Phys.*, 14(5):1614–1626, 2012.

[124] Michael J. Katz, Zachary J. Brown, Yamil J. Colon, Paul W. Siu, Karl A. Scheidt, Randall Q. Snurr, Joseph T. Hupp, and Omar K. Farha. A facile synthesis of UiO-66, UiO-67 and their derivatives. *Chemical Communications*, 49(82):9449, 2013.

[125] Greig C. Shearer, Stian Forselv, Sachin Chavan, Silvia Bordiga, Karina Mathisen, Morten Bjorgen, Stian Svelle, and Karl Petter Lillerud. In Situ Infrared Spectroscopic and Gravimetric Characterisation of the Solvent Removal and Dehydroxylation of the Metal Organic Frameworks UiO-66 and UiO-67. *Topics in Catalysis*, 56(9-10):770–782, June 2013.

[126] Min Kim and Seth M. Cohen. Discovery, development, and functionalization of Zr(iv)-based metal-organic frameworks. *CrystEngComm*, 14(12):4096–4104, 2012.

[127] C. Michael McGuirk, Michael J. Katz, Charlotte L. Stern, Amy A. Sarjeant, Joseph T. Hupp, Omar K. Farha, and Chad A. Mirkin. Turning On Catalysis: Incorporation of a Hydrogen-Bond-Donating Squaramide Moiety into a Zr Metal-Organic Framework. *Journal of the American Chemical Society*, 137(2):919–925, January 2015.

[128] Min Kim, John F. Cahill, Yongxuan Su, Kimberly A. Prather, and Seth M. Cohen. Postsynthetic ligand exchange as a route to functionalization of inert metal-organic frameworks. *Chem. Sci.*, 3(1):126–130, 2012.

[129] Paul W. Siu, Zachary J. Brown, Omar K. Farha, Joseph T. Hupp, and Karl A. Scheidt. A mixed dicarboxylate strut approach to enhancing catalytic activity of a de novo urea derivative of metal-organic framework UiO-67. *Chemical Communications*, 49(93):10920, 2013.

[130] Shunzhi Wang, William Morris, Yangyang Liu, C. Michael McGuirk, Yu Zhou, Joseph T. Hupp, Omar K. Farha, and Chad A. Mirkin. Surface-Specific Functionalization of Nanoscale Metal-Organic Frameworks. *Angewandte Chemie International Edition*, 54(49):14738–14742, December 2015.

[131] Antonella Viola, Susanne Schroeder, Yoichi Sakakibara, and Antonio Lanzavecchia. T lymphocyte costimulation mediated by reorganization of membrane microdomains. *Science*, 283(5402):680–682, 1999.

[132] F Tablin. Membrane Reorganization during Chilling: Implications for Long-Term Stabilization of Platelets. *Cryobiology*, 43(2):114–123, September 2001.

[133] Winfried Römer, Lea-Laetitia Pontani, Benoit Sorre, Carles Rentero, Ludwig Berland, Valerie Chambon, Christophe Lamaze, Patricia Bassereau, Cecile Sykes, Katharina Gaus, and Ludger Johannes. Actin Dynamics Drive Membrane Reorganization and Scission in Clathrin-Independent Endocytosis. *Cell*, 140(4):540–553, February 2010.

[134] A. J. Garcia-Saez, S. B. Buschhorn, H. Keller, G. Anderluh, K. Simons, and P. Schwille. Oligomerization and Pore Formation by Equinatoxin II Inhibit Endocytosis and Lead to Plasma Membrane Reorganization. *Journal of Biological Chemistry*, 286(43):37768–37777, October 2011.

[135] Takahiro Fujiwara, Ken Ritchie, Hideji Murakoshi, Ken Jacobson, and Akihiro Kusumi. Phospholipids undergo hop diffusion in compartmentalized cell membrane. *The Journal of Cell Biology*, 157(6):1071–1082, June 2002.

[136] Kenichi Suzuki, Ken Ritchie, Eriko Kajikawa, Takahiro Fujiwara, and Akihiro Kusumi. Rapid Hop Diffusion of a G-Protein-Coupled Receptor in the Plasma Membrane as Revealed by Single-Molecule Techniques. *Biophysical Journal*, 88(5):3659–3680, May 2005.

[137] Adam D. Douglass and Ronald D. Vale. Single-Molecule Microscopy Reveals Plasma Membrane Microdomains Created by Protein-Protein Networks that Exclude or Trap Signaling Molecules in T Cells. *Cell*, 121(6):937–950, June 2005.

[138] Didier Marguet, Pierre-Francois Lenne, Herve Rigneault, and Hai-Tao He. Dynamics in the plasma membrane: how to combine fluidity and order. *The EMBO journal*, 25(15):3446–3457, 2006.

[139] Christian Eggeling, Christian Ringemann, Rebecca Medda, Günter Schwarzmann, Konrad Sandhoff, Svetlana Polyakova, Vladimir N. Belov, Birka Hein, Claas von Middendorff, Andreas Schönle, and Stefan W. Hell. Direct observation of the nanoscale dynamics of membrane lipids in a living cell. *Nature*, 457(7233):1159–1162, February 2009.

[140] Felix Höfling and Thomas Franosch. Anomalous transport in the crowded world of biological cells. *Reports on Progress in Physics*, 76(4):046602, April 2013.

[141] J. K. Millar. DISC1 and PDE4b Are Interacting Genetic Factors in Schizophrenia That Regulate cAMP Signaling. *Science*, 310(5751):1187–1191, November 2005.

[142] Kaspar Mossman and Jay Groves. Micropatterned supported membranes as tools for quantitative studies of the immunological synapse. *Chem. Soc. Rev.*, 36(1):46–54, 2007.

[143] Nina C. Hartman, Jeffrey A. Nye, and Jay T. Groves. Cluster size regulates protein sorting in the immunological synapse. *Proceedings of the National Academy of Sciences*, 106(31):12729–12734, 2009.

[144] Christopher V. Kelly and Harold G. Craighead. Nanofabrication for the Analysis and Manipulation of Membranes. *Annals of Biomedical Engineering*, 40(6):1356–1366, June 2012.

[145] J. T. Groves, N. Ulman, and S. G. Boxer. Micropatterning fluid lipid bilayers on solid supports. *Science (New York, N.Y.)*, 275(5300):651–653, January 1997.

[146] Jay T. Groves, Nick Ulman, Paul S. Cremer, and Steven G. Boxer. Substrate-membrane interactions: mechanisms for imposing patterns on a fluid bilayer membrane. *Langmuir*, 14(12):3347–3350, 1998.

[147] T. Lohmüller, L. Iversen, M. Schmidt, C. Rhodes, H.-L. Tu, W.-C. Lin, and J. T. Groves. Single Molecule Tracking on Supported Membranes with Arrays of Optical Nanoantennas. *Nano Letters*, 12(3):1717–1721, March 2012.

[148] Jones Tsai, Eileen Sun, Yuan Gao, James C. Hone, and Lance C. Kam. Non-Brownian Diffusion of Membrane Molecules in Nanopatterned Supported Lipid Bilayers. *Nano Letters*, 8(2):425–430, February 2008.

[149] Paul Müller, Petra Schwille, and Thomas Weidemann. Pycorrfit - generic data evaluation for fluorescence correlation spectroscopy. *Bioinformatics*, page btu328, 2014.

[150] Steve Wolter, Anna Löschberger, Thorge Holm, Sarah Aufmkolk, Marie-Christine Dabauvalle, Sebastian van de Linde, and Markus Sauer. rapidSTORM: accurate, fast open-source software for localization microscopy. *Nature Methods*, 9(11):1040–1041, November 2012.

[151] Software package for multiparameter fluorescence spectroscopy, full correlation and multiparameter fluorescence imaging. http:\\www.mpc.hhu.de\software\csoftware-package.html. Accessed: 20 June 2016.

Appendix A: Abbreviations

2fFCCs	Two-focus fluorescence cross-correlation spectroscopy
ACF	Auto-correlation function
ADC	Analogue-to-digital converter
APD	Avalanche photodiode
BET	Brunauer–Emmett–Teller
BDC	1,4-benzenedicarboxylate
CCF	Cross-correlation function
ccRICS	Raster image cross-correlation spectroscopy
DMF	Dimethylformamide
DMSO	Dimethyl sulfoxide
DNA	Deoxyribonucleic acid
DOPC	1,2-dioleoyl-sn-glycero-3-phosphocholine
DPPE	1,2-Dipalmitoyl-sn-glycero-3-phosphoethanolamine
eGFP	Enhanced green fluorescence protein
EMCCD	Electron multiplying charge-coupled device
FCA	Fluorescence cumulant analysis
FCS	Fluorescence correlation analysis
FCCS	Fluorescence corr-correlation spectroscopy
FFS	Fluorescence fluctuation spectroscopy
FFT	Fast Fourier transformation
FITC	Fluorescein isothiocyanate
FLIM	Fluorescence lifetime image microscopy
FRET	Förster resonance energy transfer
Gag	Group specific antigen
GalC	Galactosylceramide
GUI	Graphical user interface
H_2BPDC	Biphenyl-4,4'-dicarboxylic acid
HIV	Human immunodeficiency virus
IC	Internal conversion
ICCS	Image cross-correlation spectroscopy
ICS	Image correlation spectroscopy
iMSD	Image mean square displacement
IR	Infrared
IRF	Instrument response function
ISC	Inter-system crossing
LSCM	Laser scanning confocal microscopy/microscope
LUV	Large unilamellar vesicles
MBP	Myelin basic protein
MNT	Mobile Thirty-Nine
MOF	Metal-organic framework

MTV	Multivariate
N&B	Number and brightness analysis
NA	Numerical aperture
PBS	Phosphate buffered saline
PCF	Pair correlation function
PCH	Photon counting histogram
PET	Photo electron transfer
PFS	Perfect focus system
PXRD	Powder X-ray diffractometry
PIE	Pulsed interleaved excitation
PLP	Myelin proteolipid protein
PMMA	Poly(methyl methacrylate)
PMT	Photomultiplier tube
PSD	Position sensing detector
PSF	Point spread function
PSM	Post-synthetic modification
RGB	Red green blue
RICS	Raster image correlation spectroscopy
ROTC	Rhodamine B isothiocyanate
RNA	Ribonucleic acid
ROI	Region of interest
SALE	Solvent assisted linker exchange
SBU	Secondary building unit
SEM	Scanning electron microscopy
SPAD	Single-photon avalanche diode
ST	Super-tetrahedron
STICS	Spatio-temporal image correlation spectroscopy
TAC	Time-to-amplitude converter
TCSPC	Time correlated single photon counting
TDC	Time-to-digital converter
TICS	Temporal image correlation spectroscopy
TIFF	Tagged image file format

Appendix B: Filters

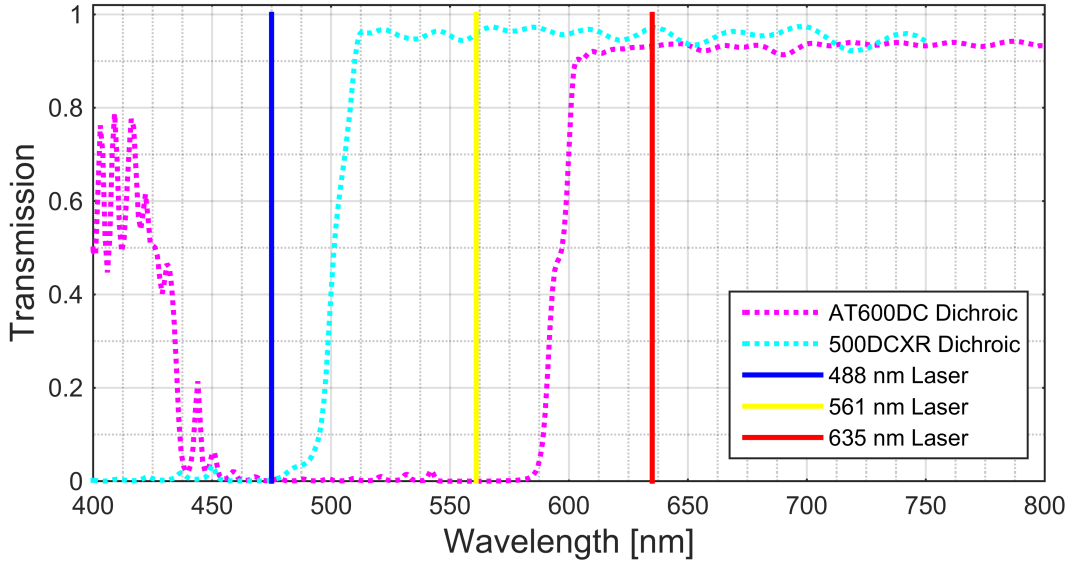

Figure B.1: Transmission spectra of the dichroic mirrors, AT600DC (magenta dotted line) and 500DCXR (cyan dotted line), used for combining the excitation lasers. The three solid lines show the wavelengths of the excitation lasers at 488 nm (blue), 561 nm (yellow) and 635 nm (red).

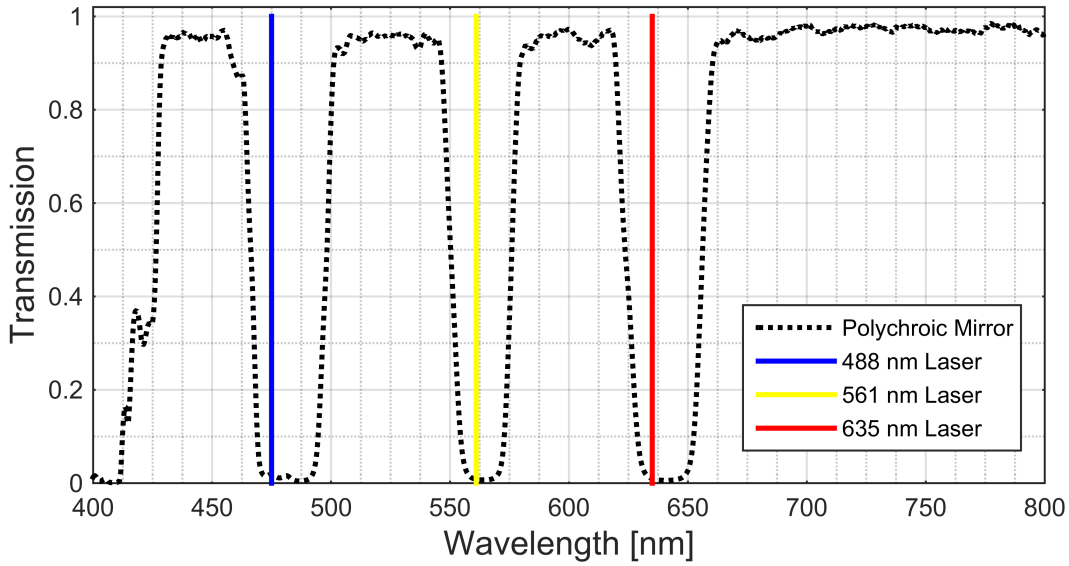

Figure B.2: Transmission spectra of the polychroic mirror,Di01-R405/488/561/635, gray dotted line), used for the separation of excitation and fluorescence light. The three solid lines show the wavelengths of the excitation lasers at 488 nm (blue), 561 nm (yellow) and 635 nm (red).

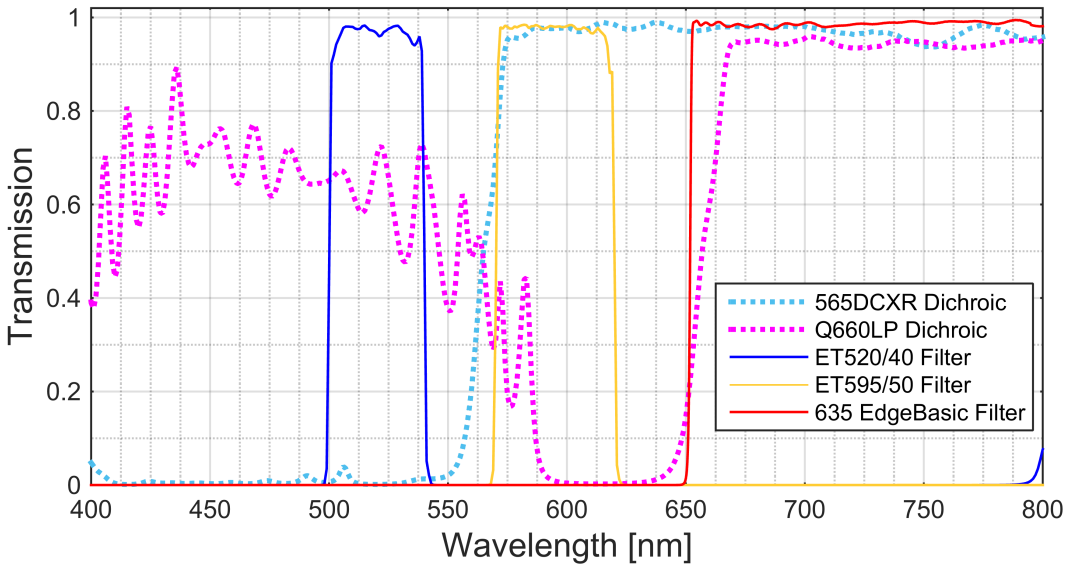

Figure B.3: Transmission spectra of the filters and polychroic mirrors used for fluorescence detection. The 565DCXR dichroic mirror (cyan dotted line) reflects the blue/green spectrum , while the Q660LP dichroic mirror reflects the orange/red light. The emission filters ET520/40, ET595/50 and 635 EdgeBasic are used in the blue/green, organge/red and red/IR detection channels, respectively.

Appendix C: Additional Data

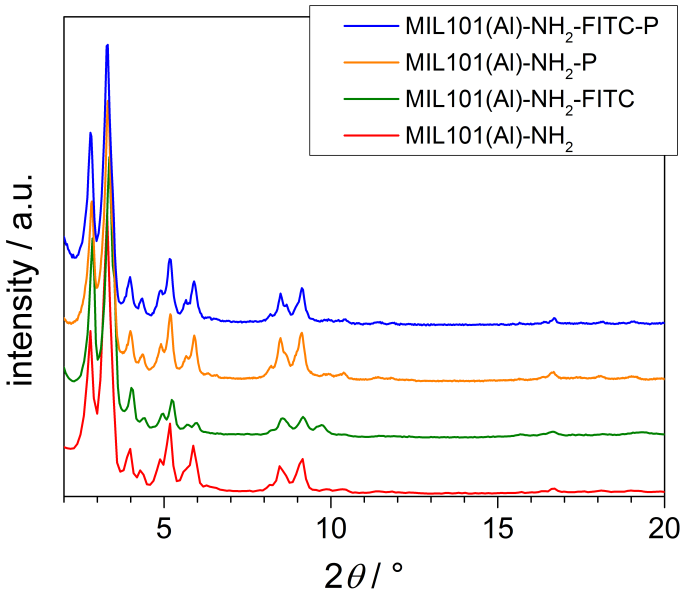

Figure C.1: X-ray powder diffraction patterns of *Type I* MIL-101(Al)-NH_2, MIL-101(Al)-NH_2-FITC, MIL-101(Al)-NH_2-P and MIL-101(Al)-NH_2-FITC/P.

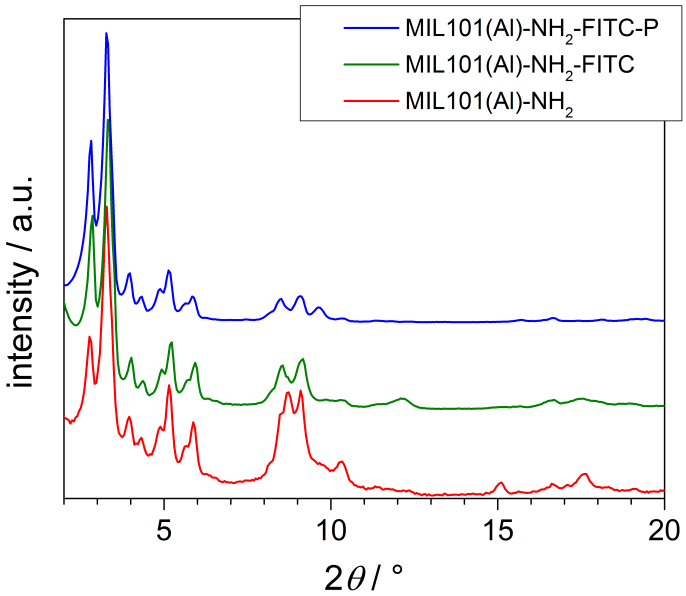

Figure C.2: X-ray powder diffraction patterns of *Type II* MIL-101(Al)-NH_2, MIL-101(Al)-NH_2-FITC, and MIL-101(Al)-NH_2-FITC/P.

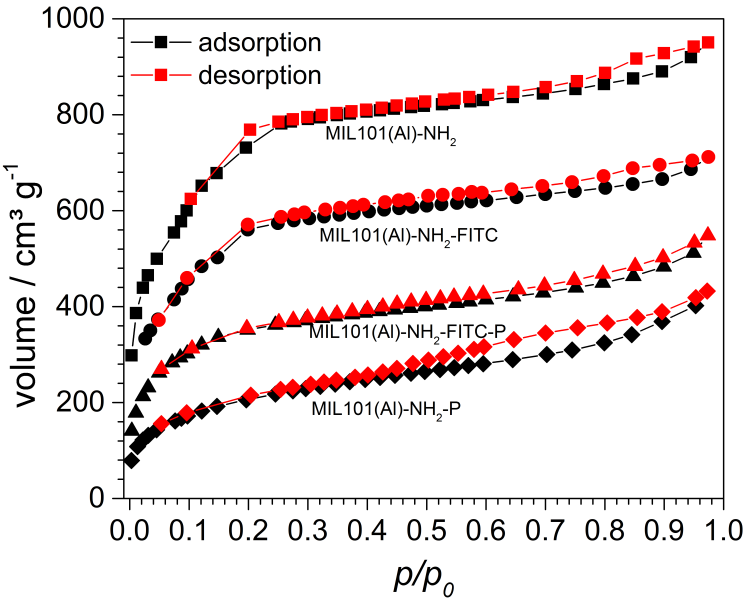

Figure C.3: Nitrogen sorption isotherms at 77 K of *Type I* MIL-101(Al)-NH_2, MIL-101(Al)-NH_2-FITC, MIL-101(Al)-NH_2-P and MIL-101(Al)-NH_2-FITC/P.

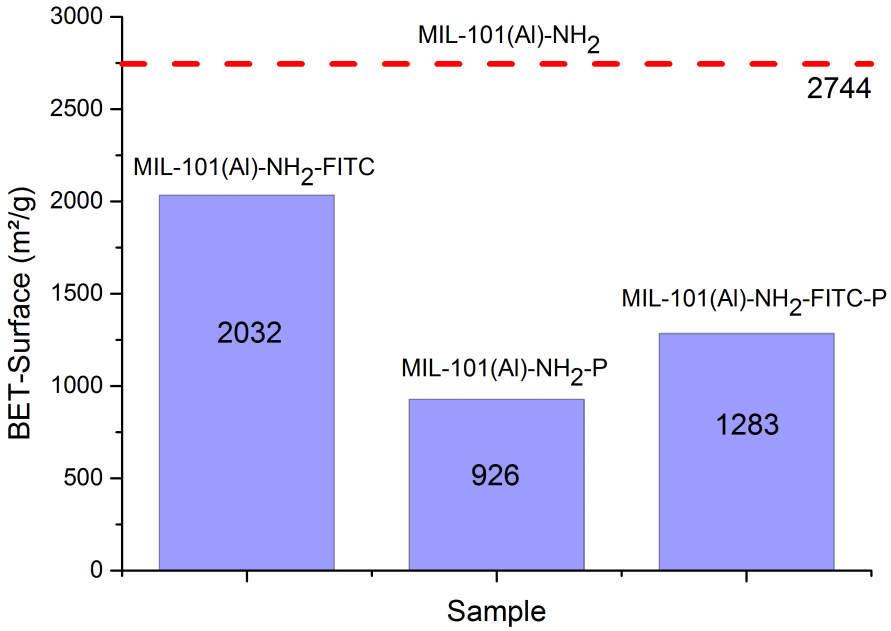

Figure C.4: BET surface areas of all samples calculated from the nitrogen sorption isotherms shown in Figure C.3 of *Type I* MIL-101(Al)-NH_2 samples.

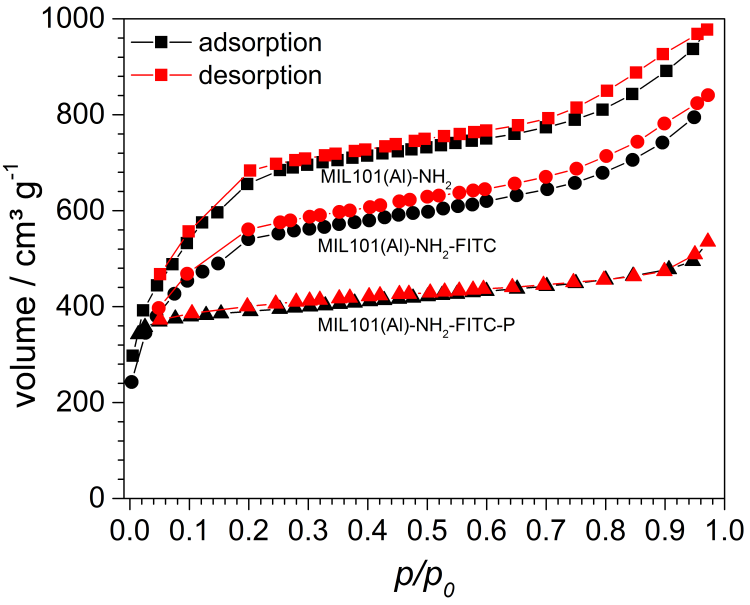

Figure C.5: Nitrogen sorption isotherms at 77 K of *Type II* MIL-101(Al)-NH_2, MIL-101(Al)-NH_2-FITC, and MIL-101(Al)-NH_2-FITC/P.

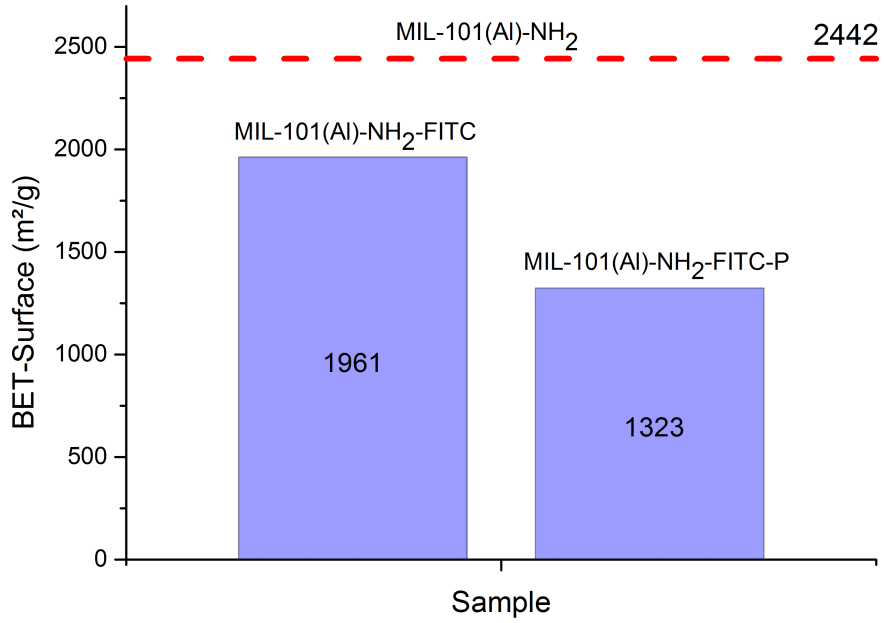

Figure C.6: BET surface areas of all samples calculated from the nitrogen sorption isotherms shown in Figure C.5 of *Type II* MIL-101(Al)-NH_2 samples.

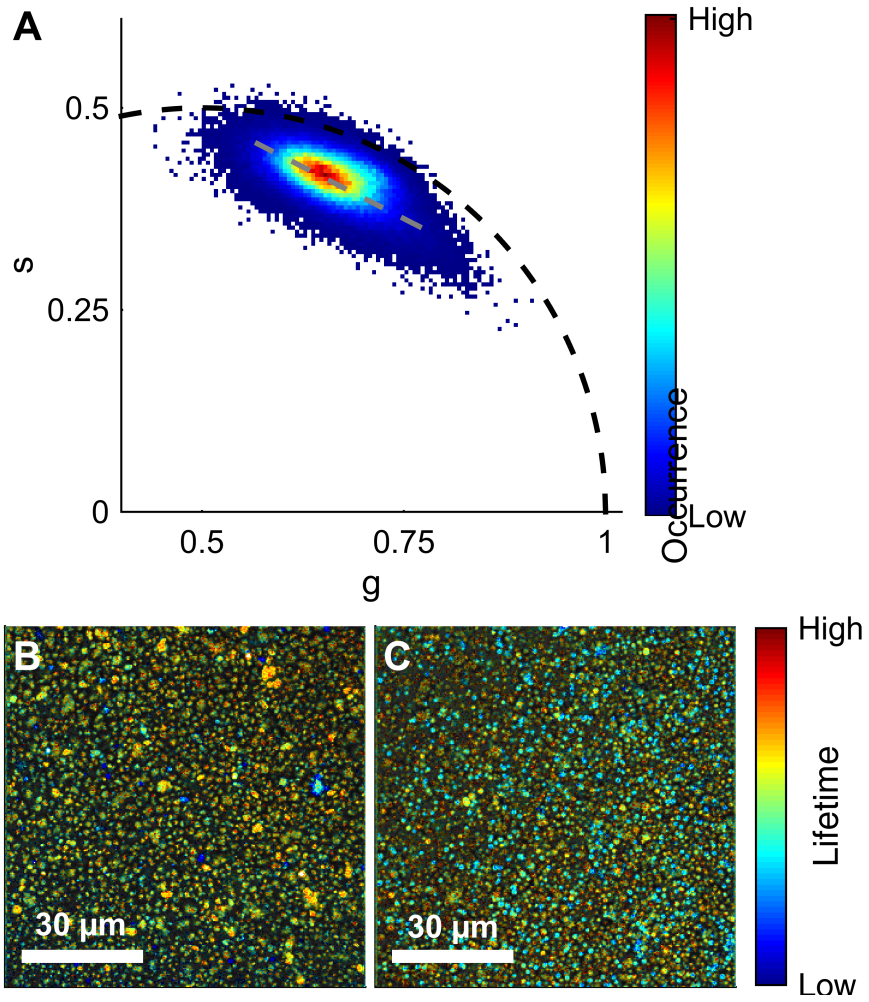

Figure C.7: Phasor data of unmodified UiO-67 autofluorescence synthesized with method 1 (B) and method 2 (C). The color code of the images corresponds to the position on the gray dashed line in the phasor plot (A). Here, blue and cyan colors are positioned at the bottom left and red and orange hues at the top right of the line.

Acknowledgments

A Doctoral thesis is not something that can be done overnight and definitely not without help. It took me six years to get here and it would not have been possible without all the people who helped and supported me, gave me advise, challenged me or sometimes just provided a well needed distraction.

At first I have to thank my thesis adviser Prof. Don C. Lamb, who gave me the opportunity to do my PhD in his lab. Thank you for having patience with me and giving me the time to find my own approach to the projects, even if in the end not all of them were successful. It was always encouraging to know that the success and wellbeing of your student is your priority.

I also have to thank my second adviser, Prof. Christoph Bräuchle, who always showed great interest in my project, even when they did not overlap with his field of research.

These thanks are extended to Prof. Joachim Rädler, Prof. Achim Hartschuh, Prof. Regina de Vivie-Riedle and Prof. Joost Wintterlin for reviewing my thesis.

I gratefully acknowledge the various agencies - SFP1032, NIM and CeNS - for funding my work and for offering a variety of informative and enjoyable seminars, workshops and events.

I thank all my collaborators whose work made my research possible. For the MOF projects I have to thank JJ, Patrick a especially Stefan whose enthusiasm was very infectious. I have to thank Dr. Theobald Lohmüller, Dr. Paul Kühler and Anastasia Babynina, who provided me with samples and many interesting discussion for the chrome nanostructures project. I also have to thank Paul Heissig and all the others for working with me on projects that did not make it into this thesis.

I thank all the people who visited our lab and with whom I had the pleasure to work - Oh, Dani, Hande and Alex. Not all our work bore fruits, but it was always challenging and fun.

I have to give a very big thank you to all colleagues, both current - Adriano, Alvaro, Anders, Bässem, Chen, Daniela, Ellen, Evelyn, Fabian, Ganesh, Ivo, Jens, Kira, Lena, Leonhard, Nader, Maria, Philipp, Sushi, Viola - and former - Doro, Giulia, Gregor, Jelle, Niko, Matthias, Martin, Sergej, Vova, and all the people for the AK Bräuchle and AK Michaelis. Science can be very tiresome and frustrating, but you made it not only bearable but also rewarding and fun. And thank you for

all the discussions, about science and beyond, especially since they often resembled monologues. Thank you for not only being great colleagues, but also friends.
I have to especially thank Lena, who is the best office mate one can hope for and an amazing friend. Lena, I forgive you for finishing before me; you really earned it.
Thank you Ellen for all the great times, the holidays and your memorable parties.
Thank you Jelle for being a mentor, even though you were the one who asked all the questions.
Thank you Anders for listening to all my questions and sorry for keeping you from your work.
Thank you Martin and Matthias for showing me the ropes when I was just a young PhD student, as unbelievable as it sounds now.
I have to thank my boulder group, Ellen, Lena and Philipp, the television group, Anders, Ellen, Kira and Nader, and all the people from the movie group. Sometimes I just needed to not think about work.

I thank my non-work friends - Consti, Dani, Flo, Joe and Linus. Although we don't see each other that much anymore, it is still a great fun when we do.

Zum Schluß muss ich den aller größten Dank an meine Familie richten, an meine Eltern Waldemar und Lydia, und an meinen Bruder Eugen. Ihr wart immer für mich da und habt mich mein Leben lang unterstützt. Ich weiß nicht, wie mein Leben ohne euch wäre, und ich möchte es auch gar nicht wissen.